

**DESIGN AND DEVELOPMENT OF AN IMPLANTABLE DRUG DELIVERY POLYMERIC
SCAFFOLD FOR THE TREATMENT OF PARKINSON'S DISEASE**

SAMANTHA PILLAY



A dissertation submitted to the Faculty of Health Sciences, University of the
Witwatersrand, in fulfillment of the requirements for the degree of

Master of Pharmacy

Supervisor:

Professor Viness Pillay
University of the Witwatersrand
Department of Pharmacy and Pharmacology
South Africa

Co-Supervisors:

Professor Michael P. Danckwerts, University of the Witwatersrand,
Department of Pharmacy and Pharmacology, South Africa
Professor Girish Modi, University of the Witwatersrand, Department of Neurology, Division of
Neurosciences, South Africa
Professor Sunny E. Iyuke, University of the Witwatersrand, School of Chemical and
Metallurgical Engineering, South Africa

Johannesburg, 2009

DECLARATION

I, Samantha Pillay declare that this dissertation is my own work. It has being submitted for the degree of Master of Pharmacy in the Faculty of Health Sciences in the University, Johannesburg. It has not submitted before for any degree or examination at this or any other University.

.....

This.....day of May 2009

RESEARCH PRESENTATIONS

POSTERS

Synthesis, Characterization and Preliminary Evaluation of Hydrophilic Nanoparticles and Scaffolds for Controlled Drug Delivery.

Samantha Pillay, Viness Pillay, Yahya E. Choonara and Michael P. Danckwerts.

Conference of the Academy of Pharmaceutical Sciences, Johannesburg, South Africa, September 2006.

Formulation of Polymeric Nanoparticles Intended for Intracranial Implantation.

Samantha Pillay, Viness Pillay, Yahya E. Choonara and Michael P. Danckwerts.

Conference of the South African Nanotechnology Initiative: NanoAfrica, Cape Town, South Africa, 26th - 29th November 2006.

Influence on Drug Molecular Structure on the Formation of Nanotubes.

Samantha Pillay, Viness Pillay, Yahya E. Choonara.

Conference of the Neurological Association of South Africa: Innovative and Practical Congress, Johannesburg, South Africa, 28th - 31st March 2007.

Design and Evaluation of Dopamine (DA) Nanoparticles Dispersed within a Scaffold.

Samantha Pillay, Viness Pillay, Yahya E. Choonara and Michael P. Danckwerts. Conference of the Controlled Release Society, Los Angeles, United States of America, 7th - 11th July 2007.

Electrospinning of DA-loaded Nanofibers.

Samantha Pillay, Viness Pillay, Yahya E. Choonara, Girish Modi and Sunny E. Iyuke.

Conference of the Academy of Pharmaceutical Sciences, Cape Town, South Africa, 4th - 7th September 2007.

Targeted Delivery of Dopamine to the Brain via an Implantable Nano-enabled Heterogeneously Designed Multi-Polymeric Device,

Samantha Pillay, Viness Pillay, Yahya E. Choonara, Girish Modi, Dinesh Naidoo and Sunny E. Iyuke.

9th US-Japan Symposium on Drug Delivery, Maui, Hawaii, 16th – 20th December 2007.

PODIUM

Determination of Size and Electrokinetic Stability of Dopamine (DA)-loaded Cellulose Acetate Phthalate Nanoparticles.

Samantha Pillay, Viness Pillay, Yahya E. Choonara, Girish Modi, Michael P. Danckwerts and Sunny E. Iyuke.

Joint Symposium for Chemical and Metallurgical Engineering, University of Pretoria, 3rd - 4th August 2007.

An Experimental Design Approach for Optimizing Dopamine-loaded Cellulose Acetate Phthalate Nanoparticles and Barium-Alginate Scaffolds for Intracranial Implantation.

Samantha Pillay, Viness Pillay, Yahya E. Choonara, Girish Modi, Michael P. Danckwerts and Sunny E. Iyuke.

Therapeutic Sciences Research Day, University of the Witwatersrand, 24th – 25th August 2007.

In Vitro and *In Vivo* Evaluation of Dopamine-loaded Cellulose Acetate Phthalate Nanoparticles Dispersed within a Scaffold for Intracranial Implantation.

Samantha Pillay, Viness Pillay, Yahya E. Choonara, Girish Modi, Dinesh Naidoo and Sunny E. Iyuke.

Presentation at the Pharmaceutical Society of South Africa (PSSA) Adcock Ingram Young Scientist Competition 2007, Conference of the Academy of Pharmaceutical Sciences, Cape Town, South Africa, 4th - 7th September 2007. Awarded First Runner-up position.

PATENTS

Polymeric Configuration for Site-Specific Drug Delivery.

Viness Pillay, Sheri-lee Harilall Samantha Pillay, Yahya E. Choonara, Girish M. Modi, Sunny E. Iyuke and Dinesh Naidoo, South Africa, Patent Application Filed, awaiting priority date.

ABSTRACT

Parkinson's disease, primarily defined as the depletion of dopaminergic neurons in the substantia nigra of the brain, gives rise to severely debilitating motor symptoms. The pharmacological gold standard treatment for the disease, Levodopa, holds great limitations yet still remains the most effective treatment for the disease for the last 40 years. There has been research into novel drug delivery systems for the treatment of the disease that include the development of implantable devices however none have been introduced onto the market. As the neurodegenerative disorder ravages the younger-aged population so the urgency for the effective chronic treatment of the disease escalates. The field of nanotechnology brings promise for the targeted delivery of drugs which is highly sought after in the treatment of central nervous system disorders. A nano-enabled scaffold device (NESD) incorporating dopamine nanoparticles into a polymeric scaffold for implantation into the brain parenchyma may be able to address and overcome the limitations of the current treatment for Parkinson's disease.

Investigations performed cellulose acetate phthalate dopamine-loaded nanoparticles, employing an adopted emulsification-diffusion approach, produced particles with a notably high drug entrapment efficiency ($63.05 \pm 0.354\%$) and desirable controlled drug release profiles (16.23% in 24hr). The employment of an experimental design, namely the Box-Behnken design, allowed for the attainment of optimized nanoparticles with high zeta potentials ($.34.00\text{mV}$), minimal particle size (197.20nm) and extended mean dissolution times (40.96).

Barium chloride was employed to crosslink calcium-alginate scaffolds formulated in an adopted freeze-drying approach. Highly resilient (63.58 ± 5.13) and porous structures (pore sizes of 100-400 μm) were developed. A statistical approach employing the Box-Behnken design resulted in the formulation of a candidate barium-alginate scaffold displaying maximum matrix resilience (82.46%) and minimal matrix erosion (18.23%) over in 30 days. In addition, dopamine-loaded nanoparticles were dispersed within the scaffold that formed the NESD with the desired drug release profiles (5.12% in 168hr).

Nanosystems of levodopa, nicotine and dopamine nanofibers were preliminary investigated. Drug release profiles for levodopa (4.21%: in 75hr), nicotine (0.42% in 24hrs) and drug entrapment efficiency for the polymeric nanofibers (75-85%) as well as data from scanning electron microscopy, zetasize analysis and drug release studies proved that these systems hold potential for the treatment of the disease and therefore require further investigation.

Ex vivo cytotoxic studies carried out on the NESD and its separate entities proved that the NESD was biocompatible with the white blood (70-80% cell viability in 24hr) and carcinomic brain cells (25% cell viability in 48hr) despite literature reports of dopamine being highly toxic in vivo.

Extensive in vivo studies resulted in the development of a protocol for the surgical implantation of the NESD in the parenchyma of the frontal lobe of the rat brain. Scanning electron microscope images showed the gradual bioerosion (26% in 30 days) of the NESD while histological findings of the brain tissue proved clinically insignificant (absence of ischemia or chronic inflammation). Ultra Liquid Performance Chromatography revealed higher concentrations of dopamine in the CSF of rats which received brain implants of the NESD (28%) than in those administered the oral preparation, Sinemet (0.000012%) in 3 days.

ACKNOWLEDGEMENTS

The author would like to express her gratitude to those without whom this work would not have been possible. To the following people my deepest appreciation:

My eternal appreciation goes to the Almighty Lord, for never letting me down in my times of need. I have felt your love even in the most desperate of times and so fueling my belief in your power.

To my parents, my world, Rodgers and Elizabeth Pillay, the pages of this dissertation is not merely enough to express my love and gratitude to you. Daddy, thank you for trusting me and allowing me the freedom to pursue a path that I felt was right for me. Mummy, thank you for always pushing me far beyond my limits and keeping me humbled. Thank you to both of you for your sacrifices, for always being the best you can be for me and your unconditional love. I pray God blesses me one day with your wisdom as parents. I will continue to make you proud as I pursue my life's journey. I love you.

My late grandmother, Lutchmama Pillay whose physical presence I was so unfortunate not to experience but whose memories and love I feel everyday of my life. A woman whose beauty both inside and out will never be forgotten.

To my grandparents, Manikum Pillay and Stella Naidoo, I am so fortunate to spend my life in your guidance and absolute warmthness. God bless you.

To my supervisor, Professor Viness Pillay, your guidance and perfection have made this work something I am truly most proud of. My best wishes to you as you continue to inspire all those around you.

My advisor and a man to watch out for, Mr. Yahya E. Choonara, the completion of this journey would have been even more difficult without your assistance.

My gratitude goes out to my co-supervisors, Professor Michael P. Danckwerts, Professor Sunny E. Iyuke and Professor Girish Modi. Thank you for your guidance.

A special thank you goes to Dr. Dinesh Naidoo, whose passion for this work was truly inspiring. Thank you for going above and beyond, your expertise added immense value to my research.

My deepest gratitude goes to Dr. Daven Compton and the Mintek Group, for allowing me the use of your facilities that added so much to research, for taking me in as one of your own and for always being available for supervision.

To Dr Hajierah Davids and Helen Panagiotopoulos for their assistance in the cytotoxic studies and their immense hours in the lab.

To my colleagues: Lisa C. du Toit, Neha Singh, Maria Paraskeva, Sheri-Lee Harilall, Sibongile Sibambo, Oluwatoyin A. Kolawole, Bongani Sibeko, Seshni Sewlall, Valence M.K. Ndesendo, Caragh S. Murphy, Deshika Reddy, Priya Bawa, Shivaan Cooppan, Yasien Docrat, Sajida Suleman and Zaheeda Khan- thank you for making the days on campus more bearable, the laughter and advice. My sincere appreciation to Vikesh Rowjee, for being an excellent research partner and always being willing to help. Good luck for your future.

My dear friends, Corinne Joseph and Rakhee Patel, you guys have been there for me through so much. My hope is that our relationship grows old with us. A special thank you is also extended to Shanaaz Goolam and Candice Fick.

To my extended family: Lekesha Padayachee, Vigie Pillay, Mogie Naidoo and Sheruna Naidoo, Pravin Reddy and Megashni Reddy, Palmer Gengan and Devrani Gengan and family – thank you for your support and believing in me.

My appreciation to the Wits staff, thank you for always being there to lend a helping hand and for fixing the mess we made.

To Jonathan Pillay and family, your pride in me is a true inspiration. Thank you for never being able to say no to me. I know I can count on you throughout my life.

To the Central Animal Service Staff at Wits, I really gave you guys a hard time yet you went out of your way to accommodate me and always with a smile.

To my brother, Keegan Pillay, you truly have become someone I can look up to in every sphere of my life. I am humbled by your willingness to always go out of your way for me and your generosity. I am extremely proud of the man you have become and know you are destined for so much more in this lifetime. To Nirisha Pillay, my special thanks for your support.

DEDICATION

This work is dedicated to the late Nivash Singh (18/08/1984-16/01/2009): my fiancé, my best friend and the love of my life. I was so blessed to spend the greatest part of my life with you. You showed me how to be a better person even though I may not always have done a good job. Belief is the strongest motivator/ inspiration and that's what you were and still are to me. Thank you for giving me the strength to complete this work in the time of my greatest sorrow.

Your unselfishness allowed me to be the best I can with you. Thank you for always being honest with me and for teaching me how to be more independent. I am what I am because of you. I will miss you every day of my life. God gave me an angel whose short life will never be forgotten.

Rest in peace my Varshen.
I love you forever and always.



TABLE OF CONTENTS

	Page
1. Introduction	
1.1. Background to this Study	1
1.2. Rationale for this Study	3
1.3. Aim and Objectives of this Study	6
1.4. Overview of this Dissertation	7
2. Current Strategies and Limitations for Drug Delivery to the Brain in the Treatment of Parkinson's Disease	
2.1. Introduction	9
2.1.1. The Physiology of the Blood Brain Barrier	9
2.1.2. Approaches Employed for Drug Delivery to the Brain	10
2.2. Parkinson's Disease: An Overview	19
2.2.1. Possible theories explicating the aetiology of Parkinson's disease	19
2.2.2. Diagnosis of Parkinson's disease	20
2.2.3. Pharmacological treatment of Parkinson's disease	21
2.2.4. Challenges of current therapy used in the treatment of Parkinson's disease	23
2.2.4.1. Limitations of Sinemet [®] for the treatment of Parkinson's disease	23
2.2.4.2. The gap in current therapy employed in the treatment of Parkinson's disease	23
2.2.5. Implantable novel polymeric drug delivery systems for the treatment of Parkinson's disease	24

2.2.5.1.	Levodopa/carbidopa loaded microspheres for implantation into the cerebellum	25
2.2.5.2.	Dopamine-loaded drug delivery systems: microspheres and a silicone pellet into the striatum	25
2.2.6.	Gene therapy	25
2.2.7.	Empirical treatments employed in the treatment of Parkinson's disease	26
2.2.8.	Current surgical approaches for the treatment of Parkinson's disease	28
2.3.	Concluding remarks	31
3.	Development and Formulation of Dopamine-loaded Nanoparticles	
3.1.	Introduction	32
3.2.	Materials and Methods	34
3.2.1.	Materials	34
3.2.1.1.	Technology Applied in the Present Study	34
3.2.1.1.1.	Application of the Zetasizer [®] NanoZS Series Instrument for Nanoparticle Analysis	34
3.2.1.1.2.	The determination of nanoparticle size	34
3.2.1.1.3.	The determination of the zeta potential of nanoparticles	35
3.2.1.2.	Rotavapor [®] R210 (BÜCHI Labortechnik AG, Flawil, Switzerland) with heating bath	37
3.2.1.3.	Identification of ideal processing conditions for successful formulation of nanoparticles	37

3.2.1.3.1. Temperature for polymer solubilization	37
3.2.1.3.2. Stirring time and speed for solvent emulsification	37
3.2.1.4. Preparation of dopamine-loaded cellulose acetate phthalate nanoparticles	38
3.2.1.5. Morphological characterization of dopamine-loaded cellulose acetate phthalate nanoparticles	38
3.2.1.6. Determination of polymeric structural variations due to dopamine-loaded cellulose acetate phthalate nanoparticle formation	38
3.2.1.7. Construction of calibration curves for spectrophotometric determination of dopamine release from cellulose acetate phthalate nanoparticles	39
3.2.1.8. Determination of dopamine entrapment efficiency of cellulose acetate phthalate nanoparticles	39
3.2.1.9. <i>In vitro</i> dopamine release studies on cellulose acetate phthalate nanoparticles	39
3.2.1.10. Determination of size and zeta potential of dopamine-loaded cellulose acetate phthalate nanoparticles	40
3.2.11. Formulation and Statistical Optimization of Nanoparticles	41
3.2.11.1. Determination of limitations for variables employed in the Box-Behnken design	41
3.2.11.2. Optimization of dopamine-loaded cellulose acetate phthalate nanoparticles	42
3.3. Results and Discussion	43

3.3.1.	Surface morphology of dopamine-loaded cellulose acetate phthalate nanoparticles	43
3.3.2	Structural variations present in the formation of dopamine-loaded cellulose acetate phthalate nanoparticles	44
3.3.3.	Calibration curve for dopamine in phosphate buffer solution (pH 6.8; 37°C) for the determination of the concentration of dopamine release from cellulose acetate phthalate nanoparticles	45
3.3. 4.	Dopamine entrapment efficiency of cellulose acetate phthalate nanoparticles	45
3.2.2.5.	<i>In vitro</i> dopamine release of cellulose acetate phthalate nanoparticles	46
3.2.2.6.	Dopamine-loaded cellulose acetate phthalate nanoparticle size and stability	46
3.2.2.6.1.	Size and zeta potential distribution profiles for cellulose acetate phthalate nanoparticles: dopamine- free and dopamine-loaded	47
3.3.7.	Experimental design for the optimization of dopamine-loaded cellulose acetate phthalate nanoparticles	49
3.3.7.1.	Measured responses for the experimental optimization of dopamine-loaded cellulose acetate phthalate nanoparticles	50
3.3.7.2.	Comparison of the experimental and fitted response values calculated for the experimental optimization of dopamine-loaded cellulose acetate phthalate nanoparticles	51
3.3.7.3.	Response analysis of Mean Dissolution Time for dopamine-loaded cellulose acetate phthalate nanoparticles	53

3.3.7.4.	Response analysis for size of dopamine-loaded cellulose acetate phthalate nanoparticles	55
3.3.7.5.	Response analysis for Zeta Potential of dopamine-loaded cellulose acetate phthalate nanoparticles	56
3.3.7.6.	The main and interaction effects on the responses:	57
3.3.7.7.	Analysis of a Box-Behnken design employed for the optimization of dopamine-loaded cellulose acetate phthalate nanoparticles	62
3.3.7.8.	Response optimization of dopamine-loaded cellulose acetate nanoparticles	65
3.3.2.9.	Desirability for the measured responses of the optimized dopamine-loaded cellulose acetate phthalate formulation	67
3.4.	Concluding remarks	68
4.	Formulation of Crosslinked-Alginate Scaffolds for the Design of a Nano-Enabled Scaffold Device	
4.1.	Introduction	69
4.2.	Materials and Methods	72
4.2.1.	Materials	72
4.2.2.	Processing conditions for the development of crosslinked alginate scaffold	72
4.2.2.1.	Temperature for the dissolution of polymer	72
4.2.2.2.	Duration required for the efficient post-curing of crosslinked alginate scaffold	73
4.2.3.	Biometric Simulation of the Nano-Enabled Scaffold Device employing computer-aided prototyping	73

4.2.4.	Preparation of crosslinked alginate scaffold	74
4.2.5.	Textural profile analysis to determine the physicochemical behaviour of the crosslinked scaffold	74
4.2.6.	Morphological characterization of crosslinked alginate scaffold	75
4.2.7.	<i>In vitro</i> Matrix Erosion studies on crosslinked alginate scaffold	75
4.2.8.	Formulation and Statistical Optimization of the Barium-Alginate Scaffolds	76
4.2.8.1.	Determination of limitations for variables employed in a Box-Behnken design	76
4.2.8.2.	Optimization of barium-alginate scaffold	77
4.2.9.	Corporeal assembly of the Nano-Enabled Scaffold Device	77
4.2.10.2.	Assimilation of the dopamine-loaded cellulose acetate phthalate nanoparticles and crosslinked scaffold into the Nano-Enabled Scaffold Device	78
4.2.11.	Determination of <i>in vitro</i> dopamine release from the Nano-Enabled Scaffold Device	80
4.2.12.	Determination of the thermal transition behaviour of the Nano-Enabled Scaffold Device and its constituents	80
4.3.	Results and Discussion	81
4.3.1.	Computer-aided prototyping for Nano-Enabled Scaffold Device design	81
4.3.2.	Matrix Resilience behaviour of crosslinked scaffolds	84
4.3.3.	Surface morphology of crosslinked alginate scaffold	86
4.3.4.	<i>In vitro</i> Matrix Erosion of the barium-alginate scaffold	87

4.3.5.	Experimental design for the optimization of barium-alginate scaffold	88
4.3.5.1.	Measured responses for the experimental optimization of barium- alginate scaffold	89
4.3.5.2.	Comparison of the experimental and fitted responses calculated for the experimental optimization of barium-alginate scaffold	90
4.3.5.3.	Response analysis for Matrix Resilience of barium-alginate scaffold	91
4.3.5.4.	Response analysis for Matrix Erosion of barium-alginate scaffold	91
4.3.5.5.	The main and interaction effects on the responses	92
4.3.5.6.	Analysis of a Box-Behnken design employed for the optimization of barium-alginate scaffold	95
4.3.5.7.	Response optimization of barium-alginate scaffold	98
4.3.5.8.	Desirability for the measured responses of the optimized barium- alginate scaffold formulation	99
4.3.6.	<i>In vitro</i> dopamine release from the Nano-Enabled Scaffold Device	99
4.3.7.	Componential thermal analysis on the Nano-Enabled Scaffold Device	100
4.4.	Concluding Remarks	103
5.	Investigation into Drug-Loaded Nanostructures for the Employment in Treatment of Parkinson's Disease	
5.1.	Introduction	104

5.2.	Investigation of Levodopa-loaded <i>Poly (lactic-co-glycolic acid)</i> Nanoparticles	106
5.2.1.	Materials and Methods	106
5.2.1.1.	Materials	106
5.2.1.2.	Preparation of levodopa-loaded poly (lactic-co-glycolic acid) nanoparticles employing a nano- precipitation technique	106
5.2.4.	Assimilation of levodopa-loaded poly (lactic-co-glycolic acid) nanoparticles and barium-alginate scaffold into the Nano-Enabled Scaffold Device	107
5.2.5.	Determination of levodopa entrapment efficiency of poly (lactic-co-glycolic acid) nanoparticles	107
5.2.6.	In vitro levodopa release studies on poly (lactic-co-glycolic acid) nanoparticles and Nano-Enabled Scaffold Device	108
5.2.7.	Morphological characterization of levodopa poly (lactic-co-glycolic acid) nanoparticles	108
5.2.8.	Determination of polymeric structural variations due to levodopa poly (lactic-co-glycolic acid) nanoparticle formation	108
5.2.8.	Determination of size and zeta potential of levodopa-loaded poly (lactic-co-glycolic acid) nanoparticles	109
5.3.	Results and Discussion	109
5.3.1.	Formulation of levodopa poly (lactic-co-glycolic acid) nanoparticles	109
5.3.2.	Levodopa entrapment efficiency of poly (lactic-co-glycolic acid) nanoparticles	110

5.3.2.	In vitro levodopa release from poly (lactic-co-glycolic acid) nanoparticles and Nano-Enabled Scaffold Device	110
5.3.4.	Morphology of levodopa poly (lactic-co-glycolic acid) Nanoparticles	111
5.3.5.	Structural polymeric variation of poly (lactic-co-glycolic acid), levodopa and levodopa-loaded poly (lactic-co-glycolic acid) nanoparticles	113
5.3.6.	Levodopa-loaded poly (lactic-co-glycolic acid) nanoparticle size and stability	114
5.4.	Investigation of nicotine-loaded cellulose acetate phthalate nanoparticles	115
5.4.1.	Material and Methods	115
5.4.1.1.	Materials	115
5.4.2.	Preparation of nicotine-loaded poly (lactic-co-glycolic acid) nanoparticles	115
5.4.4.	Determination of nicotine entrapment efficiency of cellulose acetate phthalate nanoparticles	115
5.4.5.	<i>In vitro</i> nicotine release studies on cellulose acetate phthalate nanoparticles	116
5.4.6.	Morphological characterization of nicotine-loaded cellulose acetate phthalate nanoparticles	116
5.4.7.	Determination of size and zeta potential of nicotine-loaded cellulose acetate phthalate nanoparticles	116
5.5.	Results and discussion	117

5.5.1.	Calibration curve for nicotine in phosphate buffered solution (pH 6.8; 37°C) for the determination of the concentration of nicotine in cellulose acetate phthalate nanoparticles	117
5.5.2.	Nicotine entrapment efficiency of cellulose acetate phthalate nanoparticles	117
5.5.3.	<i>In vitro</i> nicotine release from cellulose acetate phthalate nanoparticles	118
5.5.4.	Surface morphology of nicotine-loaded cellulose acetate phthalate nanoparticles	119
5.5.5.	Nicotine-loaded cellulose acetate phthalate nanoparticle size and stability	119
5.6.	Investigation of dopamine-loaded Polymeric Nanofibers	120
5.6.1.	Materials and Methods	120
5.6.1.1.	Materials	120
5.6.2.	Preparation of dopamine-loaded polymeric nanofibers	120
5.6.3.	Determination of dopamine entrapment efficiency of polymeric Nanofibers	120
5.6.4.	Morphological characterization of dopamine-loaded polymeric Nanofibers	120
5.7.	Results and Discussion	121
5.7.1.	Dopamine entrapment efficiency of polymeric nanofibers	121
5.7.2.	Size and morphology of dopamine-loaded polymeric nanofibers	121
5.8.	Concluding Remarks	123

6.	Cytotoxic Evaluation of Nano-Enabled Scaffold Device on Carcinomic Brain and Freshly Isolated, Healthy White Blood Cells	
6.1.	Introduction	124
6.2.	Materials and Methods	127
6.2.1.	Routine cell culture	127
6.2.2.	Isolation of white blood cells	127
6.2.3.	Trypsinisation and cell counting/seeding of cells	128
6.2.4.	Exposure of cells to the different compounds	129
6.2.5.	Calibration of 3-(4,5-dimethylthiazol-2-yl)-2,5-diphenyltetrazolium bromide assay	129
6.2.6.	The 3-(4,5-dimethylthiazol-2-yl)-2,5-diphenyltetrazolium bromide assay	130
6.2.7.	Preparation of 3-(4,5-dimethylthiazol-2-yl)-2,5-diphenyltetrazolium bromide solution	131
6.3	Results and Discussion	131
6.3.1.	Calibration curve of post-3-(4,5-dimethylthiazol-2-yl)-2,5-diphenyltetrazolium bromide exposure for the determination of the number of viable cells present in the media	131
6.3.2.	Cytotoxicity to white blood cells	132
6.3.3.	Cytotoxicity directed against the carcinomic SK-N-MC cells	133
6.3.4.	Limitations for the employment of 3-(4,5-dimethylthiazol-2-yl)-2,5 diphenyltetrazolium bromide assay in the present study	134
6.4.	Concluding Remarks	135

7.	<i>In Vivo</i> Evaluation of the Nano-Enabled Scaffold Device upon Implantation into the Parenchyma of the Frontal Lobe of the Rat Brain	
7.1.	Introduction	136
7.1.1.	Biocompatibility of implantable devices	136
7.2.	Materials and Methods	138
7.2.1.	Materials	138
7.2.2.	Technology Applied in the Present Study	138
7.2.2.1.	Waters® Acquity Ultra Performance Liquid Chromatography™	138
7.2.2.2.	Evaporative Light Scattering Detector	139
7.2.3.	Development of Methodology for the Surgical Implantation of Nano-Enabled Scaffold Device into the Parenchyma of the Frontal Lobe of the Sprague-Dawley Rat Brain	139
7.2.3.1.	Pre-surgical preparation of rats	139
7.2.3.2.	Pilot surgical technique for implantation of the Nano-Enabled Scaffold Device into the parenchyma of the frontal lobe of the rat brain	141
7.2.3.3..	End points for experiments that induce illness in rats	141
7.2.3.4.	Biological fluid sample collection from the rat model	142
7.2.3.5.	Histological analysis of the rat brain post-implantation of the Nano-Enabled Scaffold Device	142
7.2.3.6.	Bioerosion studies on the Nano-Enabled Scaffold Device	142
7.2.4.	Determination of <i>in vivo</i> drug release from Sinemet® and the Nano-Enabled Scaffold Device using Ultra Performance Liquid Chromatography analysis on biological fluids	143

7.2.4.1.	Preparation of priming solvents and mobile phases	143
7.2.4.2.	Preparation of standards	143
7.2.4.3.	Solid Phase Extraction blood and cerebrospinal spinal fluid	143
7.2.4.4.	Instrumentation and operating conditions of the Ultra Performance Liquid Chromatography	145
7.2.4.5.	Calibration curves and limit of quantification for dopamine in plasma	145
7.2.4.6.	Extraction yield, precision and accuracy of the method	145
7.2.4.5.	Cerebrospinal fluid and blood preparation for Ultra Performance Liquid Chromatography analysis	146
7.3.	Results and Discussion	147
7.3.1.	Brain damage in the rat from the surgical implantation of the Nano-enabled Scaffold Device	147
7.3.2.	Modifications to surgical implantation procedure	147
7.3.3.	Evaluation of modifications to surgical implantation technique	148
7.3.4.	Biocompatibility of the Nano-Enabled Scaffold Device systems employed in the study	148
7.3.4.1.	Pathological diagnosis of rat brain specimens implanted with dopamine-free Nano-Enabled Scaffold Device	148
7.3.4.2.	Pathological diagnosis of rat brain specimens implanted with Nano-Enabled Scaffold Device	149
7.3.5.	Bioerosion of the Nano-Enabled Scaffold Device post-implantation	149
7.3.6.	Solid Phase Extraction of dopamine from plasma	151
7.3.7.	Chromatograms for standards and plasma	151

7.3.8.	Calibration curve and lower limit of quantification of dopamine	153
7.3.9.	Method validation for the analysis of dopamine in plasma employing Ultra Performance Liquid Chromatography analysis	154
7.3.10.	<i>In vivo</i> dopamine release profile for the Nano-Enabled Scaffold Device	155
7.4.	Concluding Remarks	157
8.	CONCLUSIONS AND RECOMMENDATIONS	
8.1.	Conclusions	158
8.2.	Recommendations	160
9.	REFERENCES	161
10.	APPENDIX	187

LIST OF FIGURES

	Page
Figure 2.1: Schematic representation of mechanisms of drug delivery to the brain	12
Figure 3.1: Schematic representation of a charged particle and its distribution of ions	36
Figure 3.2: Scanning electron microscope images of (a) dopamine-free Nanoparticles	43
Figure 3.3: Transmission electron microscope images of (a) dopamine-free cellulose acetate phthalate nanoparticle and (b) dopamine-loaded cellulose acetate phthalate nanoparticles formed	43
Figure 3.4: Fourier transmission infrared spectra obtained for the formation of dopamine-loaded cellulose acetate phthalate nanoparticles	44
Figure 3.5: Proposed chemical interaction between dopamine and cellulose acetate phthalate	44
Figure 3.6: Dopamine calibration curve at 280nm in phosphate buffered solution (pH 6.8; 37°C)	45
Figure 3.7: Dopamine release profiles from cellulose acetate phthalate nanoparticles in phosphate buffered solution (pH 6.8; 37°C)	46
Figure 3.8: Size distribution profile for dopamine measuring 156.9nm	47

Figure 3.9:	Zetasize profiles of a) and b) size intensity and zeta potential distribution profiles of dopamine-free cellulose acetate phthalate nanoparticles, c) and d) size intensity and zeta potential distribution profiles of dopamine-loaded cellulose acetate phthalate nanoparticles respectively	48
Figure 3.10:	The Regression plots for (a) Mean Dissolution Time, (b) Particle Size and (c) Zeta Potential for the calculation of R^2 values that determine the similarity between the predicted and experimentally determined values for the responses	51
Figure 3.11:	Response surface plots correlating Mean Dissolution Time and (a) cellulose acetate phthalate concentration and poly(vinyl alcohol) concentration and (b) cellulose acetate phthalate concentration and stirring speed	53
Figure 3.12:	Release profiles depicting dopamine release from the cellulose acetate phthalate formulations	54
Figure 3.13:	Response surface plots correlating Particle Size and (a) emulsifying time and stirring speed and (b) cellulose acetate phthalate concentration and emulsifying time	55
Figure 3.14:	Response surface plots correlating Zeta Potential and (a) poly (vinyl alcohol) concentration and stirring speed (b) emulsifying time and stirring speed	56
Figure 3.15:	Typical (a) main effects plot and (b) interactions plot of the response values for Mean Dissolution Time	57
Figure 3.16:	Typical (a) main effects plot and (b) interactions plot of the response values for Particle Size	59

Figure 3.17: Typical (a) main effects plot and (b) interactions plot of the response values for Zeta Potential	60
Figure 3.18: The residual plots for the responses (a) Mean Dissolution Time (b) Particle Size and (c) Zeta Potential	62
Figure 3.19: Optimization plots displaying factor levels and desirability values for the chosen optimized formulation	66
Figure 3.20: (a) Size and (b) Zeta distribution profiles for optimized dopamine-loaded cellulose acetate phthalate nanoparticles measuring 197.2nm and -34mV respectively	67
Figure 4.1: Schematic representation of the assimilation of dopamine-loaded cellulose acetate phthalate nanoparticles and barium-alginate scaffold into the Nano-Enabled Scaffold Device	79
Figure 4.2: Three-dimensional prototype images of a) a pre-cured crosslinked-alginate scaffold, b) a barium-chloride post-cured crosslinked-alginate scaffold, and c) dopamine-loaded cellulose acetate phthalate nanoparticles embedded within the cured crosslinked alginate scaffold voids representing the Nano-Enabled Scaffold Device	82
Figure 4.3: Molecular structural models of a) interactions between water molecules in association with acetate and oxygen functional groups of cellulose acetate phthalate and b) cellulose acetate phthalate interactions and dopamine entrapment	83

Figure 4.4:	Graphical models depicting a-e) the stepwise formation of dopamine-loaded cellulose acetate phthalate nanoparticles, f) a single cellulose acetate phthalate adaptation, g) dopamine interaction and wall initiation and h) a dopamine-loaded cellulose acetate phthalate nanoparticle towards completion	84
Figure 4.5:	A typical Force-Time profile of a hydrated barium-alginate scaffold for the calculation of resilience	84
Figure 4.6 :	Scanning electron microscope images of (a) barium-alginate scaffold that was not subjected to post-curing (b) a typical pore present within the scaffold, (c) a scaffold that underwent post-curing with barium-chloride and (d) the relation of pores in respective to one another	86
Figure 4.7:	Matrix Erosion profile for barium-alginate scaffold in phosphate buffered solution (pH 6.8, 37°C) over a period of 72 days	87
Figure 4.8:	The Regression plots for (a) Matrix Resilience (%) and (b) Matrix Erosion for the calculation of R^2 values that determine the similarity between the predicted and experimentally determined values for the responses	90
Figure 4.9:	Response surface plots correlating the scaffold matrix resilience with a) alginate and crosslinker concentration and b) alginate concentration and processing temperature	91
Figure 4.10:	Response surface plots correlating scaffold Matrix Erosion with (a) alginate concentration and post-curing time and (b) processing temperature and post-curing time	91

Figure 4.11: Typical (a) main effects plot and (b) interactions plot of response values for Matrix Resilience	92
Figure 4.12: Typical (a) main effects plot and (b) interactions plot of response values for Matrix Erosion	93
Figure 4.13: The residual plots for the responses (a) Matrix Resilience and (b) Matrix Erosion percentage for scaffolds	96
Figure 4.14: Optimization plots displaying factor levels and desirability values for the chosen optimized formulation	98
Figure 4.15: Dopamine release profiles for (a) dopamine-loaded cellulose acetate phthalate nanoparticles and (b) Nano-Enabled Scaffold Device in phosphate buffered solution (pH 6.8; 37°C)	100
Figure 4.16: Temperature modulated differential scanning calorimetry profiling for Nano-Enabled Scaffold Device showing endothermic and exothermic peaks generated	102
Figure 5.1: A schematic representation of a rudimentary electrospinning device employed for the formulation of nanofibers	105
Figure 5.2: Levodopa calibration curve at 285nm in phosphate buffered solution (pH 6.8; 37°C)	110
Figure 5.3: Levodopa release profiles of (a) levodopa-loaded poly (lactic-co-glycolic acid) nanoparticles and (b) Nano-Enabled Scaffold Device in phosphate buffered solution (pH 6.8; 37°C)	110

Figure 5.4:	Transmission electron microscope images of (a) an isolated levodopa-loaded poly (lactic-co-glycolic acid) nanoparticle and (b) a cluster of levodopa-loaded poly (lactic-co-glycolic acid) nanoparticles	111
Figure 5.5:	Fourier transmission infrared spectra for levodopa, poly (lactic-co-glycolic acid), levodopa-free and levodopa-loaded poly (lactic-co-glycolic acid) nanoparticles	112
Figure 5.6:	Proposed dimethyl sulphoxide and poly (lactic-co-glycolic acid) chemical interaction	113
Figure 5.7:	Liquid Fourier transmission infrared spectra analysis for poly (lactic-co-glycolic acid) and dimethyl sulphoxide	113
Figure 5.8:	Nicotine calibration curve at 269 in phosphate buffered solution (pH 6.8; 37°C)	117
Figure 5.9:	Nicotine release profile for poly (lactic-co-glycolic acid) nanoparticles in phosphate buffered solution (pH 6.8; 37°C)	118
Figure 5.10:	Transmission electron microscope image of nicotine-loaded cellulose acetate phthalate nanoparticles	119
Figure 5.11:	Scanning electron microscope images of (a) dopamine-loaded poly (vinylalcohol) nanofibers revealed longitudinal solid fibers with a minimal length of 20µnm and (b) dopamine-loaded cellulose acetate phthalate nanofibers showed artifacts in the structure	121

Figure 5.12:	Transmission images of dopamine-loaded poly (vinylalcohol) nanofibers (a) displaying an uneven distribution of poly (lactic-co-glycolic acid) and dopamine along its length and (b) a closer look showed fibers of minimal diameters of 5nm	121
Figure 5.13:	Transmission electron microscope images of dopamine-loaded cellulose acetate phthalate nanofibers revealed a diameter of 1.5µm	122
Figure 6.1:	Schematic representation of one of the possible mechanisms involved in the metabolism of dopamine leading to cytotoxic and genotoxic events	125
Figure 6.2:	<i>In vivo</i> colorimetric reaction that occurs in living cells when exposed to 3-(4,5-dimethylthiazol-2-yl)-2,5-diphenyltetrazolium bromide	126
Figure 6.3:	Diagrammatic representation of the separation of blood that occurs upon it's centrifugation in Ficoll-Hypaque gradient (3:1) tubes (Lifelearn Inc, 2004)	127
Figure 6.4:	A schematic representation of the layout of the compounds in the 96-well plate as used in the 3-(4,5-dimethylthiazol-2-yl)-2,5-diphenyltetrazolium bromide assays on white blood cells and SK-N-MC cells	130
Figure 6.5:	3-(4,5-dimethylthiazol-2-yl)-2,5-diphenyltetrazolium bromide calibration curve for (a) white blood cells and (b) SK-N-MC	131

Figure 6.6:	Graph displaying percentage cell viability of white blood cells after a 24hr exposure period to the various compounds. Cell viability is reported in relation to the control cell sample which was equated to 100%.	133
Figure 6.7:	Graphs displaying percentage cell viability of SK-N-MC cells after exposure periods to the various compounds. Cell viability is reported in relation to the control cells which was equated to 100%.	134
Figure 7.1:	Schematic diagrammatic representation of immunological response to implant within the central nervous system	137
Figure 7.2:	Schematic diagram representing the number of rats required for <i>in vivo</i> studies	140
Figure 7.3:	Diagrammatic account of the strategy for the optimization of the generic Solid Phase Extraction method	144
Figure 7.4:	Photographic representation of the surgical procedure (a) manual drill used for incision, (b) actual perforation of the skull and (c) suturing of the incision	147
Figure 7.5:	Light microscope images of histological slides of the site of implantation into the brain, stained using Haematoxylin & Eosin, in (a) control and (b) test brain tissue following 5 days of implantation of Nano-Enabled Scaffold Device	149
Figure 7.6:	<i>In vivo</i> bioerosion profile for Nano-Enabled Scaffold Device over a period of 30 days	150

Figure 7.7.	Light microscope (top) and Scanning electron microscope images (below) of Nano-Enabled Scaffold Device matrix (a) pre-implantation and (b) blood perfused post-euthanasia and removal from rat brain post-7 day implantation showing 16% bioerosion	150
Figure 7.8:	A typical chromatograph depicting the peak ($R_t = 0.4925$) for dopamine employing Ultra Performance Liquid Chromatography at 280nm in double deionised water	152
Figure 7.9:	A typical chromatograph depicting the peak ($R_t = 1.579$) for theophylline(internal standard) employing Ultra Performance Liquid Chromatography at 280nm in double deionised water	152
Figure 7.10:	A typical Ultra Performance Liquid chromatogram depicting the distinct separation of dopamine ($R_t=0.49$) and theophylline ($R_t=1.64$) at 280nm from the Sprague Dawley rat plasma samples	153
Figure 7.11.:	Dopamine calibration curve at 280nm in plasma employing Ultra Performance Liquid Chromatograph in double deionised water	154
Figure 7.12.:	<i>In vivo</i> profile for dopamine release from Sinemet®	156
Figure 7.13:	<i>In vivo</i> profile for dopamine release from the Nano-Enabled Scaffold Device	156

LIST OF TABLES

	Page
Table 2.1: Selected nano-therapeutic molecules on the market for the treatment of various diseases	15
Table 2.2: The diverse architectures of nano-systems	17
Table 2.3: Parkinson's disease syndrome brain bank diagnostic criteria (United Kingdom)	21
Table 2.4: The current pharmacological treatment for Parkinson's disease and their limitations	22
Table 2.5 Selected neurorestorative and neuroprotective agents for the treatment of Parkinson's disease	27
Table 2.6: Surgical strategies employed for the treatment of Parkinson's disease	29
Table 3.1: Processing conditions for the rotaveporation in formulating dopamine-loaded cellulose acetate phthalate nanoparticles	37
Table 3.2: Illustrates the variations in formulations that were used to identify the limits for a Box -Behnken design to optimize dopamine-loaded cellulose acetate phthalate nanoparticles and their dopamine entrapment efficiency percentage	41
Table 3.3: The variables for the dopamine-loaded cellulose acetate phthalate nanoparticles used in the 4-factor Box-Behnken design	42
Table 3.4: Illustration of variations in formulations employed for a Box-Behnken design for the optimization of dopamine-loaded cellulose acetate phthalate nanoparticles	49

Table 3.5:	Measured responses for the experimental optimization of dopamine-loaded cellulose acetate phthalate nanoparticles	50
Table 3.6:	Full ANOVA analysis for the measured responses (Mean Dissolution Time, Particle Size and Zeta Potential for dopamine-loaded cellulose acetate phthalate nanoparticles)	64
Table 4.1:	Illustrates alginate-based drug delivery systems that have are being investigated for the treatment of various diseases	70
Table 4.2:	Parameters employed to measure the Matrix Resilience of hydrated/unhydrated samples employing the textural analyser	75
Table 4.3:	Illustration of variations in formulations that were used to identify the limits for a Box -Behnken design to optimize barium-alginate scaffolds and their Matrix Resilience	76
Table 4.4:	The variables for the barium-alginate scaffold used in the 4-factor, 3-level Box-Behnken design	77
Table 4.5:	Temperature modulated differential scanning calorimetry settings employed for thermal analysis of the Nano-Enabled Scaffold Device constituents	81
Table 4.6:	Percentage Matrix Resilience of crosslinked alginate scaffolds in both hydrated and unhydrated states	85
Table 4.7:	Illustrates variations in formulations employed for a Box-Behnken design for the optimization of barium-alginate scaffold	88
Table 4.8:	Measured responses for the experimental optimization of barium-alginate scaffold	89

Table 4.9: Full ANOVA analysis for the measured responses (Matrix Resilience and Matrix Erosion)	97
Table 4.10: Salient thermal events for dopamine-loaded cellulose acetate phthalate nanoparticles, barium-alginate scaffold and Nano- Enabled Scaffold Device compared to native cellulose acetate phthalate	101
Table 7.2. Illustrates the data obtained to assess the validation of the method	154

CHAPTER 1

INTRODUCTION

1.1. Background to this Study

Parkinson's disease (PD) is characterized by a progressive loss of dopaminergic neurons in the substantia nigra pars compacta of the brain (Moos and Jensen, 2004). This results in the loss of striatal dopaminergic terminals and their ability to store and regulate the release of dopamine (DA). DA is a neurotransmitter found in a region of the brain namely the substantia nigra. The transmitter plays a role in behaviour, learning and cognition as well as aids in the execution of controlled muscular movements. DA does not cross the blood brain barrier (BBB) therefore an exogenous supply needs to be orally administered in its levo-form known as Levodopa (L-dopa) (Lai and Yu, 1997). Accordingly, striatal DA receptor activation becomes increasingly dependent on the peripheral availability of an exogenously administered dopaminergic agent (Mrin *et al.*, 2008). As the disease progresses, the patient begins to experience motor abnormalities such as akinesia, a resting tremor, and rigidity. The advancement of the disease results in worsening of these symptoms (Yulmetyev *et al.*, 2006). The disease affects one in every 100 persons above the age of 65 years and is the second most common neurodegenerative disease after Alzheimer's disease (de Rijk *et al.*, 2000). The current treatments for the disease have extensive side-effect profiles and issues with loss of efficacy after prolonged periods of time therefore validating the urgency for new treatment modalities.

Drug delivery to the brain remains a highly challenging and essential field of study. Due to the numerous protective barriers surrounding the Central Nervous System (CNS), there is still an urgent need for effective treatment of patients living with neurodegenerative diseases such as PD (Singh *et al.*, 2007).

The Blood Brain Barrier (BBB) is a defensive mechanism (Misra *et al.*, 2003). The passage of substances into the brain is highly selective and prevents the entry of high molecular mass hydrophilic compounds. This is a major impediment for drug delivery to the brain as numerous drugs are aqueous in nature and therefore unable to penetrate the BBB (Siepmann, 2006). The alternative is that drugs may be delivered systemically (as in the case with current drug therapy) however only a small percentage of drug reaches the brain due to hepatic degradation as well as the inability to cross the BBB, and the associated side effects

related to peak-to-trough fluctuation of plasma drug levels that leads to a lack in patient dose-regimen compliance (Whintey, 2007). High dose parental drug administration is often necessary to reach sufficient concentrations of the drug in the brain parenchyma (Pardridge, 2006) however since neurodegeneration is a chronic disease, this option seems impractical.

L-dopa still remains the gold standard for the treatment of PD. Oral administration of L-dopa is rapidly decarboxylated to DA (only 5% DA bioavailability) in extracerebral tissues so that only a small portion (<1%) of a given dose is transported unchanged to the CNS. Due to its significant peripheral metabolism, large doses of L-dopa are required for an adequate therapeutic effect and often produces severe nausea, memory loss and nervousness (Whintey, 2007). Carbidopa inhibits decarboxylation of peripheral L-dopa, increasing the bioavailability of L-dopa by 99% to the brain. It does not cross the BBB nor affects the metabolism of L-dopa within the CNS. Sinemet[®] (Merck & Co., Inc and Bristol-Myers Squibb, NJ and NY, USA), an immediate release preparation, is a combination of carbidopa and L-dopa and so significantly increases the bioavailability of L-dopa. Sinemet[®]CR is a controlled release preparation that allows for a once-a-day dosage. Unlike Sinemet[®] which is dosed three times a day (Yeh *et al.*, 1989). However there are numerous limitations to the use of L-dopa as well as other anti-parkinson drugs that will be further highlighted in section Chapter 1 Section 1.2 of this dissertation.

Nicotine (NT) has received considerable attention for its possible employment as a neuroprotectant for PD. Smokers have shown a decline in the occurrence of PD as compared to the non-smoker population (Quik *et al.*, 2007). Studies have shown that nicotine may be responsible for an augmentation *in vitro* as well as *in vivo* DA release (Rusted *et al.*, 2000). The neuroprotectant effects of NT are further discussed in chapter 2 Table 2.5 of this dissertation.

Nanotechnology has a long fairly unexplored history and may overcome limitations posed by current non-targeted drug delivery systems. Nanoparticles are small (mainly polymeric) particles in the nanometer range and are normally spherical depending on the nature of production and can be loaded with various drugs. Due to the small size of nanoparticles, they are able to penetrate the BBB (Liu *et al.*, 2005) and are therefore easily imbibed within cells, allowing for efficient drug accumulation at targeted sites within the brain (Gelperina *et al.*, 2005). The use of biodegradable polymeric material for nanoparticulate formation may also allow sustained drug release at the targeted site over a period of days or even weeks after

implantation and ideally would erode *in vivo* (Yetkin *et al.*, 2000). Furthermore, nano-enabled delivery devices should be able to maintain its physicochemical properties for the period of drug release and erode with subsequent elimination from the body without producing any toxic by-products (Middleton and Tipton, 1998).

Thus, the aim of this research was to combine polymer and nanoscience to design and develop a Nano-Enabled Scaffold Device (NESD) for the delivery of DA to allow for its localised and controlled delivery of DA for the treatment of PD. The NESD was implanted into the parenchyma of the frontal lobe of the Sprague-Dawley rat brain.

1.2. Rationale for this Study

Polymeric nanotechnology has been researched for its application in cancer therapy (Alexis *et al.*, 2008). However it has yet to be extensively explored for the treatment of neurodegenerative diseases. The treatment of cancer and neurodegenerative diseases are similar in that they both require targeted drug delivery to optimize bioavailability and reduce systemic side-effects experienced with CNS drugs (Abbot and Ramero, 1996).

Nano-drug delivery devices have the potential to (i) maintain therapeutic levels of drug, (ii) reduce harmful side-effects, (iii) decrease the quantity of drug needed, (iv) reduce the number of dosages, and (v) facilitate the delivery of drugs with short *in vivo* half-lives (Kohane, 2006; Gelperina *et al.*, 2005; Langer, 1998).

Drug-loaded nanoparticles can be injected at the site of action but the inclusion of nanoparticles into a biodegradable polymeric scaffold is advantageous for targeted drug delivery as the nanoparticles allow for higher drug loading, due to the high surface area to volume ratio in comparison to other polymeric systems, and are able to facilitate opening of tight junctions between cells for penetrating the BBB (Kreuter, 2001). Furthermore, by employing biodegradable polymers during formulation avoids the need for surgical procedures in order to remove the device once its drug-load has been depleted (Middleton and Tipton, 1998).

L-dopa is essentially the levorotatory isomer of dihydroxy-phenylalanine (dopa) which is the metabolic precursor of DA. L-dopa presumably is converted into DA in the basal ganglia. The reason for the formulation and current widespread use of the L-dopa is to enhance transport of the drug across the BBB. Initial therapy with L-dopa significantly restores normal

functioning for the patient with PD and every PD-patient will need L-dopa at some time during the course of the disease (Samii *et al.*, 2007). However the major limitation to the use of L-dopa arises after long-term use. The phenomenon is known as the 'end-of-dose wearing-off', where the therapeutic benefits of each dose of L-dopa lasts for shorter periods (Hely *et al.*, 2000). The patient begins to experience motor fluctuations prior to the time of the next dose. This occurs when the prescribed dose is no longer able to effectively manage the symptoms of the disease. In many patients, 'off' periods of motor immobility are associated with pain, panic attacks, severe depression, confusion and a sense of death (Papapetropoulos and Mash, 2005), which makes the clinical status even more distressing for patients as well as their care-givers. Clinicians attempt to overcome this phenomenon by either increasing the frequency/quantity of the dose or by replacing immediate release preparations with a sustained release preparation for example Sinemet[®] CR. Increasing the dose places the patient at risk for dyskinesia (the inability to control muscles) which occurs at peak plasma drug levels (Chen and Obering, 2005). The dose also needs to be increased on a regular basis in order to overcome "the wearing-off" effect which results in an increase in side-effects. Sinemet[®] CR provides a benefit in that drug plasma levels are maintained over a 24-hour period (Uitti *et al.*, 1997). However, side-effects such as dizziness, insomnia, abdominal pain, dyskinesia, headache and depression are still experienced with sustained release preparations. The inclusion of carbidopa (75-100mg daily) tends to exacerbate psychiatric, gastrointestinal and motor side-effects. Patients also find that while the dosing schedule proves convenient, there is still evidence of dyskinesia (Miyawaki *et al.*, 1997). There have also been reports that, with both Sinemet[®] preparations, food retards absorption of the drug (Roos *et al.*, 1993). Therefore in order to overcome these limitations, a NESD implanted into the parenchyma of the frontal lobe of the rat brain was developed in this study. The inclusion of DA avoids the need for metabolism to the active (as it is already in its active form) and peripheral loss of the DA thereby increasing its bioavailability.

A Nano-Enabled Scaffold Device (NESD) implanted into the parenchyma of the frontal lobe of the brain will ensure DA is delivered in a controlled manner for a prolonged period of time and DA delivery will be targeted to the affected areas of the brain and a lower effective dose would be required with no systemic side-effects. The major benefit of the NESD will be sustained release of DA with increased efficacy in the treatment. This will ensure maintenance of steady-state cerebrospinal fluid (CSF) DA levels which is imperative to prevent the 'end-of-dose wearing-off' phenomenon. The ultimate goal is to increase the patient's quality of life and restore their daily functioning. Currently, there is no product

available on the market that is able to ensure long-term efficiency and control of the motor manifestations of the disease without the aggravation of side-effects such as the psychiatric manifestations and cardiovascular effects (Katzung *et al* , 2004). The NESD will prove superior in that it serves to overcome the major barriers of current drug delivery systems available for the treatment of PD.

Ex vivo and *in vivo* studies proved essential in this study as the employment of a NESD in the brain is a fairly unexplored field of study and so there are insufficient CNS animal models for correlation purposes. While this study extensively explored *in vitro* studies performed on the NESD, none served to sufficiently simulate *in vivo* conditions of the parenchyma of the frontal lobe of the brain. An *ex vivo* cytotoxic study on brain and white blood cells was developed that allowed for the determination of the potential safety/toxicity of the NESD prior to the undertaking of *in vivo* animal studies. Animal studies allowed for the determination of the potential CNS effects that the NESD may have within living organisms, unlike the static conditions provided by the *in vitro* environment. The inclusion of animal studies provided significant data on the DA release kinetics and biodegradation behaviour of the NESD.

In order to assess the versatility of the NESD, NT was loaded into the nanoparticles. NT transdermal patches and gums used for the cessation of smoking have proven to be advantageous in stimulating DA release and therefore for the employment in PD (Singh *et al.*, 2007). These findings justify the need for the formulation and thereby investigation into a controlled drug delivery system containing NT.

1.3. Aim and Objectives of this Study

- To review current novel drug delivery systems for the treatment of PD and thereby validate the need for the development of a NESD
- To identify a suitable method to develop DA-loaded Cellulose Acetate Phthalate (CAP) nanoparticles that can be incorporated into a crosslinked alginate scaffold
- To identify a suitable method to develop implantable crosslinked alginate scaffolds
- To investigate the physicochemical and physicochemical properties of the newly formed DA-loaded CAP nanoparticles and crosslinked alginate scaffold
- To synthesis variants of DA-loaded CAP nanoparticles and crosslinked alginate scaffold employing a Box-Behnken Experimental Design followed by physicochemical and physicochemical analysis
- To establish the optimum parameters necessary for the formulation of the desired DA-loaded CAP nanoparticles and crosslinked alginate scaffold that will form the NESD
- To disperse the DA-loaded CAP nanoparticles into a crosslinked alginate scaffold and thereafter evaluate *in vitro* DA release and matrix erosion behaviour of the NESD
- To test the cytotoxicity of the NESD on carcinomic brain and white blood cells
- To undertake *in vivo* animal studies and determine DA release kinetics and biocompatibility of the NESD
- To investigate novel configurations for the design of diverse nano-systems that may be employed for the treatment of PD.

1.4. Overview of this Dissertation

Chapter One outlines the problem and highlights the rationale for the study. It is an introduction to the study that covers the background and introduction. A summary of the aims and objectives is included in this chapter.

Chapter Two focuses on drug delivery to the brain and the strategies employed. Furthermore, there is a detailed outline of PD, its treatment and their limitations. The concepts and definitions of nanotechnology are discussed as well as its application in drug delivery.

Chapter Three describes the formulation and development of DA-loaded nanoparticles. Preliminary formulation methods which investigated the stability and size of the nanoparticles are detailed. In addition, formulation parameters were established to allow for the construction of a Box-Behnken followed by optimization that lead to a candidate nanoparticle formulation. Furthermore, physicochemical and physicochemical properties were analysed as well as *in vitro* DA release.

Chapter Four describes the formulation and development of barium-alginate scaffolds. Preliminary formulation methods highlight the need for increased matrix resilience and decreased mass loss of the scaffold. In addition, formulation parameters were established to allow for the construction of a Box-Behnken followed by optimization that lead to a candidate scaffold formulation. Furthermore, physicochemical and physicochemical properties were analysed. This chapter also looked at the incorporation of the DA-loaded nanoparticles into the Ba-alginate scaffold and the *in vitro* release from NESD.

Chapter Five is a further development of nanosystems incorporating bioactive compounds such as L-dopa and NT for the treatment of PD. The chapter includes the preliminary *in vitro* investigation into these systems.

Chapter Six is a comprehensive description of the *ex vivo* cytotoxic testing on brain and white blood cells. Descriptions of the assays employed and the handling of results are contained within the chapter.

Chapter Seven contains an explanation of the *in vivo* animal studies undertaken in the Sprague-Dawley rat model. Development of a protocol for the surgical implantation into the brain, biocompatibility and DA release are the highlights of the chapter. In addition, sample collection of blood and cerebrospinal fluid is described.

Chapter Eight presents the conclusions and recommendations for future work.

CHAPTER 2
CURRENT STRATEGIES AND LIMITATIONS OF DRUG DELIVERY TO THE BRAIN IN THE
TREATMENT OF PARKINSON'S DISEASE

2.1. Introduction

2.1.1. The Physiology of the BBB

The BBB serves to protect the brain from the external environment (the rest of the body) by regulating the passage of molecules to the brain. The absence of fenestrations and the presence of tight junctions between the endothelial cells that form the capillaries of the BBB, provide this regulation and protection (Kemper *et al.*, 2004). Approximately 100% of large-molecule drugs and more than 98% of all small, hydrophilic molecules (larger than 400–500 Daltons) do not cross the BBB (Pardridge, 2006). Lipophilic molecules may passively diffuse through the endothelial cells but are generally limited to smaller sized molecules. Other parameters that influence the uptake of a drug in brain tissue are (Summerfield *et al.*, 2007) the degree of ionization of the drug; plasma protein and tissue binding, its affinity for specific carriers as well as local cerebral blood flow.

2.1.1.1. Approaches Employed for Drug Delivery to the Brain

The diverse mechanisms of drug delivery to the brain are illustrated in Figure 2.1. and briefly discussed hereunder.

Passive diffusion of small molecules to the brain

The movement of drug from the luminal to the ablumina interface of the BBB, occurs only within lipid-soluble small molecules that have a molecular mass of less than 400 daltons. This is a highly selective and restrictive approach of delivering drug to the brain (Pardridge, 2006).

Osmotic disruption of the BBB employing hyperosmolar solutions

It is a temporary procedure involving the use of hyperosmolar agents such as mannitol and arabinose (Rapoport, 2000). The administration of these solutions causes the contraction of endothelial cells that constituent the tight junctions. The dysfunction of the cells increases the intracellular spaces thereby allowing access of molecules into the brain (Kemper *et al.*, 2004). This method holds grave consequences in that the disruption is not as temporary as previously stated. The recovery to normal state takes several hours in many instances and may lead to the non-selective entry of toxic substances as well as the rapid influx of fluid into the brain. The employment of osmotic disruption has shown minimal decrease in patient morbidity and it's inevitable risks still hold cause for concern (Kemper *et al.*, 2004).

Chemical modification of the drug and it's penetration through the BBB

Lipidization is most commonly used to increase the likelihood of drug passing or bypassing the BBB. However, Pardridge (2006) reported that "to date there is not a single CNS drug prescribed to patients that is an example of a water-soluble drug being converted into a CNS active drug by medicinal chemistry". Furthermore with chemical modification of the drug comes changes in the pharmacokinetic profile as well which could have negative consequences on the biological activity of the drug (Pardridge, 2006; Gaillard and de Boer 2006).

Transcranial drug delivery mechanisms

There are three major categories for this type of delivery: intracerebroventricular (ICV) infusion, the intracerebral (IC) implantation and the convection-enhanced diffusion (CED) of drug (Pardridge, 2006). These techniques allow for the delivery of drug at the brain parenchyma. In order for the approach to prove beneficial, the drug needs to be placed into the target site to avoid loss of drug through diffusion (Pardridge, 2006). In addition, the CSF

turnover rate far supersedes the diffusion rate of drug throughout the brain. CED is the continuous infusion of drug-infused fluid into the brain tissue. This procedure involves serious consequences in that the brain lacks an efficient mechanism to remove this access fluid (Pardridge, 2006; Pathirana et al., 2006).

Active efflux of molecules for transportation to the brain

An active efflux pump works by ejecting certain molecules from the brain to the systemic circulation. Molecules should have a moiety attached to their structure that would enable inhibition of the efflux transporter, thereby allowing increased brain penetration of the therapeutic drug (Pardridge, 2006; Kusuhara and Sugiyama, 2001).

Receptor mediated transport of large molecules through the BBB

The attachment of drug onto specific receptors allow for their transportation/endocytosis into the brain. Examples of these include transferrin receptor (holo-transferrin), neonatal Fc (IgG) and receptor type I scavenger receptor (lipoproteins) (Pardridge, 2006; Roberts *et al.*, 1993).

Trojan horse receptor mediated transport: an alternative system for the transportation of larger molecules across the BBB

This system embodies another approach to deliver larger molecules to the brain. Drug binds to the receptor-specific monoclonal antibody portion of the Trojan horse (a "piggy back" receptor molecule) which binds to an exofacial epitope on the endogenous BBB peptide receptor. Trojan horses allow for the "carrying" of the molecule across the BBB on the endogenous peptide receptor mediated transport system (Pardridge, 2006; Dietz and Bohr, 2004).

Carrier mediated transport of water soluble molecules through the BBB

These receptors allow for the transportation of water soluble molecules through the BBB. Examples of these carriers include hexose, lactate, glucose and phenylalanine among others. In actuality, the mainstay therapy for PD, L-dopa utilizes the neutral amino acid carrier (used for the transportation of phenylalanine) to cross the BBB. Utilization of the body's intrinsic system to overcome the BBB may be employed to other water soluble drugs. Furthermore, drugs may be converted to the analogues of natural molecules that have transporters within the BBB, thereby allowing entry of drug into the BBB (Tsuji, 2001; Pardridge, 1991).

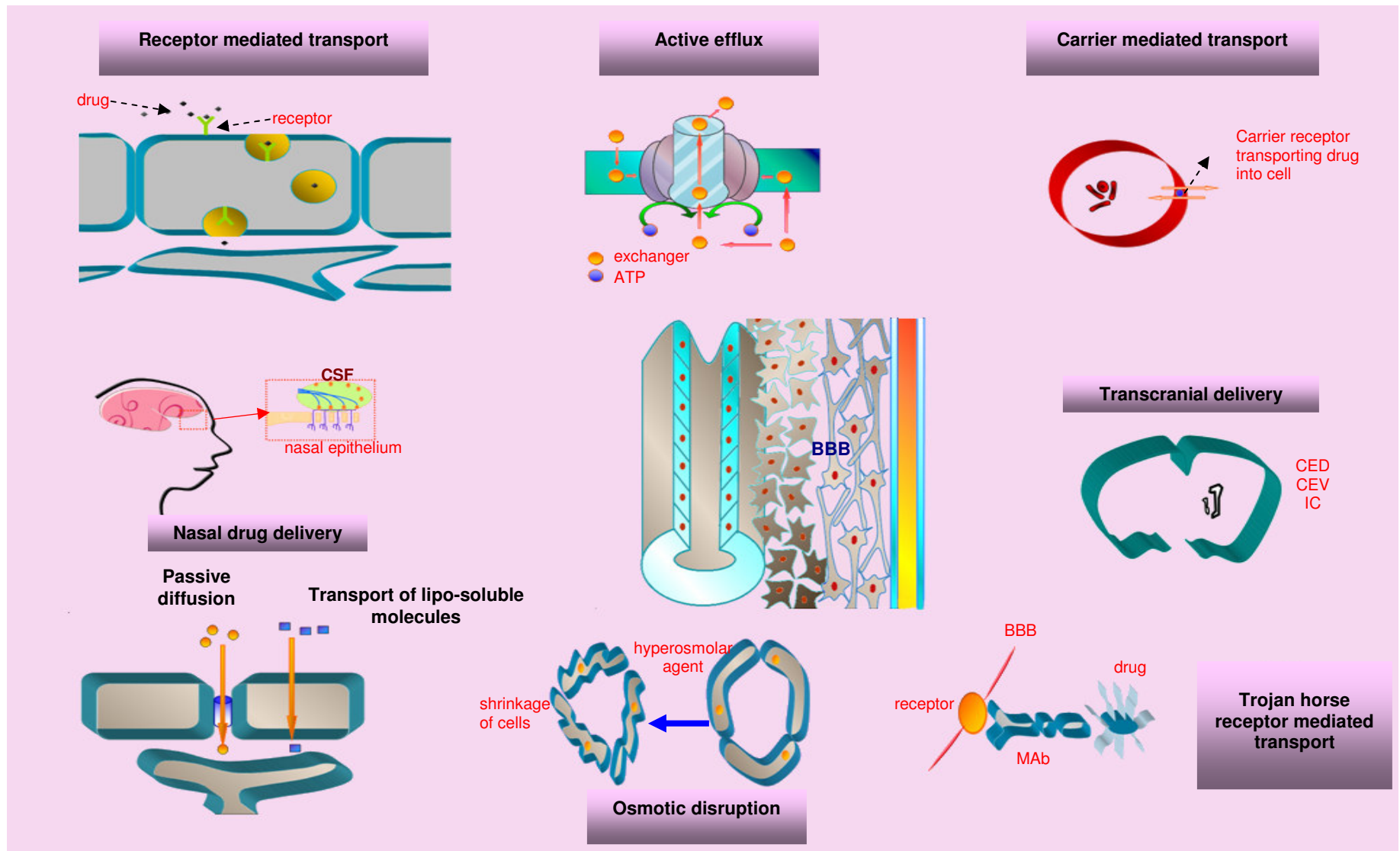


Figure 2.1: Schematic representation of mechanisms of drug delivery to the brain (Rapoport 1976, Pardridge 2002, Pardridge 2005, Abbott et al., 2006)

Nasal Drug Delivery: an approach for the treatment of central nervous system conditions

The administration of drug via the nasal route allows for bypassing the BBB (Mishr, 2004). Drug is transported from the nasal cavity into the olfactory part of the nasal epithelium to enter into the submucus space (adjacent to the olfactory CSF) and then into the CSF compartment of the brain. While drug does not have to pass through the BBB, a prerequisite for nasal drug delivery is a lipophilic drug with a $M_w = 400$ daltons. Once there is a significant restriction in the drugs that may be delivered using this approach. Another process is to considerably obliterate nasal mucosa by instilling larger molecules ($>400M_w$) into the nostrils, this causes trauma to the epithelium resulting in the molecules entering through the nasal membrane (Pardridge, 2006; Liu *et al.*, 2001).

Nano-therapeutic molecules

Nanotechnology comprises ideally of materials with size ranges from 1-100nm. These materials exhibit large surface areas which in turn results in the increase of the particle surface energy and may give rise to biological reactivity (Oberdörster *et al.*, 2005). Nano-engineered materials and devices aimed at biology and medicine in general and neuroscience in particular are designed to interface with cells and tissues at a fundamental molecular level (Silva, 2007). The process of nano-sizing allows for the potential elimination of obstacles arising from low drug solubility, degradation, fast clearance rates, non-specific toxicity, and inability to cross biological barriers (Kingsley *et al.*, 2006). The site-specific delivery of nano-drugs allows for the maximization of therapeutic effect and minimization of side-effects.

Nanodiagnosics: The early recognition and detection of disease states is imperative to the prognosis. Nano-enabled molecular imaging have been made in all imaging modalities including optical, nuclear, ultrasound, computed tomography and magnetic resonance imaging (Caruthers *et al.*, 2007). The increased surface area per volume of nanoparticles ensures that there is no need to load each targeted particle with a high concentration of imaging agent. Examples of these include nanoparticulate iron oxides may be used as contrast agents in magnetic resonance imaging. They monitor gene expression or detection of metastases in prostate cancer, atherosclerotic plaques and brain inflammation (Moghmini, 2005). These imaging agents may further be coupled with a nanosized drug delivery system to allow for multifunctionality allowing for the early detection and treatment of disease (Bawa, 2007).

Table 2.1 lists the selected nano-therapeutic molecules on the market for the treatment of various diseases

Table 2.1: Selected nano-therapeutic molecules on the market for the treatment of various diseases (adapted from Nijhara and Balakrishnan, 2006, du Toit et al., 2007 and Zhang et al., 2007)


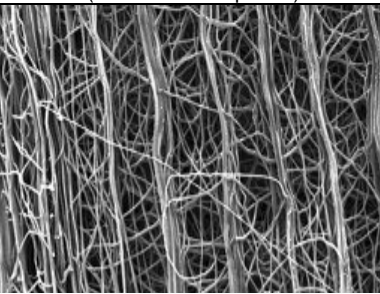
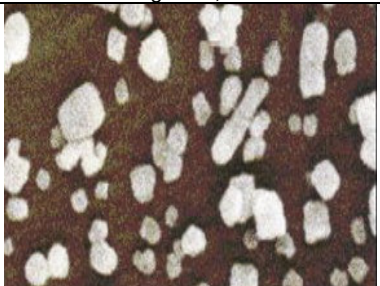
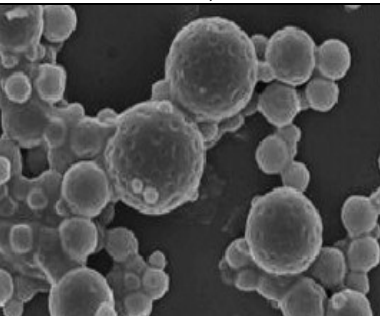
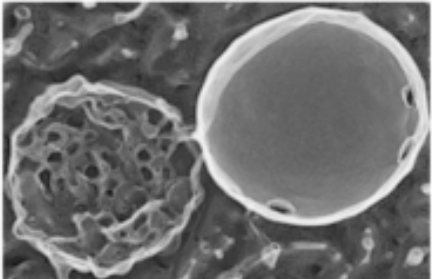
Drug name	Manufacturer(s)	Indications	Size (nm)	Major benefits	FDA Approval
Rapamune® (Sirolimus)	Wyeth, Elan (Madison, New Jersey, US)	Immunosuppressant in kidney transplant patients	<200	Enhanced bioavailability, convenient dosage formulation, and extended shelf-life, compared with its microformulated counterpart	August 2000
Emend® (Aprepitant)	Merck, Elan (New Jersey, US)	Delayed nausea and vomiting in chemotherapy patients	<1000	First FDA-approved drug for the treatment of delayed nausea and vomiting in chemotherapy	March 2003
TriCor® (Fenofibrate)	Abbot (Illinois, US)	Primary hypercholesterolemia, mixed lipidemia, hypertriglyceridemia	<1000	Minimal fasted and fed variability in bioavailability of the drug, when compared with its microformulated counterpart.	December 2004
Abraxane® (Abraxane)	American Pharmaceutical Partners, Inc. (Illinois, US)	Metastatic breast cancer	130	Eliminates the use of toxic solvents that were essential for its microformulated counterpart	January 2005
Doxil® (Doxorubicin)	ALZA Corporation (California, US)	Anti-cancer drug for the treatment of refractory ovarian cancer and Kaposi's Sarcoma	100	First FDA-approved drug for cancer therapy	February 2005

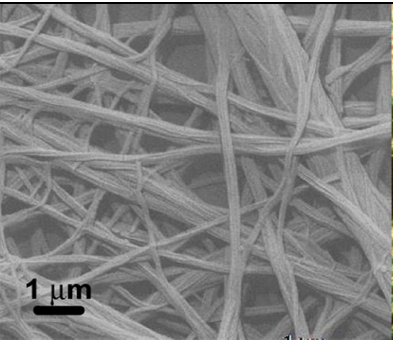
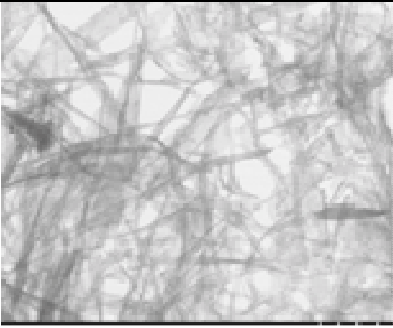
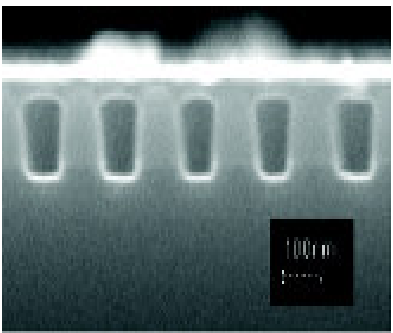
Nano-drug delivery systems currently under investigation

- Dalargin poly(butylcyanoacrylate) nanoparticles for central analgesia (Schroeder, 1998);
- Doxorubicin poly(butylcyanoacrylate) nanoparticles coated with polysorbate 80 for the treatment of cancerous tumors (Mitra *et al.*, 2003);
- Diminazenediaceturate (diminazene) polysorbate 80 nanoparticles for the treatment of second stage Human African Trypanosomiasis (Olbrich *et al.*, 2004);
- Amphotericin B chitosan dextran sulfate nanoparticles for the treatment of systemic fungal infection (Tiyaboonchai and Limpeanchob, 2007);
- Delavirdine, stavudine and saquinavir poly (butylcyanoacrylate), methylmethacrylate-sulfopropylmethacrylate, and solid lipid nanoparticles for the treatment AIDs Dementia Complex (Kuo and Su, 2007);
- Indomethacin polylactic acid nanoparticles used for the reduction of fever, pain and inflammation (Závišová *et al.*, 2007);
- Insulin fluorescein isothiocyanate nanoparticles for the management of diabetes mellitus (Damgé *et al.*, 2007); and
- Paclitaxel poly (DL-lactide-co-glycolide) nanoparticles for the treatment of cancerous tumors (Feng *et al.*, 2007).

Nano-drug delivery systems are by no means limited to nanoparticles and may be manufactured in various configurations. These range from typical nanogels formed from crosslinked hydrophilic polymers to nanofluidics. These structural diversifications are further outlined in Table 2.2.

Table 2.2: The diverse architectures of nano-systems

Nanosystem	Description	Image of the nanosystem
Nanogels	These are crosslinked nanoparticles consisting of hydrophilic polymers that give rise to an increase in viscosity of the material (du Toit <i>et al.</i> , 2007)	 <p data-bbox="915 548 1406 596">Cabot Corp Nanogel™, New Hampshire, US, 2003. (www.cabot-corp.com)</p>
Nanofibers	These are fibers with dimensions <100nm prepared via electrospinning or interfacial polymerization techniques (Yang <i>et al.</i> , 2007)	 <p data-bbox="1073 888 1248 909">Wang <i>et al.</i>, 2008</p>
Nanocrystals	These are crystalline material of nanosize. Applications include fluorescent semi-conductor nanocrystals employed as probes to allow for imaging and diagnostics (Parak <i>et al.</i> , 2003)	 <p data-bbox="1081 1192 1240 1215">Shin <i>et al.</i>, 2007</p>
Dendrimers	These are tree-like macromolecules with branches reaching out from the core. These molecules are of particular interest as their production allows for reproducibility and the formation of highly defined structures. They epitomize the concept of multi-functionality medicinal systems as they permit the attachment of various therapeutic and imaging molecules to their surface (du Toit <i>et al.</i> , 2007)	 <p data-bbox="1062 1528 1260 1551">Kong and Pan, 2008</p>
Nanoliposomes	A lipid layer/s surrounds An aqueous core. These systems may be able to carry both hydrophobic drugs (lipid layer) as well as hydrophilic drugs (aqueous layer). In addition, liposomes may carry charged drugs within its core that will neutralize upon contact to bodily fluids thereby transversing through the surrounding membranous layer (Zaru <i>et al.</i> , 2007)	 <p data-bbox="984 1839 1338 1883">University of Washington, 2000-2008 (www.washington.edu)</p>

<p>Nanowires</p>	<p>These are two dimensional structures with surfaces that can be functionalised to promote targeting, biocompatibility, solubility and controlled drug release (Kwon <i>et al.</i>, 2007)</p>	 <p>Huang <i>et al.</i>, 2008</p>
<p>Nanotubes</p>	<p>Employment of porous membranes to create nanosized hollow tubes of various dimensions. Functionalization of these tubes allows for the attachment of various drugs to the structure</p>	 <p>Xiong <i>et al.</i>, 2004</p>
<p>Nanofluidics</p>	<p>The infamous "lab on a chip". These systems look at the movement of nanoscale drops of fluid into and out of bodily fluids to deliver drug to their target (Hu and Li, 2007)</p>	 <p>Guo , 2005</p>

2.2. Parkinson's disease: An Overview

In 1817, James Parkinson wrote "An Essay on the Shaking Palsy" which aptly described the clinical manifestations of the disease which later bore his name (Lim, 2005). PD is characterized by the depletion of dopaminergic nigrostriatal neurons. It is the most common movement disorder and second, only to Alzheimer's disease, as the cause of age-related neurodegeneration (Mosley *et al.*, 2006). As the numbers of the aging population escalates so does the prevalence of neurodegenerative disorders such as PD. Dopamine (DA) replacement therapy is essential to manage the motor manifestations of PD.

2.2.1. Possible theories explicating the aetiology of PD

Oxidative stress leading to DA neuronal degeneration

It has been reported that the brain has an increased risk (in comparison to the rest of the body) of oxidative stress due to its inability to counteract radicals (Owen *et al.*, 1996). Furthermore the metabolism of DA leads to the formation of hydrogen peroxide (H_2O_2) (Czerniczyniec *et al.*, 2007). This hypothesis is further believed as studies have confirmed that (Owen *et al.*, 1996):

- DA turnover is likely to be increased in surviving neurons with a resultant increase in oxidation and thereby increased formation of H_2O_2 ;
- Levels of reduced and total glutathione are decreased in the pars compacta of the substantia nigra (SNc) suggesting decreased protection against OH formation;
- Iron concentration is increased in the SNc thereby increasing the likelihood of an interaction with H_2O_2 and consequent OH formation; and
- Lipid peroxidation is increased in the SNc.

Exposure to environmental toxins

This theory is based on the symptoms and clinical finding, in animals and humans, when exposed to toxins such as 1-methyl-4-phenyl-1,2,3,6-tetrahydropyridine (MPTP) and 6-hydroxydopamine (6-OHDA) being the same as in PD. Research has shown that there is a possible link between the exposure to environmental toxins and the development of PD (Rajput, 2001).

An inherited disease

It has been reported that the lifetime risk in first degree relatives of sporadic cases is estimated to be as high as 17% with the mutated genes, α -synuclein and parkin, being identified as the genes responsible for the inheritance of PD (Popovic and Brundin, 2005).

Increased risk of PD with age

The increase in age has an additive effect on cell atrophy that in turn causes the degeneration of specific areas of the brain, detrimental neuropathology and therefore an increase in the prevalence of PD (Elbaz and Tranchant, 2007). However; recent findings have shown that an increase in age may not be significant in the cause of PD (Calne and Kumar, 2007).

Pathology of PD:

Lewy bodies are considered to be the hallmark feature for PD diagnosis (Lu *et al.*, 2005). These are described as intra-cytoplasmic, single or multiple, spherical or elongated, eosinophilic masses possessing a dense core and a peripheral halo (Wakabayashi *et al.*, 2006). The core consists of microscopic, dense deposits of abnormal protein, formed as products of the mutated α -synuclein gene.

Other factors that may trigger the onset of PD include viral infection; excess iron and manganese in the diet (responsible for additional oxidation and thereby degeneration of the brain cells); CNS disorders (brain tumors, hydrocephalus, encephalitis, meningitis and stroke); traumatic injury to the brain; abuse of antipsychotic drugs and intravenous 1-methyl 4-phenyl 1,2,3,6-tetrahydropyridine (resulting in mitochondrial dysfunction); and carbon monoxide poisoning (Carson-De Witt, 2003).

2.2.2. The diagnosis of PD

Diagnosis and subsequent treatment of PD is sufficiently delayed due to the fact that approximately 80% of striatal nerve terminals and up to 60% of dopaminergic neurons in the substantia nigra have been lost before clinical presentation of symptoms of PD becomes apparent (Agid, 1991). Compensatory mechanisms such as; increased dopaminergic activity in the substantia nigra, down-regulation of DA transporters and up-regulation of postsynaptic DA receptors in the striatum account for the lack of symptoms at an earlier stage of the disease (Nyholm, 2003). There is no definitive test for the diagnosis of PD. Diagnosis is made on the

development of symptoms of the disease including gait changes, trembling and difficulty speaking or writing. The United Kingdom PD Society (UK PDS) Brain Bank diagnostic criterion is a guideline tool used to aid in diagnosis (Table 2.3).

Table 2.3: *Parkinson's disease syndrome brain bank diagnostic criteria (United Kingdom) (extracted from Hughes et al., 1992)*

Step 1 - Diagnosis of Parkinsonian syndrome

Bradykinesia plus at least one of the following:

Muscular rigidity

Rest tremor

Postural instability

Step 2 - Exclusion criteria including:

History of repeated strokes

History of repeated head injury

History of definite encephalitis

Step 3 - Supportive prospective criteria (at least three required):

Unilateral onset

Rest tremor present

Evidence of progression

Persistent asymmetry

Excellent response to L-dopa

Severe L-dopa-induced chorea

L-dopa response for 5+ years

Clinical course of 10+ years

2.2.3. Pharmacological treatment of PD

Treatment of PD is based on strategies that either prevent dopaminergic cell degeneration and death; stimulate dopaminergic cell proliferation; or compensate depletion of DA (Popovic and Brundin, 2005). Their pharmacological treatment, recommended dosages, side-effects and the limitations are outlined in Chapter 2 Table 2.4 of this dissertation.

Table 2.4: The current pharmacological treatment for PD and their limitations (adapted from Cutson et al., 1995, Comella and Tanner, 1995 and Katzung , 2004)

Class	Drug	Dose	Side-effects	Limitations
Dopaminergic	L-dopa	<i>L-dopa</i> (ratio represent that of carbidopa to L-dopa in mg) <i>1:10 ratio :</i> 50:200 tds/qid <i>1:4 ratio:</i> 25:100 L-dopa tds/qid	<ul style="list-style-type: none"> • Hair loss • Psychiatric manifestations 	<ul style="list-style-type: none"> • On-off Syndrome • Multiple dosing ($t_{1/2} = 1.3\text{hrs}$) • Sinemet[®] CR-pulsed rather than constant drug levels Patient variation in absorption results in patient's mood state during the course of the day (United States Patent 4883666, 1989)
MAO inhibitors	Selegine <i>Rasagiline</i>	<i>Selegine:</i> 5mg bd <i>Rasagiline:</i> 1mg bd or 0.5mg bd(with L-dopa)	<ul style="list-style-type: none"> • Orthostatic hypertension • Insomnia • Impotence 	<ul style="list-style-type: none"> • Hypertensive crisis • Combination of Rasagiline with L-dopa may possibly increase blood levels of Rasagiline or exacerbate pre-existing dyskinesia (Product information, 2006)
Antivirals	Amantadine	<i>Amantadine:</i> 100mg bd is thought to either, promote the release, prevent the reuptake, or have an influence on the synthesis of DA.	<ul style="list-style-type: none"> • Slurred speech • Shortness of breath • Visual disturbances 	<ul style="list-style-type: none"> • Effect is short lived therefore used as a diagnostic tool
COMT-inhibitors	<i>Tolcapone</i> <i>Entacapone</i>	<i>Tolcapone:</i> 100mg tds (with Sinemet [®]) <i>Entacapone:</i> 200mg tds (with Sinemet [®])	<ul style="list-style-type: none"> • Dyskinesias • Hepatotoxicity (talcapone) 	<ul style="list-style-type: none"> • May only be used in combination with L-dopa • Talcapone - use is limited due to risk of causing potentially fatal, acute fulminant liver failure (should only be used in patients where there is no alternative)
Anticholinergics	<i>Trihexyphenidyl</i> <i>Benztropine</i>	<i>Trihexyphenidyl:</i> 2mg tid <i>Benztropine:</i> 1mg tds Specifically effective against tremor	<ul style="list-style-type: none"> • Blurred vision • Difficult or painful urination (especially in older men) • Dryness of membranes 	<ul style="list-style-type: none"> • There is little to no corrective effect on rigidity or bradykinesia or akinesia • Increased side-effect profile
DA Agonists	Ergot derivatives: <i>Bromocriptine</i> <i>Pergolide</i> Non-ergot derivatives: <i>ropinirole</i> <i>pramipexole</i>	<i>Pergolide:</i> 1mg tds <i>Bromocriptine:</i> 5mg bd	<ul style="list-style-type: none"> • Psychiatric disturbances • Possibility of myocardial infarctions and subsequent death 	<ul style="list-style-type: none"> • Limited to use as adjunctive therapy • Exacerbation of adverse effects in elderly • Increased half life will decrease the risk of motor complications but brings increase in price, poorer control of symptoms and DA effects
	<i>Apomorphine</i>	<i>Apomorphine:</i> 0.06mg/kg (0.6mL/kg) Alleviates the "off" periods experienced when taking L-dopa	<ul style="list-style-type: none"> • formation of skin nodules • nausea 	<ul style="list-style-type: none"> • Short <i>in vivo</i> half-life = 100min • Impractical administration route (s.c) for chronic use

2.2.4. Challenges of current therapy used in the treatment of PD

2.2.4.1. Limitations of Sinemet[®] for the treatment of PD

Sinemet[®] is currently the leading treatment used for PD but numerous limitations:

- Loss of efficacy: Sinemet[®] loses its efficacy in 50% of patients as soon as 5-15 years following continuous administration. Patients begin to experience debilitating dyskinesia ("on-period") and profound tremor, rigidity, and akinesia ("off-periods") (Arica *et al.*, 2005);
- Response fluctuations: Sinemet[®] has wide distribution throughout the body and patient variation is often documented;
- Accelerated premature metabolism: L-dopa causes delayed gastric emptying, increasing absorption rate in the stomach where L-dopa is absorbed. Dopa decarboxylase is present within the gastric mucosa and will prematurely convert L-dopa into DA which further serves to stimulate DA receptors in the stomach leading to further delays in the gastric emptying rate (Pfeiffer, 2005);
- Minimal BBB transport: approximately 1% of the administered dose is available to the brain;
- Large doses related to side-effects: severe nausea, vomiting and orthostatic hypotension;
- Controlled released preparations: controlled release L-dopa therapy (Sinemet[®] CR) – a "once-a-day" treatment results in pulsed rather than constant drug levels (Hely *et al.*, 2002) which alleviates the "wearing-off" phenomenon. In addition, the degree to which Sinemet[®] CR increases the $t_{1/2}$ of L-dopa is minimal (40min). Moreover, it has a distinct disadvantage, especially in advanced PD, because its effects are more unpredictable than those of immediate-release L-dopa (Popovic and Brundin, 2005);
- Drug holidays: involves the temporary withdrawal of L-dopa for a predetermined period. This approach is employed as an attempt to resensitize DA receptors in the striatum so that L-dopa therapy can be reintroduced at lower doses with fewer side-effects. This strategy however is highly controversial due to possible serious effects such as neuroleptical malignant-like syndrome and therefore only used as a last resort (Koziorowski and Friedman, 2001); and
- Continuous infusion: the infusion of L-dopa/carbidopa (Duodopa[™], NeoPharma AB,

Uppsala, Sweden), into the duodenum or subcutaneous apomorphine infusion over at least 6 months - this seems highly impractical and requires hospitalization for the first series of infusions (Koziorowski and Friedman, 2001).

- Transdermal patches: Neupro[®] (Schwartz Pharma Neupro[®], Monheim, Germany). The patch allows for sustained release of DA over a 24 hour period resulting in steady state plasma drug levels and essentially the reduction/elimination of the 'on-off' phenomenon. However, the patch needs to be applied and removed once daily and may lead to issues of patient compliance. In addition, there is a limitation to the quantity of drug that may be delivered per square meter of skin (Rascol, 2005) and the resulting continuous stimulation of the receptors may lead to putative desensitization (Pfeiffer, 2007).

2.2.4.2. The gap in current therapy employed in the treatment of PD

Development of novel drug delivery system for the treatment of PD needs to address (Stocchi, 2006) neuroprotection where drug therapy not only provides relief from the immediate symptoms but also serve to restore and repair further neuronal damage in order to inhibit the progression of PD. Furthermore elimination of "end of dose" dyskinesias as with L-dopa and easy administration and favorable dosing schedules need to be achieved with new treatment options. Research into drugs that treat both motor and non-motor symptoms (depression and memory loss) is also encouraged so as to provide holistic treatment for PD.

2.2.5. Implantable novel polymeric drug delivery systems for the treatment of PD

Optimization of drug release, stability and sterility as well as size and shape of the implant needs to be scrutinized to ensure the long-term controlled release and biocompatibility of an implanted system (Fournier *et al.*, 2003). Furthermore, an implantable system for any chronic cardiovascular or neurodegenerative disorder should retain the bioactivity of the drug. (Vats *et al.*, 2005).

Implantation of a DA-loaded biodegradable polymeric device is necessary in incidences where patients (Taylor and Minger, 2005) show refractoriness to conventional drug therapy; have a complete loss of DA-producing neurons; require targeted delivery of DA; and/ or wish to avoid ethical and moral consequences that come with the implantation of fetal or tissue cells.

2.2.5.1. L-dopa/Carbidopa loaded microspheres for implantation into the cerebellum

Arica *et al.*, 2004 conducted studies on these microspheres implanted into the cerebellum of the rat brain. Results showed that test rats had significantly reduced apomorphine rotations as compared to the control group, beginning at week one up to eight post-implantation holding promise as a new treatment for PD. The drawback with the study may have been the employment of two separate costly drugs into the formulation whereas DA-loaded drug delivery systems prove more feasible in that the drug-loaded microspheres system was implanted directly into the brain (Arica *et al.*, 2004).

2.2.5.2. DA-loaded drug delivery systems: microspheres and a silicone pellet into the striatum

In two separate studies, DA was loaded into drug delivery systems for the treatment of PD. In the first study, DA-loaded microspheres were implanted into the striatum of the rat brain and released drug in 120min and while it did decrease the rate of release of drug, the quantity was the same as for non-encapsulated, free drug (McRae-Degueurce *et al.*, 1988). In a later study, rats were implanted with DA-releasing pellets which showed a 50% reduction in apomorphine-induced rotational behaviour, and this effect persisted for the 2-month duration of the experiment (Becker *et al.*, 1989).

2.2.6. Gene Therapy

The early onset of the disorder may be due to genetic predispositions of PD. Gene therapy is being investigated to slow the progression of the disease. The vector adenoassociated viral (AAV2) not only provides for the attachment of genes but is responsible for the restoration of the Aromatic L-Amino Acid Decarboxylase (AADC) enzymatic function and allows for the conversion of L-dopa to DA, which is significantly reduced in PD. These studies are still underway and have now moved onto clinical trials (Fiandaca *et al.*, 2007).

Genes being investigated are:

- AAV2 Glutamic Acid Decarboxylase (GAD): rate-limiting enzyme for synthesis of the major inhibitory neurotransmitter in the brain, γ -amino butyric acid (Fiandaca *et al.*, 2007);
- AAV2 Human Aromatic L-Amino Acid Decarboxylase (hAADC): has an additive effect on the function of AADC and so may decrease the dose of L-dopa required as well as increase its efficacy (Fiandaca *et al.*, 2007); and
- AAV2 neurotrophic factor neurturin (NTN): may prevent the degeneration and provide neuroprotection for the DA-neurons in the striatum (Gasmi *et al.*, 2007).

2.2.7 Empirical treatments employed in the treatment of PD

Novel symptomatic treatments that target the non-dopaminergic areas will eliminate the motor side effects that arise from the use of dopaminergic agents (Colosimo *et al.*, 2006). Examples of these include α -2 adrenergic antagonists, adenosine A2A receptor antagonists, α -amino-3-hydroxy-5-methylisoxazole-4-propionate receptor antagonists, neuronal synchronization modulators and agents that interact with serotonergic systems.

In addition, there has been investigation into various agents that may be used to provide neurorestoration and protection in PD, these are outlined in Table 2.5.

Table 2.5: Selected neuroprotective and neurorestorative agents under investigation for the treatment of PD

Drug Name	Mechanism Of Action	Short comings/Side-effects	Animal model evidence	References
<i>Co-enzyme Q10</i>	Anti-oxidant	Not regulated by the FDA Expensive*	Administration of 200mg/kg/day of Co-enzyme Q10 for a period of five weeks resulted in a decrease in striatal DA concentrations in MPTP-lesioned mice	Co-enzyme Q10 and nicotinamide are neuroprotective against mitochondrial toxins <i>in vivo</i> (Beal <i>et al.</i> , 1994)
<i>Creatinine</i>	Enhances mitochondrial function and anti-oxidant properties	Weight gain, oedema, nausea, vomiting and diarrhea*	Administration of 1% creatinine for a period of two weeks resulted in a 10% loss of dopamine neurons in MPTP-lesioned mice in comparison to a 70% loss in untreated mice	Creatinine and cyclocreatine attenuate MPTP neurotoxicity (Matthews, 1999).
<i>GM1 ganglioside</i>	Possible inhibition of cell apoptosis, protection against excitotoxicity and has been hypothesised to reduce the sensitivity of DA-neurons to toxins	Chronic administration may lead to increased serum cholesterol, triglycerides and apolipoprotein B levels*	Administration of GM1 to MPTP-lesioned cats resulted in an enhanced sensorimotor behavioral recovery compared to the untreated group. Results show enhanced release and reuptake of DA in GM1-treated animals and an increase in functional DA terminals	Differences in release and clearance of extracellular dopamine in the striatum after spontaneous or GM1-ganglioside-stimulated recovery from experimental Parkinsonism (Schneider <i>et al.</i> , 2000)
<i>Minocycline</i>	Might inhibit microglia-related inflammatory events, and also nitric oxide synthase production thereby inhibiting apoptotic (Frankish, 2003 Peschanski, 1994)	Anorexia, nausea, vomiting, dizziness, rash, hypersensitivity reactions and headache (Peng <i>et al.</i> , 2006)	Administration of minocycline to weaver mice decreased the degeneration of DA neurons. Mice (aged 3 weeks) showed a 30% loss of nigral neurons in comparison to untreated mice who displayed a 50%.	Nigrostriatal dopaminergic neurodegeneration in the <i>weaver</i> mouse is mediated via neuroinflammation and alleviated by minocycline administration (Peng <i>et al.</i> , 2006)
<i>NSAIDs</i>	Potent inhibitors of cyclooxygenase enzymes resulting in reduction of inflammation involved in PD pathogenesis (Chen <i>et al.</i> , 2003)	All NSAIDs have shown to be toxic to DA-neurons, except for ibuprofen (Chen <i>et al.</i> , 2003)	The content of DA in striatum showed significantly decreased after MPTP intoxication in ibuprofen-treated animals compared with control and non-ibuprofen-treated animals	Ibuprofen and the mouse model of Parkinson's disease (Kurkowska-Jastrzebska <i>et al.</i> , 2006)
<i>Nicotine</i>	Stimulation of nicotinic receptor evokes the release of DA and is a possible free radical scavenger (Singh <i>et al.</i> , 2007)	The benefits of the treatment are far overshadowed by the harmful respiratory and addictive effects	Nicotine treatment prevented the striatal DA loss after a 6µg 6-OHDA injection when administered 4hr before and 20hr, 44hr and 68hr post- toxin	Nicotine prevents striatal dopamine loss produced by 6-hydroxydopamine lesion in the substantia nigra (Costa <i>et al.</i> , 2001)
<i>Melatonin</i>	Potent free radical scavenger which can enhance antioxidant activity (Kadanthode, 2003)	Increased drowsiness	Chronic administration of melatonin prevented nigral dopaminergic cell death induced by 6-ODHA in the rat model	Protective effect of melatonin in a chronic experimental model of Parkinson's disease (Antolín <i>et al.</i> , 2002)

* (National Institute of Neurological Strokes and Disorders, 2005)

2.2.8. Current surgical approaches for the treatment of PD

The surgical approach for the treatment of PD has lost favour due to complications and the introduction of effective pharmacological treatments such as L-dopa (Walter and Vitek, 2004). However the current failure in the treatment has lead to resurgent interest in this approach (Follett, 2000).

Patient selection for surgical intervention (Walter and Vitek, 2004):

- Non-Parkinson's Plus patients: patients who are responsive to pharmacological treatment;
- Age: younger patients seem to tolerate the surgery well;
- Patients who are on medication that still display significantly debilitating symptoms;
- Patients should not display significant neuropsychological dysfunction ;
- Patients should not show any intracranial pathology that could result in surgical complications; and
- Depression or mood disorders adequately controlled with medication.

Table 2.6 highlights the three major surgical treatments for PD patients that includes restorative (cell transplantation); ablative (pallidotomy and thalamotomy); and electrophysiological (deep brain stimulation) (Kolchinsky, 2001).

Table 2.6: Surgical strategies employed for the treatment for PD

Class		Description	Symptom Improvement	Complication/ Limitation	Success Rate in Particular Studies
Ablation	<i>Pallidotomy</i>	Performed on the side contralateral to the most debilitating symptoms. Surgical lesioning of the globus pallidus, a deep sub-region of the basal ganglia, situated near the thalamus (Dewey, 2004). Irreversible procedure	Tremor L-dopa induced bradykinesia Rigidity (Thompson, 2001)	Visual impairment Facial Paresis Hemiparesis Speech and voice Memory impairment (Bilateral pallidotomy gives rise to more serious complications) May exacerbate speech and gait disorders in some patients (Dewey, 2004)	Increased success rate <70yrs Bilateral thalamotomies result in a prohibitively high rate of cognitive and speech problems (Dewey, 2004)
	<i>Thalotomy</i>	As per pallidotomy but performed on the thalamus	Tremor (Diamond <i>et al.</i> , 2007)	Speech disturbance Apraxia (Clarke and Moore, 2007)	Tremor has reappeared in a few weeks or months in a small percentage of patients (Hallett, 1999)
Electrophysiological	<i>Deep Brain Stimulation (DBS)</i>	A microelectrode is implanted in subthalamic nucleus of globus pallidus (GPi) or in the thalamus. The electrode delivers electrical current at a high frequency that stimulates the tremor control centre resulting in tremor reduction. Non-destructive, non-invasive and reversible (National Institute of Neurological Disorders and Strokes, 2007)	Reduction in symptoms of advanced PD (implanted in subthalamic nucleus or GPi) Reduction in tremor (implanted in thalamus)	Fatal intracerebral infection Cognition-mania Depression Problems with balance Expensive procedure Generator needs to be replaced every 5-8 years (Panikar and Kishore, 2003)	Reduction of PD questionnaire score by 9.5 points and United PD Rating Scale scores by 19.6 in comparison to the pharmacologically treated group, six months post-DBS (Hamani <i>et al.</i> , 2005). Thirty months post-surgery there was a lasting decrease in fluctuations by more than 50%, and dyskinesias were reduced by about 70% (Toda <i>et al.</i> , 2004)
Restorative	<i>Embryonic stem(ES) cell transplantation</i>	ES cells can be cultured then induced to differentiate into DA-neurons. Initially cells are obtained from developing human embryos, this is a one-time event and so therefore morally acceptable (Walter and Vitek, 2004)	All motor symptoms	Dystonia and dyskinesia development (1 year or more beyond surgery and continued to have persistent dyskinesia despite reduction or elimination of dopaminergic drugs) Poor survival of the grafts, poor cell purity (University of Pittsburgh Study in Neurosurgery, 2007)	Although stem-cell transplants have not yet been used in clinical trials for PD, early animal studies are underway and have shown some ability to produce cells with dopaminergic differentiation

	<i>Fetal Mesencephalic Dopamine-secreting Cells</i>	Ventral mesencephalic tissue from aborted fetuses, after being matched to the patient for ABO blood antigens, can be implanted stereotactically through the caudate and putamen via needle tracks in an attempt to replace the lost nigrostriatal neurons (Drucker-Colín and Verdugo-Díaz, 2004)	All motor symptoms L-dopa induced dyskinesia	Ethical concerns (3-8 embryos are required for a single patient transplantation which does not provide assured success) (Hallett, 1999). Development of "runaway" dyskinesias	30% success rate in patients younger than 60 years old
	<i>Xenotransplantation</i>	May be derived from the ventral mesencephalon tissue from porcine embryos and implanted into the striatum of the human brain (Brevig <i>et al.</i> , 2000)	All motor symptoms	Obsessive compulsive disorder Auditory hallucinations Variance of dyskinesias Worsening of PD symptoms (Peschanski 1994) Fatal or handicapping intracerebral hemorrhages and abscess (Palfi, 2004) Risk of microbe transmission	The success rate depends on the gestational period of the donor tissue as well as volume of tissue implanted The survival of newly transplanted cells is very low (Sayles <i>et al.</i> , 2004) Unsuccessful integration with the existing neural circuitry, cells may ability to release DA and it's a complicated non-reproducible procedure (Brevig <i>et al.</i> , 2000)
Miscellaneous	<i>Radiosurgery and the Gamma Knife</i>	Allows for the precise location and radiation of specific areas in the brain. Investigation for use as a tool for both thalamotomy and pallidotomy in patients who are not candidates for standard surgery (Swedish Medical Center, 2007)	Depends on the type of ablation that is being employed as well as the electrophysiologic al surgery	Mortality Weakness Partial paralysis Tissue necrosis Morbidity (Okun <i>et al.</i> , 2001)	Operated areas were significantly off target (Peschanski <i>et al.</i> , 1994)
	<i>Transcranial Magnetic Stimulation (TMS)</i>	Non-invasive technique that employs high frequency magnetic pulses that are placed on specific area on the scalp so as to target affected areas of the brain. An alternate for patients who may not undergo DBS (Erhardt <i>et al.</i> , 2004)	Motor symptoms (bradykinesia, tremor, postural imbalance) Depressive and visual symptoms (del Olmo <i>et al.</i> , 2007)	Symptoms may actually worsen with this approach (Boylan <i>et al.</i> , 2001)	Acute left frontal reverse TMS (20 Hz) was able to modulate dopaminergic neurotransmission release (30% increase) in a rat study (Kanno <i>et al.</i> , 2004)

2.3. Concluding Remarks

This chapter addressed the challenges of delivery of drug to the BBB and the approaches employed to overcome this. Nanotechnology and its applications in drug delivery, in particular to the brain, were investigated. Furthermore, a synopsis of PD was given as well as the current pharmacological treatment used to treat this disorder and the limitations thereof. The employment of implantable and novel drug delivery devices was discussed. Finally, surgical approaches for the treatment of PD were revisited. Overall the urgency for newer and effective treatment was highlighted.

CHAPTER 3

DEVELOPMENT AND FORMULATION OF DOPAMINE-LOADED CELLULOSE ACETATE PHTHALATE NANOPARTICLES

3.1. Introduction

The size range of <100nm has been the defining term for nanotechnology (Igarashi, 2008). However in DA delivery, this size limitation is not critical and various therapeutically active nano-enabled systems have been used for the treatment of various ailments such as Abraxane[®] 130nm (Abraxis BioScience Corporate Offices, California, USA), Taxol[®] 160nm (Bristol-Myers, New York, USA), Adriamycin[®] 200-400nm (Pharmacia & Upjohn, S.P.A, Milan, Italy) (Farokhzad and Langer, 2006). Nanoparticles may be synthesized employing a number of well established procedures (Peltonen *et al.*, 2004). Salting-out, emulsification-diffusion and nanoprecipitation are among the many examples of these procedures (Olivier, 2005).

Salting-out of nanoparticles

This involves the combinatory use of an organic and aqueous phase under high magnetic stirring rates for a period of 15-20min to facilitate emulsification. Deionised water is subsequently added to induce the diffusion of the organic phase into the external solvent resulting in nanoparticle formation (Galindo-Rodríguez *et al.*, 2005).

Solvent evaporation/ emulsification-diffusion

The polymer and drug are dissolved in an organic phase. The resulting solution is then emulsified by immersing it into an aqueous solution producing an oil in water (o/w) emulsion. Surfactant and/or emulsifying agent may then be added to ensure the stability of the formulation. The organic phase is evaporated by increasing the temperature under reduced pressure. The resultant solution is then centrifuged to produce nanoparticles (Piñón-Segundo *et al.*, 1996; Galindo-Rodríguez *et al.*, 2005).

Spontaneous emulsification or solvent diffusion

A water soluble solvent and a water insoluble organic phase are mixed to produce an oil phase (used for hydrophobic drugs). An emulsion is then prepared as per the solvent evaporation method and nanoparticles are formed. The size of the particles may be significantly reduced by increasing the concentration of the water-soluble solvent (Mohanraj and Chen, 2006).

Supercritical fluid (SF) technology

This method limits the toxicity that occurs as a result of surfactants and/or solvents used during formulation. The chosen solute is solubilised in SF. The solution is then pushed through a nozzle allowing the solute to precipitate (completely free of solvent). The disadvantage of this method is that it may only be used for low molecular mass polymers (Pathak *et al.*, 2005).

Coercervation or ionic gelation

Two diverse aqueous phases are blended (one phase being a hydrophilic polymer solution). The polymers comprise charged groups for electrostatic interaction. The result is the production of nano-size coacervates (Agnihotri *et al.*, 2004). DAs may be encapsulated, covalently attached or adsorbed onto the surface of the nano-carriers (Olivier, 2005). Nanoparticles may be further modified to release DA upon external environmental stimuli such as pH, heat, magnetic fields or chemical changes (Mohanraj and Chen, 2006).

3.2. Materials and Methods

3.2.1. Materials

Cellulose acetate phthalate (CAP) ($M_w=2534.12\text{g/mol}$), poly(vinyl alcohol) (PVA) ($M_w=49,000\text{g/mol}$), acetone, methanol and dopamine hydrochloride (DA) ($M_w=189.64\text{g/mol}$) were all purchased from Sigma Aldrich (St. Louise, MO, USA). Deionized water was obtained from a Milli-Q water purification system (Milli-Q, Millipore, Billerica, MA, USA). All other reagents were of analytical grade and used as purchased.

3.2.2. Technology Applied in the Present Study

3.2.2.1. Application of the Zetasizer[®] NanoZS Series Instrument

The Zetasizer[®] Nano Series (Malvern Instruments, Worcestershire, UK) is an evolution in the analysis of nanoparticles. The instrument allows for measurements imperative and exclusive to nanotechnology. Applications include the determination of particle size and zeta potential (which were employed in the present study) as well as the molecular mass of drugs.

3.2.2.2. The determination of the size of the nanoparticles

Particle size is determined by dynamic light scattering (DLS) that measures the Brownian motion of the particles. Brownian motion relates to particle size in that smaller particle sizes are expected to move more rapidly than larger particles therefore exhibiting greater Brownian motion.

Factors that may affect the rate of particle diffusional speed are:

- Ionic media: a conductive media will increase the electric double layer (Figure 3.1) around the particle, decreasing its speed and thereby increasing its size measurement;
- Surface structure: the arrangement or shape of the particle surface that leads to greater protruding surfaces or reduced, flattened surfaces; and
- Non-spherical particles: the assumption with the DLS technique, employed in this study, is that all particles are spherical. Non-spherical particles may give rise to changes in diffusional speed and therefore size of particles.

The particle size is computed as the hydrodynamic diameter calculated by means of the Stokes-Einstein equation (Kusaka and Adachi, 2007):

$$d(H) = \frac{kT}{3\pi\eta D}$$

Equation 3.1

Where $d(H)$ is the hydrodynamic diameter, D is the translational diffusion coefficient, k is Boltzmann's constant, T is the absolute temperature and η is the viscosity of the liquid/solvent employed. Parameters, such as temperature and viscosity of the liquid/s used, need to be known as it is imperative as these will affect the calculated hydrodynamic diameter. Temperature needs to be kept constant to ensure that the viscosity of the liquid is maintained throughout the measurement process.

3.2.2.3. The determination of the zeta potential of the nanoparticles

The zeta potential, also known as the particle surface charge, may arise from the adsorption of charged surfactant, the ionization of charged groups of DA and CAP and/or surfactants (PVA) employed and the loss of ions from the newly formed nanoparticles. The surface charge influences the rheology, interactions with electrolytes present in the body and stability of the formulation.

Stability may be calculated by employing the Derjaguin, Verwey, Landau and Overbeek theory (DVLO) theory (Derjaguin 1940; Verwey and Overbeek, 1948):

$$V_{\text{total}} = V_R + V_A + V_S$$

Equation 3.2

Where V_S is the potential due to the solvent and V_A and V_R are the forces of electrostatic born repulsion and van derWaals attraction respectively that exist between the particles. A charge of $\pm 30\text{mV}$ is an indication of a stable formulation that will not aggregate.

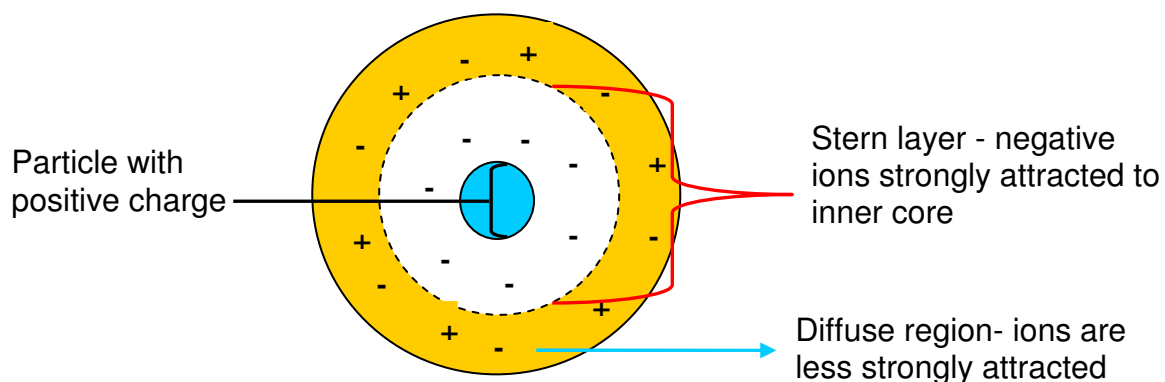


Figure 3.1: Schematic representation of a charged particle and its distribution of ions

An imaginary border exists within the diffuse region, where the sum of the charges of the unstable particles gives rise to the zeta potential measured (Lyklema *et al.*, 1999).

The present chapter focuses on the formulation of DA-loaded polymeric nanoparticles with the employment of CAP as the primary polymer. Investigations leading to the development of an experimental design for the DA-loaded CAP nanoparticles was the focal point of this Chapter. The ultimate goal being the identification of a candidate optimized DA-loaded CAP nanoparticle formulation for incorporation into the NESD.

In this study, the emulsification-diffusion (ED) method was selected for formulating the DA-loaded CAP nanoparticles. Reasons for employing the ED approach are:

- The ED method allowed for the use of a permutated organic solvent system in which both DA and CAP were soluble in both aqueous and organic solvents.
- Organic solvents employed in the formulation were highly volatile and therefore could easily be removed by the process of rota-evaporation;
- Surfactants could be added in the emulsion to impart stability to the formulation; and
- Noticeable incompatibility between CAP and PVA at high concentrations. The ED method allows for smaller quantities to be added that would maintain a satisfactory DA entrapment of >60%.

3.2.3. Rotavapor® R210 (BÜCHI Labortechnik AG, Flawil, Switzerland) with heating bath

The apparatus allows for the distillation of organic solvents under reduced pressure thereby concentrating the sample. The reduction of pressure facilitating liquid evaporation at a lower temperature. The distillation tube transfers the distilled solvent into a condenser. A sealed outlet at the end of the distillation tube prevents sample from entering the condenser that may result in contamination.

3.2.4. Identification of ideal processing conditions for the successful formulation of DA-loaded CAP nanoparticles

The conditions under which the Rotavap was operated is listed Table 3.1.

Table 3.1: Processing conditions for rotaveporation in formulating DA-loaded CAP nanoparticles

Processing Condition	Settings
Temperature (°C)	60
Rotavapor time (min)	60
Rotation speed (rpm)	40
Flask size (mL)	100
Heating media	deionized water

3.2.4.1. Temperature for CAP solubilization

A magnetic stirrer equipped with a heat adjustable plate (Fried Electric, Haifa, Israel) allowed for the control of temperature during formulation. Heat played a significant role in the rate of CAP dissolution in an acetone: methanol solvent system. A temperature of $30\pm 0.5^{\circ}\text{C}$ was chosen to provide a balance between the efficient solubilization of CAP as well as inhibition of evaporation and degradation of the highly volatile CAP solution. Parafilm was also used to cover beakers however the volatility of the sample coupled with the high stirring speeds resulted in the degradation of the film and thereby evaporation of solvent.

3.2.4.2. Stirring time and speed for solvent emulsification

A minimum emulsification/stirring time of 30min was maintained (Quintanar-Guerrero *et al.*, 1996). This duration was increased to 60min to enable greater agitation and to allow for a further reduction in particle size. The maximum stirring speed 700rpm was chosen to maintain favourable hydrodynamicity of the solution.

3.2.5. Preparation of DA-loaded CAP nanoparticles

DA-loaded CAP nanoparticles were prepared using an adapted emulsification–diffusion technique, previously reported (Piñón-Segundo *et al.*, 1996). Briefly, 500mg of CAP and 50mg DA were dissolved in acetone and methanol (3:7 mixture), to which, a 1%^{w/v} PVA solution was added. The solution was agitated for 30min using a magnetic stirrer (Fried Electric, Haifa, Israel) set at 700rpm. A submicronized oil in water emulsion was spontaneously formed due to immediate reduction of the interfacial tension with rapid diffusion of organic solvent into the aqueous phase representative of the Marangoni Effect (Poletto *et al.*, 2008). Excess solvent was evaporated from the suspension using a Rotavap (Rotavapor[®] R210, Switzerland) at 60°C for 1hr and the resulting solution was centrifuged (Optima[®] LE-80K, Beckman, USA) at 20,000rpm for 20min. The sediment layer containing DA-loaded CAP nanoparticles was removed and lyophilized for 24hr at 25mtorr to obtain a powder.

3.2.6. Morphological characterization of DA-loaded CAP nanoparticles

Morphological characterization of the nanoparticles revealed the shape, surface, structure and size homogeneity and possible degree of aggregation. Surface morphology was characterized by Scanning Electron Microscopy (SEM), (JEOL, JEM 840, Tokyo Japan). Photomicrographs were taken at different magnifications and samples were prepared after sputter-coating with carbon or gold (N=10). Nanoparticle size and shape was further explored using cryo-Transmission Electron Microscopy (TEM) (JEOL 1200 EX, Tokyo, Japan, 120keV) for higher definition and resolution. Samples were prepared by placing a dispersion of nanoparticles in ethanol on a copper grid with a perforated carbon film followed by evaporation and viewing at room temperature (N=10).

3.2.7. Determination of polymeric structural variations due to DA-loaded CAP nanoparticle formation

The structure of native CAP, PVA and DA-loaded CAP nanoparticles produced were assessed using Fourier Transmission Infrared (FTIR) spectroscopy to assess the potential for any variations in vibrational frequencies and subsequent CAP and PVA structure as a result of DA, CAP and PVA interactions during DA-loaded CAP nanoparticle formation. Changes in the CAP backbone may alter the inherent stability and therefore affect the physicochemical and physicommechanical properties of the selected polymer type for the intended purpose. Samples of DA-free and DA-loaded CAP nanoparticles were blended with potassium bromide (KBr) in a 1%^{w/w} ratio and compressed into 1×13mm disks using a Beckmann Hydraulic

Press (Beckman Instruments, Inc., Fullerton; USA) set at 8 tons. The sample disks were analyzed in triplicate at high resolution with wavenumbers ranging from 4000-400 cm^{-1} on a Nicolet Impact 400D FTIR Spectrophotometer coupled with Omnic FTIR research grade software (Nicolet Instrument Corp, Madison, WI, USA).

3.2.8. Construction of calibration curves for spectrophotometric determination of DA release from CAP nanoparticles

A calibration curve for DA was constructed using a known series of concentrations of DA (0-0.08mg/mL) in phosphate buffered solution (PBS) (pH 6.8; 37°C). A linear curve was plotted with the observed absorbance on the y-axis and concentration (mg/mL) on the x-axis. The R^2 (a statistical value represented the degree at which a function fits a set of values (Phaser Scientific Software, Florida, USA) was calculated to a value more than 0.95.

3.2.9. Determination of DA entrapment efficiency of CAP nanoparticles

In order to assess the entrapment efficiency of DA within the CAP nanoparticles, post-lyophilized powdered samples were accurately weighed and completely dissolved in PBS, (pH 6.8; 37°C). The DA content was analyzed by UV spectrophotometry at $\lambda_{280\text{nm}}$ (Hewlett Packard 8453 Spectrophotometer, Germany) and computed from a standard linear curve of DA in PBS (pH 6.8; 37°C) ($R^2=0.99$). Equation 3.3 was utilized to compute the DA Entrapment Efficiency (DEE).

$$DEE\% = \frac{D_a}{D_t} \times 100 \quad \text{Equation 3.3.}$$

Where $DEE\%$ is the DA entrapment efficiency, D_a is the actual quantity of DA (mg) measured by UV spectroscopy and D_t is the theoretical quantity of DA (mg) added in the formulation.

3.2.10. *In vitro* DA release studies on CAP nanoparticles

In vitro release studies were performed on the DA-loaded CAP nanoparticle formulations utilizing a shaking incubator (Labex, Stuart SBS40[®], Gauteng, South Africa) set at 20rpm. The DA-loaded CAP nanoparticles was immersed separately in 100mL phosphate-buffered saline (PBS) (pH 6.8, 37°C) contained in 150mL glass jars. At predetermine time intervals 3mL samples of the release media were removed, filtered through a 0.22 μm Cameo Acetate membrane filter (Millipore Co., Bedford, MA, USA) and centrifuged at 20,000rpm (Redhead, 2001). The supernatant was then removed and analyzed by UV spectroscopy at a maximum

wavelength of $\lambda_{280\text{nm}}$ for DA content analysis. DA release was quantified using a linear standard curve ($R^2=0.99$). An equal volume of DA-free PBS was replaced into the release media to maintain sink conditions.

In addition, the Mean Dissolution Time (MDT) values were calculated at 8hr, for each of the samples generated in the experimental design, using Equation 3.4. Computing the release data in this manner allowed for the effective model-independent comparison of all formulations in terms of their respective DA release behavior. All release studies were performed in triplicate. Furthermore, the MDT was calculated for formulations generated in the experimental design.

$$ME\% = \frac{M_{\infty} - M_t}{M_{\infty}} \times 100 \quad \text{Equation 3.4}$$

Where M_t is the fraction of dose released in time $t_i=(t_i + t_{i-1}) / 2$ and M_{∞} corresponds to the loading dose.

3.2.11. Determination of particle size and zeta potential of DA-loaded CAP nanoparticles

The zeta potential value provides an indication of the shelf life stability of the nanoparticles. A high absolute value of zeta potential ($\geq 30\text{mV}$) indicates a high electric charge on the surface of the DA-loaded CAP nanoparticles, which may cause strong repellent forces among particles to prevent aggregation in buffered solution. The nanoparticle zeta potential measurements were obtained using a Zetasizer Nano ZS (Malvern Instruments Ltd, Malvern, Worcestershire, UK). Each sample (1% $^{w/v}$) was appropriately diluted with deionised water, filtered (0.22 μm filter Millipore Co., Massachusetts, USA) to maintain the number of counts per second in the region of 600 (Layre *et al.*, 2006) and placed into disposal cuvettes (size) or capillary cells (zeta potential) (Malvern Instruments Ltd, Malvern, Worcestershire, UK. The viscosity and refractive index of the continuous phase were set to those specific to deionized water. Measurements were taken in triplicate with multiple iterations for each run in order to elute size intensity and zeta potential distribution profiles. Furthermore, the particle size and zeta potential was calculated for formulations generated in the experimental design.

3.2.11. Formulation and Statistical Optimization of DA-loaded CAP Nanoparticles

An experimental strategy, namely the Box-Behnken design, was developed and employed for the statistical optimization of the DA-loaded CAP Nanoparticles.

3.2.11.1. Determination of limitations for variables employed in the Box-Behnken design

The formulation variables listed in Table 3.2 were subjected to their higher and lower limits and thereafter DEE was calculated for each formulation. The most influential variables were selected for the employment in the Box-Behnken design.

Table 3.2: Illustrates the variations in formulations that were used to identify the limits for a Box -Behnken design to optimize DA-loaded CAP nanoparticles and their DA entrapment efficiency percentage

Formulation number	Variables	DEE%
1	Increased quantity of CAP (0.5-1g)	64.30
2	Increased quantity of DA (0.05-0.1g)	68.97
3	Increased emulsification time (0.5-3hr)	18.39
4	Increased rotavap time (0.5-1hr)	42.19
5	Increased [PVA] (0.5-2% ^{w/v})	18.11
6	Reduced [PVA] (0.5% ^{w/v})	63.20
7	Increased stirring speed (300-700rpm)	65.64

- Concentration of CAP – [CAP] was chosen on the basis of [DA] within the formulation. At least 0.5g of CAP was needed to successfully entrap DA. However a limit of 1g was decided on to reduce the formation of DA-free CAP nanoparticles
- Stirring speed - such a parameter is imperative to the size of nanoparticles formed. Stirring speed was set at 300rpm as this allows for minimal agitation while 700rpm was chosen as the upper limit. This was the highest speed at which the vessel could be controlled.
- Emulsification time - a duration of 30min was required to allow for minimal interaction between the aqueous and organic phase while 3hr was chosen as the maximum so as to reduce solvent loss.
- PVA concentration - a concentration less than 0.5%^{w/v} and more than 2%^{w/v} caused precipitation of the PVA and thereby did not produce DA-loaded CAP nanoparticles.

A 4-factor (stirring speed, emulsifying time, [CAP] and [PVA]) Box-Behnken design on the measured responses (zetasize analysis and *in vitro* DA release) was established for formulation optimization.

The variables listed in Table 3.3 were selected for the employment in the Box-Behnken design. Furthermore, the measured responses and for the design and the objectives thereof was established.

Table 3.3: The variables for DA-loaded CAP nanoparticles used in the 4-factor Box-Behnken design

Independent Variables	Values		
	Low	High	
CAP (g)	0.5	1	
PVA (%w/v)	0.5	2	
Stirring speed (rpm)	300	700	
Emulsifying time (min)	30	180	
Dependent Variables	Low	High	Objective
<i>In vitro</i> DA release (MDT)	38	42	Maximize
Zeta Potential (mV)	-20	-39	Minimize
Particle Size (nm)	150	350	Minimize

3.2.11.2. Optimization of DA-loaded CAP nanoparticles

Polynomial equations relating the dependent and independent variables were generated, and the formulation process was optimized under constrained conditions to obtain formulations displaying the desirable Particle Size (minimal), Zeta Potential (minimal) and MDT (maximum).

3.3. Results and Discussion

3.3.1. Surface morphology of DA-loaded CAP nanoparticles

Figures 3.2 and 3.3 are microscopic images that display the morphology and sizes of DA-loaded CAP nanoparticles formulated in an adopted emulsification-diffusion approach

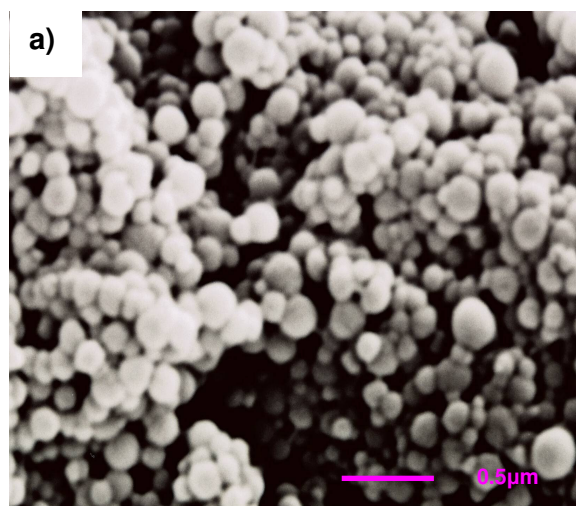


Figure 3.2: SEM images of DA-free CAP nanoparticles

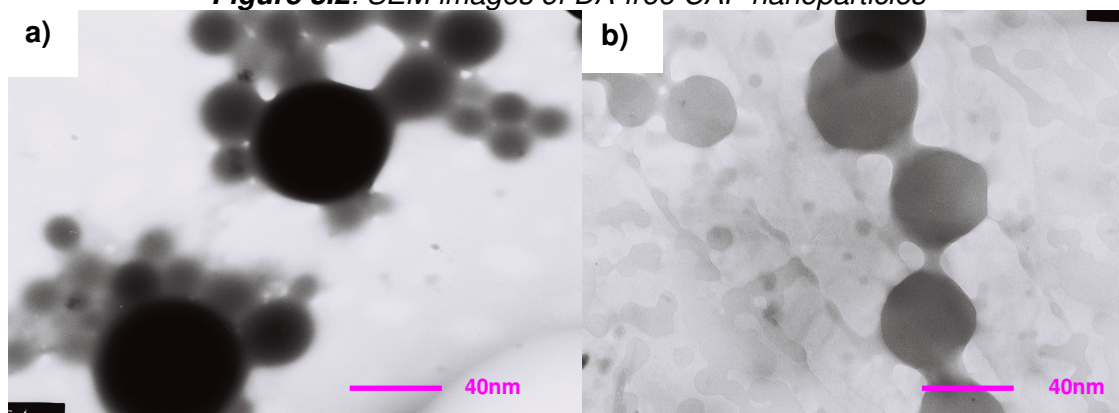


Figure 3.3: TEM images of (a) DA-free CAP nanoparticles and (b) DA-loaded CAP nanoparticles formed

The SEM images (Figure 3.2) show CAP nanoparticles in both DA-free and DA-loaded states. The flocculated particles were uniform in size, spherically shaped and were well-individualised. TEM images of non-DA loaded CAP particles (Figure 3.3a) revealed dense structures with variations in size; however the rounded-shape was maintained. DA-loaded CAP nanoparticles (Figure 3.3b) proved to be slightly transparent with a transient aggregation between them (further explained in 3.2.2.6). Overall both DA-free and DA-loaded CAP nanoparticles showed homogeneous solid matrix structures void of any crystalline surface morphologies.

3.3.2. Structural variations present in the formation of DA-loaded CAP nanoparticles

Chemical structural variations are depicted in Figure 3.4 in the formation of DA-loaded CAP nanoparticles. The variations confirmed the interaction of DA, CAP and PVA in the formation of DA-loaded CAP nanoparticles. Figure 3.4 is the possible chemical reaction that may have occurred between DA, CAP and PVA and therefore provides a further explanation for the structural variations that arose in the formation of the DA-loaded CAP nanoparticles.

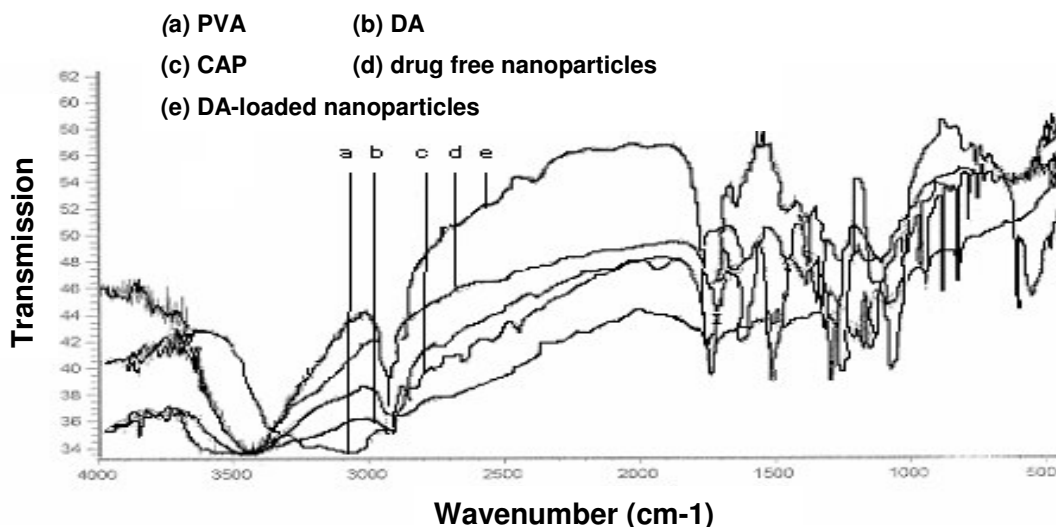


Figure 3.4: FTIR spectra obtained for the formation of DA-loaded CAP nanoparticles

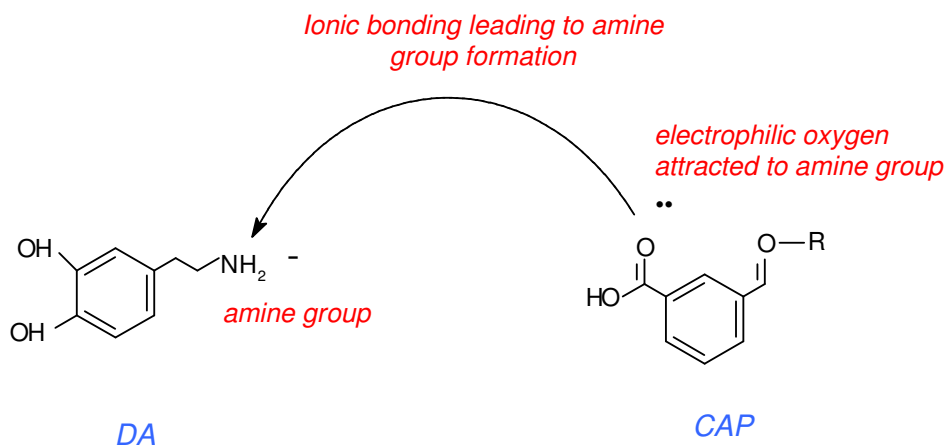


Figure 3.5: Proposed chemical interaction between DA and CAP

FTIR spectra for DA-free CAP nanoparticles (Figure 3.4) revealed a broad stretch band (1070-1242 cm^{-1} and 3200-3600 cm^{-1}) representing OH⁻ groups and a stretch band (2926 cm^{-1}) indicating alkane moieties while a band at 1731 cm^{-1} revealed the presence of -C=O within the CAP nanoparticle structure. The interpretation demonstrates the definitive presence of impervious CAP in DA-free CAP nanoparticles. The spectra for DA-loaded CAP nanoparticles also confirmed the presence of CAP (bands at 1070, 1242 and 2926 cm^{-1}) while the possible interaction of CAP OH⁻ functional groups with the -NH₂ group of DA (Figure 3.5) may have resulted in the formation of nitro compounds (1390 cm^{-1}). The interaction between the H⁺ of the NH₂ group on DA and the O⁻ atom of the OH⁻ group on CAP may have culminated in the proposed physical interactions of the two compounds retarding DA release.

3.3.3. Calibration curve for DA in PBS (pH 6.8; 37°C) for the determination of the concentration of DA release from CAP nanoparticles

Figure 3.6 displays a calibration curve obtained for DA in PBS (pH 6.8; 37°C) employing a UV spectrophotometry at λ_{280} (Hewlett Packard 8453 Spectrophotometer, Germany).

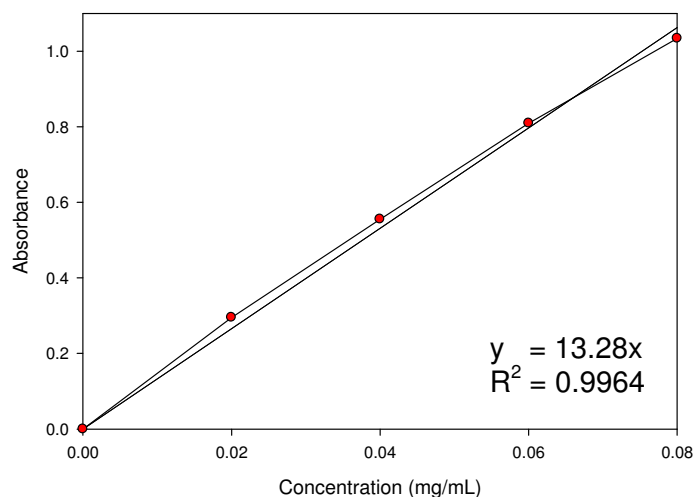


Figure 3.6: DA calibration curve at 280nm in PBS (pH 6.8; 37°C)

3.3.4. DA entrapment efficiency of CAP nanoparticles

A DA entrapment value of 63±0.354% was calculated for the DA-loaded CAP nanoparticles. This is considerably high for a nanoparticle formulation which exhibits a large surface area and thereby DA can be easily adsorbed on to the surface instead of being encapsulated within the particle. The DEE value can be attributed to DA having a greater affinity for the aqueous phase of the emulsion therefore significantly increasing the entrapment of DA.

3.3.5. *In vitro* DA release of CAP nanoparticles

The DA-loaded CAP nanoparticles showed minimal release (2%) at $t = 0.5\text{hr}$ (Figure 3.7). The release of DA could be ascribed to release of DA that was adsorbed onto the surface of the particles while the steady release at $t = 2.5\text{hr}$ could be the result of DA entrapped within the polymeric matrix. Total DA release at 24hr was 16% proving that there was a high degree of prolonged DA delivery. Figure 3.7 is a diagrammatic account of the *in vitro* release of DA from the CAP nanoparticles over a 25hr period.

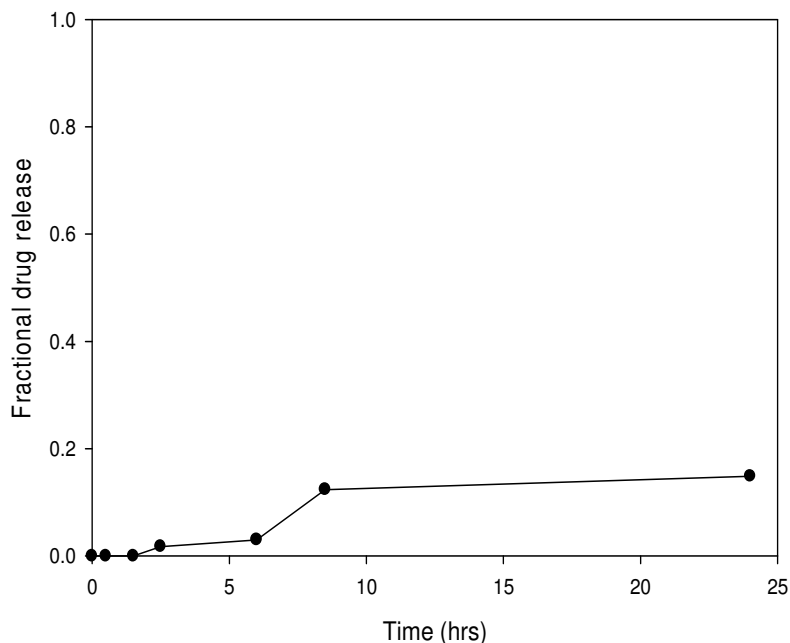


Figure 3.7: DA release profiles for CAP nanoparticles in PBS (pH 6.8; 37°C), ($SD \leq 0.005$)

3.3.6. DA-loaded CAP nanoparticle size and stability

A nanoparticle z-average size of 241nm and 165nm was recorded for DA-free and DA-loaded CAP nanoparticles, respectively (Figures 3.8a and c). The result was atypical as it was expected that the DA-free CAP nanoparticles would have a smaller size in comparison to the DA-loaded particles due to the absence of DA. However, the zeta potential of DA-loaded CAP nanoparticles displayed increased stability in comparison to the DA-free particles. DA-free particles therefore aggregated more easily, contributing to the relative increase in size. A polydispersity index (Pdl) value of 0.030 was calculated for the DA-loaded CAP nanoparticles indicating minimal variation in particle size (165-174nm) and highlighting the uniformity of particle size in the formulation. Zeta potential values of -23.1mV and -35.2mV were recorded for DA-free and DA-loaded CAP nanoparticles respectively (Figures 3.8b and d). While this

result was indicative of the desirable lack of particle agglomeration in both DA-free and DA-loaded particles, it also revealed that the DA-loaded CAP nanoparticles displayed superior stability in comparison to DA-free particles.

3.3.6.1. Size and zeta potential distribution profiles for CAP nanoparticles: DA-free and DA-loaded

The distribution profiles for size and zeta potential of DA (Figure 3.8), DA-free (Figure 3.9a and b) and DA-loaded (Figure 3.9c and d) CAP nanoparticles were obtained using the Zetasizer Nano ZS (Malvern Instruments Ltd, Malvern, Worcestershire, UK). A single peak defines a sample with limited distribution in size or zeta potential.

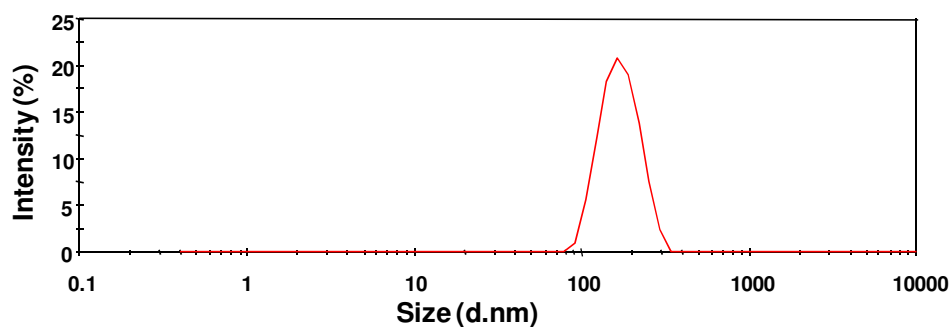


Figure 3.8: Size distribution profile for DA measuring 156.9nm

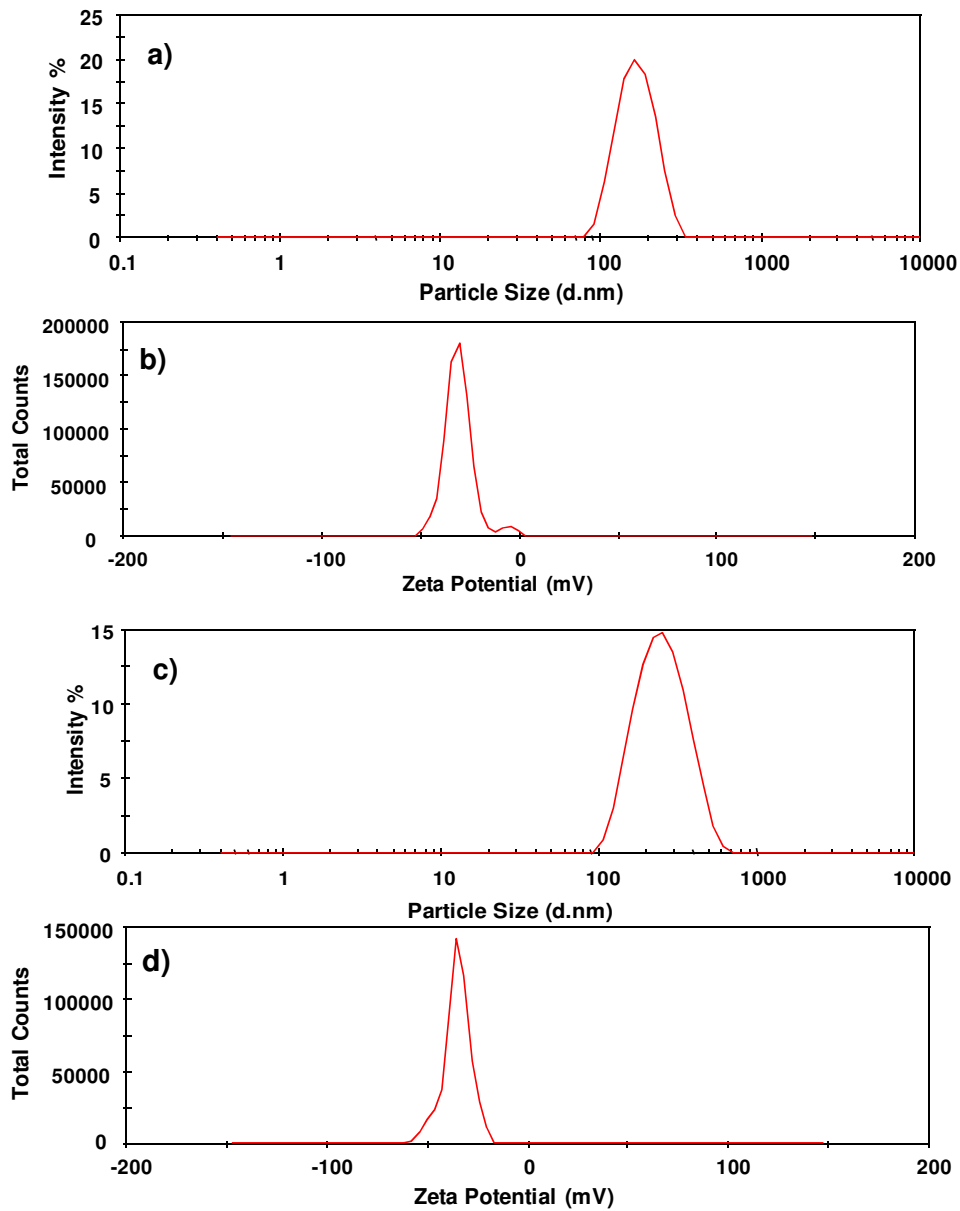


Figure 3.9: Zetasize profiles of a) and b) size intensity and zeta potential distribution profiles of DA-free CAP nanoparticles, c) and d) size intensity and zeta potential distribution profiles of DA-loaded CAP nanoparticles respectively

3.3.7. Experimental design for the optimization DA-loaded CAP nanoparticles

The Box-Behnken study design, requiring a total of 27 experimental runs (formulation combinations), was generated and analyzed using Minitab® V14 (Minitab Inc, PA, USA). The variables for each formulation are listed in Table 3.4.

Table 3.4: Illustration of variations in formulations employed for a Box-Behnken design for the optimization of DA-loaded CAP nanoparticles

Formulation number	CAP (g)	PVA (% ^w /v)	Emulsifying time (min)	Stirring speed (rpm)
1	1	1.25	30	500
2	1	1.25	180	500
3	0.75	0.5	180	500
4	0.75	1.25	105	500
5	0.75	1.25	180	30
6	1	1.25	105	30
7	0.75	1.25	105	500
8	0.75	0.5	105	700
9	10.5	0.5	105	500
10	0.75	1.25	105	500
11	0.5	1.25	105	700
12	0.75	1.25	30	700
13	0.75	1.25	180	700
14	0.5	2	105	500
15	0.5	1.25	105	300
16	0.75	2	105	700
17	1	2	105	500
18	0.75	2	105	300
19	0.5	1.25	30	500
20	0.75	2	30	500
21	1	0.5	105	500
22	0.75	0.5	30	500
23	1	1.25	105	700
24	0.75	0.5	105	300
25	0.5	1.25	180	500
26	0.75	1.25	30	300
27	0.75	2	30	500

3.3.7.1. Measured responses for the experimental optimization of DA-loaded CAP nanoparticles

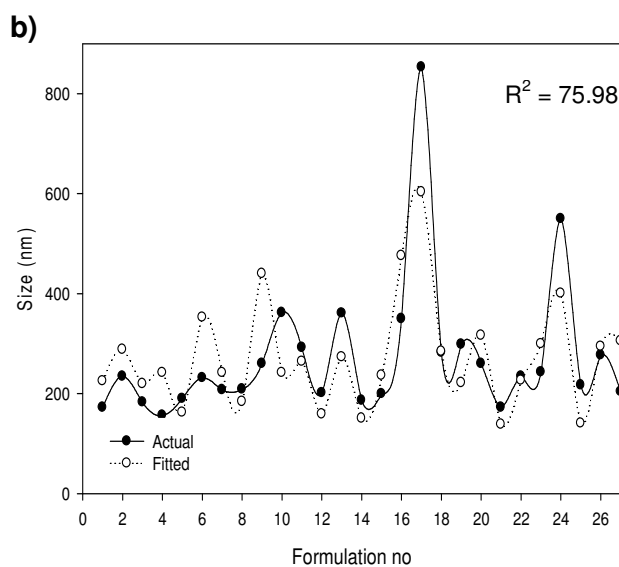
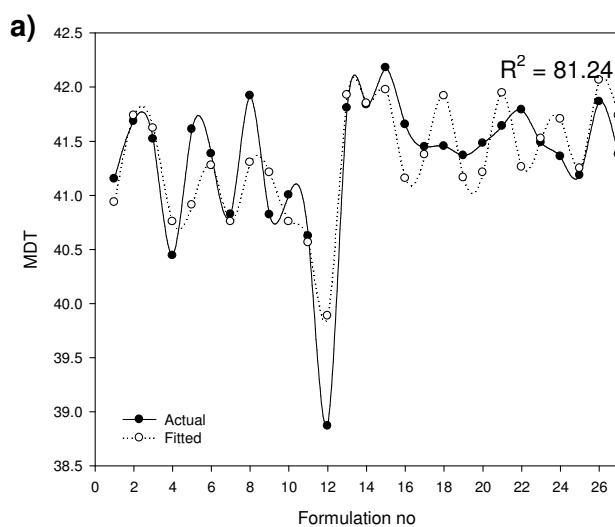
The measured responses (Zeta Potential, Particle Size and MDT) for each of the 27 formulation employed in the Box-Behnken design are listed in Table 3.5.

Table 3.5: Measured responses for the experimental optimization of DA-loaded CAP nanoparticles

Formulation number	Zeta Potential (mV)	Size (nm) (Pdl)	MDT (DEE %)
1	-22.10	164.47 (0.05)	41.15 (32.71)
2	-14.77	221.83 (0.16)	41.68 (46.43)
3	-1.258	224.87 (0.27)	41.52 (35.33)
4	-28.13	158.93 (0.03)	40.44 (30.48)
5	-32.03	237.83 (0.31)	41.61 (39.56)
6	-25.90	232.93 (0.06)	41.38 (41.34)
7	-22.73	209.33 (0.01)	40.82 (21.13)
8	-23.80	212.70 (0.08)	41.92 (50.36)
9	-10.97	265.27 (0.04)	40.82 (30.04)
10	-35.97	365.93 (0.09)	41.00 (37.68)
11	-12.07	300.13 (0.015)	40.62 (31.34)
12	-26.60	199.00 (0.03)	38.87 (16.97)
13	-30.77	367.40 (0.41)	41.81 (62.10)
14	-17.43	187.60 (0.02)	41.84 (56.57)
15	-26.13	200.43 (0.03)	42.18 (20.11)
16	-28.70	360.10 (0.09)	41.65 (45.33)
17	-27.80	817.20 (0.28)	41.45 (49.52)
18	-29.73	330.23 (0.24)	41.45 (39.50)
19	-32.13	297.63 (0.22)	41.37 (37.23)
20	-23.73	265.03 (0.03)	41.48 (41.38)
21	-18.00	172.60 (0.04)	41.64 (48.55)
22	-28.53	221.83 (0.11)	41.79 (44.88)
23	-33.37	240.27 (0.20)	41.49 (36.71)
24	-17.37	416.53 (0.43)	41.36 (34.96)
25	-38.30	218.73 (0.19)	41.18 (28.59)
26	-30.00	258.03 (0.12)	41.87 (56.48)
27	-31.37	200.63 (0.05)	41.38 (48.13)

3.3.7.2. Comparison of the experimental and fitted response values calculated for the experimental optimization of DA-loaded CAP nanoparticles

The plots for experimental versus fitted responses for MDT (Figure 3.10a), Particle Size (Figure 3.10b) and Zeta Potential (Figure 3.10c) showed R^2 values of 81.24, 75.98 and 74.39 respectively. These values show a close agreement between the experimental and predicted values for the responses, proving the Box-Behnken design was robust for the determination of MDT, Particle Size and Zeta Potential. Overall, the plots showed the applicability of the regression models and robustness of the design employed for the optimization of DA-loaded CAP nanoparticles.



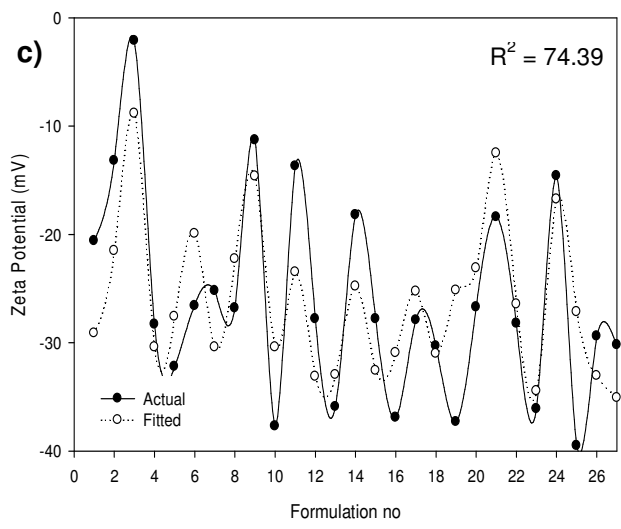


Figure 3.10: The Regression plots for (a) MDT, (b) Particle Size and (c) Zeta Potential for the calculation of R^2 values that determine the correlation between the fitted and experimentally determined values for the formulation responses

3.3.7.3. Response analysis of MDT for DA-loaded CAP nanoparticles

The differing DA release profiles for the respective nanoparticulate formulations are represented in Figure 3.12, signifying their variable capabilities to DA release from their matrix structures. A physical incompatibility described by discontinuous aggregation and subsequent clustering between the predominant polymers CAP and PVA was noted. The incompatibility is confirmed in Figure 3.11a where an increase in [CAP] (0.75-1g) and decrease [PVA] (0.5%^{w/v}) led to a desirable MDT value (>41.5) and vice versa. An increase in [PVA] resulted in an increased MDT (Figure 3.11b) therefore stating that the increase in [PVA] (1.5-2%^{w/v}) controlled and limited DA release. Lower stirring speeds (300rpm) also displayed higher MDT values (41.75) presumably due to the efficient entrapment of DA at lower agitation during processing (Figure 3.11b).

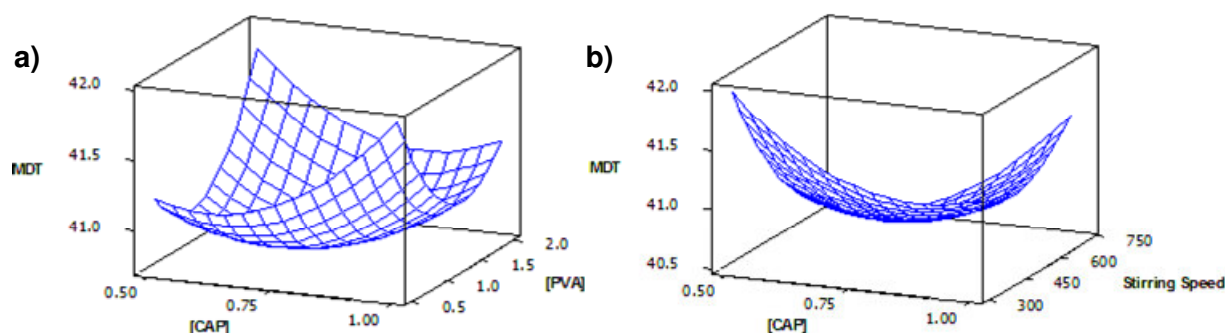


Figure 3.11: Response surface plots correlating MDT and (a) [CAP] and [PVA] and (b) [CAP] and stirring speed

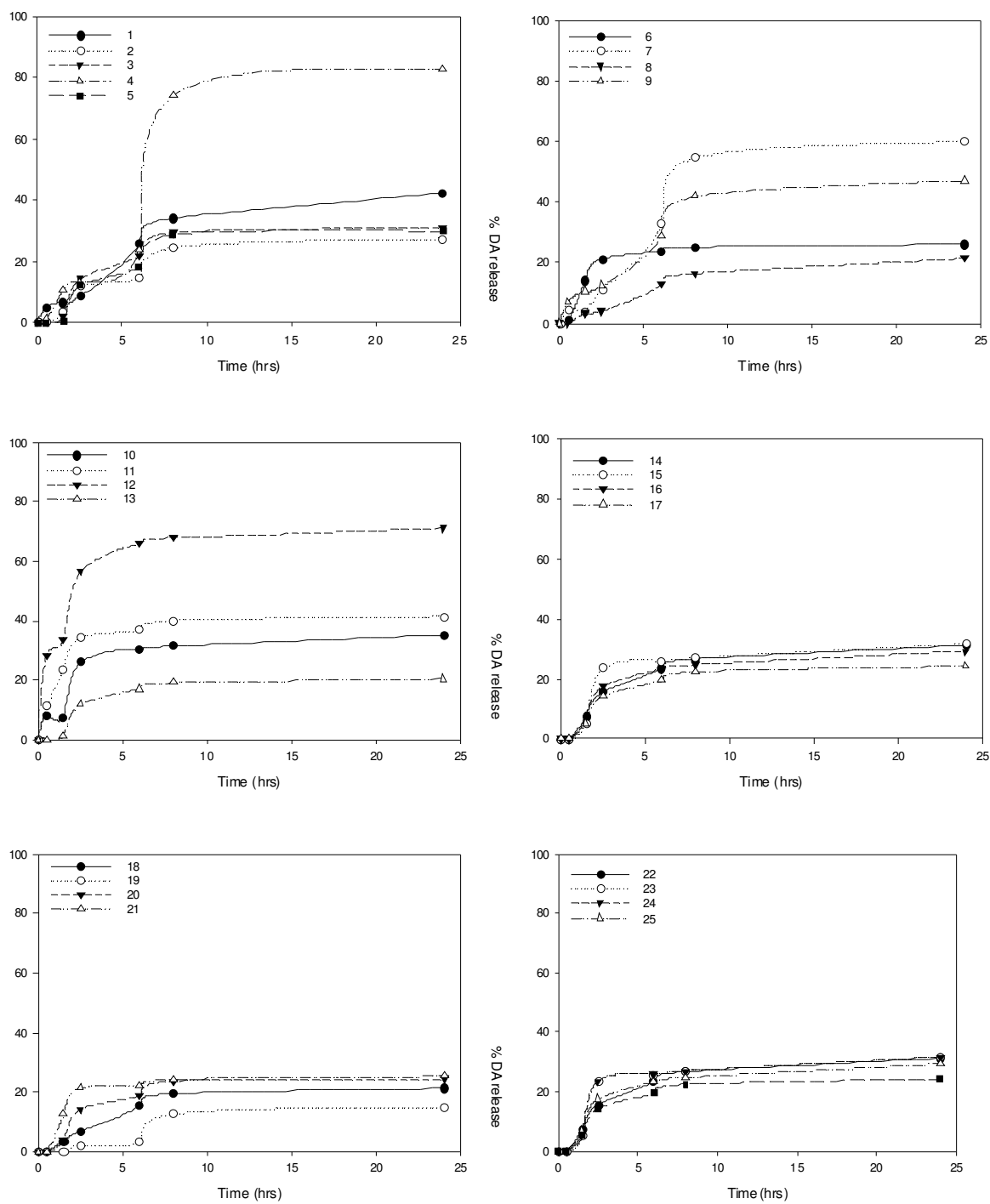


Figure 3.12: Release profiles depicting DA release from the CAP formulations

3.3.7.4. Response analysis for size of DA-loaded CAP nanoparticles

Figure 3.13a showed that an increase in stirring speed (300-700rpm) had an unfavourable effect on the Particle Size (150-300nm). Higher stirring speeds may have resulted in greater inter-particle collisions thereby leading to coagulation of particles (Sugih *et al.*, 2007). A prolonged emulsification phase of between 150-180min coupled with a desirable lower stirring speed resulted in the formation of dispersed non-aggregated particles with a reduced Particle Size of maximum 200nm. An interesting observation (Figure 3.13b) was a decrease in [CAP] (0.5g) resulting in an increase Particle Size (200-225nm). DEE results obtained from the experimental design template (Table 3.4) demonstrated that a significantly lower DEE was achieved with an increase in [CAP] which may have resulted in decreased Particle Sizes. (DA=156.9nm as per Figure 3.8).

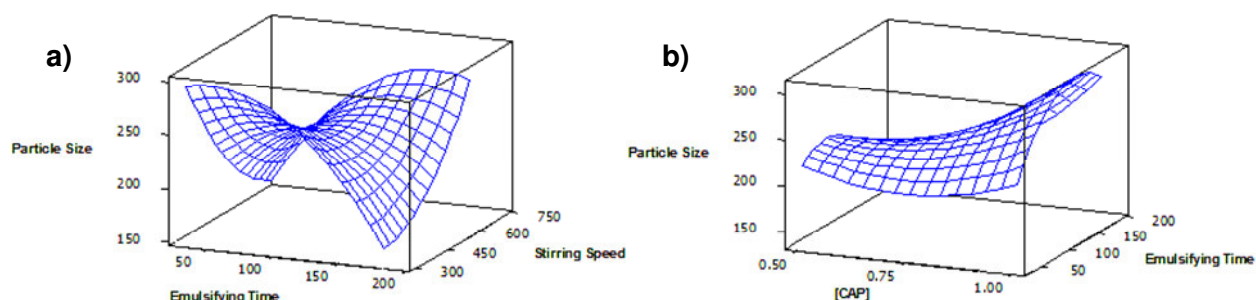


Figure 3.13: Response surface plots correlating Particle Size and (a) emulsifying time and stirring speed and (b) [CAP] and emulsifying time

3.3.7.5. Response analysis for Zeta Potential of DA-loaded CAP nanoparticles

The increase in [PVA] (1.5-2%^{w/v}) gave rise to increased, desirable Zeta Potential (-33 to -35mV) (Figure 3.14a). This was expected as the PVA was added to the formulation due to its ability to act as an absorptive surfactant, decreasing interfacial tension and imparting stability to the formulation. Figure 3.14b showed that an increased in stirring speed (500-700rpm) and decrease in emulsifying time (30min) resulted in high Zeta Potentials (-30 to -35mV). The higher agitation velocity prevented the particles from aggregating and eliminated the possibility of sedimentation or caking of the nanoparticles.

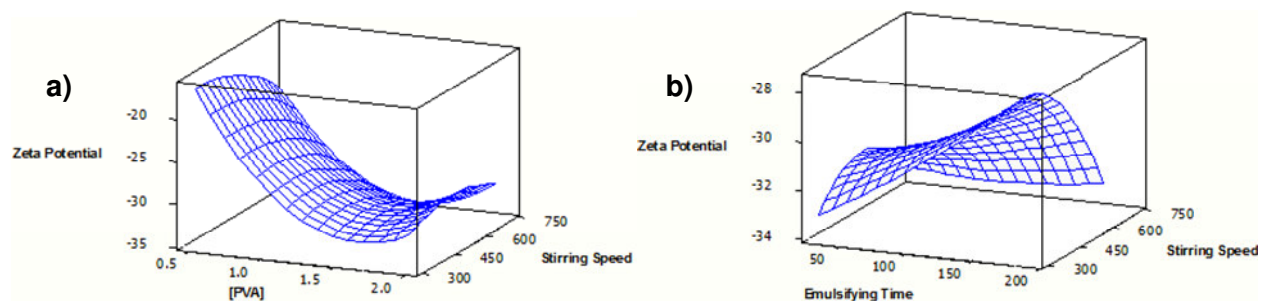
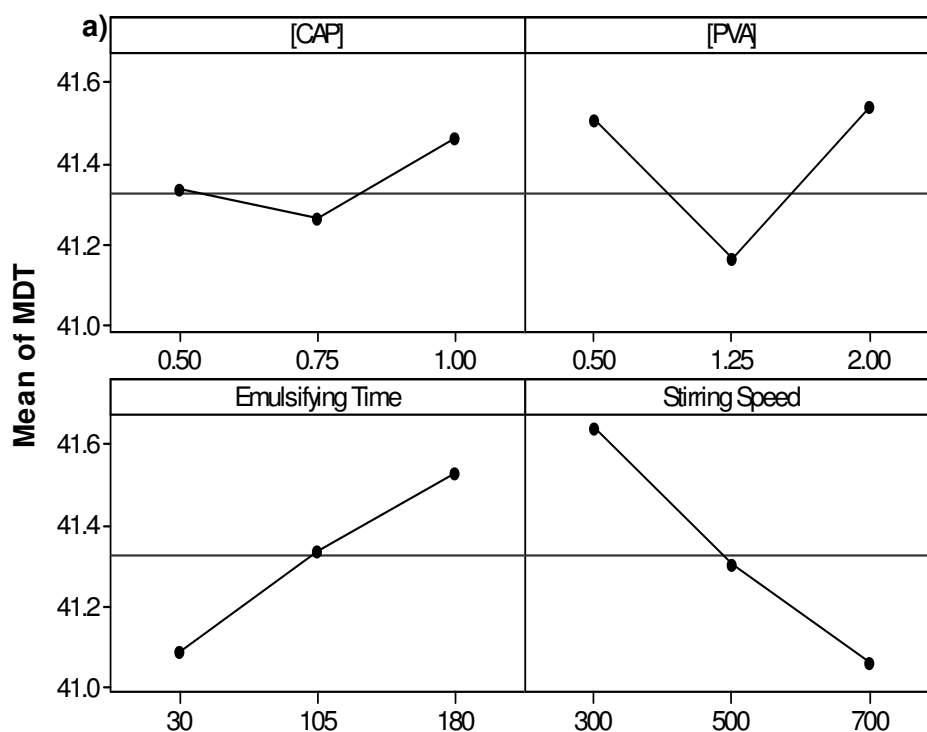


Figure 3.14: Response surface plots correlating Zeta Potential and (a) PVA and stirring speed (b) emulsifying time and stirring speed

3.3.7.6. The main and interaction effects on the responses:

Mean Dissolution Time

The main effects on the MDT (Figure 3.15a) noted that [PVA] had a significant effect ($p = 0.052$) on MDT, where concentrations that were either $<$ or $>$ 1.25%^{w/v} had a positive effect on the MDT. This showed that the increase in [PVA] (1.5-2%^{w/v}) was able to control and limit DA release. While interaction plots (Figure 3.15b) for MDT displayed that a high MDT value was most significantly influenced by a decrease in stirring speed and time ($p = 0.091$). Therefore overall, a decreased stirring speed may allow for the adequate homogenation of the formulation components prior to micronisation of the particles. This would significantly increase the DA entrapment efficiency within the polymer thereby controlling release of DA from the CAP nanoparticles.



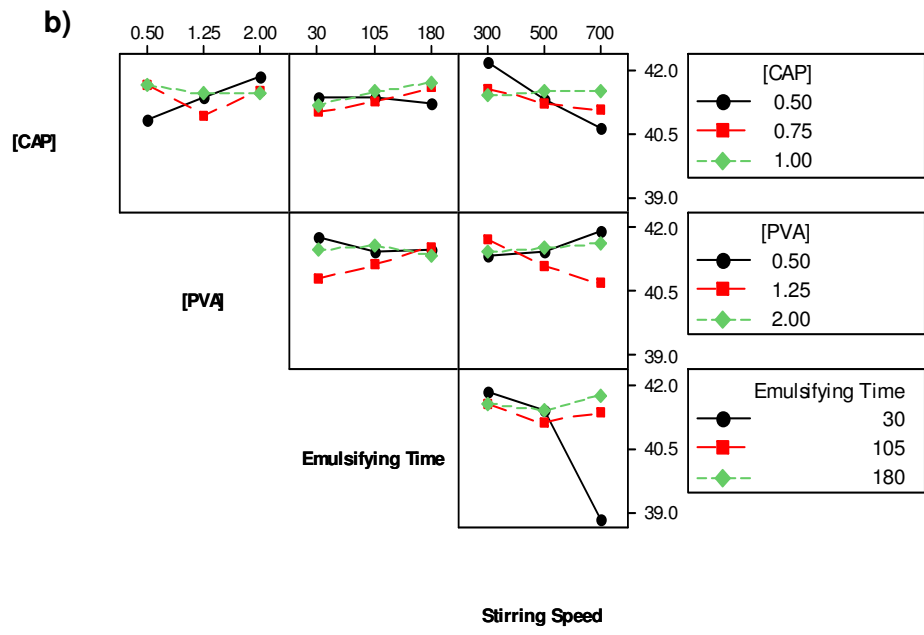


Figure 3.15: Typical (a) main effects plot and (b) interactions plot of the response values for MDT

Particle Size

[PVA] was once again a significant variable in influencing the Particle Size ($p = 0.034$), with Particle Sizes increasing with an increase in [PVA] being a main effect (Figure 3.16a). However, interaction plots (Figure 3.16b) revealed a higher stirring speed and decreased [PVA] produced smaller particles (<300nm). The rate at which PVA was agitated was sufficient to ensure homogeneity and the impartation of surfactant properties to the formulation thereby reducing the risk of particle attraction that could produce unfavorably larger Particle Sizes.

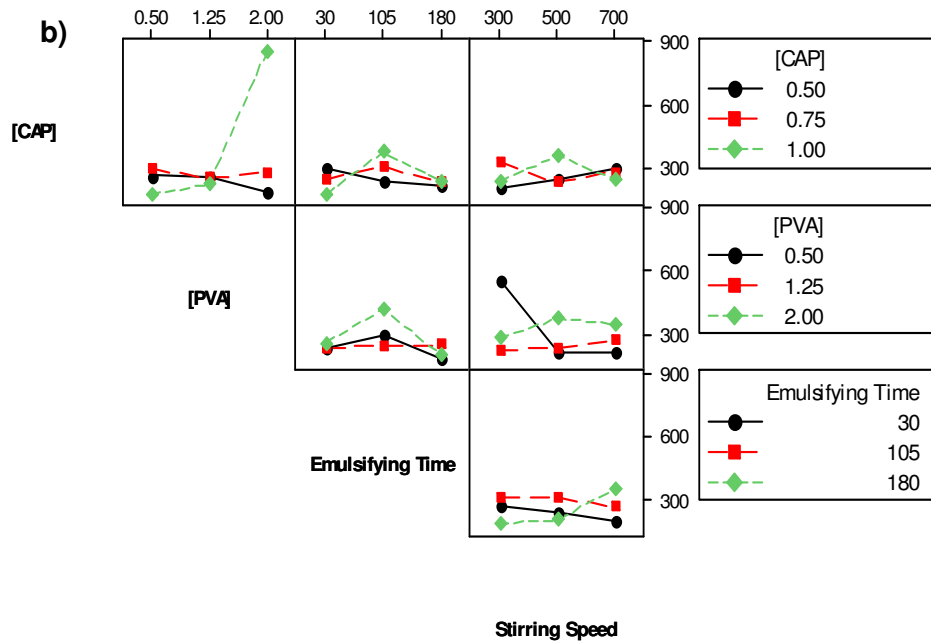
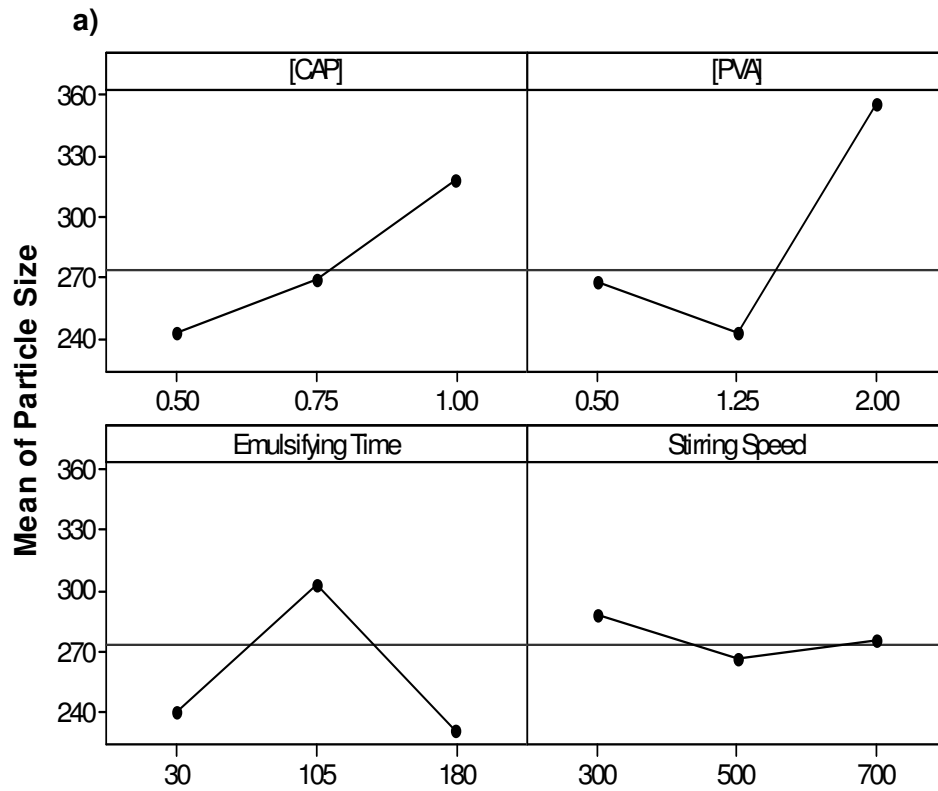
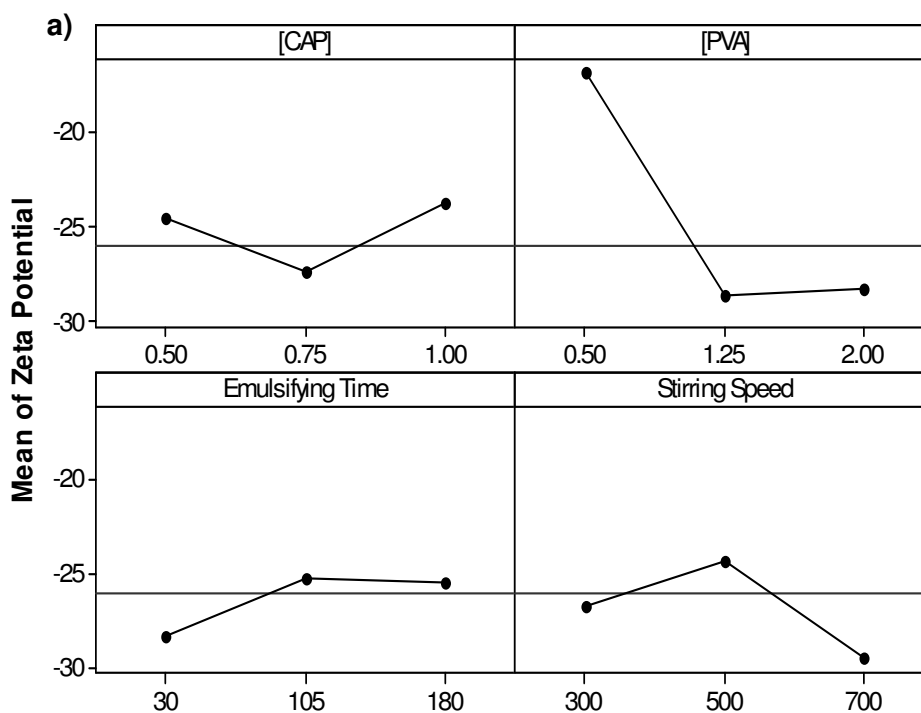


Figure 3.16: Typical (a) main effects plot and (b) interactions plot of the response values for Particle Size

Zeta Potential

The main effects on Zeta Potential proved that [PVA] has a significant effect on the negative Zeta Potential (Figure 3.17a) and thereby confirmed its capacity to impart stability to the formulation ($p= 0.051$). In the interaction plots (Figure 3.17b), there was a distinct relationship between a decreased [CAP] and increase Zeta Potential and this was noted in consideration of the physical incompatibility between CAP and PVA.



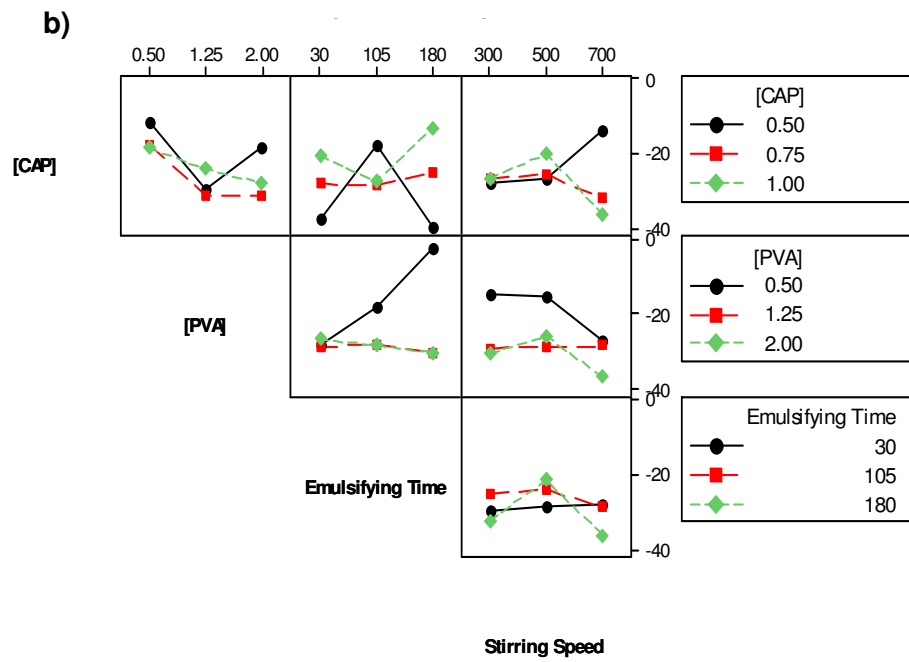
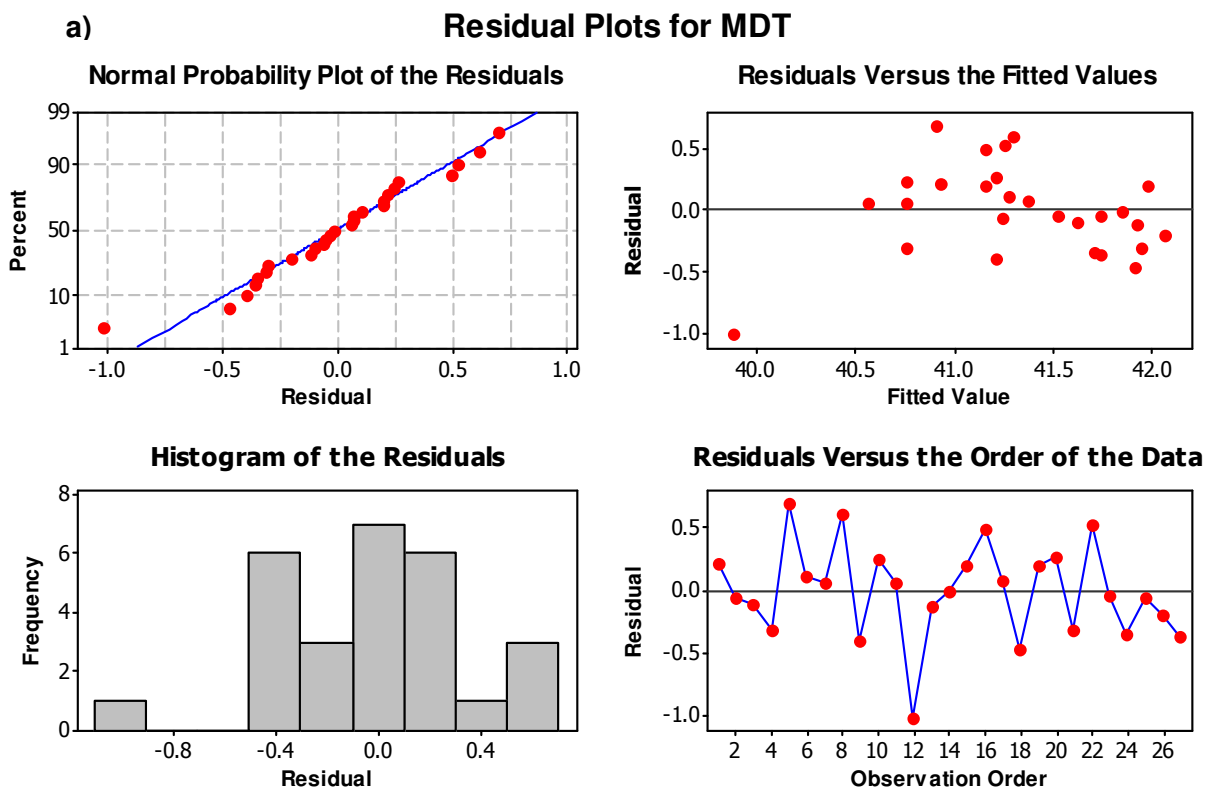


Figure 3.17: Typical (a) main effects plot and (b) interactions plot of the response values for Zeta Potential

3.3.7.7. Analysis of the Box-Behnken design employed for optimization of DA-loaded CAP nanoparticles

The assessment of the regression models can be undertaken employing residual plots (Figure 3.18). Residual plots are essentially a linear comparison between observed values and model predictions for those observations (Stewardson and Whitfield, 2004).



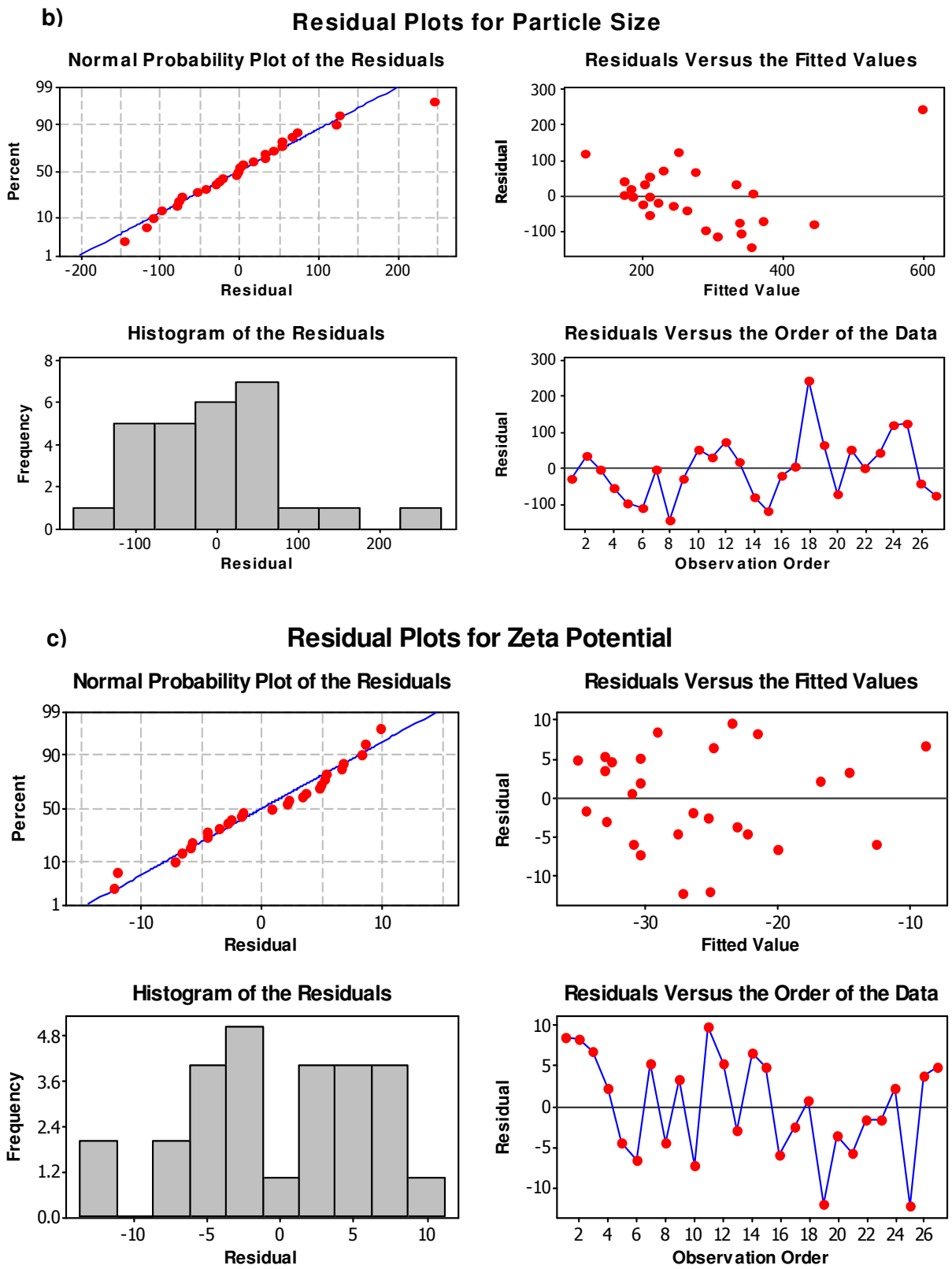


Figure 3.18: The residual plots for the responses (a) MDT, (b) Particle Size and (c) Zeta Potential

Residual analysis for MDT (Figure 3.18a), Particle Size (Figure 3.18b) and Zeta Potential (Figure 3.18c) showed the indiscriminate distribution of data. The normal plot of residuals formed a linear curve showing normality. The residuals versus fitted plots showed a random pattern of residuals on either side of 0 with no identifiable patterns in the plot thereby indicative of a random scatter and no trends. The histogram supported that the residuals have a normal distribution with zero mean and constant variance. The residuals versus the order of the data was used to identify and non-random error, the plot displayed a negative correlation is indicated by rapid changes in the signs (\uparrow, \downarrow) of the consecutive residuals. A significant effect is indicated by a p-value of ≤ 0.05 for any factor. The factors and the respective p-values are displayed in Table 3.6.

Table 3.6: Full ANOVA analysis for the measured responses (MDT, Particle Size and Zeta Potential for DA-loaded CAP nanoparticles)

Term	p-value		
	MDT	Particle Size	Zeta Potential
[CAP]	0.687	0.412	0.877
[PVA]	0.918	0.034	0.051
[ET]	0.187	0.886	0.605
[SS]	0.091	0.352	0.617
[CAP] ²	0.195	0.544	0.293
[PVA] ²	0.0520	0.226	0.115
[ET] ²	0.443	0.823	0.941
[SS] ²	0.309	0.437	0.698
[CAP]*[PVA]	0.292	0.837	0.889
[CAP]*[ET]	0.526	0.916	0.610
[CAP]*[SS]	0.156	0.456	0.222
[PVA]*[ET]	0.882	0.851	0.132
[PVA]*[SS]	0.748	0.031	0.765
[ET]*[SS]	0.013	0.783	0.777

Where SS = stirring speed, ET = emulsifying time, MDT = mean dissolution time, PVA = poly(vinylalcohol) and CAP = cellulose acetate phthalate

The complete regression equations generated for MDT, Particle Size and Zeta Potential are indicated below:

$$\begin{aligned} \text{MDT} = & -1.049E-13 + 8.196E-14[\text{CAP}] - 3.972E-15[\text{PVA}] + 0.500[\text{ET}] + 2.031E-16[\text{SS}] - 1.204E- \\ & 14[\text{CAP}]^2 - 2.69E-15[\text{PVA}]^2 - 2.561E-19[\text{ET}]^2 - 1.276E-19[\text{SS}]^2 + 1.585E14[\text{CAP}*\text{PVA}] - 8.771E- \\ & 16[\text{CAP}*\text{ET}] + 3.723E-18[\text{CAP}*\text{SS}] + 3.370E-17[\text{PVA}*\text{ET}] - 1.596E-17[\text{PVA}*\text{SS}] - \\ & 3.817E-19[\text{ET}*\text{SS}] \end{aligned} \quad \text{Equation 3.5}$$

$$\begin{aligned} \text{Particle Size} = & -131.441 - 406.807[\text{CAP}] + 395.560[\text{PVA}] + 0.985[\text{ET}] + 0.861[\text{SS}] \\ & 547.133[\text{CAP}]^2 + 124.081[\text{PVA}]^2 - 0.002[\text{ET}]^2 + 0.0012[\text{SS}]^2 - 70.933[\text{CAP}*\text{PVA}] + 0.361[\text{CAP}*\text{ET}] - \\ & 0.974[\text{CAP}*\text{SS}] - 0.216[\text{PVA}*\text{ET}] - 1.027[\text{PVA}*\text{SS}] - 0.001[\text{SS}*\text{ET}] \end{aligned} \quad \text{Equation 3.6}$$

$$\begin{aligned} \text{Zeta Potential} = & -25.415 - 53.170[\text{CAP}] \\ & 25.842[\text{PVA}] + 0.120[\text{ET}] + 0.119[\text{SS}] + 69.820[\text{CAP}]^2 + 11.973[\text{PVA}]^2 + 5.289E-05[\text{ET}]^2 - 3.935E- \\ & 05[\text{SS}]^2 - 3.467[\text{CAP}*\text{PVA}] + 0.128[\text{CAP}*\text{ET}] - 0.118[\text{CAP}*\text{SS}] - 0.131[\text{PVA}*\text{ET}] + 0.009[\text{PVA}*\text{SS}] - \\ & 8.833E-05 [\text{SS}*\text{ET}] \end{aligned} \quad \text{Equation 3.7}$$

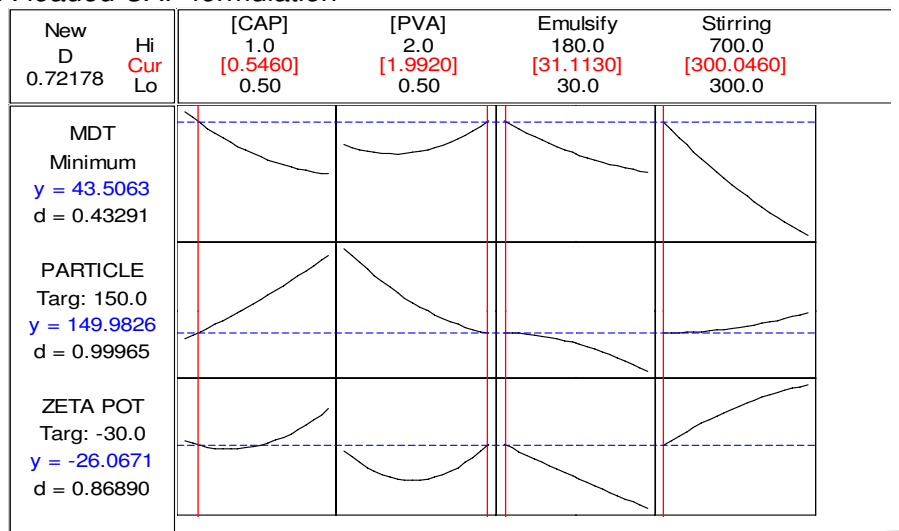
3.3.7.8. Response optimization of DA-loaded CAP nanoparticles

This was carried out employing statistical software (Minitab[®], V14, Minitab Inc[®], PA, USA) to determine the optimum level for each variable. The optimization process resulted in the attainment of various formulations with a low desirability for all three outcomes therefore a selection of the most influential desired outcome was necessary to the detriment of the other two outcomes. MDT of DA-loaded nanoparticles could be controlled further by the incorporation of these nanoparticles into the scaffold while Zeta Potential could be altered by uniform distribution throughout the scaffold during formulation. Therefore, the DA-loaded CAP nanoparticle formulation displaying the smallest Particle Size with high desirability (>99%) was selected as the optimal formulation.

The formulation was optimized for the measured responses of *MDT, Particle Size and Zeta Potential* (Figure 3.19). Optimization was carried out so as to obtain the levels of [CAP],

[PVA], emulsifying time and stirring speed that would maximize the measured responses (Palamakula *et al.*, 2004).

Figure 3.19: Optimization plots displaying factor levels and desirability values for the chosen optimized DA-loaded CAP formulation



Measured response	Predicted values	Experimental values	Desirability (%)
Zeta Potential (mV)	-26.072	-34.000	76.682
Size (nm)	150.175	197.200	76.154
MDT	43.505	40.956	94.414

3.3.7.9. Desirability for the measured responses of the optimized DA-loaded CAP formulation

The value for MDT desirability (94.41%) was the most promising outcome and therefore DA release from the CAP nanoparticle system would be controlled and sustained for the period of time desired. With reference to the particle size (possessing a statistical desirability of 76.15%); while the value of 197nm (Figure 3.20a) was not ideal it was within size range of previously marketed medicinal nano-therapeutic systems (Table 2.1). Furthermore, the particles do not need to cross through the BBB and so the size may exceed 100nm. The desirability value of 76.68% obtained for the Zeta Potential optimization (Figure 3.20b) signified that it differed substantially from the fitted value with a superior value of -34.00mV for the optimized system in terms of stability. Overall, the optimized system displayed the desirable DA release, size and stability required for been utilized as an intracranial device for the prolonged and controlled delivery of DA to the brain tissue.

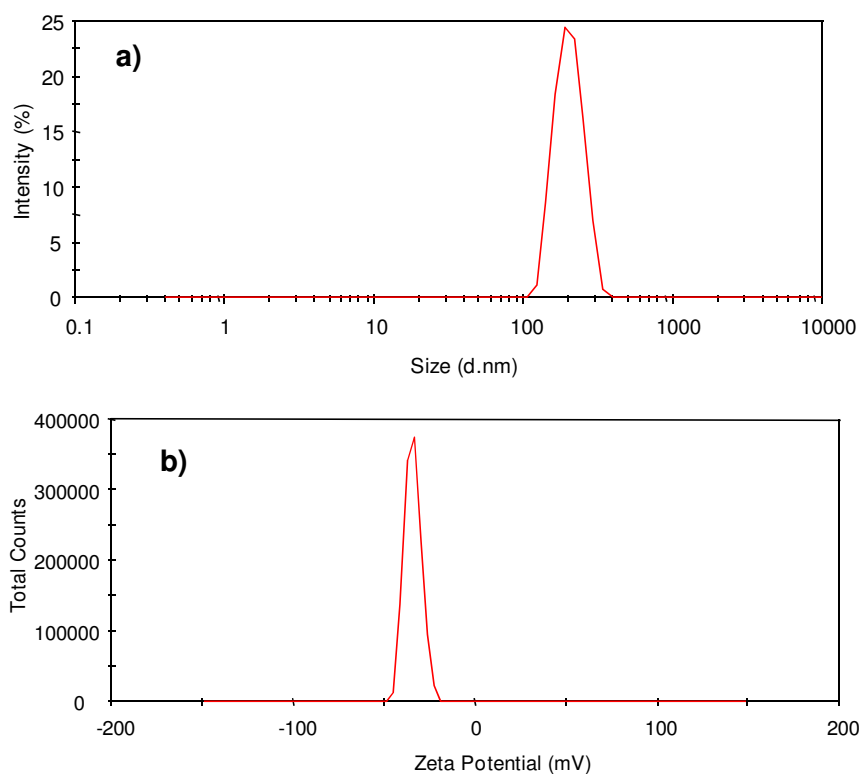


Figure 3.20: (a) Size and (b) Zeta distribution profiles for optimized DA-loaded CAP nanoparticles measuring 197.2nm and -34mV respectively

3.4. Concluding Remarks

This chapter served in the development of DA-loaded CAP nanoparticles using an adopted emulsification-diffusion approach. Parameters such as Particle Size, Zeta Potential and MDT were chosen as the significant responses for the formulation due to the ability of these to control DA release. DA entrapment proved significantly high for CAP nanoparticles which compensated for the rapid *in vitro* release of the DA. Micrographs (TEM and SEM) further revealed the uniform spherical shape and morphology of the DA-loaded CAP nanoparticles. FTIR analysis confirmed the presence of both DA, CAP AND PVA within the DA-loaded CAP nanoparticles as well the ionic interaction. Data from size and zeta potential intensity profiles proved formulations were stable and within the desirable nano-range of 165.4-174.1nm. A Box-Behnken statistical design was employed for the optimization of the formulation. [CAP] and [PVA] as well as the stirring speed and emulsifying time where identified as the significant formulation variables. The design generated diverse formulations giving rise to various differences in responses (MDT, Particle size and Zeta Potential). Evaluation of the statistical significance of the design confirmed the applicability to the present study. Optimization of the formulation resulted in DA-loaded CAP nanoparticles with a Zeta Potential of -34mV, Particle Size of 198nm and MDT value of 40.96. The DA-loaded CAP nanoparticles were foremostly optimized for a maximum MDT value that resulted in controlled DA release. The DA-loaded CAP nanoparticles were incorporated into a Ba-alginate scaffold and further evaluated for *in vitro* DA release and will be detailed in Chapter 4 of this dissertation.

CHAPTER 4

FORMULATION OF CROSSLINKED ALGINATE SCAFFOLDS FOR THE DESIGN OF A NANO-ENABLED SCAFFOLD DEVICE

4.1. Introduction

Prototyping technology has created a significant impact in biomedical materials design. Molecular modeling facilitates the design of accurately customized structural models of polymeric devices for various applications (Levy *et al.*, 1997; Ono *et al.*, 1999; Chua *et al.*, 2000; Curodeau *et al.*, 2000; Porter *et al.*, 2001 and Cheah *et al.*, 2002), therefore prompting the adoption of a similar approach to fabricate the NESD with controlled micro-architecture and higher consistency than conventional unsighted techniques. Free-form prototyping technology was used to design the NESD via a three-dimensional (3D) crosslinked alginate scaffold model incorporating DA-loaded CAP nanoparticles. Prototyping provides an alternative that aims to improve the NESD design by employing archetype data manipulation to pre-assemble the complex internal scaffold architectures and nanostructures of the NESD in conjunction with a Box-Behnken statistical design for optimization and an integrated corporeal manufacturing approach that is consistent, reproducible and formulation-specific.

While the formulation and development of DA-loaded CAP nanoparticles, for incorporation into a crosslinked-alginate scaffold, was previously discussed in Chapter 3, the present chapter addresses the development of crosslinked-alginate scaffolds which formed part of the NESD.

Alginate was selected as the ideal polymer for the formulation of the scaffolds. The polymer is a hydrophilic polymer, has been used extensively in both the food and pharmaceutical industry for its desirable gelling, degradation and biocompatible properties (Chan *et al.*, 2002). Alginate is a co-polymer extracted from various types of brown algae and is made up of D-mannuronic acid (M) and L-guluronic acid (G). The monomers may be varied in concentration so as to impart various characteristics to the system in which it is employed (Martinsen *et al.*, 1989). Furthermore, alginates may be crosslinked with a selection salts from Hofmeister series such as calcium, barium and zinc, resulting in the ability to form a gel (Ciofani *et al.*, 2007) with decreased degradation kinetics. In terms of bioadhesivity, the alginates are anionic polymers with carboxyl end groups and therefore have excellent

mucoadhesivity which has desirable properties for drug absorption and bioavailability (Rastogi *et al.*, 2007).

The biocompatibility of these polymers has been extensively discussed in literature and the oral administration thereof proves non-toxic however there is still a significant lack in *in vivo* data for intravenous as well as implants (Becker *et al.*, 2000; Orive *et al.*, 2005; Ciofani *et al.*, 2007). Alginate-based drug delivery systems have been researched for their possible employment as drug delivery systems for the treatment of various ailments.

Table 4.1: Illustrates alginate-based drug delivery systems that have are being investigated for the treatment of various diseases

Drug delivery system	Treatment	Reference
Intratumoural injection of hollow chitosan-alginate microspheres	Cancer	Liu <i>et al.</i> , 1997
Ophthalmic drops containing gatifloxacin-loaded alginate/hydroxyl propylmethyl cellulose	Bacterial infections	Liu <i>et al.</i> , 2006
Stomach-specific metronidazole-loaded alginate beads	<i>Helicobacter pylori</i>	Ishak <i>et al.</i> , 2007
Colon-specific delivery of 5-aminosalicylic acid from chitosan calcium alginate microparticles	Ulcerative colitis	Mladenovska <i>et al.</i> , 2007

The appropriate selection of the grade as well as formulation methodology employed may result in variations in pore size, degradation and drug release rates (Ciofani *et al.*, 2007).

Biodegradable polymeric scaffolds have been employed extensively in tissue regeneration (Whang *et al.*, 2000) for their ability to interact with cellular tissue and in drug delivery for their ability to control drug release rate (Edlund and Albertsson, 2001). Issues such as drug loading capacity and rate of drug release, degradation and toxicity are imperative in the formulation of these drug delivery devices (Sokolsky-Papkov *et al.*, 2007). Conventional fabrication methods may be adapted so as to impart desired properties onto the scaffold. The following conventional methods have been employed for the formulation of polymeric scaffolds:

Gas-foaming under increased pressure

Polymers are made into a solid form and placed into an incubator of gas at high pressure for up to 3 days at which point the pressure is rapidly decreased to atmospheric pressure. This method holds favour as there is avoidance of toxic solvents. However the use of heat to compress the polymer may damage the excipients and actives (Mikos and Temenoff, 2000). The average pore size present in such scaffolds is 100 μ m.

Solvent/ particulate leaching of crystals from polymeric solutions

A polymeric solution is immersed in a petri dish consisting of a water soluble salt (pyrogen). The solvent is then evaporated and the resultant material is placed in water for upto 2 days to leach out the salt. Modifications of the size of the salt crystals result in changes in pore size while salt concentration results in alterations of porosity. The employment of organic solvents limits the use of therapeutic active agents and may result in toxicity while the duration of the procedure can be extensive (Mikos and Temenoff, 2000).

Phase separation/ emulsification followed by lyophilization of the emulsion

An emulsion is formed by adding an aqueous phase to an organic phase (with dissolved polymer). The emulsion is then placed into a mould and quenched with liquid nitrogen (Calvin, 2003). The resultant material is then lyophilized to ensure the removal of excess solvent and the formation of a scaffold with almost nanoscopic pore sizes (13-35 μ m) (Mikos and Temenoff, 2000). The limitation in this technique is that the toxicity of solvents employed is highly questionable. In liquid-liquid phase separation, there is the utilization of a non-solvent and solvent. The polymer is dissolved in the solvent and then subjected to temperature variations and subsequent lyophilized. This method is highly specific and thorough preliminary testing needs to be undertaken prior to formulation (Leong *et al.*, 2003)

Bonding of nano-fibers to form meshes

The technique of fiber bonding involves the formation of polymer fibers by electrospinning. The fibers are bonded by means of immersion and subsequent evaporation of a polymer solution (separate from the polymeric fibers being formed). The fibrous solution is then heated to a temperature above the melting point of both polymers, allowing the polymers to fill spaces between the fiber network (Mikos and Temenoff, 2000). Excess polymer solution is removed using an appropriate reagent to adsorb the solution. The technique results in the formation of a highly porous matrix with an average pore size of 500 μ m (Calvin, 2003). The disadvantage is the possible toxicity of the solvent and the high temperature combination.

In the present study, lyophilization was chosen for the fabrication of crosslinked-alginate scaffolds. Reasons for employment of this approach include:

- Suitable method for the formation of scaffolds employing a hydrophilic polymer-alginate;
- Porosity of the scaffold could be controlled, in terms of size and shape, which influences the rate of Matrix Erosion (ME) and subsequent DA release; and
- Efficiency and reproducibility of the method is desirable.

4.2. Materials and Methods

4.2.1. Materials

Alginate (Protanal[®] LF10/60; 30% mannuronic acid, 70% guluronic acid residues) was purchased from FMC Biopolymer (Drammen, Norway). Calcium gluconate [(HOCH₂(CHOH)₄COO)₂Ca], barium chloride (BaCl₂), cellulose acetate phthalate (CAP) (M_w=2534.12g/mol), poly(vinyl alcohol) (PVA) (M_w=49,000g/mol), acetone, methanol and dopamine hydrochloride (DA) (M_w=189.64g/mol) were purchased from Sigma Aldrich (St. Louise, MO, USA). Deionized water was obtained from a Milli-Q water purification system (Milli-Q, Millipore, Billerica, MA, USA). All other reagents used were of analytical grade. A lyophilizer (Virtis, Gardiner, NY, USA) was used to remove excess moisture and solidify the formulation in order to produce crosslinked alginate scaffolds.

4.2.2. Processing conditions for the development of crosslinked alginate scaffolds

A lyophilization time of 36hr at 1.2mTorr and condenser temperature of -60°C was established as the optimum conditions for the removal of excess moisture from the alginate scaffold.

4.2.2.1. Temperature for alginate solubilization

Heat is an essential component in the solubilization of the alginate powder in deionised water. The gradual addition as well as increase in temperature allowed for the efficient dissolution of the alginate. A minimal temperature of 50°C was chosen to allow for sufficient heat to aid the dissolution process and to refrain from destroying the alginate structure (FMC BioAlginate, USA). In addition, parafilm was used to seal the beakers as to prevent solvent evaporation from the formulation.

4.2.2.2. Duration required for the efficient post-curing of crosslinked alginate scaffold

Post-curing the alginate scaffold, which entailed the further crosslinking of the $[(\text{HOCH}_2(\text{CHOH})_4\text{COO})_2\text{Ca}]$ -crosslinked alginate scaffolds in salt solutions (2%^{w/v}), resulted in slow erosion rate of the scaffold in PBS (pH 6.8, 37°C). While a prolonged post-curing period holds positive implications for Matrix Resilience (MR), it can be highly detrimental to the DEE of the system and therefore a maximum post-curing time of 3hr was established. Furthermore, scaffolds were cured for up to 12hr with no significant effect (SD = 2.65) onMR. N=3.

4.2.3. Biometric simulation of the NESD employing computer-aided prototyping

The implicit design of the NESD required customization of the crosslinked-alginate scaffold for embedding the DA-loaded CAP nanoparticles with the ability to support bioadhesion and the physicochemical stability for intracranial implantation of the device. CAP and $[(\text{HOCH}_2(\text{CHOH})_4\text{COO})_2\text{Ca}]$ -crosslinked alginate were selected for producing the DA-loaded CAP nanoparticles and scaffold components of the NESD respectively. The crosslinked scaffold was subsequently cured in a BaCl_2 solution as a secondary crosslinking step. The componential NESD properties were modulated through computational prototyping to produce a viable scaffold embedded with stable DA-loaded CAP nanoparticles. The fundamental design parameters were pivoted on the polymer assemblage, curing methods, surface properties, macrostructure, physicochemical properties, nanoparticle fixation and biodegradation of the NESD. In order to incorporate fine control within the complexities of three-dimensional (3D) design, the physical properties of the crosslinked alginate scaffold such as the pore size, shape, wall thickness, interconnectivity and networks for nanoparticle diffusion was regulated to produce a 3D prototype NESD model. The NESD topography was predicted for intracranial implantation with pre-defined micro-architecture and physicochemical properties equilibrating frontal lobe brain tissue as the site of implantation to provide mechanical support during sterilizability prior to function. A suppositional 3D graphical model with potential inter-polymeric interactions during formation was generated on ACD/I-Lab, V5.11 Structure Elucidator Application (Add-on) biometric software (Advanced Chemistry Development Inc., Toronto, Canada, 2000) based on the step-wise molecular mechanisms of scaffold and nanoparticle formation, polymer interconversion and DA-loaded CAP nanoparticle fixation as envisioned by the chemical behavior and physical stability. A combination of a computationally rapid Neural Network (NN) and a modified Hierarchical Organization of Spherical Environments (HOSE) code approach were employed as the fundamental algorithms in designing the prototype NESD. The associated energy

expressions were chemometrically designed based on the assumption of the scaffold behaving initially as a gel-like structure with higher states of combinatory energy for the complete NESD.

4.2.4. Preparation of crosslinked alginate scaffold

A 2%^{w/v} alginate solution in deionized water (Milli-DI[®] Systems, Bedford, MA, USA) was prepared at 50 °C and a primary 0.4%^{w/v} [HOCH₂(CHOH)₄COO]₂Ca crosslinking solution was added and agitated until a homogenous mixture was obtained. The resulting mixture was then placed in Teflon moulds and lyophilized for 24hr at 25mtorr (Virtis, Gardiner, NY, USA). Thereafter the lyophilized structures were immersed in a secondary 2%^{w/v} ZnCl₂, CaCl₂ or BaCl₂ crosslinking solution for 3hr as a curing step followed by a further lyophilization phase of 24hr at 25mtorr. The resultant cured scaffolds were removed from the moulds, washed with 3×100mL deionized water to leach out unincorporated salts and air-dried under an extractor.

4.2.5. Textural profile analysis to determine the physico-mechanical behaviour of the crosslinked alginate scaffold

One of the key approaches to intricate crosslinked polymeric scaffold engineering is the assessment of the physico-mechanical properties of the scaffold matrix following 3D prototyping and prior to sterilization and implantation. Textural profile analysis was therefore conducted to characterize the 3D salient core regions of the crosslinked alginate scaffold using a Texture Analyzer (TA.XT^{plus} Stable Microsystems, Surrey, UK) in terms of the scaffold matrix resilience (MR). Hydrated samples of the crosslinked alginate scaffold were analyzed. Serial Force-Time profiles were sufficient to perform the necessary computations of MR (N=5). The MR of the crosslinked scaffolds was calculated employing the TA, the settings of which are outlined in Table 4.2. Furthermore, the MR was calculated for formulations generated in the experimental design.

Table 4.2: Parameters employed to measure the MR of hydrated/unhydrated samples employing the texture analyzer

Parameter	Settings
Test Mode	Compression
Pre-Test Speed	1.0mm/sec
Test Speed	1.5mm/sec
Post-Speed Speed	1.5mm/sec
Target Mode	Strain
Strain	50%
Trigger Type	Force
Trigger Force	0.05N

4.2.6. Morphological characterization of crosslinked alginate scaffold

Morphological characterization of the crosslinked alginate scaffold was instituted. Scaffold parameters such as the micro-structure, pore length, pore distribution and inter-pore wall thickness was also examined. The surface morphology of the cured and un-cured crosslinked alginate scaffolds were also characterized to assess the influence of crosslinking and subsequent curing on potential surface morphological transitions (N=10). SEM, (JEOL, SEM 840, Tokyo Japan) was employed and photomicrographs were captured at various magnifications for analyzing the scaffold samples that were prepared after sputter-coating with carbon or gold.

4.2.7. *In vitro* matrix erosion studies of crosslinked alginate scaffold

Samples of the biodegradable crosslinked alginate scaffolds were immersed in 100mL PBS (pH 6.8, 37°C) and agitated at 20rpm in a shaking incubator (Labex, Stuart SBS40®, Gauteng, South Africa). At pre-determined time intervals samples were removed, blotted on filter paper and dried to a constant mass at 40°C in a laboratory oven. Equation 4.1 was then used to compute the extent matrix erosion (ME) after gravimetric analysis. Furthermore, the ME was calculated for formulations generated in the experimental design.

$$ME\% = \frac{M_0 - M_t}{M_0} \times 100 \quad \text{Equation 4.1}$$

Where $ME\%$ is the extent of scaffold matrix erosion, M_t is the mass of the scaffold at time t and M_0 is the initial mass of the scaffold.

4.2.8. Formulation and Statistical Optimization of the Ba-Alginate Scaffold

An experimental strategy, namely the Box-Behnken design, was developed and employed for the statistical optimization of the Ba-alginate scaffold.

4.2.8.1. Determination of limitations for variables employed in a Box-Behnken design

The formulation variables listed in Table 4.3 were subjected to their higher and lower limits and thereafter MR was calculated for each formulation. The most influential variables were selected for the employment in the Box-Behnken design.

Table 4.3: Illustrates the variations in formulations that were used to identify the limits for a Box -Behnken design to optimize Ba-alginate scaffold and their MR

Formulation number	Variables	MR %
1	Increased [alginate] (1-3% w/v)	78.72
2	Increased lyophilization time (24-48hr)	73.43
3	Increased post-curing time (0.5-1.5hr)	80.34
4	Reduced [alginate] (1% w/v)	73.05
5	Reduced [(HOCH ₂ (CHOH) ₄ COO) ₂ Ca] (0.2% w/v)	80.11
6	Increased temperature to (50-70 °C)	36.47
7	Increased [BaCl] to (0.2-0.6% w/v)	67.06

- [Alginate]- concentrations between 1-3% w/v was selected. Concentration of <1% w/v and <3% would not provide desirably crosslinking and >4% w/v, the solution crosslinked too extensively to place into moulds (also produced a heterogeneous solution).
- [BaCl₂]- concentrations between 0.2-0.6% w/v were selected. A concentration of greater 0.6% w/v gave rise to excessive crosslinking.
- Heat-the temperature limits were set 50-70°C. The solution required at least 50°C to allow for the alginate to dissolve in the deionised water. A temperature exceeding 70°C would destroy the polymer's integrity.
- Post-curing time-a minimum of 30min was required in order to facilitate the crosslinking of scaffolds however it was found that scaffolds post-cured for 6hr or longer even 12hr showed no greater MR in comparison to those crosslinked for 1.5hr.

This study design, requiring a total of 27 experimental runs (formulation combinations), was generated and analyzed using Minitab[®] V14 (Minitab Inc[®], PA, USA). A 4-factor, 3 level (post-curing time, [Alginate], [(HOCH₂(CHOH)₄COO)₂Ca] and heat) Box-Behnken design on the

measured responses (MR and ME %) was established for this optimization. The independent factors and the dependent variables used in the design are listed in 4.7.

The variables listed in Table 4.4 were selected for the employment in the Box-Behnken design. Furthermore, the measured responses and for the design and the objectives thereof was established.

Table 4.4: *The variables for Ba-alginate scaffold used in the 4-factor, 3-level Box-Behnken design*

Independent Variables	Values		
	Low	High	
Alginate (% ^{w/v})	1	3	
[(HOCH ₂ (CHOH) ₄ COO) ₂ Ca] (% ^{w/v})	0.2	0.6	
Temperature (°C)	50	70	
Post-curing time (min)	30	90	
Dependent Variables	Low	High	Objective
MR (%)	86	94	Maximize
ME (%)	3	59	Minimize

4.2.8.2. Optimization of Ba-alginate scaffold

Polynomial equations relating the dependent and independent variables were generated, and the formulation process was optimized under constrained conditions for to obtain formulations displaying the desirable percentage ME (minimal) and percentage MR in the hydrated state (maximum).

4.2.9. Corporeal assembly of the NESD

Production of the NESD required the initial componential preparation of the DA-loaded CAP nanoparticles and the Ba-alginate scaffold. Once the two components were optimized (Figure 4.11; scaffolds and Chapter 3, Figure 3.20 of this dissertation) the DA-loaded CAP nanoparticles were incorporated via intermittent blending and lyo-fusion (spontaneous freezing followed by lyophilization) into the [(HOCH₂(CHOH)₄COO)₂Ca]-crosslinked and subsequently Ba-alginate scaffold.

4.2.9.1. Assimilation of DA-loaded CAP nanoparticles and Ba-alginate scaffold into the NESD

The NESD was assembled by a lyo-fusion process (Figure 4.1). Briefly, the optimally defined DA-loaded CAP nanoparticles (200mg) were placed into moulds containing a [HOCH₂(CHOH)₄COO]₂Ca and alginate solution (2mL) obtained in accordance with set optimization constraints. The mixture was agitated and spontaneously frozen at -70°C for 24hs. Thereafter the structures were lyophilized for 48hr at 25mtorr and immersed in a 2%^{w/v} BaCl₂ crosslinking solution for 3hr as a curing step followed by a further lyophilization phase of 24hr at 25mtorr to induce fusion of the DA-loaded CAP nanoparticles and the Ba-alginate scaffold.

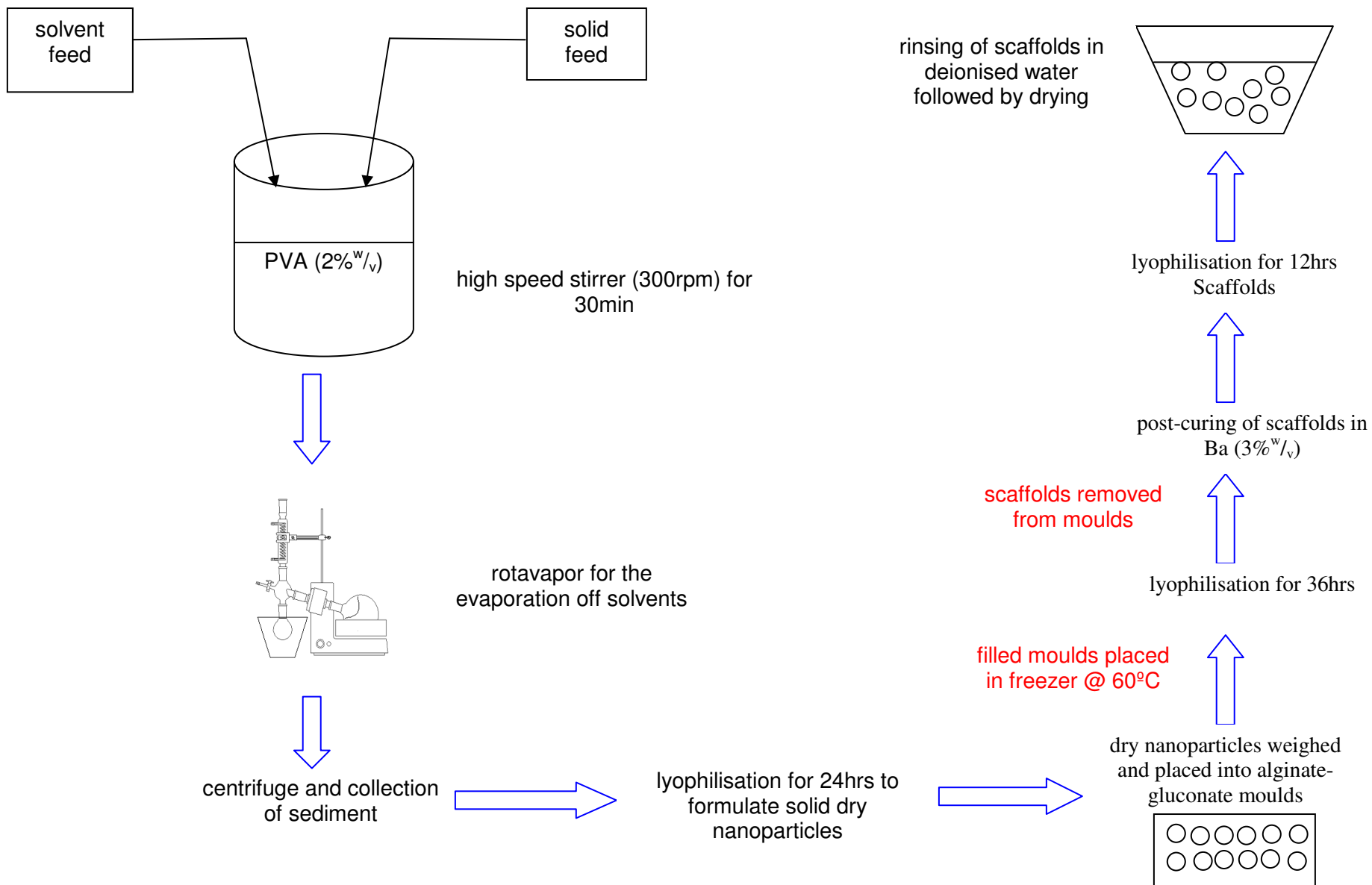


Figure 4.1: Schematic representation of the assimilation of DA-loaded CAP nanoparticles and Ba-alginate scaffold into the NESD

4.2.11. Determination of *in vitro* DA release from the NESD

In vitro release studies were performed on the the final NESD utilizing a shaking incubator (Labex, Stuart SBS40[®], Gauteng, South Africa) set at 20rpm. The NESD was immersed separately in 100mL phosphate-buffered saline (PBS) (pH 6.8, 37°C) contained in 150mL glass jars. At predetermine time intervals 3mL samples of each release media were removed, filtered through a 0.22µm Cameo Acetate membrane filter (Millipore Co., Bedford, MA, USA) and centrifuged at 20,000rpm (Reading, 2001). The supernatant was then removed and analyzed by UV spectroscopy at a maximum wavelength of $\lambda_{280\text{nm}}$ for DA content analysis. DA release was quantified using a linear standard curve ($R^2=0.99$). An equal volume of DA-free PBS was replaced into the release media to maintain sink conditions.

4.2.12. Determination of the thermal transition behaviour of the NESD and it's constituents

The inherent and sequential transient thermal behavior of polymers may influence the physicochemical and physicommechanical properties as well as the final performance of the system (Liu *et al.*, 2003). Temperature Modulated Differential Scanning Calorimetry (TMDSC) was therefore performed to provide a distinct interpretation of the polymeric thermal transitions with improved sensitivity and the ability to separate reversible glass transition temperatures (T_g) that have minimal changes in heat capacity (ΔH) from overlapping non-reversible relaxation endotherms (Reading, 1993) (Ferrero *et al.*, 1999) (Sandor *et al.*, 2002). Thermal analysis was therefore undertaken on the DA-loaded CAP nanoparticles, the Ba-alginate scaffold and the assimilated NESD in order to assess thermal behavior using TMDSC (Mettler Toledo DSC1, STAR^e System, Switzerland). Thermal transitions were assessed in terms of the T_g , measured as the reversible heat flow due to variation in the magnitude of the C_p -complex values (ΔC_p); melting temperature (T_m) and crystallization temperature (T_c) peaks that were consequences of irreversible heat flow corresponding to the total heat flow. The temperature calibration was accomplished with a melting transition of 6.7mg indium. The thermal transitions of native CAP were compared to the CAP nanoparticles. Samples of 5mg were weighed on perforated 40µL aluminum pans and ramped within a temperature gradient of 150-500°C under a constant purge of N_2 atmosphere in order to diminish oxidation. The instrument parameter settings employed comprised a sine segment starting at 150°C with a heating rate of 1°C/min at an amplitude of 0.8°C and a loop segment incremented at 0.8°C and ending at 500°C. The instrument parameter settings employed are shown in Table 4.5.

Table 4.5: TMDSC settings employed for thermal analysis of the NESD constituents

Segment Type	Parameter Setting
SINE	
Start	150 °C
Heating rate	1 °C /min
Amplitude	0.8 °C
Period	0.8 °C
LOOP	
To segment	1
Increment	0.8 °C
End	500
Count	436

4.3. Results and Discussion

4.3.1. Computer-aided prototyping for NESD design

An output format of serial bitmap images generated via the prototyping technology employed enabled the step-wise 3D volumetric construction of the NESD model. 3D construction was initiated by ascribing an assumed height to each image in order to represent a volume unit or a stacked voxel depicting a prototype model of the NESD described by the grayscale intensity threshold images shown in Figure 4.2. Prototyping of the NESD device revealed that the functional properties of the NESD depended on the characteristics of the polymeric materials employed, the processing technique, and the subsequent interaction of fixated DA-loaded CAP nanoparticles within the crosslinked alginate scaffold. The 3D prototype design of the device permitted the porosity, surface area, and surface characteristics to be semi-optimized in the pre-cured and post-cured phases with BaCl_2 for each component of the NESD (Figure 4.2a). Fine control of the micro-architectural characteristics influenced the mechanical properties of the scaffold that was significant for nanoparticle fixation and mechano-transduction in order to control the release of DA. A significant advantage of employing prototyping technology to develop the NESD was the elimination of reliance on individual skills that are required for conventional techniques of device fabrication. Commencing with a limited range of fundamental structural units a NESD with precise micro-architectures was designed using prototyping technology with internal channels or cavities resembling the negative image of the final required NESD as depicted in Figures 4.2a, b and c. Visibly, the scaffold models depicted channels that extended through the entirety of the tetragon matrices in both horizontal and vertical axes with consistency in the strand layout after DA-loaded CAP nanoparticle fixation. At the periphery of the matrix, a region of thick

and blurred pore deposition was visible after curing the alginate scaffold in BaCl_2 (Figure 4.2b). This entire matrix region was approximately $5 \times 3 \text{ mm}$ at the edge of the tetragon (Figure 4.2. enlarged for clarity). SEM images confirmed the strut and pore widths to be in the range of $100\text{-}200 \mu\text{m}$. Furthermore, the unconnected pore space, when inspected qualitatively, comprised diminutive cavities within the matrix for controlling the outward diffusion of the DA-loaded CAP nanoparticles from the crosslinked alginate scaffold.

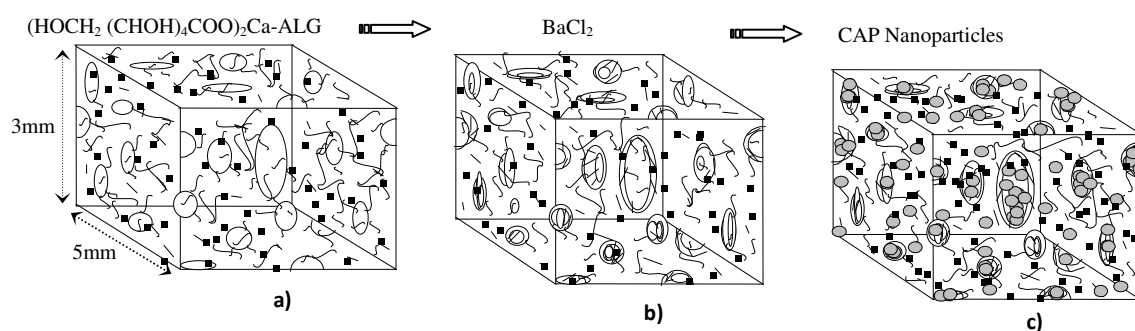


Figure 4.2: Three-dimensional prototype images of a) a pre-cured crosslinked-alginate scaffold, b) a BaCl post-cured crosslinked-alginate scaffold, and c) DA-loaded CAP nanoparticles embedded within the cured crosslinked alginate scaffold voids representing the NESD

The computational design process revealed that curing of the crosslinked alginate scaffold in BaCl_2 involved the residual crosslinking of open, approachable and chemically reactive molecular functional groups that possessed chemical affinity towards BaCl_2 as the secondary crosslinker and produced an equivalent of edging and interlocking of the matrix surface functional groups with a superiorly compact matrix structure (Figure 4.2b). Furthermore DA was not covalently bonded to the CAP with no amide bond formation but interacted ionically via physical associations involving H-bonding and smaller force interactions through the influence of the external crosslinking medium. Figure 4.3a represents a structural model of the interactions between H_2O molecules in association with CH_3COO^- and O_2 functional groups of strongly hydrophilic CAP sites. DA, other ionic species and molecules revealing an interactive model of CAP and DA entrapment constituents are also depicted in Figure 4.3b.

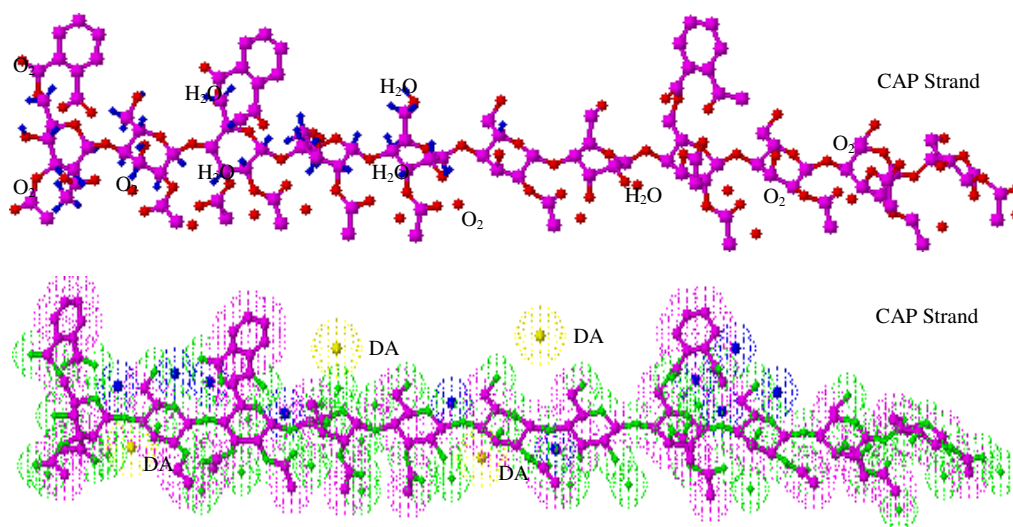


Figure 4.3: Molecular structural models of a) interactions between H_2O molecules in association with CH_3COO^- and O_2 functional groups of CAP and b) CAP interactions and DA entrapment

Figure 4.4a-e depicts a step-wise single CAP chain structural model under the influence of surrounding interactive forces within the emulsified medium such as solvent molecules at the periphery, PVA as the surfactant and DA. The affinity interactions with explicit lipophilic and hydrophilic orientations towards the formation of a nanoparticle wall are also shown (Figure 4.4f-h). CAP was initially suspended in the binary acetone: methanol solvent system as unorganized random orientations with irregular lipophilic rings (Figure 4.4a). The addition of DA and ionic or physical interactions with the hydrophilic functional groups of CAP and free DA molecules resulted in CAP conforming to orientations of the affinity-wise molecular sites in terms of lipophilicity and hydrophilicity of the medium (Figure 4.4b). DA also influenced the overall polarity spectrum of the medium. The addition of PVA as a surfactant produced strong molecular associations and crosslinker ions with the subsequent energy supplied via agitation and processing temperatures contributing to surface interactions that produced CAP molecules pivoted toward surface minimization, compactness and orientations of the lipophilic regions (Figure 4.4c). The stronger energetic orientations and the presence of PVA as the surfactant tended to sphericalize the CAP strands (Figure 4.4d). The CAP strands sphericalized completely to produce nanoparticles under the primary influence of solvent diffusion phenomena and the presence of PVA with the inner core containing DA molecules and lipophilic regions of CAP conforming toward the periphery as the boundary between the outer hydrophilic medium (Figure 4.4e). Thus, DA molecules orientated within the hydrophilic voids of the nanoparticles shielded by the lipophilic boundary to form stable CAP nanoparticles.

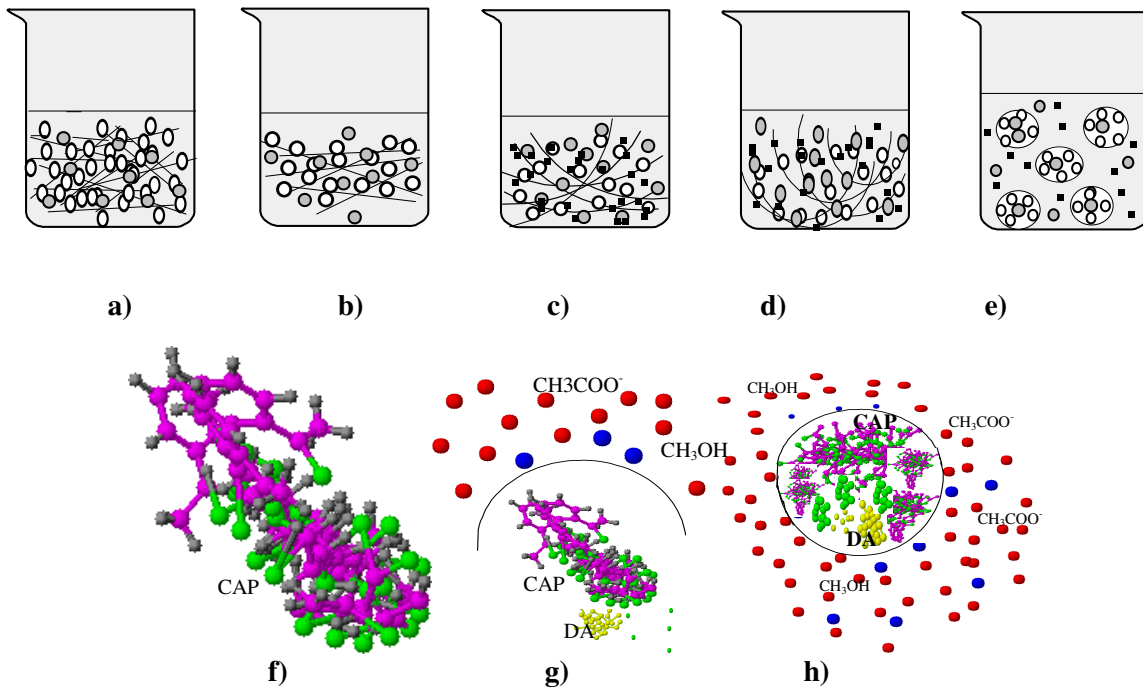


Figure 4.4: Graphical models depicting a-e) the stepwise formation of DA-loaded CAP nanoparticles, f) a single CAP adaptation, g) DA interaction and wall initiation and h) a DA-loaded CAP nanoparticle towards completion

4.3.2. MR behaviour of crosslinked scaffolds

Figure 4.5 depicts a typical Force-Time profile used to calculate the MR which is represented as a percentage of the ratio between the Area Under the Curve (AUC) of anchors 1 and 2 ($AUC_{1 \text{ and } 2}$), and 2 and 3 ($AUC_{2 \text{ and } 3}$)

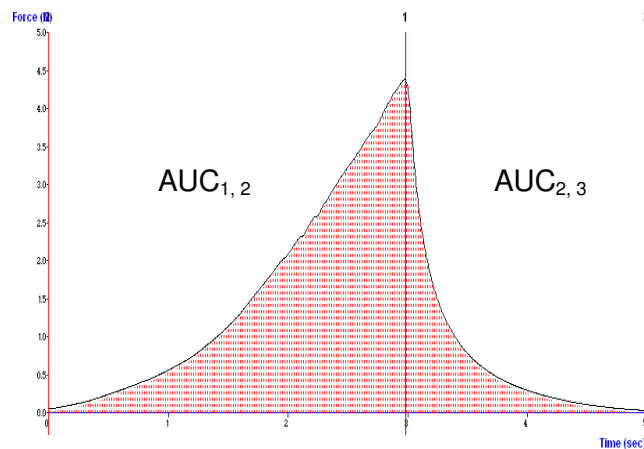


Figure 4.5: A typical Force-Time profile of a hydrated Ba-alginate scaffold for the calculation of MR

The Force-Time profiles for each sample, in both the hydrated and unhydrated states, was used to calculate the MR and thereby establish the most integral crosslinker reagent for the formulation of $[(\text{HOCH}_2(\text{CHOH})_4\text{COO})_2\text{Ca}]$ -crosslinked alginate scaffolds.

Table 4.6: Percentage MR of crosslinked alginate scaffolds in both hydrated and unhydrated states.

Formulation type	MR (%)	
	Hydrated	Unhydrated
Zn-Alginate	9.34	32.68
	7.29	26.18
	10.44	29.59
Ba-Alginate	62.34	66.44
	59.18	72.21
	69.21	66.23
Ca-Alginate	27.51	41.88
	33.15	39.35
	29.98	38.53

TA results proved that the Ba-alginate scaffolds were relatively the most resilient in both the hydrated and unhydrated states. The unhydrated samples for both Ca-alginate and Zn-alginate scaffolds showed greater integrity than the hydrated. The Ba-alginate scaffolds showed only a increase ($\pm 5\%$) in MR in the hydrated state in comparison to the unhydrated state, indicating that the scaffold may maintain its integrity in both formulation and *in vivo* conditions. MR has important implications for not only DA delivery but product storage as well. In drug delivery, the MR profile of a drug delivery device provides data for the possible *in vitro* degradation and in turn the drug release behaviour of the system. In this formulation, it is particularly imperative to have a rigid scaffold so as to be able to withstand the demands of further formulation processes involved during the incorporation of DA-loaded CAP nanoparticles. Ba-alginate scaffolds were chosen as the candidate formulation, due to the superior MR in both the hydrated and unhydrated states, for the dispersal of DA-loaded CAP nanoparticles.

4.3.3. Surface morphology of crosslinked alginate scaffold

Figures 4.6 are microscopic images that display the morphology and pore sizes of Ba-alginate scaffolds formulated in an adopted freeze-drying approach.

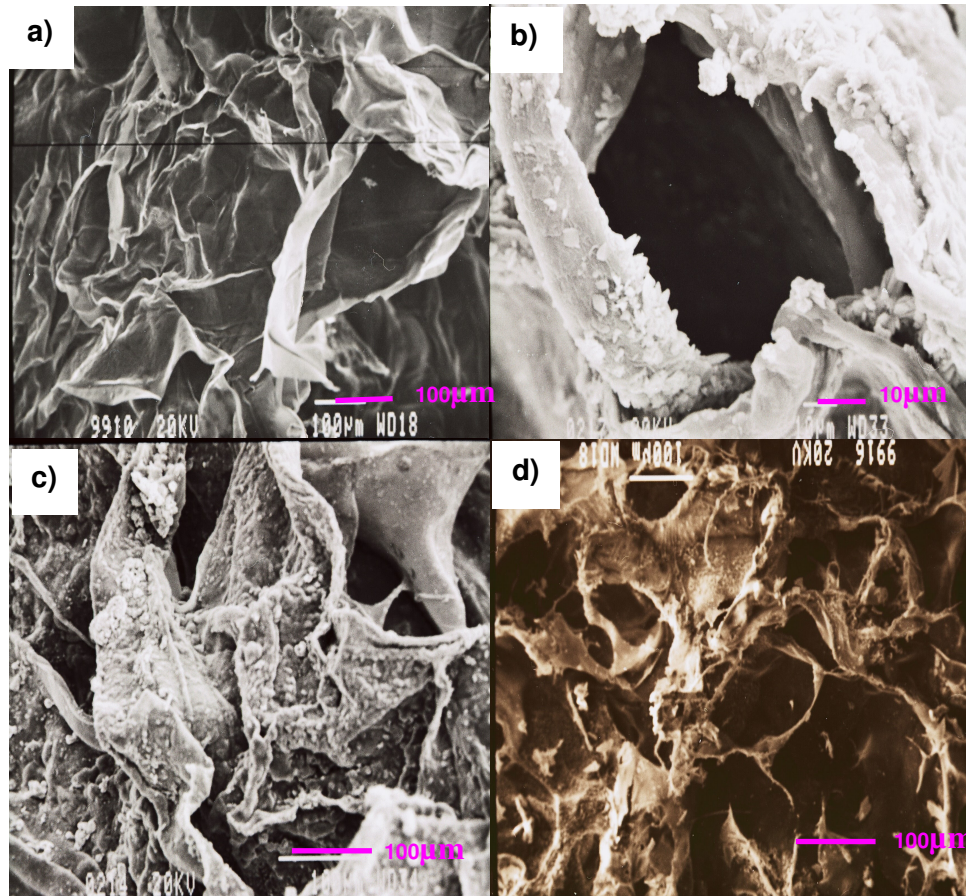


Figure 4.6: Scanning electron microscope images of (a) Ba-alginate scaffold that was not subjected to post-curing (b) a typical pore present within the crosslinked alginate scaffold, (c) scaffold that underwent post-curing with BaCl and (d) the relation of pores in respect to one another

The crosslinked alginate scaffold displayed an average pore size of 100-400 μ m with a wall thickness calculated at an average of $10\pm 1.04\mu$ m. (Figure 4.6d). Scaffolds that were not subjected to post-curing in a secondary crosslinking BaCl₂ solution revealed a "tissue-like" appearance (Figure 4.6a) in comparison to the evenly distributed porous granular yet compact appearance of post-cured scaffolds (Figure 4.6b) Ba-alginate scaffolds revealed a granular yet intact appearance with an even distribution of pores along its surface (Figure 4.6c).

4.3.4. *In vitro* ME of the Ba-alginate scaffold

Minimal ME (12.1%) of the Ba-alginate scaffolds occurred within the first 60 days (Figure 4.7) thereafter there was a mere ME loss of 2.96% in 12 days. Results confirmed that further crosslinking (post-curing) provided robust scaffolds.

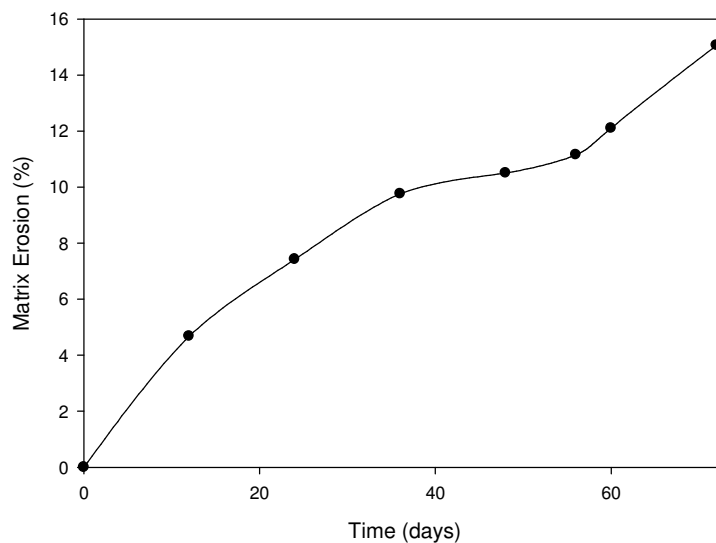


Figure 4.7: ME profile for Ba-alginate scaffold in PBS (pH 6.8, 37°C) over a period of 72 days (SD≤0.23)

4.3.5. Experimental design for the optimization of Ba-alginate scaffold

The Box-Behnken study design, requiring a total of 27 experimental runs (formulation combinations), was generated and analyzed using Minitab[®] V14 (Minitab[®] Inc, PA, USA). The variations of the variables for each formulation are listed in Table 4.7.

Table 4.7: Illustration of variations in formulations employed for a Box-Behnken design for the optimization of Ba-alginate scaffold

Formulation number	Alginate (% ^w / _v)	Stirring Temperature (°C)	[(HOCH ₂ (CHOH) ₄ COO) ₂ Ca] (% ^w / _v)	Post Curing Time (min)
1	3	60	0.2	60
2	3	60	0.6	60
3	2	50	0.6	60
4	2	60	0.4	60
5	2	60	0.6	30
6	3	60	0.4	30
7	2	60	0.4	60
8	2	50	0.4	90
9	1	50	0.4	60
10	2	60	0.4	60
11	1	60	0.4	90
12	2	60	0.2	90
13	2	60	0.6	90
14	1	70	0.4	60
15	1	60	0.4	30
16	2	70	0.4	90
17	3	70	0.4	60
18	2	70	0.4	30
19	1	60	0.2	60
20	2	70	0.2	60
21	3	50	0.4	60
22	2	50	0.2	60
23	3	60	0.4	90
24	2	50	0.4	30
25	1	60	0.6	60
26	2	60	0.2	30
27	2	70	0.6	60

4.3.5.1. Measured responses for the experimental optimization of Ba-alginate scaffold

The measured responses (MR and ME) for each of the 27 formulation employed in the Box-Behnken design are listed in Table 4.8.

Table 4.8: Measured responses for the experimental optimization of Ba-alginate scaffold

Formulation number	MR (%)	ME (%) in 30 days
1	82.95	24.12
2	85.06	25.03
3	84.85	58.92
4	83.73	9.21
5	87.89	12.183
6	94.37	6.93
7	83.73	9.21
8	94.53	15.72
9	84.813	20.68
10	83.73	9.21
11	82.50	3.57
12	81.17	23.14
13	84.78	27.63
14	86.53	6.83
15	81.4	37.91
16	82.38	49.42
17	93.45	3.21
18	86.23	34.89
19	83.33	8.99
20	81.89	14.09
21	81.10	62.19
22	76.81	5.83
23	80.75	6.83
24	94.75	18.143
25	85.07	51.26
26	78.50	11.30
27	84.83	38.81

4.3.5.2. Comparison of the experimental and fitted responses calculated for the experimental optimization of Ba-alginate scaffold

The plots of the experimental versus fitted responses for MR (Figure 4.8a) and ME (Figure 4.8b) of Ba-alginate scaffold showed R^2 values of 72.23% and 68.86% respectively. These values show a satisfactory correlation between the experimental and fitted values for the responses, proving the experimental design was robust in the undertaking of this research.

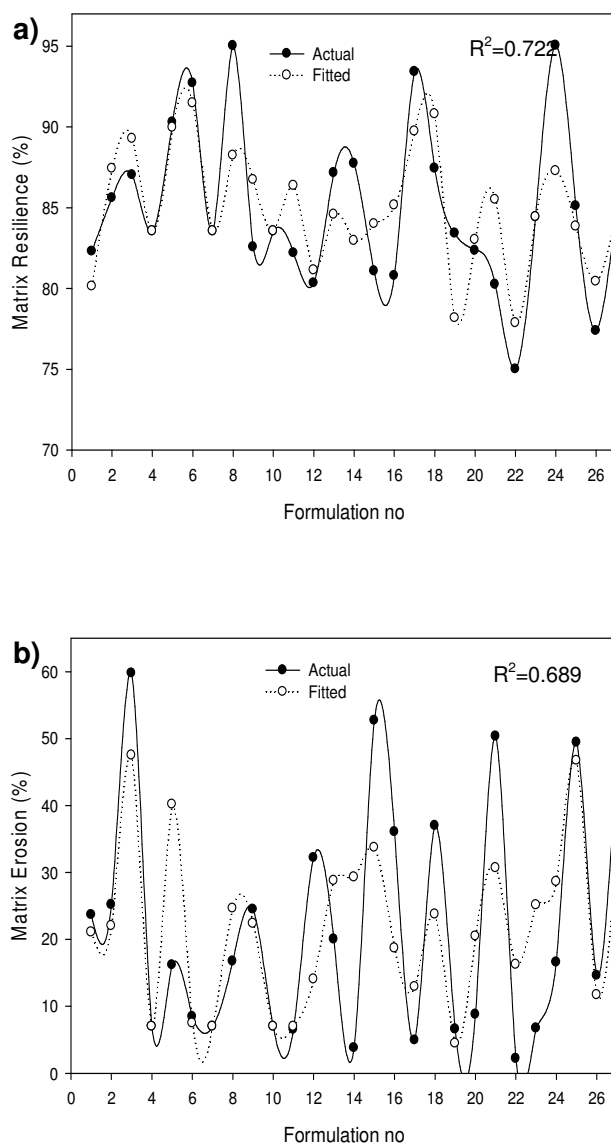


Figure 4.8: The Regression plots for (a) MR (%) and (b) ME for the calculation of R^2 values that determine the similarity between the predicted and experimentally determined values for the responses

4.3.5.3. Response analysis for MR of Ba-alginate scaffold

An increased MR was seen at higher alginate (2-3%^{w/v}) and [HOCH₂(CHOH)₄COO]₂Ca concentrations (0.3-0.4%^{w/v}) (Figure 4.9a). This was expected as at higher [alginate] an advanced degree of crosslinking occurs producing a superiorly robust and interconnected polymeric networked structure with the increased availability of [HOCH₂(CHOH)₄COO]₂Ca. Higher processing temperatures (60-70°C) and lower [alginate] (1%^{w/v}) also provided a desirable MR value (Figure 4.9b). This was attributed to the enhanced molecular mobility of alginate polymeric chains at higher temperatures that induced participation in the crosslinking reaction resulting in the preferred micromechanical behavior.

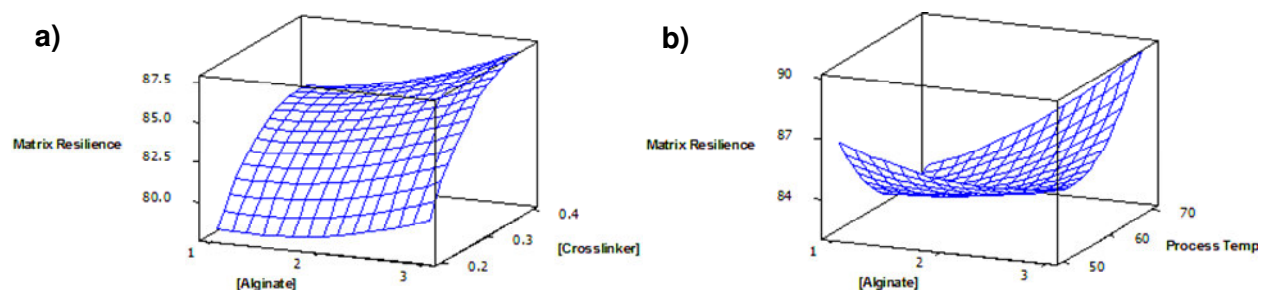


Figure 4.9: Response surface plots correlating the MR with a) alginate and [crosslinker] and b) [alginate] and processing temperature

4.3.5.4. Response analysis for ME of Ba-alginate scaffold

An increase in [alginate] (2-3%^{w/v}) resulted in reduced ME (Figure 4.10a) as a result of a superiorly compact scaffold produced from a precursor solution of increased viscosity. Furthermore, an increase in [HOCH₂(CHOH)₄COO]₂Ca resulted in a greater degree of crosslinking, thereby increasing the scaffold rigidity and retarding ME. An increase in temperature (60-70°C) and post-curing time (60-90min) retarded ME of the scaffold (Figure 4.10b). Higher temperatures enhanced the aqueous solubility of [HOCH₂(CHOH)₄COO]₂Ca (Material Data Safety Sheet, www.sciencelab.com) in water. A prolonged period of post-curing time will allow for the optimal level of crosslinking within the formulation, thereby reducing ME.

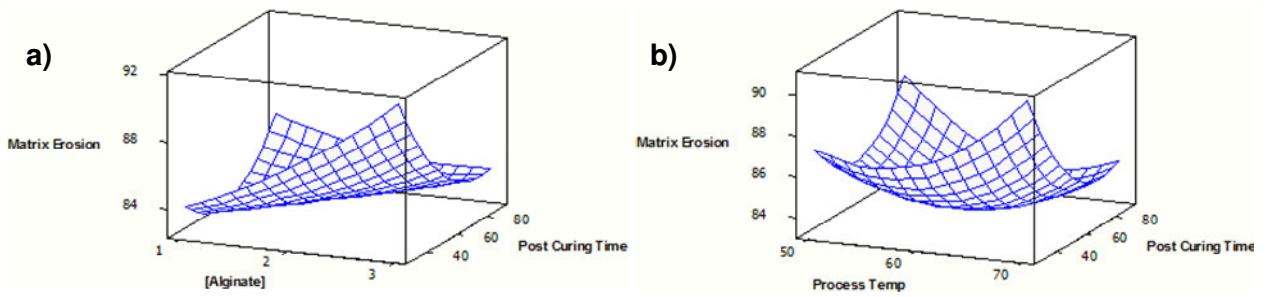
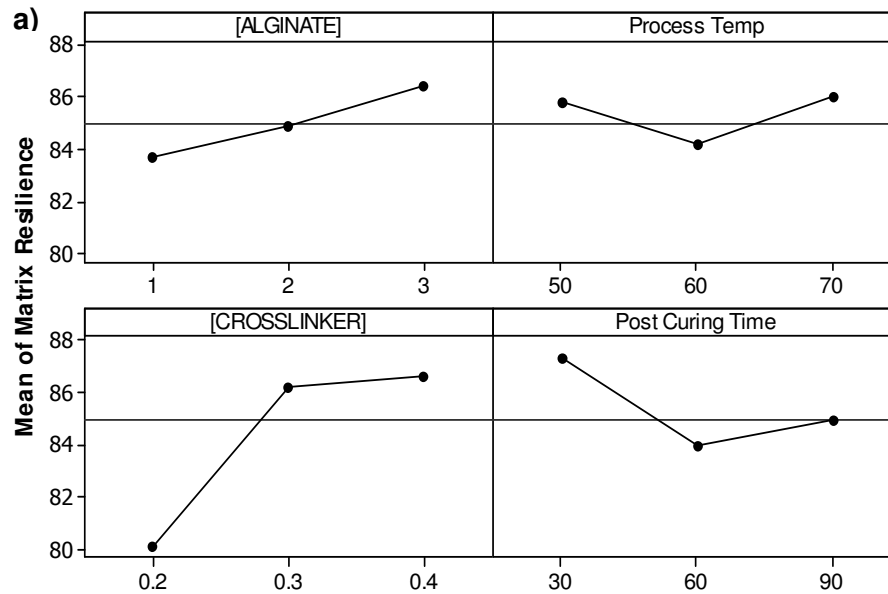


Figure 4.10: Response surface plots correlating scaffold ME with a) [alginate] and post-curing time and b) processing temperature and post-curing time

4.3.5.5. The main and interaction effects on the responses:

Matrix Resilience

The concentration of $[\text{HOCH}_2(\text{CHOH})_4\text{COO}]_2\text{Ca}$ had the most significant effect (Figure 4.11a and 4.11b) in terms of achieving superior MR ($p \leq 0.05$) with increased concentrations providing higher MR values, while the processing temperature displayed the most significant role in matrix design ($p \leq 0.05$). A processing temperature of 50°C also provided desirable MR values. However this was not relevant for post-curing times of 60 minutes.



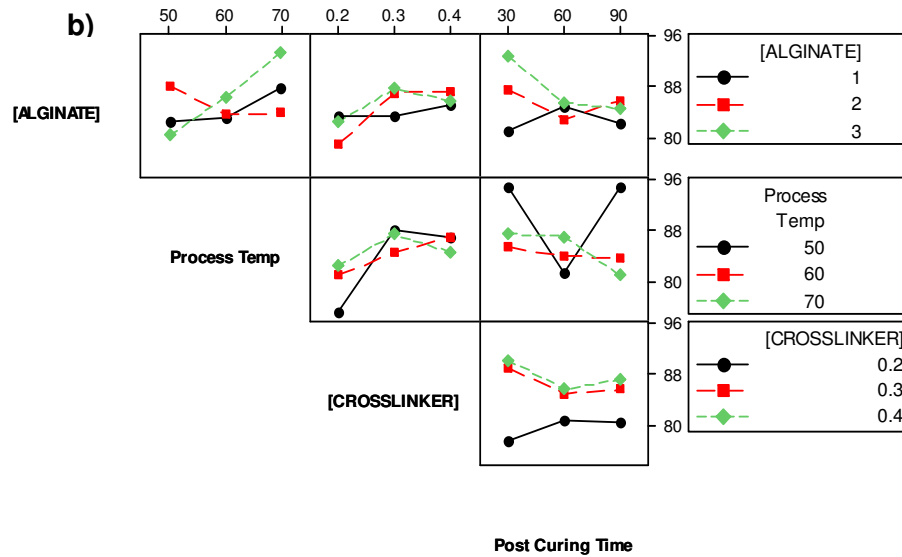


Figure 4.11: Typical (a) main effects plot and (b) interactions plot of response values for MR

Matrix Erosion

The main effects plots showed that an increase in [crosslinker] promoted ME ($p=0.098$) (Figure 4.12a). This was unexpected however this could have resulted from sequestration of ions where the phosphate ions in the buffer caused the sequestration of the calcium ions on the crosslinker, thereby resulting in the rapid dissolution of the highly water soluble crosslinker from the scaffold, decreasing scaffold mass. A higher temperature coupled with decreased [alginate] gave rise to reduced ME (Figure 4.12b) shown in the interaction plots. Higher temperatures resulted in more efficient annealing of the alginate which ultimately improved mechanical integrity of matrix with resultant decreased ME.

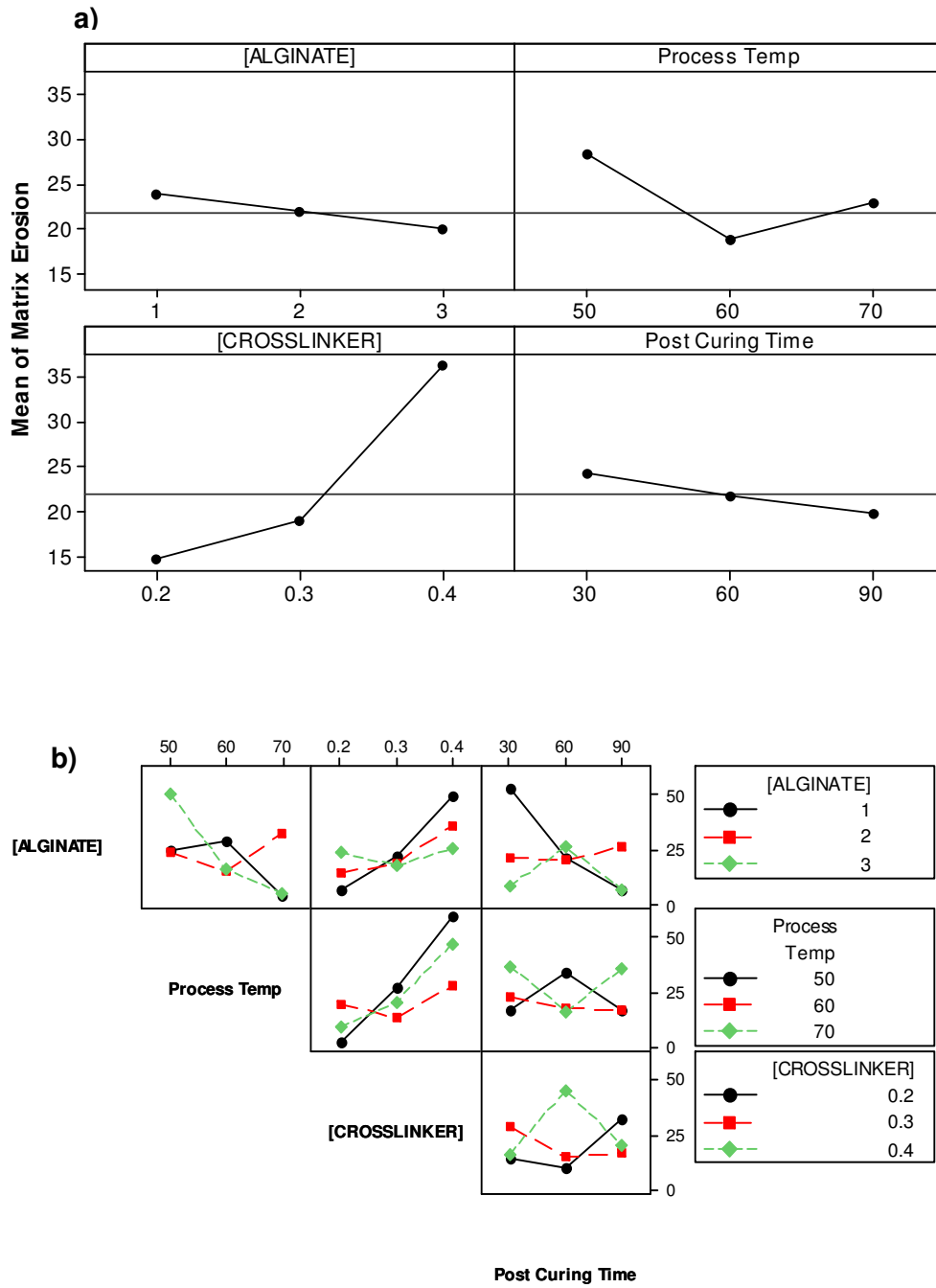
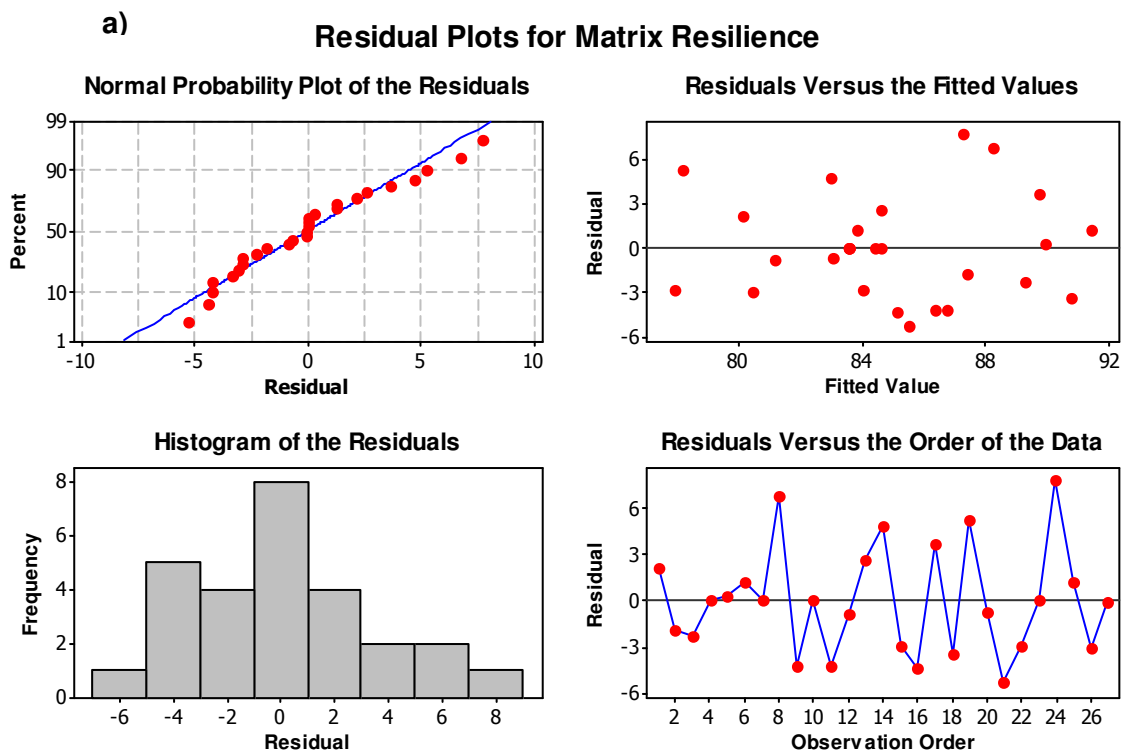


Figure 4.12: Typical (a) main effects plot and (b) interactions plot of response values for ME

4.3.5.6. Analysis of a Box-Behnken design employed for the optimization of Alginate scaffold

The assessment of the regression models can be undertaken employing residual plots (Figure 4.13). Residual plots are essentially a linear comparison between observed values and model predictions for those observations (Stewardson and Whitfield, 2004).



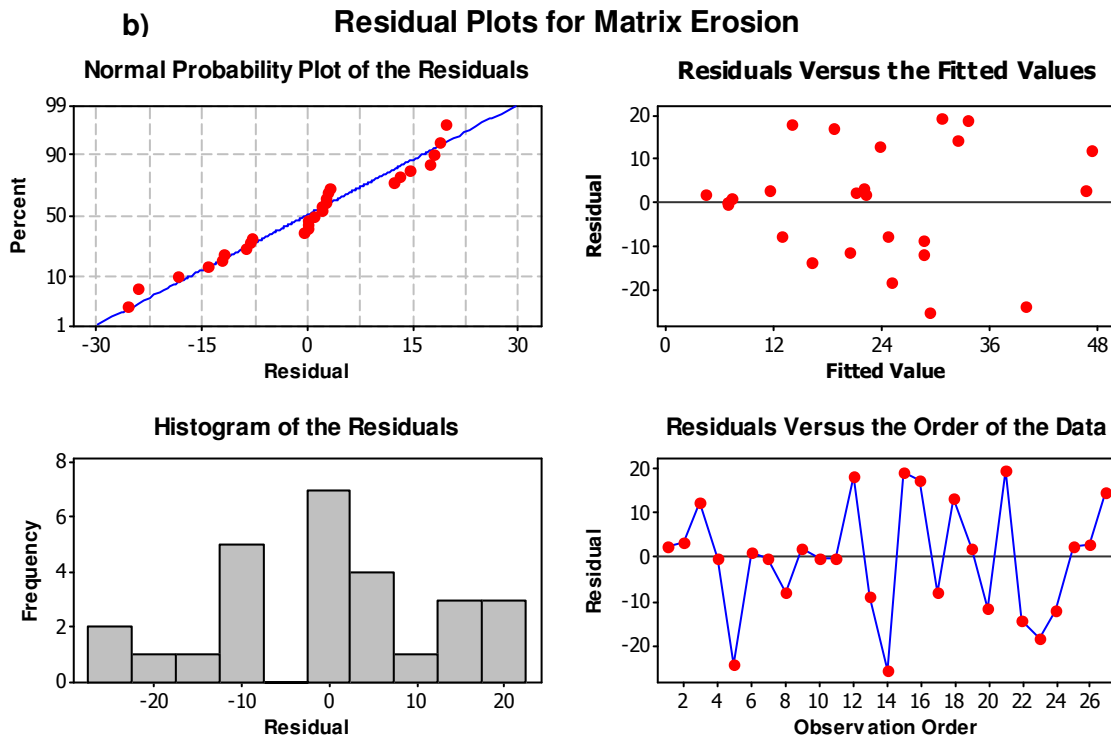


Figure 4.13: The residual plots for the responses (a) MR and (b) ME % for Ba-alginate scaffold

Residual analysis for MR (Figure 4.13a) and ME (Figure 4.13b) showed the casual distribution of data. The normal plot of residuals displayed slight curvatures of the lines which occurred due to the decreased observation points (less than 50) however the plot still showed normal distribution of the data. The residuals versus fitted plot showed randomly scattered data points around the horizontal line (residual = 0), with some fanning indicative of a degree of non-constant variance, and were within 3 standard deviations of the mean, i.e., zero. The histogram supported that the residuals have a normal distribution with zero mean and constant variance. The residuals versus the order of the data was used to identify non-random error, the plot showed a both a positive (clustering of formulations 4-12) and a negative correlation indicated by rapid changes in the signs ($\bar{}/_{+}$) of the consecutive residuals thereafter.

A significant effect is indicated by a *P* value of ≤ 0.05 for any factor. The factors and the respective *P*-values are displayed in Table 4.9.

Table 4.9: Full ANOVA analysis for the measured responses (MR and ME)

Term	p-value	
	MR	ME
[ALG]	0.366	0.740
[PT]	0.940	0.657
[CRL]	0.048	0.098
[PCT]	0.443	0.710
[ALG] ²	0.760	0.656
[PT] ²	0.387	0.380
[CRL] ²	0.420	0.391
[PCT] ²	0.314	0.649
[ALG]*[PT]	0.449	0.561
[ALG]*[CRL]	0.877	0.338
[ALG]*[PCT]	0.376	0.304
[PT]*[CRL]	0.354	0.648
[PT]*[PCT]	0.530	0.979
[CRL]*[PCT]	0.563	0.744

The complete regression equations generated for MR and ME are indicated below:

$$\begin{aligned}
 MR = & 83.391 - 9.883[ALG] - 1.703[PT] + 313.375[CRL] + 0.290[PCT] + 0.692[ALG]^2 + 0.019[PT]^2 - \\
 & 184.833[CRL]^2 + 0.003[PCT]^2 + 0.199[ALG*PT] + 4.050[ALG*CRL] - 0.078[ALG*PCT] - 2.463 \\
 & [PT*CRL] - 0.005[PT*PCT] - 0.507[CRL*PCT]
 \end{aligned}
 \tag{Equation 4.2}$$

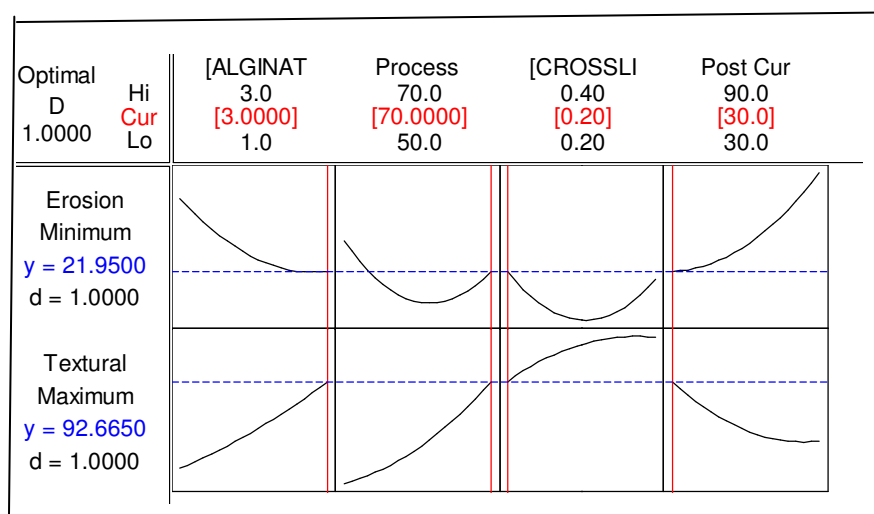
$$\begin{aligned}
 ME = & 344.335 + 21.368[ALG] - 10.984[PT] + 16.183[CRL] - 1.180[PCT] + \\
 & 5.605[ALG]^2 + 0.112[PT]^2 + 1095.29[CRL]^2 + 0.006[PCT]^2 - 0.617[ALG*PT] - \\
 & 103.325[ALG*CRL] + 0.37[ALG*PCT] - 4.833[PT*CRL] - 9.083E-04[PT*PCT] \\
 & - 1.146[CRL*PCT]
 \end{aligned}
 \tag{Equation 4.3}$$

4.3.5.7. Response optimization of Ba-alginate scaffold

This was carried out employing statistical software (Minitab[®], V14, Minitab Inc[®], PA, USA) to determine the optimum level for each variable. The optimization process resulted in the attainment of various formulations with a significantly low desirability for all three outcomes therefore a selection of the most influential desired outcome was necessary to the detriment of the other two outcomes. MR and ME were the most important and essential characteristics for the scaffold and so a scaffold formulation displaying both characteristics at optimal level was selected.

The formulation was optimized for the measured responses of *MR and ME*. Optimization was carried out so as to obtain the levels of [CAP], [PVA], emulsifying time and stirring speed that would maximize the measured responses (Palamakula *et al.*, 2004).

Figure 4.14: Optimization plots displaying factor levels and desirability values for the chosen optimized formulation



Measured response	Predicted values	Experimental values	Desirability (%)
MR (%)	92.6650	82.455	88.982
ME (%)	21.9500	18.23	83.052

4.3.5.8. Desirability for the measured responses of the optimized Ba-alginate scaffold formulation

With reference to the optimized Ba-alginate scaffold, the MR of the experimental formulation (82.46%) displayed favorability to the fitted formulation (88.98%). While the experimental formulation had slightly lower MR than fitted, this was counteracted as the ME was lower than predicted (only 18.23% after 7 days) (Figure 4.14). The optimized formulation proved have the desired characteristics of increased MR and decreased ME.

4.3.6. *In vitro* DA release from the NESD

DA release from the NESD could be separated in two phases: (1) diffusion of nanoparticles. Upon contact with this media, the scaffold will become infused with PBS thereby releasing nanoparticles through the pores. The gradual ME of the scaffold will result in an increased diffusion rate of nanoparticles out of the matrix and (2) dissolution of the nanoparticles in PBS thereby releasing DA. The nanoparticles (Figure 4.15a) showed a release of 0.25% in the first 2.5hr, however the release profile for DA-loaded CAP nanoparticles incorporated into the scaffold (Figure 4.15b) showed a lag phase for the initial hr (prior to 6hr) of the study followed by the steady increase in the release of DA thereafter. A release of 5.12% was noted after 168hr. This type of release was attributed to the degradation and increase in pore formation in the scaffold. The DA release pattern was attributed to the ME behaviour of the scaffold (Figure 4.7). The release of DA was highest at the point where ME of the scaffold was at maximum (12-30hr) thereafter both DA release and ME maintain a constant profile. SEM images showed an increase in the number of pores and the size post-ME studies (30 days) allowing for the increased flow of buffer into the pores thereby facilitating a further diffusion of DA out of the pores. Zeta potential and size of the nanoparticles also aided in DA release. DA-loaded CAP nanoparticles had high zeta potentials (-35.2mV) and reduced particle sizes (165.4nm) illustrated in Chapter 3 Figure 3.20 of this dissertation. The charges on the particles would electrostatically repel them from one another assisting in their molecular movement through the scaffold.

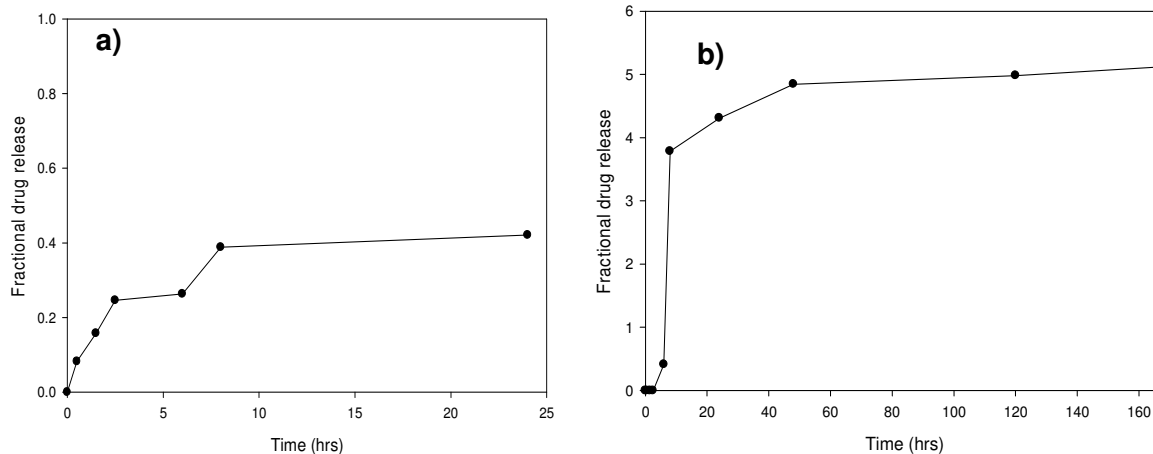


Figure 4.15: DA release profiles for (a) DA-loaded nanoparticles ($SD \leq 0.02$) and NESD in PBS, pH 6.8; 37°C), ($SD \leq 0.16$)

4.3.7. Componential thermal analysis on the NESD

TMDSC profiles portrayed the paradigms of the thermal behavior in the three componential elements of the NESD that included the CAP nanoparticles, the crosslinked alginate scaffold and the NESD as shown in Figures 4.16a, b and c. The changes in T_g , T_m and T_c that occurred upon the formation of DA-loaded CAP nanoparticles, the crosslinked alginate scaffold and the assimilated NESD when compared to native CAP employed for nanoparticle fabrication is depicted in Figures 4.16a-c.

Table 4.10: Salient thermal events for DA-loaded CAP nanoparticles, Ba-alginate scaffold and NESD compared to native CAP

Formulation Component	Temperature transition points (°C)		
	T _g	T _c	T _m
DA-loaded CAP nanoparticles	260	160 262 378	268
Crosslinked alginate scaffold	210	158 238 330	390
NESD	260	158 315 358	390
Native CAP	160-170	180	192

T_g = glass transition temperature; T_c = crystallization temperature and T_m = melting temperature

All components presented with triple exothermic peaks depicting a coincidental similarity in crystallization behaviors (T_c) (Figures 4.16a, b and c). The similarity in thermal behavior between the crosslinked alginate scaffolds and NESD portrayed a direct indication of the high degree of crystallinity imparted by the secondary crosslinker BaCl₂ that was employed as a curing step for scaffold formation. Noteworthy was the significantly large variation in T_g and T_m between the native CAP (T_g=160-170°C; T_m=192°C) and the DA-loaded CAP nanoparticles (T_g=260°C; T_m=268°C). The apparent shifts in T_g and T_m elucidated a possible interfacing between CAP and DA molecules that contributed to the formation of physical interactions culminating into the thermal behaviour observed. The large positive shifts in thermal events may have also influenced the release of DA from the CAP nanoparticles as supported by the initial prototyping technology employed and DA release profiles discussed later on. The presence of transient melting endothermic peaks and further shifts in T_g observed on the TMDSC signals of the NESD samples clearly reflected the effect of altered thermal properties produced by initial crosslinking between [HOCH₂(CHOH)₄COO]₂Ca and alginate and further the dispersion of DA-loaded CAP nanoparticles within the BaCl₂ solution as a post-curing process. The altered thermal behaviour influenced the physicomaterial behaviour as supported by the earlier morphological, textural profile and FTIR analysis.

Overall, the thermal behavior observed may be due to variation in the ΔH involved, ability to attain near-equilibrium conditions during measurement, and the rapid rate of change in molecular rearrangement compared to the ΔT . These pertinent intermolecular interactions, which resulted in the observed thermal transitions (Figures 4.16a, b and c), may have also contributed substantially to the superior control of DA released from the NESD.

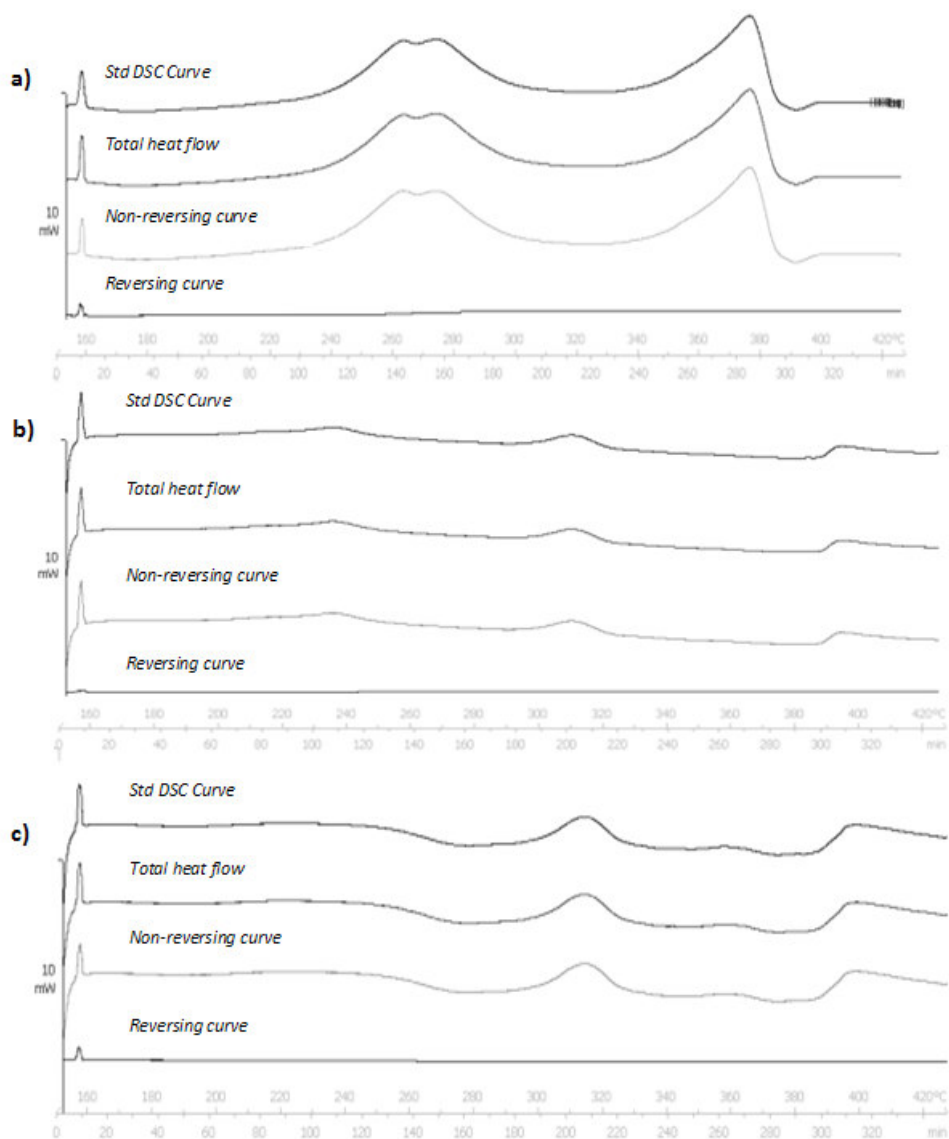


Figure 4.16: Temperature modulated differential scanning calorimetry profiling for NESD showing endothermic and exothermic peaks generated

4.4. Concluding Remarks

In this chapter, alginate was chosen as the polymer for the employment in scaffolds. The crosslinking of this with various agents resulted in Ba-alginate scaffolds being selected as the ideal candidate for its MR. A porous structure yet high integrity was revealed in the micrographs of the Ba-alginate scaffolds. A ME of 15% was calculated only at 60hr, showing minimal rapid degradation throughout the period of investigation. The Box-Behnken design was employed to optimize the formulation and gave rise to 27 formulations where [alginate] and [Ba] were altered as well as processing factors such as post-curing time and heat. MR and ME % were chosen as the imperative properties to be optimized. A single candidate optimal formulation displaying MR of 82.455% and a ME of 18.23% in 30 das was selected. In this chapter, the DA-loaded CAP nanoparticles were incorporated into the Ba-alginate scaffold (optimal formulations) and analysed, generating for *in vitro* release profiles. The addition of the nanoparticles into a Ba-alginate scaffold significantly reduced DA release (5.12% release in 168hr) and was established as the main contributor to the controlled DA release. Significant shifts in thermal events noted with TMDSC analysis of the DA-loaded CAP nanoparticles and NESD supported the mechanism by which modulated release of DA occurred from the device. Biometric simulation and prototyping technology in conjunction with Box-Behnken statistical experimental designs as preparation and optimization strategies for the scaffold and nanoparticles proved robust in selecting optimal components for assembling the NESD.

CHAPTER 5
INVESTIGATION INTO DRUG-LOADED NANOSTRUCTURES FOR THE EMPLOYMENT
IN TREATMENT OF PARKINSON'S DISEASE

5.1. Introduction

Nanotechnology has widened the horizon for novel therapeutic opportunities for agents that cannot be formulated using conventional drug techniques; due to poor drug instability and/or bioavailability allowing for site specific delivery of medicine to diseased tissues and cells thereby dramatically increase the chances of healing in affected individuals. Polymeric nanofibers, an example of a nanosystem, are uniquely shaped two dimensional structures that may be formed employing a simple yet reproducible electrospinning technique. Examples of nanofiber drug delivery systems include dexamethasone-loaded PLGA nanofibers in neural prosthetics (Abidian *et al.*, 2006) and ketapofen-loaded PVA nanofibers for inflammation (Kenawy *et al.*, 2007). Furthermore, the polymer fibers may be coated with an electro-conductive polymer which can be stimulated by an external electrical current. These fibers may contract/dilate according to the stimuli received so as to reduce/increase drug delivery at their target site. An example of this system is poly (3, 4-ethylenedioxythiophene) for implantation into the brain (Richardson-Burns *et al.*, 2007).

Electrospinning involves the application of electricity to form nanofibers (Reneker and Yarin, 2008). A polymeric solution of the appropriate viscosity is placed in a capillary tube/pipette. A high voltage is sent through an electrode that is placed within the capillary tube. This gives rise to an electric field which opposes the surface tension (present at the end of the capillary tube). As a result, a conical shaped protrusion known as the Taylor cone (Figure 3.1). The polymeric solution forms at the end of the tube (Welle *et al.*, 2007). A jet of polymeric solution is ejected from the tip, which is attracted to a grounded metal screen lined with foil, resulting in nanofibers.

The following variables influence the length and uniformity of the fibers and can be controlled (Welle *et al.*, 2007): Viscosity of the polymeric solution; flow rate of the polymeric solution; distance of the capillary end from screen; and voltage from the external supply.

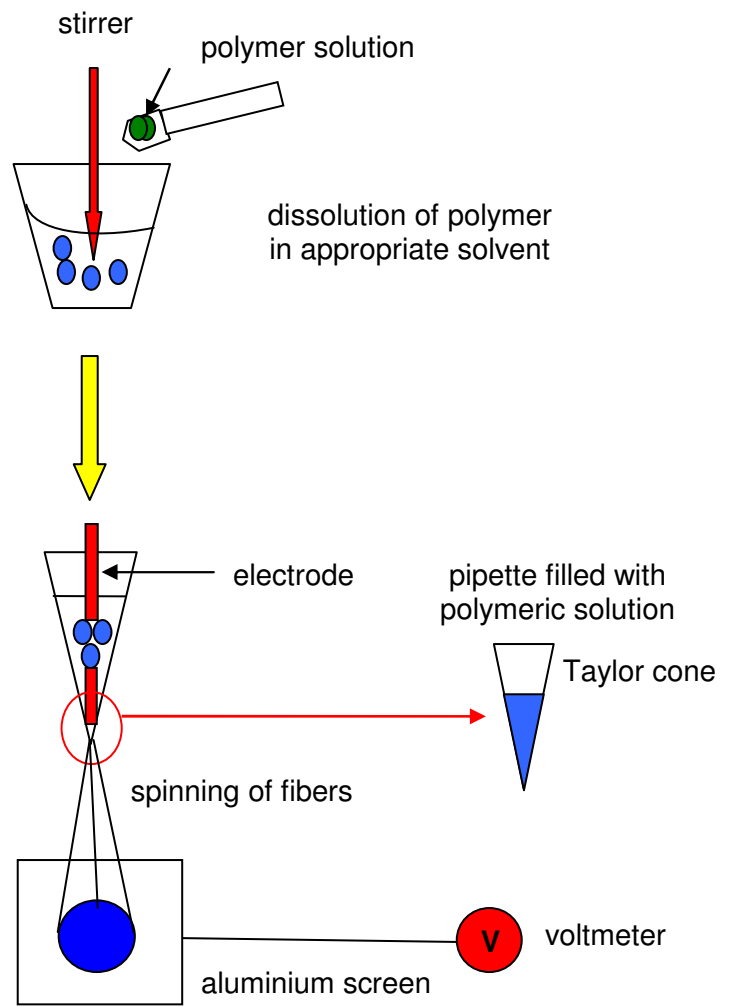


Figure 5.1: A schematic representation of a rudimentary electrospinning apparatus employed for the formulation of nanofibers

The impetus of this chapter greatly revolves around the development of a controlled drug delivery systems for pharmacological agents used in the treatment of PD that reduces the dosages thereby reducing the “off” period experienced and reducing the side effect profile. This will increase compliance and most of all the development of a common drug delivery platform that can be used to deliver both previously and newly formulated drugs in a targeted approach to treat CNS disease states.

This chapter sought to address the need for alternate nanosystems, L-dopa and NT nanoparticles and DA nanofibers, which may be employed for the treatment of PD.

5.2. Investigation of L-dopa-loaded Poly (lactic-co-glycolic acid) Nanoparticles

5.2.1. Materials and Methods

5.2.1.1. Materials

3-(3,4-dihydroxy phenyl)-l-alanine, (L-dopa), ($M_w=197.19\text{g/mol}$), cellulose acetate phthalate (CAP) ($M_w=2534.12\text{g/mol}$), poly(vinyl alcohol) (PVA) ($M_w=49,000\text{g/mol}$) was purchased from Sigma Aldrich (St. Louise, MO, USA), hydrochloric acid (HCl), 32%, was purchased from SAARCHEM (Johannesburg, South Africa). Poly (DL-lactide-co-glycolide) (PLGA), resomer RG504 ($M_w=48000\text{g/mol}$) purchased from Boehringer Ingelheim (Ingelheim, Germany) and dimethyl sulphoxide (DMSO) ($M_w=78.13\text{g/mol}$) from obtained from Merck (Johannesburg, South Africa). Deionized water was obtained from a Milli-Q water purification system (Milli-Q, Millipore, Billerica, MA, USA). All other reagents were of analytical grade and used as purchased.

5.2.2. Preparation of L-dopa-loaded PLGA nanoparticles employing a nano-precipitation technique

The precipitation method adopted in this study is based on work previously reported by Fessi *et al* in 1989 which involved a lipophilic drug/polymer/acetone or ethanol (solvent)/ water (non-solvent) system which was then altered to a more versatile solvent-non-solvent scheme (Bilati *et al.*, 2005). The limited solubility of the polymer (PLGA) and drug (L-dopa) led to the employment of the nano-precipitation rather than the previously adopted emulsification-diffusion method stated in Chapter 3, Section 3.2.5. of this dissertation. The selection of this method also allowed for the investigation of versatility of the NESD by means of incorporating drug-loaded polymeric nanoparticles, produced employing different techniques, into the Ba-alginate scaffold.

Preparation of the non-solvent system: Two separate solvent systems were used; (1) consisted of buffer (pH 6.8, 20mL) and (2) consisted of buffer (pH 6.8, 19mL) and PVA (1%^{w/v}, 1mL).

Preparation of the solvent system: A PLGA (0.5 %^{w/v}) solution was prepared by dissolving PLGA (1g) in DMSO (20mL). Three separate solutions of this PLGA (0.5% ^{w/v}) were prepared, to which 0.1% ^{w/w}, 0.3% ^{w/w} and 0.5% ^{w/w} of L-dopa to polymer was added. Drug-free nanoparticles were prepared in a similar manner.

Incorporation of non-solvent to solvent system to formulate L-dopa-loaded PLGA nanoparticles

The solvent system was infused into the non-solvent system with a syringe and a needle of varying gauge (25G and 21G). Needles of different gauge sizes were employed to investigate the effect that friction has on the characterization of nanoparticles (will be hereon referred to as nanoparticles). The ratio of non-solvent to solvent was maintained at 20:1. In each case the infusion process took place either under moderate magnetic stirring at 300rpm (Hibi[®] magnetic stirrer, Gauteng, S.A) or utilising a three blade propeller overhead stirrer at 1000rpm (Heidolph[®], Lebotec, Gauteng, S.A). The suspended precipitate was collected, centrifuged at 8000rpm (Optima[®] LE-80K, Beckman, USA). The sediment was collected and subsequently lyophilised (Virtis lyophiliser, Virtis[®], Gardiner, NY, USA), refer to Chapter 4, Table 4.3 of this dissertation for parameter and settings, for a 24hr period.

5.2.3. Assimilation of L-dopa-loaded PLGA nanoparticles and Ba-scaffold into the NESD

L-dopa loaded nanoparticles (200mg) were placed into moulds containing a Ba-alginate solution (2mL) vigorously stirred and immediately placed in a freezer set at -70°C for 24hr. Thereafter the scaffolds were freeze dried for 48hr and crosslinked with calcium gluconate as per the method in Chapter 4 Section 4.2.9.1 of this dissertation.

5.2.4. Determination of L-dopa entrapment efficiency of PLGA nanoparticles

A calibration curve for L-dopa was determined using a known series of concentrations of L-dopa in PBS pH 6.4. Samples were accurately weighed and completely dissolved in 0.1M HCl (100mL) and left under vigorous magnetic stirring (700rpm) for a period of one week. The L-dopa content was analyzed by UV spectrophotometry at λ_{280nm} (Hewlett Packard 8453 Spectrophotometer, Germany) and computed from a standard linear curve of DA in PBS (pH

6.8; 37°C) ($R^2=0.99$). Chapter 3, Equation 3.1 of this dissertation was utilized to compute the Drug Entrapment Efficiency (DEE).

5.2.6. *In vitro* L-dopa release studies on PLGA nanoparticles and NESD

In vitro release studies were performed on the L-dopa-loaded PLGA nanoparticles and NESD utilizing a shaking incubator (Labex, Stuart SBS40[®], Gauteng, South Africa) set at 20rpm. The L-dopa loaded nanoparticles and NESD was immersed separately in 100mL PBS (pH 6.8, 37°C) contained in 150mL glass jars. At predetermine time intervals 3mL samples of each release media were removed, filtered through a 0.22 μ m Cameo Acetate membrane filter (Millipore Co., Bedford, MA, USA) and centrifuged at 20,000rpm (Redhead *et al.*, 2001). The supernatant was then removed and analyzed by UV spectroscopy at a maximum wavelength of $\lambda_{280\text{nm}}$ for L-dopa content analysis. L-dopa release was quantified using a linear standard curve ($R^2=0.99$). An equal volume of DA-free PBS was replaced into the release media to maintain sink conditions.

5.2.7. Morphological characterization of L-dopa-Loaded PLGA nanoparticles

Morphological characterization of the nanoparticles revealed the shape, surface, structure and size homogeneity and possible degree of aggregation. Surface morphology was characterized by Scanning Electron Microscopy (SEM), (JEOL, JEM 840, Tokyo Japan). Photomicrographs were taken at different magnifications and samples were prepared after sputter-coating with carbon or gold (N=10). Nanoparticle size and shape was further explored using cryo-Transmission Electron Microscopy (TEM) (JEOL 1200 EX, Tokyo, Japan, 120keV) for higher definition and resolution. Samples were prepared by placing a dispersion of nanoparticles in ethanol on a copper grid with a perforated carbon film followed by evaporation and viewing at room temperature (N=10).

5.2.8. Determination of polymeric structural variations due to L-dopa-loaded PLGA nanoparticle formation

The structure of native PLGA, L-dopa and the PLGA nanoparticles produced were assessed using Fourier Transmission Infrared (FTIR) spectroscopy to assess the potential for any variations in vibrational frequencies and subsequent polymer structure as a result of L-dopa-polymer interactions during nanoparticle formation. Changes in the PLGA backbone may alter the inherent stability and therefore affect the physicochemical and physicomechanical properties of the selected polymer type for the intended purpose. Samples of L-dopa-free and L-dopa loaded PLGA nanoparticles were blended with potassium bromide (KBr) in a 1%^{w/w}

ratio and compressed into 1×13mm disks using a Beckmann Hydraulic Press (Beckman Instruments, Inc., Fullerton; USA) set at 8 tons. The sample disks were analyzed in triplicate at high resolution with wavenumbers ranging from 4000-400 cm⁻¹ on a Nicolet Impact 400D FTIR Spectrophotometer coupled with Omnic FTIR research grade software (Nicolet Instrument Corp, Madison, WI, USA).

Liquid FTIR analysis: The FTIR analysis of the liquid (DMSO) used in the formulation of L-dopa-loaded nanoparticles identified their chemical interaction on a molecular level that took place prior to precipitation. These were performed on PLGA and DMSO solutions employing a Bruker Tensor 27 (OPUS software) FTIR instrument (Bruker Daltonik GmbH, Germany) with frequency range 4000 to 400 cm⁻¹.

5.2.9. Determination of size and zeta potential of L-dopa-loaded PLGA nanoparticles

The nanoparticle zeta potential measurements were obtained using a Zetasizer Nano ZS (Malvern Instruments Ltd, Malvern, Worcestershire, UK). Each sample (1%^{w/v}) was appropriately diluted with deionised water, filtered (0.22µm filter Millipore Co., Massachusetts, USA) to maintain the number of counts per second in the region of 600 (Layre *et al.*, 2006) and placed into disposal cuvettes (size) or capillary cells (zeta potential) (Malvern Instruments Ltd, Malvern, Worcestershire, UK). The viscosity and refractive index of the continuous phase were set to those specific to deionized water. Measurements were taken in triplicate with multiple iterations for each run in order to elute size intensity and zeta potential distribution profiles.

5.3. Results and Discussion

5.3.1. Formulation of L-dopa-loaded PLGA nanoparticles

L-dopa is slightly soluble in the non-solvent system. Hence the pH was altered to 6.7 by adding HCl to the solution and thereby decreasing the solubility of L-dopa even further. At pH 6.7, L-dopa is almost unionized in the non-solvent system and therefore remains in the solvent system, thereby increasing the DEE within the polymer during the process of precipitation at the step of infusion. Equation 5.1 further motivates the employment of PBS pH 6.7:

$$pH = pKa - \log\left(\frac{100 - x}{x}\right) \quad \text{Equation 5.1}$$

Where pH is that of the PBS in which L-dopa is unionized, $pKa = 9.7$ and is that of the grade of L-dopa being employed and $x = 0.1$ and i is the % ionization of L-dopa that occurs at pKa 9.7.

5.3.2. L-dopa entrapment efficiency of PLGA nanoparticles

A calibration curve was set up as shown in Figure 5.2 and the DEE for L-dopa-loaded nanoparticles was calculated to be 61.22%. L-dopa is slightly soluble in water, 66mg in 40mL, (Budavari, 1996) water during the infusion process the L-dopa dissolved into the non-solvent (water) from the solvent system, this is referred to as the leaking of L-dopa. Hence the solvent system was adjusted to pH 6.7 which would prevent the L-dopa from going into dissolution in the non-solvent system, thus enhancing the DEE (14.8 ± 0.7).

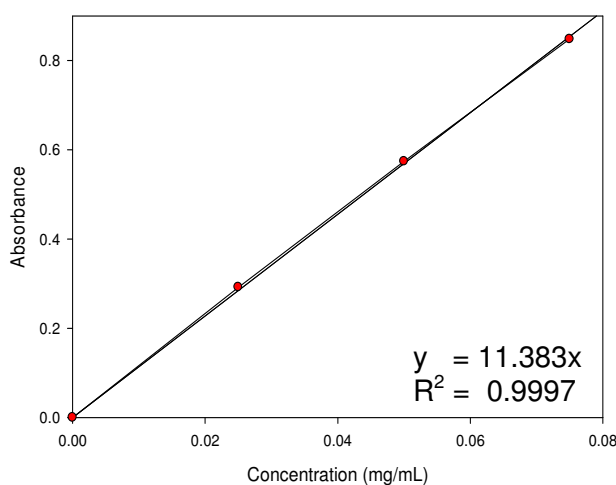


Figure 5.2: L-dopa calibration curve at 285nm in PBS (pH 6.8; $37^{\circ}C$)

5.3.3. *In vitro* L-dopa release from PLGA nanoparticles and the NESD

L-dopa release from the nanoparticles over a 75hr period was 4.21% (Figure 5.3a). The second hour saw the majority of L-dopa release (0.019%), in comparison to the total amount of L-dopa release. L-dopa release over the sampling period occurred gradually with minimal increment of L-dopa release. The scaffold retarded the release of L-dopa significantly which can be attributed to the M_w of PLGA ($M_w=48000$) and the hydrophobicity of its constituents (PLA and PGA) which imparts high erosion resistance (von Burkersroda *et al.*, 2002). The capacity of the PLGA polymer to undergo hydrolysis and consequently biodegradation is influenced by the crystalline properties of the PLGA polymer (Jain, 2002). L-dopa release from the PLGA nanoparticles dispersed within the scaffold (Figure 5.3b) displayed a lag

phase of 2hrs compared to the native nanoparticles. It can therefore be deduced that the scaffold aided in controlling DA release by creating diffusion resistance pathways.

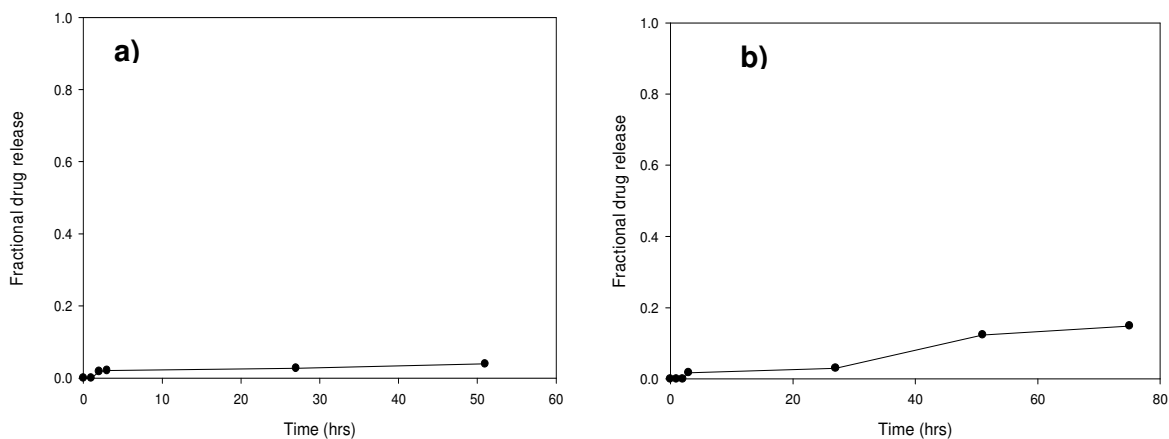


Figure 5.3: L-dopa release profiles from (a) L-dopa-loaded PLGA nanoparticles ($SD \leq 0.0012$) and (b) NESD in PBS (pH 6.8; 37°C); ($SD \leq 0.006$)

5.3.4. Morphology of L-dopa-loaded PLGA nanoparticles

Figure 5.4a shows uniformly distributed L-dopa-loaded PLGA nanoparticles and presence of aggregation. Figure 5.4b depicted an isolated L-dopa-loaded PLGA nanoparticle indicating PLGA and encapsulated L-dopa

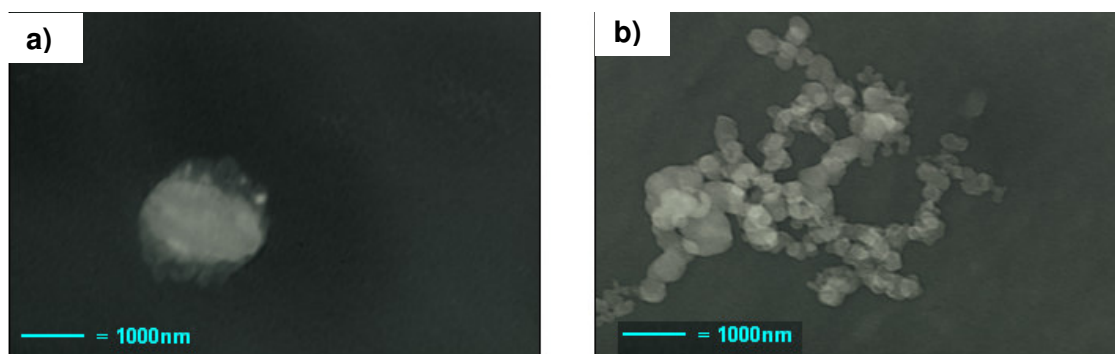


Figure 5.4: TEM images of (a) an isolated L-dopa-loaded PLGA nanoparticle and (b) a cluster of L-dopa-loaded PLGA nanoparticles

5.3.5. Structural polymeric variation of polymer, L-dopa and L-dopa-loaded PLGA nanoparticles

L-dopa is decarboxylated to DA by the enzyme dopa decarboxylase. The only structural difference between L-dopa and DA is the presence of a -COOH (2500cm^{-1} - 3000cm^{-1}), positioned on the terminal group of alanine, on L-dopa displayed in the FTIR (Figure 5.5). The -C=O that forms part of -COOH group is displayed at 1748.93cm^{-1} . These groups indicated the presence of L-dopa in the L-dopa-loaded PLGA nanoparticles. The primary amine and the aromatic -OH groups present on both molecules L-dopa and DA are essential for activity of the molecules. FTIR of both the native L-dopa and L-dopa-loaded PLGA nanoparticles have peaks of 1087.36cm^{-1} which falls in the range in which an aliphatic -C-N stretch occurs. However, the peak of the aromatic -OH in the L-dopa-loaded PLGA nanoparticles group which occurs very strongly in the $3200\text{-}3600\text{cm}^{-1}$ range, could be masked by the peaks occurring in the polymer over the same wavelength range. The FTIR spectra indicated that PLGA and L-dopa (native) maintained its backbone structure in the formation of L-dopa-loaded PLGA nanoparticles. There was an absence of any newly formed compounds that may have aided in retarding L-dopa release. However the FTIR spectra confirmed that nanoparticles were made up of both L-dopa and PLGA.

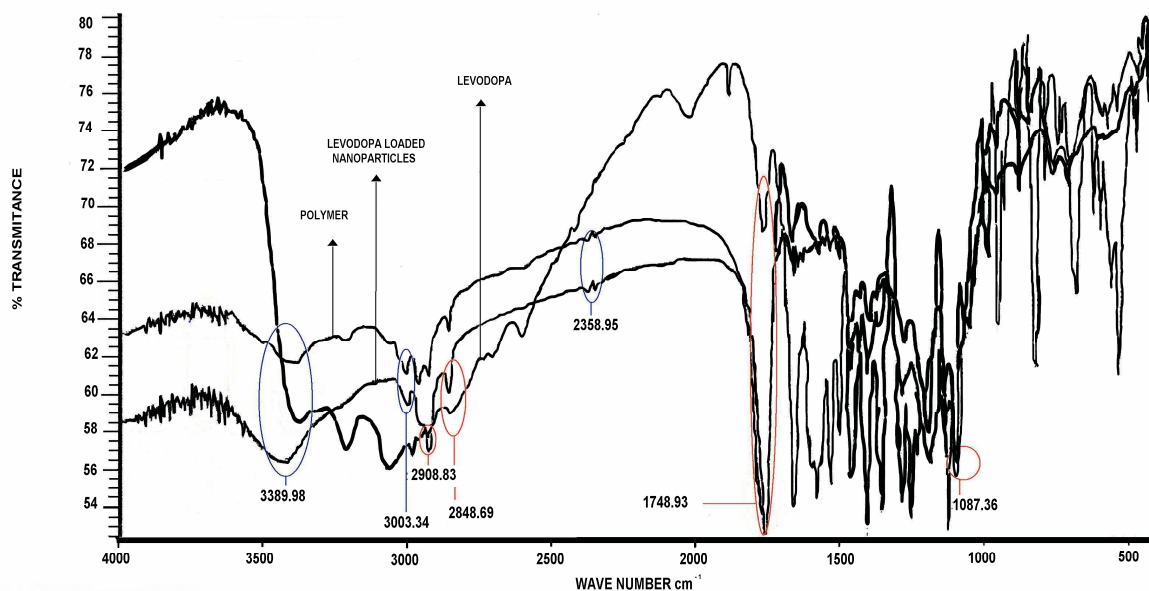


Figure 5.5: FTIR spectra for L-dopa, PLGA, L-dopa free and L-dopa-loaded PLGA nanoparticles

Proposed PLGA and DMSO employing liquid FTIR analysis

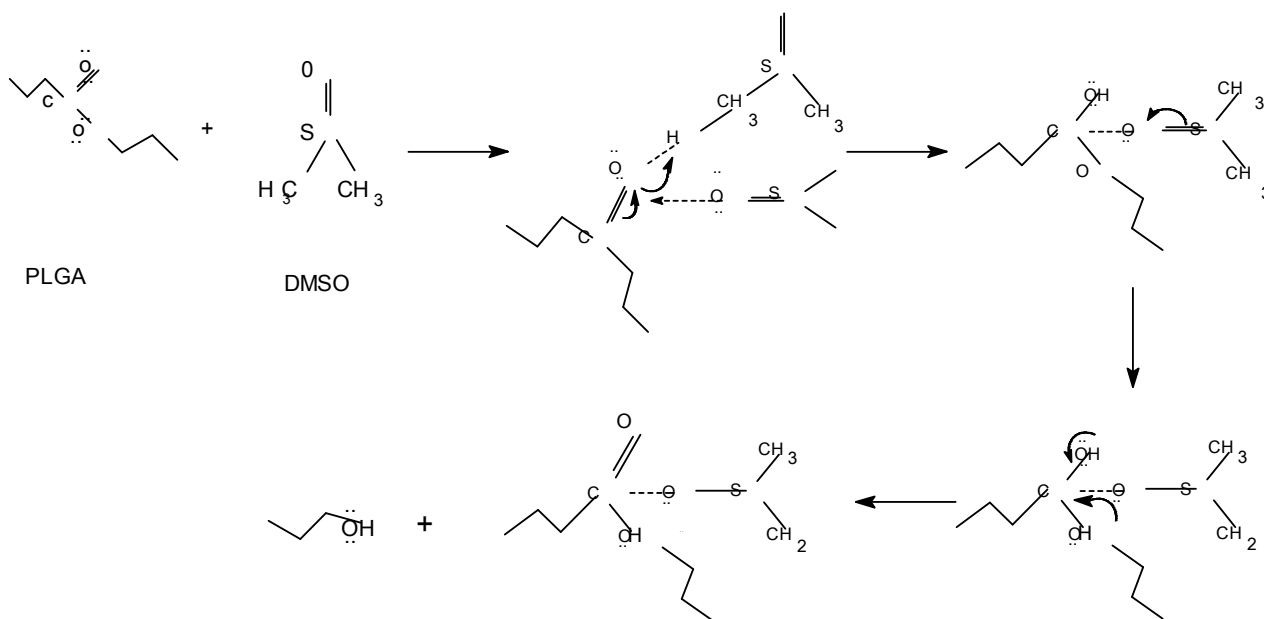


Figure 5.6: Proposed PLGA and DMSO chemical interaction

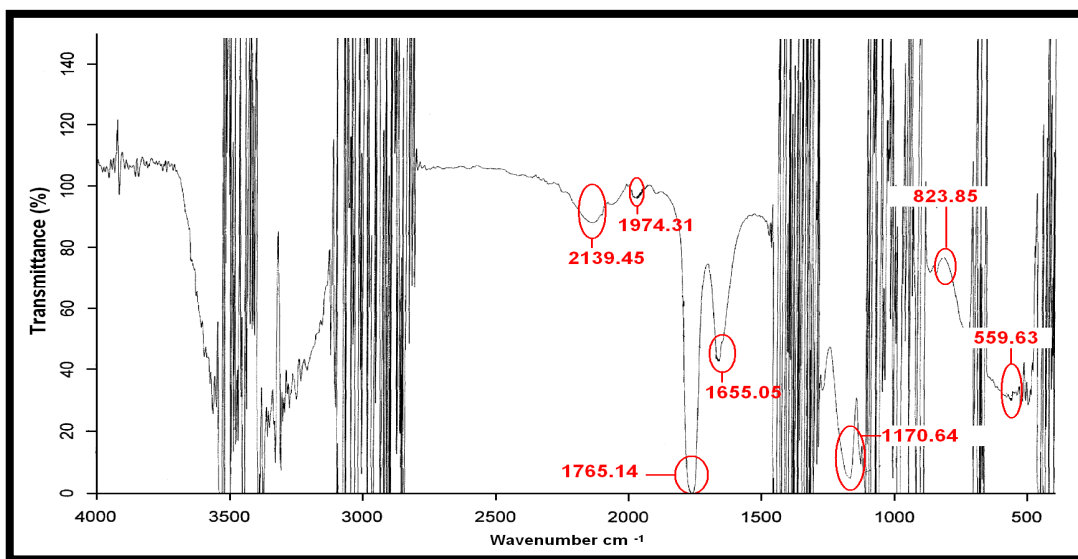


Figure 5.7: Liquid FTIR spectra for PLGA and DMSO

In Figure 5.7, the broad band in the 3200-2600 cm^{-1} region is due to the oxygen-hydrogen (O-H) stretch of the hydroxyl group. The IR spectra of carboxylic acid derivatives resulted in the formation a strong C=O stretch in the 1690-1760 cm^{-1} region (as indicated in the 1765.14 cm^{-1} band). The C-O bond occurred over the 1080-1300 cm^{-1} region (as indicated in the 1170.64 cm^{-1} band). The thiocarbonyl (C=S) and S-OR ester possessed a stretched frequency at 1050-1200 cm^{-1} and 700 and 900 cm^{-1} region respectively. These spectra are supported by the chemical reaction in Figure 5.6.

5.3.6. L-dopa-loaded PLGA nanoparticle size and stability

The L-dopa-loaded nanoparticles showed a smaller size (113nm), and zeta potential (-32.8mV) in comparison to L-dopa-free nanoparticles (175nm, 0.019 and -23mV). The reduced size of the L-dopa-loaded nanoparticles could be attributed to the disturbance of interfacial turbulence due to the presence of the L-dopa. The principles of interfacial flow and turbulence is explained by the Maragoni effect (Fessi *et al.*, 1989) in that liquids with high surface tensions will pull on their surrounding media more strongly in comparison to liquids with low surface tension. Turbulence arises from the spontaneous agitation of these liquids with different surface tensions resulting in changes in flow. The negative zeta potential may be attributed to the presence of carboxyl groups of PLGA. The use of the overhead stirrer was seen to have the potential to decrease particle size (143.2nm) in relation to the magnetic stirring, nanoparticle size (194.5nm), but also resulted in an irregular zeta potential value at 0.072mV. The addition of PVA under magnetic stirring did not produce favourable results on particle size (213.2nm) and zeta potential (-14.5mV). It however stabilized the irregular zeta potential values that resulted from the use of the overhead stirrer. The irregularities that occurred in particle size range was due to the surfactant that suppressed interfacial flow, which is a crucial stage in the nano precipitation method. The effect of varying needle gauge size had no significant effect on nanoparticle size, distribution and zeta potential.

5.4. Investigation of NT-loaded CAP Nanoparticles

5.4.1. Material and Methods

5.4.1.1. Materials

Cellulose acetate phthalate (CAP) ($M_w=49,000\text{g/mol}$), poly(vinyl alcohol) (PVA), acetone, methanol and NT ((-)-1-Methyl-2-(3-pyridyl)pyrrolidine) ($M_w=162.23\text{g/mol}$) (NT) were all purchased from Sigma Aldrich (St. Louise, MO, USA). All other reagents were of analytical grade and used as purchased.

5.4.2. Preparation of NT-loaded CAP nanoparticles

NT-loaded nanoparticles were prepared using an adapted emulsification–diffusion technique, previously reported (Piñón-Segundo *et al.*, 1996). Briefly, 500mg of CAP and 50mg NT were dissolved in acetone and methanol (3:7 mixture), to which, a 1%^{w/v} PVA solution was added. The solution was agitated for 30min using a magnetic stirrer (Fried Electric, Haifa, Israel) set at 700rpm. A submicronized oil in water emulsion was spontaneously formed due to immediate reduction of the interfacial tension with rapid diffusion of organic solvent into the aqueous phase representative of the Marangoni Effect (Poletto *et al.*, 2008). Excess solvent was evaporated from the suspension using a Rotavap (Rotavapor[®] R210, Switzerland) at 60°C for 1hr and the resulting solution was centrifuged (Optima[®] LE-80K, Beckman, USA) at 20,000rpm for 20min. The sediment layer containing nanoparticles was removed and lyophilized for 24hr hours at 25mtorr to obtain a free-flowing powder.

5.4.3. Determination of NT entrapment efficiency of CAP nanoparticles

A calibration curve for NT was determined using a known series of concentrations of NT in PBS pH 6.8. In order to assess the entrapment efficiency of NT within the CAP nanoparticles, post-lyophilized powdered samples were accurately weighed and completely dissolved in PBS (pH 6.8; 37°C). The L-dopa content was analyzed by UV spectrophotometry at $\lambda_{269\text{nm}}$ (Hewlett Packard 8453 Spectrophotometer, Germany) and computed from a standard linear curve of DA in PBS (pH 6.8; 37°C) ($R^2=0.99$). Chapter 3, Equation 3.3 of this dissertation was utilized to compute the Drug Entrapment Efficiency (DEE).

5.4.4. *In vitro* NT release studies from CAP nanoparticles

In vitro release studies were performed on the NT-loaded nanoparticles utilizing a shaking incubator (Labex, Stuart SBS40[®], Gauteng, South Africa) set at 20rpm. The NT-loaded nanoparticles were immersed separately in 100mL PBS (pH 6.8, 37°C) contained in 150mL glass jars. At predetermine time intervals 3mL samples of each release media were removed, filtered through a 0.22µm Cameo Acetate membrane filter (Millipore Co., Bedford, MA, USA) and centrifuged at 20,000rpm (Redhead *et al.*, 2001). The supernatant was then removed and analyzed by UV spectroscopy at a maximum wavelength of λ_{269nm} for NT content analysis. NT release was quantified using a linear standard curve ($R^2=0.99$). An equal volume of NT-free PBS was replaced into the release media to maintain sink conditions.

5.4.5. Morphological characterization of the NT-loaded CAP nanoparticles

Morphological characterization of the nanoparticles revealed the shape, surface, structure and size homogeneity and possible degree of aggregation. Surface morphology was characterized by Scanning Electron Microscopy (SEM), (JEOL, JEM 840, Tokyo Japan). Photomicrographs were taken at different magnifications and samples were prepared after sputter-coating with carbon or gold (N=10). Nanoparticle size and shape was further explored using cryo-Transmission Electron Microscopy (TEM) (JEOL 1200 EX, Tokyo, Japan, 120keV) for higher definition and resolution. Samples were prepared by placing a dispersion of nanoparticles in ethanol on a copper grid with a perforated carbon film followed by evaporation and viewing at room temperature (N=10).

5.4.6. Determination of size and zeta potential of NT-loaded CAP nanoparticles

The nanoparticle zeta potential measurements were obtained using a Zetasizer Nano ZS (Malvern Instruments Ltd, Malvern, Worcestershire, UK). Each sample (1%^{w/v}) was appropriately diluted with deionised water, filtered (0.22µm filter Millipore Co., Massachusetts, USA) to maintain the number of counts per second in the region of 600 (Layre *et al.*, 2006) and placed into disposal cuvettes (size) or capillary cells (zeta potential) (Malvern Instruments Ltd, Malvern, Worcestershire, UK). The viscosity and refractive index of the continuous phase were set to those specific to deionized water. Measurements were taken in triplicate with multiple iterations for each run in order to elute size intensity and zeta potential distribution profiles.

5.5. Results and Discussion

5.5.1. Calibration curve for NT in PBS (pH 6.8; 37°C) for the determination of the concentration of NT in CAP nanoparticles

Figure 5.8 displays a calibration curve obtained for NT in PBS (pH 6.8; 37°C) employing a UV spectrophotometry at λ_{269} (Hewlett Packard 8453 Spectrophotometer, Germany).

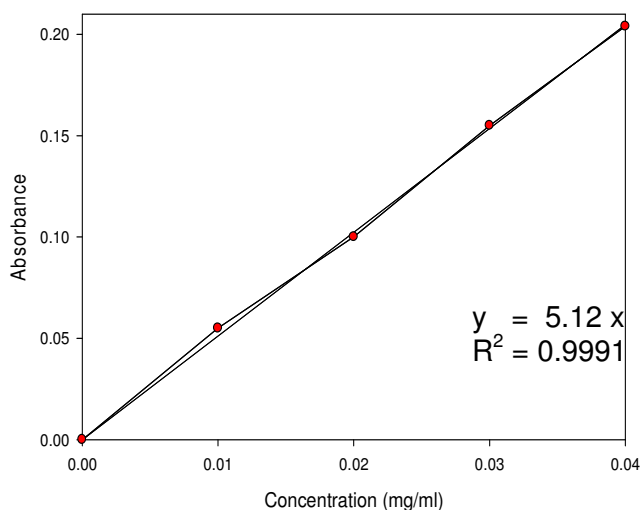


Figure 5.8: NT calibration curve at 269 in PBS (pH 6.8; 37°C)

Series concentrations of NT were made up ranging from 0.01mL to 0.04mL. A calibration curve for NT was constructed (Figure 5.7) and employed for the determination of DEE%.

5.5.2. NT entrapment efficiency of CAP nanoparticles

The DEE was calculated at $58\% \pm 2.47$, this was much lower in comparison to the other nanosystems formulated in this study. This may be attributed to the water solubility of NT (50mg/100mL) being lower than that of DA (100mg/mL), causing the NT to diffuse into the organic phase thereby decreasing the DEE.

5.5.3. *In vitro* NT release from CAP nanoparticles

Figure 5.9 illustrates the *in vitro* release profile of NT from the CAP nanoparticles over a 25hr period.

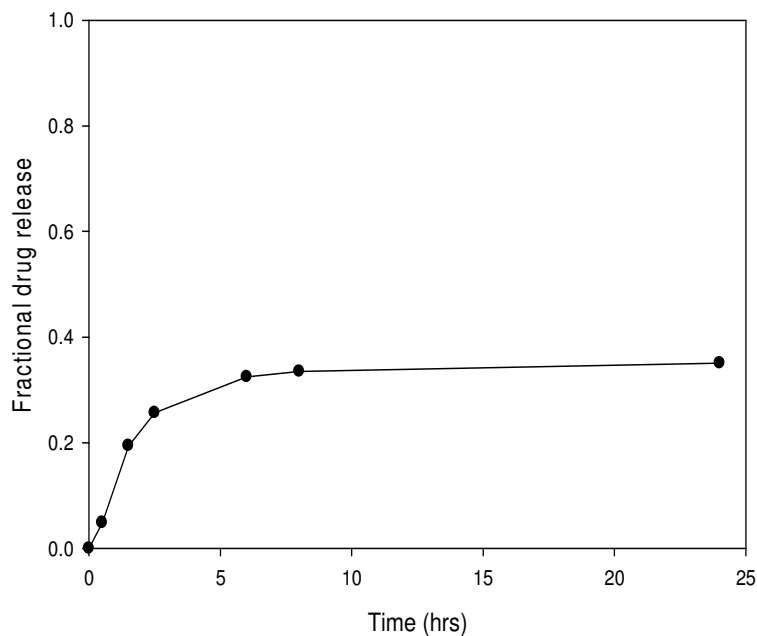


Figure 5.9: Profile of NT release from CAP nanoparticles ($SD \leq 0.01$) in PBS (pH 6.8; 37°C)

The release profiles for NT further confirmed the decreased solubility of NT in PBS (pH 6.8; 37°C). The drug delivery system showed enhanced control release of NT (0.415% release in 24hr) as the phenomenon of NT release was regulated by dissolution of the polymer and thereafter NT. This process occurred at a slower rate due to poor solubility of NT in an aqueous environment.

5.5.4. Surface morphology of NT-loaded CAP nanoparticles

Figure 5.10 is a microscopic image that displays the morphology and sizes of NT-loaded CAP nanoparticles formulated in an adopted emulsification-diffusion approach

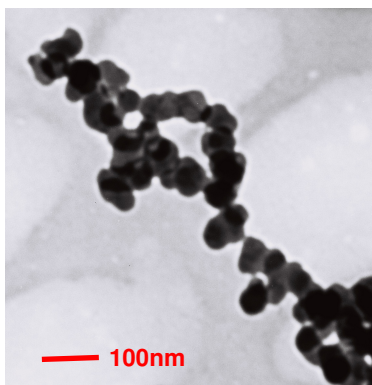


Figure 5.10: TEM image of NT-loaded CAP nanoparticles

TEM images (Figure 5.10) of NT-loaded CAP formulations revealed uniform spherical shaped NT-loaded CAP nanoparticles with a size range of 25-100nm and embedded NT particles with a size range of 2-20nm within their structure. A helical arrangement/ association was present in the images and this instability was further confirmed by the undesirable zeta potential.

5.5.5. NT-loaded CAP nanoparticle size and zeta potential

Results revealed a particle size of 172nm, this shows that while the particle size was in the desirable range (<200nm), the variation in size (Pdl value) was significantly high. The zeta potential profile for NT was erratic displaying two peaks in the distribution curves with a value of -15.4mV revealing that the formulation did not display suitable stability. The method employed for the formulation of NT nanoparticles was not reproducible in that there was an absence in uniformity of particle size which could be attributed to the low zeta potential that may have caused the particles to agglomerate resulting in a variation in particle size.

5.6. Investigation of DA-loaded Polymeric Nanofibers

5.6.1. Materials and Methods

5.6.1.1. Materials

Cellulose acetate phthalate (CAP) ($M_w=2534.12\text{g/mol}$), poly(vinyl alcohol) (PVA) ($M_w=49,000\text{g/mol}$), acetone, methanol and dopamine hydrochloride (DA) ($M_w=189.64\text{g/mol}$) were all purchased from Sigma Aldrich (St. Louise, MO, USA). Deionized water was obtained from a Milli-Q water purification system (Milli-Q, Millipore, Billerica, MA, USA). All other reagents were of analytical grade and used as purchased.

5.6.2. Preparation of DA-loaded polymeric nanofibers

DA (0.9g) was added to a PVA solution (9%^{w/v}) and a CAP in acetone solution (0.16%^{w/v}) and agitated for 15min @50°C using a magnetic stirrer (Fried Electric, Haifa, Israel) to produce DA-loaded PVA and DA-loaded CAP nanofibers respectively. Polymeric solutions (1mL), DA-free and DA-loaded, were placed into 5mL pipettes and secured to a custom-built electrospinning device equipped with a voltmeter. The voltage was increased at 0.5Kv/sec until the Taylor Cone was visible and allowed for the spinning of fibers which were collected on an aluminum screen for analysis. The voltage was set at 12kV at a distance of 3cm and 14Kv at a distance of 1cm, from the pipette stand to the aluminium screen, for the DA-loaded PVA and DA-loaded CAP nanofibers respectively. DA-free polymeric nanofibers were formed in a similar manner.

5.6.3. Determination of DA entrapment efficiency of polymeric nanofibers

In order to assess the entrapment efficiency of DA within the CAP and PVA nanofibers, electrospun samples were accurately weighed and completely dissolved in PBS (pH 6.8; 37°C). The DA content was analyzed by UV spectrophotometry at $\lambda_{280\text{nm}}$ (Hewlett Packard 8453 Spectrophotometer, Germany) and computed from a standard linear curve of DA in PBS (pH 6.8; 37°C) ($R^2=0.99$). Chapter 3, Equation 3.3 of this dissertation was utilized to compute the Drug Entrapment Efficiency (DEE).

5.6.4. Morphological characterization of DA-loaded polymeric nanofibers

Morphological characterization of the nanofibers revealed the shape, surface, structure and size homogeneity and possible degree of aggregation. Surface morphology was characterized by Scanning Electron Microscopy (SEM), (JEOL, JEM 840, Tokyo Japan). Photomicrographs were taken at different magnifications and samples were prepared after sputter-coating with carbon or gold (N=10). Nanofiber size and shape was further explored

using cryo-Transmission Electron Microscopy (TEM) (JEOL 1200 EX, Tokyo, Japan, 120keV) for higher definition and resolution. Samples were prepared by placing a dispersion of nanofibers in ethanol on a copper grid with a perforated carbon film followed by evaporation and viewing at room temperature (N=10).

5.7. Results and Discussion

5.7.1. DA entrapment efficiency of polymeric nanofibers

DEE was calculated as $85\% \pm 3.63$ and $78\% \pm 2.60$ for the DA-loaded PVA and CAP nanofibers respectively. This result proved that DA had a greater likelihood to be entrapped into the PVA fibers due to its hydrophilic nature.

5.7.2. Size and morphology of DA-loaded polymeric nanofibers

Figures 5.11-5.13 are microscopic images that display the morphology and sizes of DA-loaded PVA and CAP nanofibers formulated in an employing an electrospinning technique.

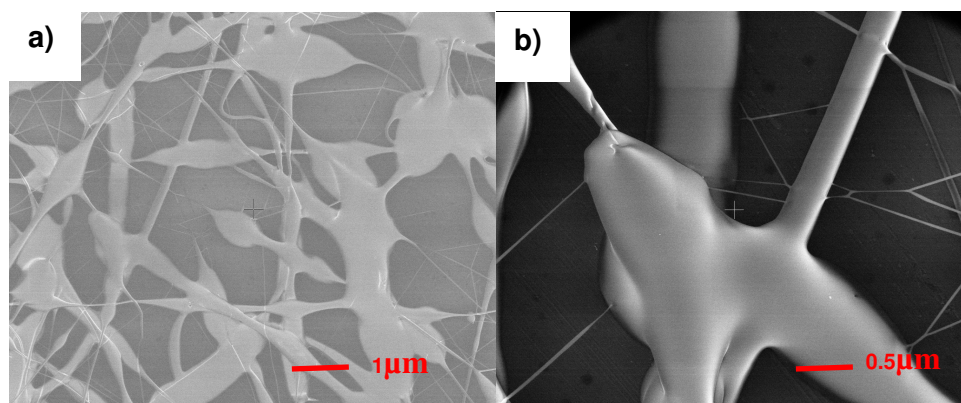


Figure 5.11: SEM images of (a) DA-loaded PVA nanofibers revealed longitudinal solid fibers with a minimal length of $20\mu\text{m}$ and (b) DA-loaded CAP nanofibers showed artifacts in the structure

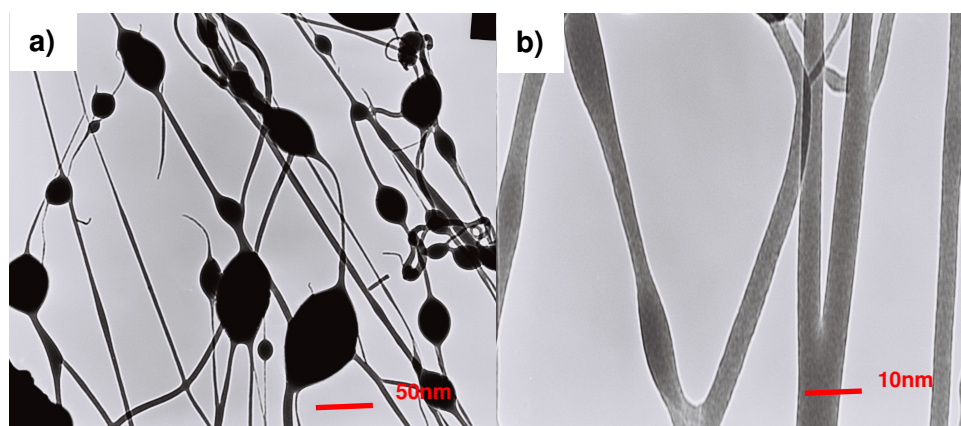


Figure 5.12: TEM images of DA-loaded PVA nanofibers (a) displaying an uneven distribution of PVA and DA along its length and (b) a closer look showed fibers of minimal diameters of 5nm

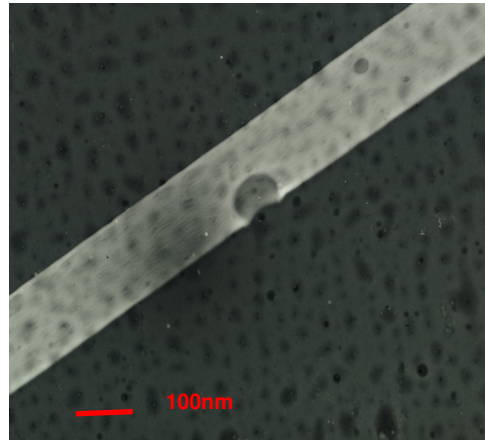


Figure 5.13: TEM image of DA-loaded CAP nanofibers revealed a diameter of $1.5\mu\text{m}$

SEM and TEM images indicated a larger diameter in the DA-loaded CAP (Figure 5.11b and Figure 5.13) nanofibers in comparison to the DA-loaded PVA nanofibers (Figure 5.11a and Figure 5.12) this could possibly be due to the presence of an ideal voltage in the DA-loaded PVA formulation that lead to an increased elongation of nanofibers. The employment of a highly volatile organic solvent (acetone) which resulted in the rapid evaporation of the acetone and the clumping of the polymeric material thereby increasing diameter. Despite the evaporation of the acetone, TEM images of DA-loaded CAP nanofibers (Figure 5.13) showed a greater degree of uniformity in structure in comparison to DA-loaded PVA nanofibers (Figure 5.12a and b) which showed an uneven distribution of mass along its length, this could be due to the continuous replacement of the DA-loaded CAP solution that took place in formulation.

5.8. Concluding Remarks

L-dopa-loaded PLGA nanoparticles were formulated employing an adopted nanoprecipitation method overcoming difficulties such as limited solubility of the L-dopa. NanoZS analysis disclosed particles, formulated under different processing techniques, of 113-213.2nm. FTIR, both solid and liquid, was conducted on the formulations that showed the various reactions that took place at the time of formulation. DEE was calculated as 61.244% as a result of the L-dopa affinity to the solvents modified in the development of the methodology of the system. TEM images sought to identify the aggregation of the particles with high yields. *In vitro* L-dopa release from the PLGA nanoparticles and NESD again proved that the scaffold provided the foundation for controlled delivery of L-dopa.

NT-loaded CAP nanoparticle formulations showed a decrease in DEE% in comparison to the other nanosystems evaluated. The particles displayed promising particle sizes however zeta size profiles and TEM images revealed aggregation and thereby instability of these formulations.

Electrospinning technology was employed in the formation of DA-loaded PVA and CAP nanofibers of minute diameters and smooth morphologies (indicated from SEM/TEM images). DEE was noted as 85% and 78% for DA-loaded PVA and CAP fibers respectively. The novel approach and ideal properties of these fibers showed great promise for their prospective employment in drug delivery systems however issues such as instability and low yield need to be addressed.

Overall, the results for all formulations showed that the methodology requires further optimization prior to its evaluation in the *in vivo* environment however the drug delivery system showed potential for the employment as an alternative treatment for various diseases.

CHAPTER 6

CYTOTOXIC EVALUATION OF NANO-ENABLED SCAFFOLD DEVICE ON CARCINOMIC BRAIN AND FRESHLY ISOLATED, HEALTHY WHITE BLOOD CELLS

6.1. Introduction

Cytotoxicity is a measure of the degree to which a compound is toxic to cells, possibly resulting in cell death. *In vitro* cytotoxic testing methods include the 3-(4,5-dimethylthiazol-2-yl)-2,5-diphenyltetrazolium bromide (MTT), trypan blue (TB), sulforhodamine B (SRB) and (4-[3-(2-methoxy-4-nitrophenyl)-2-(4-nitrophenyl)-2H-5-tetrazolio]-1,3-benzene disulfonate sodium salt) (WST) assays and clonogenic assays (Matsuoka *et al.*, 2000). These tests are vital in the research and development process and, within the context of the current study, allows for cytotoxicity levels to be evaluated prior to *in vivo* studies.

The nigrostriatal depletion of dopaminergic neurons that defines PD results in the augmentation of DA to rectify the neurotransmitter imbalance (Lai and Yu, 1997). An increase in DA concentration leads to an escalation in the production of hydrogen peroxide and thereby apoptotic events. Exogenous treatment for PD (L-dopa and DA) has been postulated to exacerbate the degeneration present in this condition (Lai and Yu, 1997) as explained in Chapter 2 in this dissertation.

DA, both endogenous and exogenous, is highly neurotoxic in a dose-dependent manner (Stokes *et al.*, 1999). The metabolism of DA results in the production of reactive oxygen species which causes cytotoxicity in cells (Stokes *et al.*, 1999). DA-induced apoptosis has been identified in chick embryonic sympathetic nerve cells (Ziv *et al.*, 1994) at high concentrations (100-300 μ M) after a 24hr exposure period, and rat neuronal cells (Walkinshaw and Waters, 1995). *In vivo* studies in rats have also shown that intrastriatal DA injections (0.05-1.0 μ M) produced dose-dependent neurotoxic events such as neuronal loss and gliosis in various areas of the brain after a 24hr exposure period (Hastings *et al.*, 1996).

The auto-oxidation of DA (Figure 6.1) leads to the formation of a highly reactive quinone, a molecule that has the potential to alter cellular components such as DNA, lipids and proteins (Stokes *et al.*, 2000). The oxidation is further accelerated by the presence of metals such as copper and iron, which, in the clinical setting, is elevated in PD. Enzyme-catalysed oxidation

of DA is also responsible for quinone formation. The excess chronic production of the reactive molecule may thus have significant consequences in terms of cell viability.

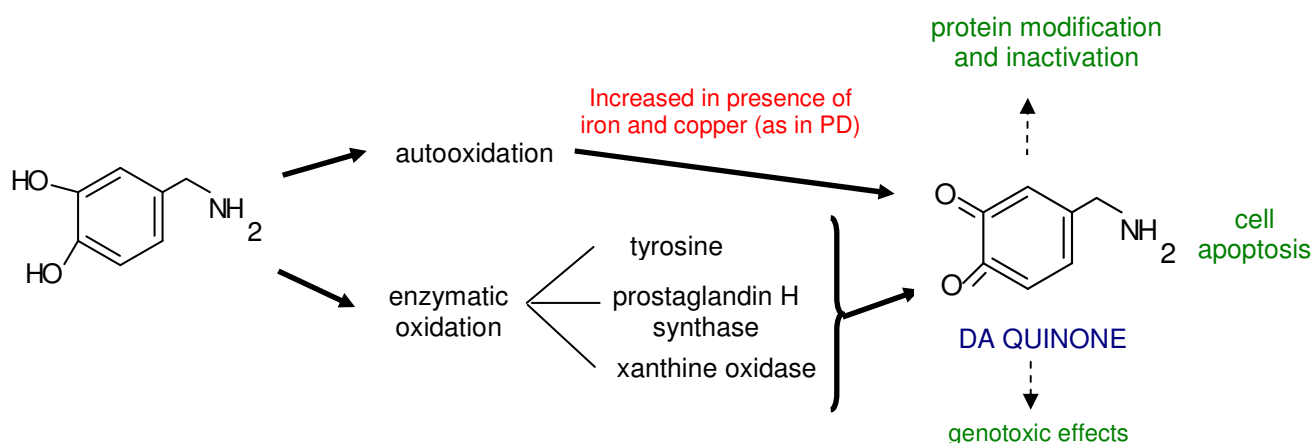


Figure 6.1: Schematic representation of one of the possible mechanisms involved in the metabolism of DA leading to cytotoxic and genotoxic events (Stokes *et al.*, 1999)

There are numerous methods used to assess the viability of cells; the 3-(4,5-dimethylthiazol-2-yl)-2,5-diphenyltetrazolium bromide (MTT) assay being one of them. The MTT assay is colorimetric in that it determines the survival and growth of cells (upon exposure to the compound, in this case) by measuring the cells ability to reduce the MTT salt (yellow) to its formazan crystal form (purple) (Freimoser *et al.*, 1999). The reduction process is indicative of the functioning of the cell's mitochondrial succinate dehydrogenase and thus indicates cell viability (Yedjou *et al.*, 2006). The reaction is outlined in Figure 6.2 as follows:

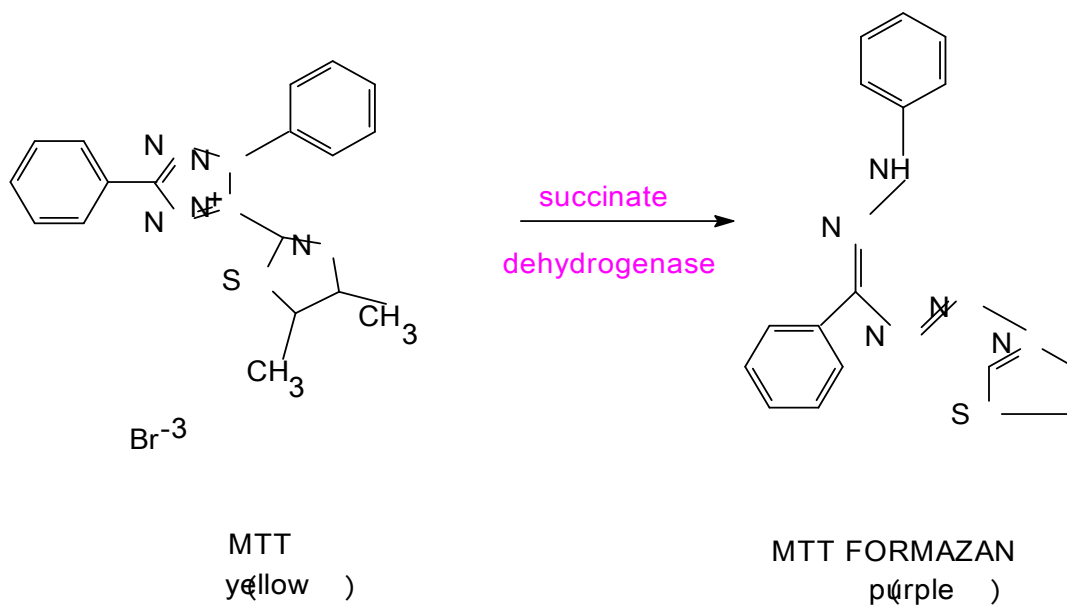


Figure 6.2: *In vivo* colorimetric reaction that occurs in living cells when exposed to MTT (Dojindo Laboratories, 2000)

At the outset, this chapter sought to address the possible cytotoxicity of the NESD and its components in carcinomic SK-N-MC as well as healthy white blood cell lines. The determination of the cytotoxic activity of these compounds allowed for the progression of the study into *in vivo* implantation of the NESD in the rat brain.

6.2. Materials and Methods

6.2.1. Routine cell culture

The SK-N-MC cells (ATCC, U.S.A.) are derived from a neuroepithelioma of human origin. The cells were routinely maintained in complete growth medium consisting of Minimum Essential medium (Eagle) with 2mM L-glutamine and Earl's Balanced Salt Solution adjusted to contain 1.5g/L sodium bicarbonate, 0.1mM non-essential amino acids and 1mM sodium pyruvate, further supplemented with 10% heat-inactivated foetal bovine serum. All products were purchased from Invitrogen (BD Bioscience, California, USA). The cells were incubated at 37°C in a humidified incubator circulated with 95% O₂ /5% CO₂ (Afrox, South Africa).

6.2.2. Isolation of white blood cells

Blood (6mL) was collected by venous puncture from healthy individuals (Human Ethics Clearance no. M070519, see Appendix of this dissertation). White blood cells (WBCs) were isolated using a Ficoll- Hypaque gradient (3:1) tube (Latimer *et al.*, 1989, US Patent 4591557). The tubes were centrifuged for 30min at 1500rpm (Sorvall T6000D, GMI Incorporated, Minnesota, USA). Upon centrifugation, blood separates according to the weights of the different components

(Figure 6.3) thereby allowing for the separation of the specific cells. The buffy coat, containing WBCs, was used in the WBCs cytotoxicity assay.

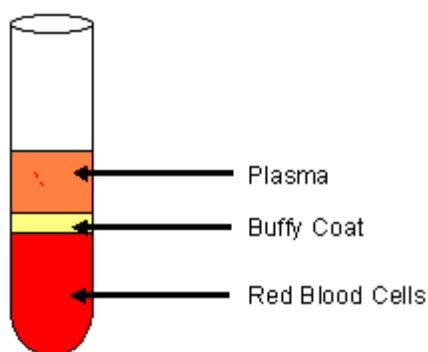


Figure 6.3: Diagrammatic representation of the separation of blood that occurs upon it's centrifugation in Ficoll- Hypaque gradient (3:1) tubes (Lifelearn Inc, 2004)

The buffy coat was removed using a pipette (1mL) and washed three times with sterile red cell lysis buffer (500µL) containing ammonium chloride (0.15M), potassium carbonate (1mM) and ethylenediaminetetraacetic acid (0.1mM). The buffy coat and red cell lysis buffer were inverted five times and thereafter placed in an incubator (HERAcell® 240 CO₂ Incubator, Thermo Scientific, USA) (5% CO₂; 37°C) for 5min. The solution was centrifuged for 10min at 5500rpm (Jouan MR1812, Scientific Products, South Africa), the supernatant removed and the process repeated until a clear solution (pure WBC) was obtained. The WBC sediment was resuspended in fresh RPMI-1640 media and counted using a hemocytometer (Neubauer 0.025mm, depth 0.1mm). WBCs were seeded into sterile 96-well plates at a density of 30000cells/well, to a final volume of 180 µL. 20µL of each treatment was added to the wells (Section 6.2.4) and incubated at 37°C for 24hr. The MTT assay was then conducted to determine cell viability.

6.2.3. Trypsinisation and cell counting / seeding of cells

The SK-N-MC cells were trypsinised using 500µL 0.25% trypsin containing 0.1% EDTA (Highveld Biologicals, SA) and incubated at 37°C for 10min. The cells were resuspended in fresh complete medium and centrifuged at 1000 rpm for 5min to pellet the cells. The cell pellet was then resuspended in ~5 mL medium. The number of cells per mL was determined using the trypan blue exclusion assay in which viable cells appear yellow, while non-viable cells stain blue. Only cell suspensions with a viability in excess of 95% were used in the assays.

Cells (180µL) were seeded into sterile 96-well plates at a density of 15 000 cells per well. Cells were incubated overnight to facilitate attachment to the wells. Thereafter, 20µL of each treatment was added to the wells as described in Chapter 6 Section 6.2.4 in this dissertation, and incubated at 37°C for 24 and 48hr. The MTT assay was then conducted to determine cell viability.

6.2.4. Exposure of cells to the different compounds

Cells were exposed to the following compounds for 24hr (WBCs) and 48hr (SK-N-MC cells):

- a) DA-free NESD (0.5mL alginate)
- b) NESD (5mg DA in 1mL of alginate)
- c) DA (3.79mg)
- d) DA-loaded CAP nanoparticles (1mg)
- e) 5'FU (260.16mg)
- f) Control (cells with medium only)

All assays were performed in triplicate.

6.2.5. Calibration of MTT assay

Cells were centrifuged at 1000rpm (Optima[®] LE-80K, Beckman, USA) for 3min. The cell pellet was resuspended in 20mL of media. 200 μ L of each dilution was added to eppendorfs, to which 50 μ L MTT (5mg/mL) was added. The samples were then incubated for 2hr at 37°C. The samples were then centrifuged at 1000rpm (Optima[®] LE-80K, Beckman, USA) for 5min and the supernatant removed. The cell pellet was resuspended in 200 μ L DMSO and the absorbance was measured at 540nm with a microplate reader (Absorbance Labsystems Multiskan MS Version 2.4). Equation 6.1 was used to determine the number of viable cells in each sample.

$$\% \text{ cell viability} = [\text{no of viable treated cells}] / [\text{no of viable control cells}] \times 100\% \quad \text{Equation 6.1}$$

6.2.6. The MTT assay

The WBCs and SK-N-MC cells were each treated with compounds (20 μ L) as shown in Figure 6.4.

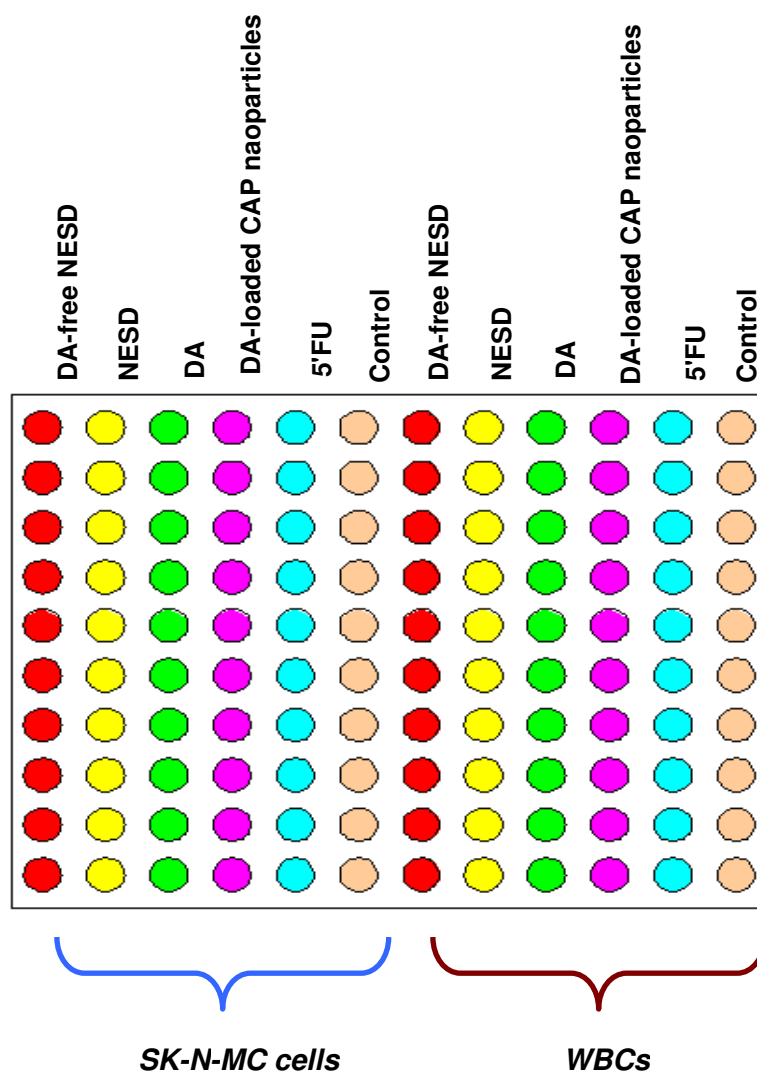


Figure 6.4: A schematic representation of the layout of the compounds in the 96-well plate as used in the MTT assays on WBCs and SK-N-MC cells

After the incubation period, 50 μ L MTT was added to each well. The plates were incubated at 37°C for 2hr. Thereafter, the plates were centrifuged at 3000rpm for 10min and the supernatant removed. Formazan crystals were dissolved in 200 μ L DMSO, and the absorbance read at 540nm using a microplate reader (Absorbance Labsystems Multiskan MS Version 2.4)

6.2.7. Preparation of MTT solution

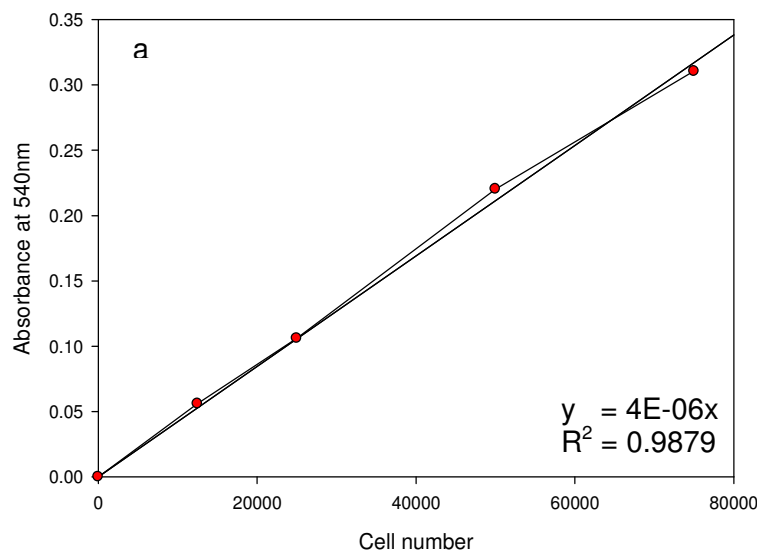
MTT (0.5%^{w/v}) was prepared as per United Scientific Protocol (USA). MTT (5g), obtained from Sigma (Johannesburg, South Africa), was dissolved in 1000mL PBS (pH 7.4). The solution was filter-sterilised using a 0.22µm Cameo acetate membrane filter (Millipore Co., Bedford, Massachusetts) and stored in the dark at 4°C until use.

6.3 Results and Discussion

6.3.1. Calibration curve of post-MTT exposure for the determination of the number of viable cells present in the media

All experiments were conducted in triplicate and the results represented as mean ± standard error (SE). The statistical significance of all treatments were evaluated using the GraphPad Prism3 Instat package, using ANOVA, Student-Newman-Keuls test. A probability limit of $p < 0.05$ was considered to be significant.

The calibration curve obtained for both WBC and SK-N-MC cells (Figure 6.5a and b, respectively) showed a linear correlation ($R^2 = 0.99$). This means that the resultant absorbance obtained at 540nm is directly proportional to the number of viable cells present in each well. The absorbance readings were thus used to calculate the number of viable cells present in the wells after the respective exposures to the different compounds.



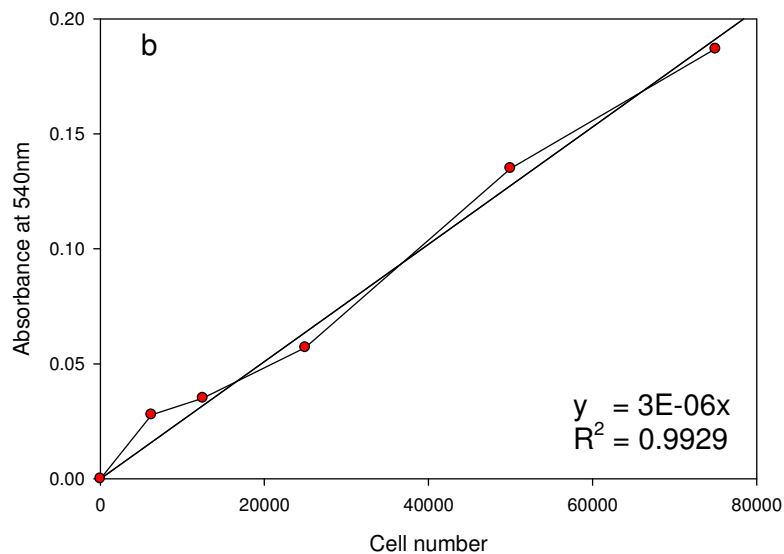


Figure 6.5: MTT calibration curve for (a) WBCs and (b) SK-N-MC cells

6.3.2. Cytotoxicity to WBCs

DA-free and DA-loaded NESD reduced cell viability to 70-80% (Figure 6.6). The DA-loaded CAP nanoparticles did not adversely affect cell viability as $\pm 100\%$ cell viability was noted, while DA appeared to have increased the number of cells by approximately $\pm 15\%$. It was noted that the DA and DA-loaded CAP nanoparticles showed similar cell viability profiles proving that the inclusion of CAP into the formulation did not have a detrimental effect of cell growth. Once again, 5'FU showed a cytotoxic effect (50% cell growth) on the WBCs confirming its purpose in the study as a positive control.

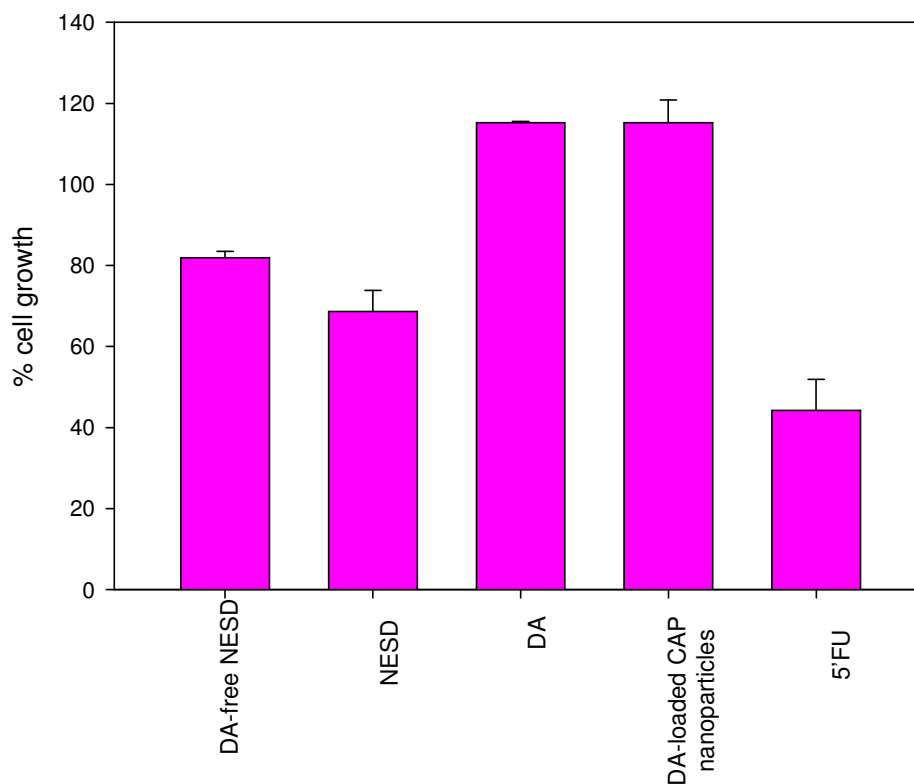


Figure 6.6: Graph displaying percentage cell viability of WBCs after a 24hr exposure period to the various compounds. Cell viability is reported in relation to the control cell sample which was equated to 100%.

6.3.3. Cytotoxicity directed against the carcinomic SK-N-MC cells

After a 24hr incubation period (Figure 6.6), the DA-loaded and DA-free NESD significantly ($p < 0.05$) reduced the viability of the SK-N-MC cells ($\pm 25\%$ viability). This decrease was also significantly ($p < 0.05$) greater than the exposure to 5'-FU. DA did not adversely affect cell viability, as 100% viability was noted, while the DA-loaded CAP nanoparticles only reduced cell viability to $\pm 75\%$.

After 48hr (Figure 6.7), cell viability of the DA-free and DA-loaded particles did not differ significantly ($p > 0.05$ for both) from the results obtained after the 24hr exposure period, while a significant reduction in cell viability was noted after 48hr exposure to the DA-loaded CAP nanoparticles ($p < 0.05$). This is also seen for the 5'-FU-treated cells. DA did not significantly reduce cell viability after 48 hr.

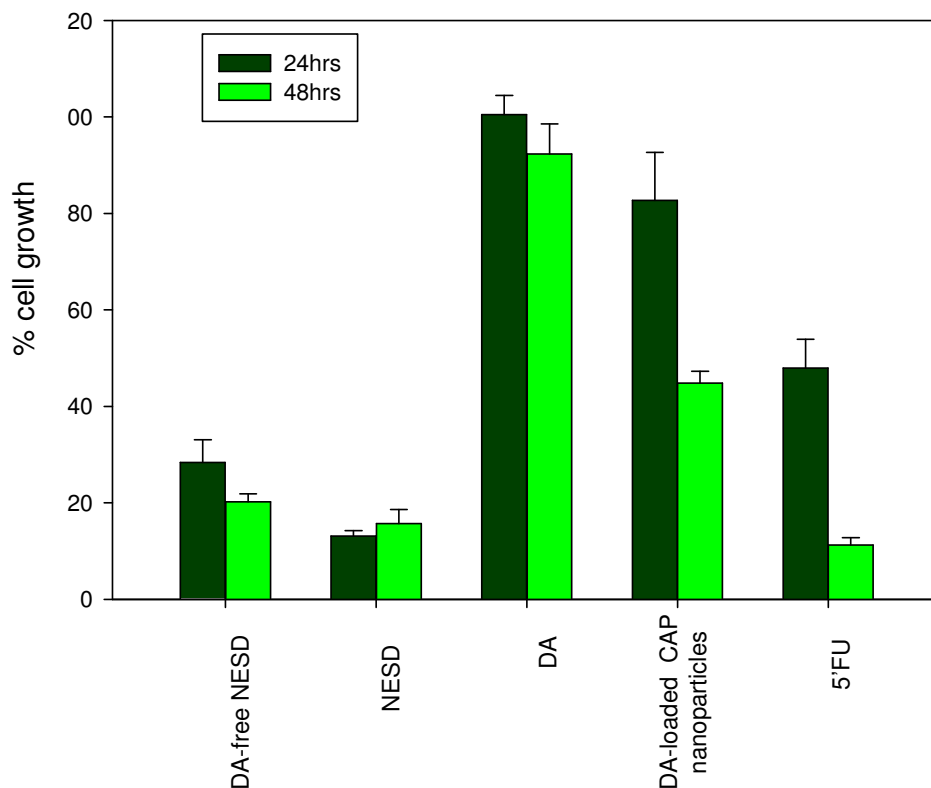


Figure 6.7: Graphs displaying percentage cell viability of SK-N-MC cells after exposure periods to the various compounds. Cell viability is reported in relation to the control cells which was equated to 100%.

6.3.4. Limitations for the employment of MTT assay in the present study

The following effects could have interfered with the MTT assay and resulted in erroneous results:

- The colour of the media discoloured upon addition of the DA-loaded CAP nanoparticles and thus was noted to have lowered the pH of the media. Attempts to change the solvent for this sample failed to cause dissolution of the particles.
- Upon its addition to the media, the NESD matrix absorbed some of the media.
- The NESD size may have hindered growth of the cells competing with the cells for space by occupying the majority of the space within the plates and thereby space for the cells to grow.
- Some of the MTT was absorbed onto the NESD, thereby preventing interaction with the mitochondria in the viable cells.

6.4. Concluding Remarks

This chapter sought to address the possible cytotoxic effects of the NESD on WBCs and human carcinomic SK-N-MC cells. The use of the colorimetric MTT assay allowed for the determination of cell growth upon exposure to the treatment compounds. Results for the assays on the WBCs and SK-N-MC cells revealed that DA-free and DA-loaded NESD were the most cytotoxic to the cells. It was later established that these results could be attributed to the absorptive nature of the NESD, causing them to soak up the cell media, thereby hindering cell growth. In earlier studies, (Weingarten and Zhou, 2001; Lai and Yu, 1999, Clement *et al.*, 2002) DA had been reported to be cytotoxic to cells at higher doses (mM). In the present study, the concentrations of DA employed were much lower (nM) and so could have attributed to the growth of both carcinomic and healthy cells. DA-loaded CAP nanoparticles were confirmed to be detrimental to carcinomic cell growth with an increase in the exposure duration whereas results from the healthy WBC study showed that DA-loaded CAP nanoparticles promoted cell growth. The DA-loaded CAP nanoparticles may have a selective anti-cancer effect on the cells. Overall, results for the MTT assays on both carcinomic WBCs and SK-N-MC cells revealed that the NESD does not display any noteworthy unfavorable effects on cell survival and growth.

CHAPTER 7
IN VIVO EVALUATION OF THE NANO-ENABLED SCAFFOLD DEVICE UPON
IMPLANTATION INTO THE PARENCHYMA OF THE FRONTAL LOBE OF THE RAT
BRAIN

7.1. Introduction

Animal models are an invaluable tool in experimental medical science because they enable one to study the pathogenetic mechanisms and thereby the possible therapeutic strategies of human diseases. Once the causative mechanism is understood, PD does not naturally occur in animals however scientists have found neurotoxins that sufficiently mimic the disease (Gerlach, 1996).

Mice have become the most established animal model for research into PD however there are several drawbacks in the lack of anatomical similarity between the mouse model and humans. For this reason, the monkey model has received much favor in that the anatomical structures present within the animal are most similar to that of the human. However, tremendous ethical constraints limit the use of the monkey model in *in vivo* drug studies (Halbach, 2005). The Sprague-Dawley rat model was selected for use in this study. The rat model held the advantage of greater brain volume for implantation of the NESD than the mouse model.

7.1.1. Biocompatibility of implantable devices

"The ability of a material to perform with an appropriate host response in a specific application" (Williams, 1999). The interest in biocompatible polymeric devices for implantation into the body has gained a surge of interest in the fields of orthopedics, cardiovascular and ophthalmics to name a few (Katz, 2001). The concept of biocompatibility is further explained in Figure 7.1.

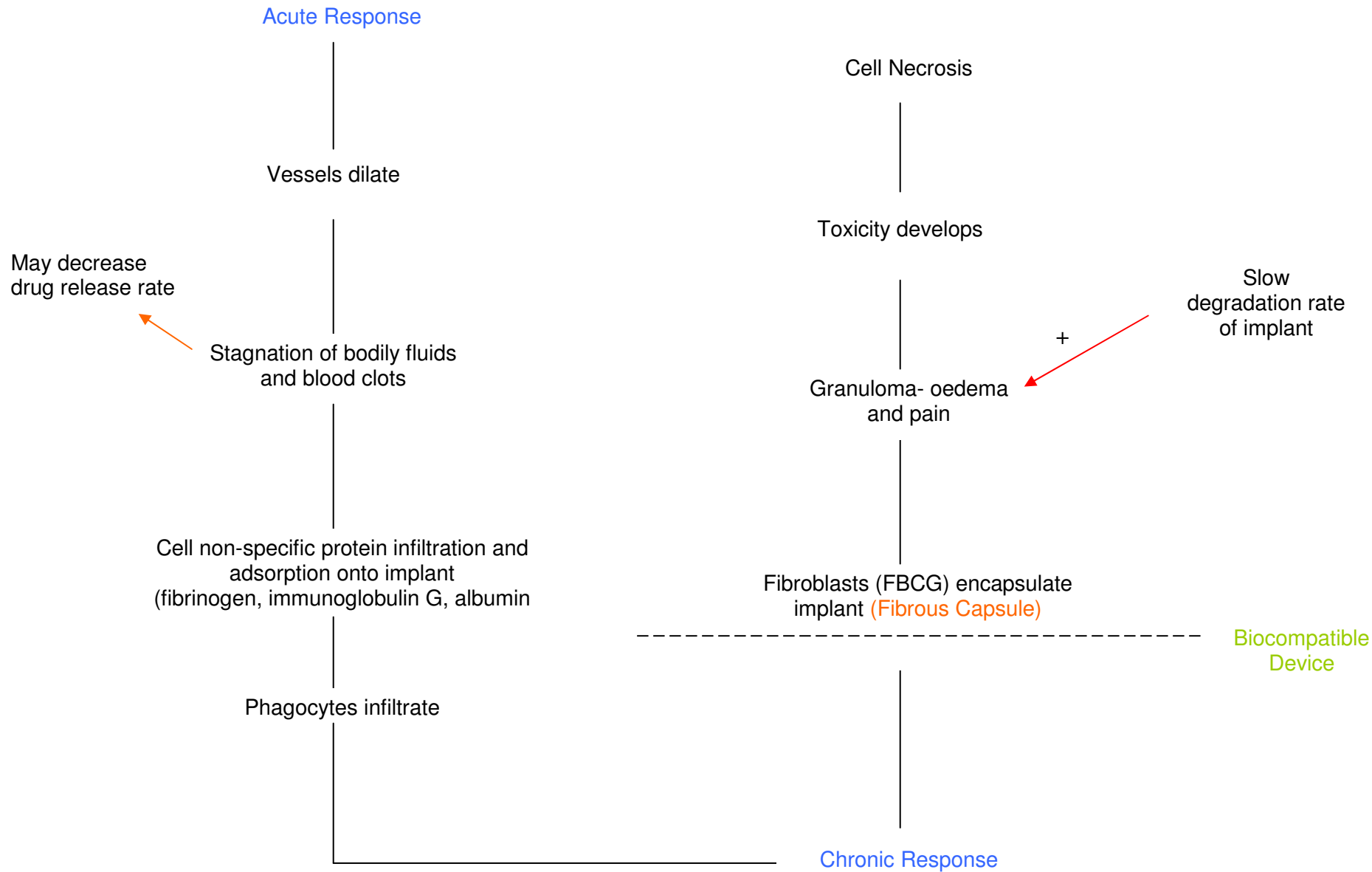


Figure 7.1: Schematic diagrammatic representation of immunological response to implant within the CNS (adapted Fournier et al., 2003; Polikov et al., 2005)

This chapter sought to develop a protocol for the surgical implantation of the NESD into the Sprague-Dawley rat brain model. Furthermore, issues of biocompatibility and bioerosion of the device were addressed while the elucidation of its *in vivo* drug release profile formed the crux of this chapter.

7.2. Materials and Methods

7.2.1. Materials

Solvents used for UPLC–MS/MS measurements were of UPLC grade, and all other reagents were of analytical grade. Double deionized water was obtained from a Milli-Q system, (Milli-Q, Millipore, Johannesburg). Oases HLB were provided by Waters (Milford, MA, USA). Control blank rat plasma was supplied by healthy donors. Ammonium acetate ($M_w=77.08\text{g/mol}$), acetic acid (CH_3COOH) ($M_w=60.05\text{g/mol}$), sodium hydroxide ($M_w=40.00\text{g/mol}$), dopamine hydrochloride (DA) ($M_w=189.64\text{g/mol}$) theophylline ($M_w=180.17\text{g/mol}$) from Sigma Aldrich (St. Louise, MO, USA). Healthy adult Sprague Dawley rats were used for the *in vivo* release study

7.2.2. Technology Applied in the Present Study

7.2.2.1.. Waters® Acquity Ultra Liquid Performance Chromatography™ (UPLC)

The UPLC allows for samples to be run with the shortest run time, highest sensitivity, but without compromising the selectivity of the assay (Dongre *et al.*, 2008). Typically, UPLC refers to applications using porous sub-2 μm particles at high linear velocities (Waters supplies catalogue, 2008). UPLC parameters such as pH, flow rate, column type, and buffer concentration can be optimized to achieve the best sensitivity, peak shape and selectivity (Everley and Croley 2008). The UPLC allows for the identification of various compounds and the determination of their concentrations. Its application is with compounds that are non-volatile in comparison to their mobile phase at the time of analysis. The concentration of the compounds is calculated by means of Beer-Lamberts Law:

$$A = \epsilon bc$$

Equation 7.1

Where A is the absorbance (calculated for each diode of the system) of the sample measured, ϵ is the molar absorptivity of the sample, b is the pathlength of the cuvette (1cm) and c is the concentration of the sample in moles per liter.

7.2.2.2. Evaporative Light Scattering (ELS) Detector

The UPLC is coupled with an ELS detector which is responsible for the qualitative and quantitative analysis of drug loaded samples.

The process ELS detection has three stages:

- *Nebulization*: the effluent is transformed into a fine aerosol using nitrogen as a carrier gas;
- *Desolvation*: the mobile phase is evaporated and condensed thereafter moving to the detector phase. The mobile phase should have a low viscosity and high volatility so as to increase the rate of evaporation thereby increasing the quality of the sample; and
- *Detection*: the light source is exposed onto the particles, the particle size determines the intensity measured.

The detector may be further coupled with a mass spectrophotometer or absorbance detector to assess the quality of the samples and ensure that all compounds present are identified.

7.2.3.. Development of Methodology for the Surgical Implantation of the NESD into the Parenchyma of the Frontal Lobe of the Sprague-Dawley Rat Brain

7.2.3.1. Pre-surgical preparation of rats

Healthy male Sprague–Dawley rats (350±20g) were employed in this pilot study (Figure 7.2.). Rats were housed in cages, maintained under a 12hr light/dark cycle, fed a commercial diet, and given water *ad libitum*.

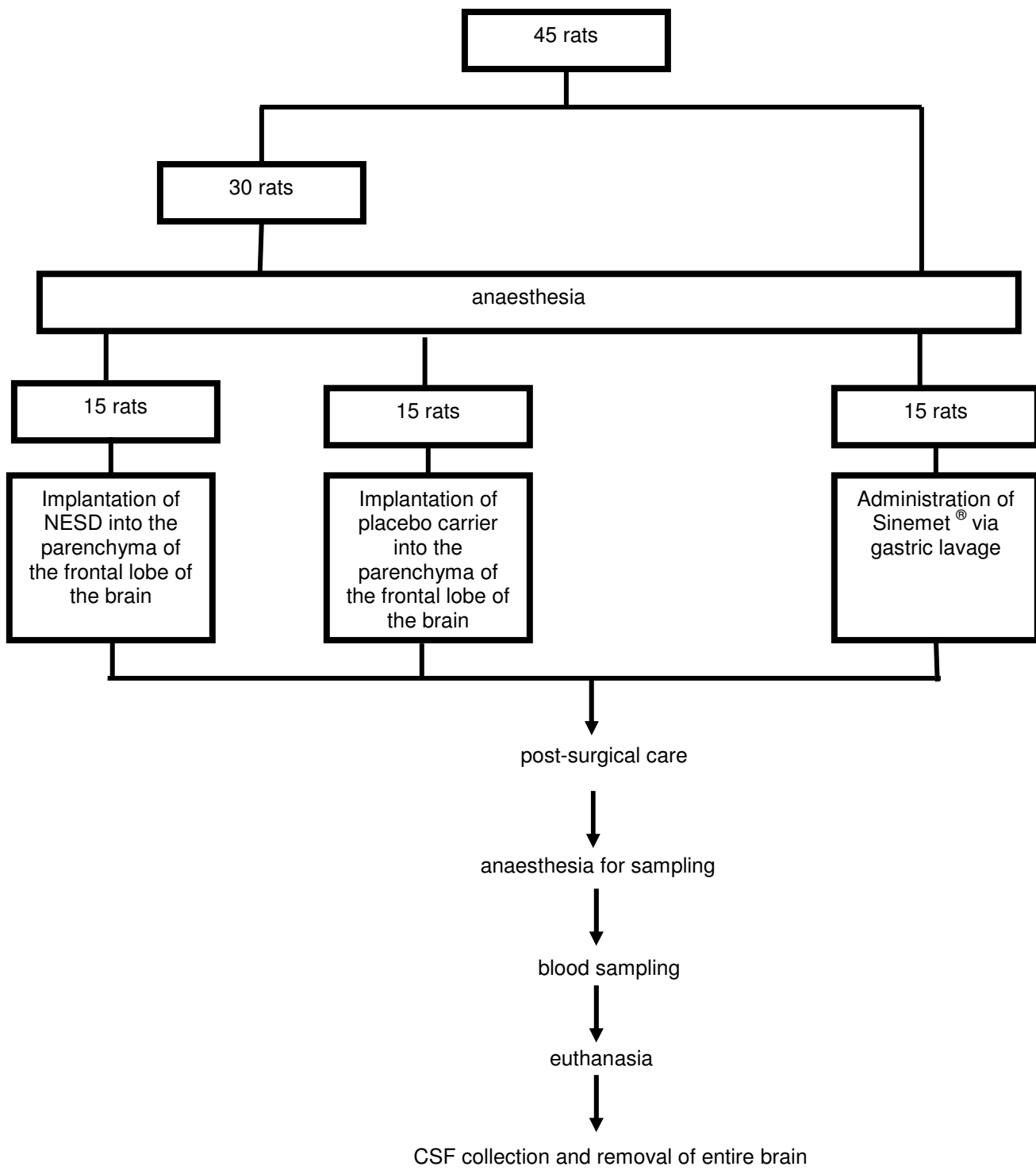


Figure 7.2: Schematic diagram representing the number of rats required for in vivo studies

Note: Rats had undergone surgical implantation with device at day 0. Sampling had taken place on days 3, 7, 14, 21 and 30 followed by euthanasia (n = 3).

7.2.3.2. Pilot surgical technique for implantation of the NESD into parenchyma of the frontal lobe of the rat brain

Animal Ethics no. 2007/76/4 (see Appendix of this dissertation). The technique for the insertion is analogous to the technique used for the insertion of an intracranial pressure monitor in the human subject. The rat was anaesthetized for the duration of the procedure which was performed in an aseptic manner.

Rats were anesthetized with a mixture of ketamine (65mg/kg) and xylazine (7.5mg/kg). A small (0.5-1cm) para-midline right sided scalp skin incision was made. A hand-held twist drill was then used to make a controlled perforation of the skull. The resultant skull opening was approximately 0.5mm in diameter. The skull opening was followed by sharp incision of the dural lining; this was likely to be associated with a small volume of self-limiting bleeding. The brain parenchyma was then ready for insertion of the implant. The cylindrically shaped implant had a volume of approximately 0.000354cm^3 (length = 0.5cm, diameter = 0.3cm). The volume of the rat brain varies from $0.865 \pm 0.026\text{cm}^3$ to $1.165 \pm 0.071\text{cm}^3$ depending of the age of the rat i.e. implant was less than 20% of the rat brain volume.

The skull defect was sealed with wax and the scalp insertion was closed with a single layer of appropriately sized non-absorbable suture. The rat then received Temgesic: (0.1mL diluted to 1mL with ultra purified water), at a dose of 1mL post-operatively for pain relief with a rehydration treatment of 5% glucose in 0.9% saline. A series of behavioral asymmetry tests were performed on the rats to assess any degree of motor dysfunction present

7.2.3.3. End points for experiments that induce illness in rats

Rats that had experienced any degree of distress were removed from the study. Weight, eating and grooming habits were monitored periodically. Any significant fluctuations in these areas led to the removal of the rat affected from the study. The inclusion of a placebo NESD group allowed for the comparison against the experimental group in terms of the assessment of the degree of distress experienced by the rats.

7.2.3.4. Biological fluid sample collection from the rat model

Rats received anesthesia with ketamine/xylazine mixture (as per 7.2.1.2)) prior to the sample collection.

Blood: Sequential blood samples (5mL) were collected via cardiac puncture into heparin-containing test tubes at predetermined time intervals. Plasma was separated by centrifugation for 8min at 1000g and stored at -70°C until analysis.

Cerebrospinal Fluid (CSF): The technique being analogous to that employed in Ethics Application 2005/86/5. The rats were euthanized prior to the procedure with sodium pentobarbitone (200mg/kg) and the skin overlapping on the neck (this is the skin where the head and neck meet to allow for insertion of the needle) was shaven. A device was specially made up consisting of a 25G needle attached to polyethylene tubing at one end and a 1mL syringe at the other end. The device was inserted into the cisterna magna to obtain the CSF (100-150 μL). CSF samples were transferred to ependorfs (1.5mL) and placed on ice. Thereafter, the samples were centrifuged @10 000rpm (Optima[®] LE-80K, Beckman, USA) for 20min, the supernatant was removed and stored in refrigerator @ -70°C .

Brain Tissue: The entire brain was removed and placed in formalin solution (10% v/v).

7.2.3.5. Histological analysis of the rat brain tissue post-implantation of the NESD

Rats were euthanized with sodium pentobarbitone and decapitated. Brain tissue was removed and placed in 10% v/v neutral buffered formalin. The tissue was then dehydrated, infiltrated and embedded in paraffin followed by transversion into 400 μm slices and stained with hemotoxylin and eosin. The slides were then viewed microscopically to assess the presence/absence of inflammatory cell infiltration and markers of necrosis.

7.2.3.6. Bioerosion studies on the NESD

Devices were removed at various predetermined time intervals (5, 7, 14, 21 and 30 days) and their bioerosion was assessed using SEM (JEOL, JEM 840, Tokyo Japan). Photomicrographs were taken at different magnifications and samples were prepared after sputter-coating with carbon or gold.

7.2.4. Determination of *in vivo* drug release from Sinemet[®] and the NESD using UPLC analysis on biological fluids

7.2.4.1. Preparation of priming solvents and mobile phases

Strong Wash: Acetonitrile (90% v/v) and water (10% v/v).

Weak Wash: Acetonitrile (10% v/v) and water (90% v/v).

Mobile Phase A (98%): Ammonium acetate (7.09g) was dissolved in 1L of water, to give a 0.1M solution. acetic acid was added to adjust the pH to 5.0

Mobile Phase B (2%): Acetonitrile (100% v/v).

Double deionised water (Milli-Q, Millipore, Johannesburg) of 18.2 MΩ cm⁻¹ resistivity was used. The mobile phases were filtered a 0.22µm pore size Cameo Acetate membrane filter (Millipore Co., Bedford, Massachusetts).

7.2.4.2. Preparation of standards

Primary stock solutions of DA (100mg/mL) were prepared in doubly deionised water. The stock solutions were stored in polypropylene tubes with screw caps and kept in a refrigerator at 5 C. Working standard solutions of DA were prepared by diluting the primary solution with doubly deionised water. Drug-free human plasma (0.4mL) was spiked with appropriate working solutions of DA to produce final DA concentrations ranging from 0.0008-15.00µg/mL. Solutions of theophylline (internal standard, IS)) was constituted in doubly distilled water (1mg/mL).

All solutions were filtered with a 0.22µm pore size Cameo Acetate membrane filter (Millipore Co., Bedford, Massachusetts).

7.2.4.3. Solid Phase Extraction of blood and CSF

The Generic Oasis[®] HLB Solid Phase Extraction (SPE) method was employed to determine the concentrations of methanol that would increase the purity of the analyte (DA) thereby allowing the determination of drug concentration in the samples. Oasis[®] HLB cartridges enabled with the Visiprep Vacuum Manifold and Standard Lid (Waters,) were conditioned with

methanol (1mL) and deionized water (1mL). The prepared calibration standards and plasma samples (as in 7.2.1.3.2.) were loaded onto the cartridges post-conditioning followed by a mild wash with 5% methanol (1mL). The strong wash entailed the employment of a gradient of concentrations (10-100%) of methanol (Figure 7.3) which were collected in separate testtubes (5mL) to which theophylline (0.1mL) was added. The samples were then placed in Waters certified vials (1.5mL) for analysis (Li *et al.*, 2005).

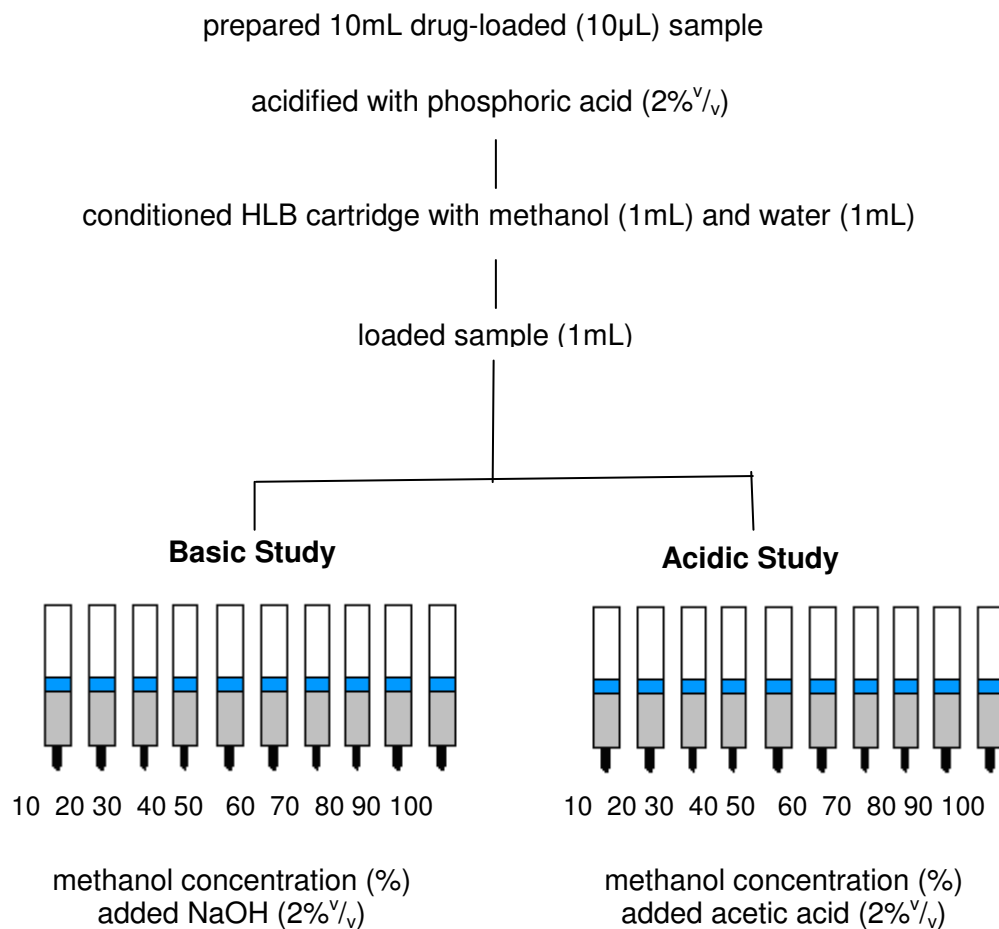


Figure 7.3: Diagrammatic account of the strategy for the optimization of the generic SPE method

7.2.4.4. Instrumentation and operating conditions of the UPLC system

UPLC analyses were performed with a Waters Acquity Ultra Performance LC system (Waters, Milford, MA, USA) coupled with a PDA detector. UPLC separation was achieved on an Acquity UPLC BEH C18 column (50 mm × 2.1mm, i.d., 1.7µm particle size, Waters) maintained at 25 °C. The compounds were injected in the mobile phase with an injection volume of 3.7µl (partial-loop injection). Run time of 2min and flow rate of 0.500mL/min was calculated for the study. The equipment was primed with the washes and mobile phases for 10 cycles of 5min each. Acetonitrile (100% v/v) was injected into the system so as to remove residue sample material from the column prior to the sample runs. Aliquots (1µL) of samples were injected into the UPLC system and thereafter processed.

7.2.4.5. Calibration curves and limit of quantification for DA in plasma

Analyte standard solutions (0.4mL) at 8 different concentrations, were added to 0.4mL of blank plasma. Acetonitrile (0.4mL) was added to each sample and centrifuged (Optima[®] LE-80K, Beckman, USA) at 15000rpm for 10min. The supernatant of these samples were removed, subjected to the SPE procedure as detailed in 7.4.2.4. and injected into Waters Acquity Ultra Performance LC system (Waters, Milford, MA, USA). The analyte/IS peak area ratios were plotted against the corresponding analyte concentrations (expressed as ng/mL⁻¹). Linearity equations and correlation coefficients (r_c) were obtained by means of the least square method.

The limit of quantitation (LOQ) is defined as the analyte concentrations, which gives rise to chromatographic peaks whose height was equal to 10 and 3 times to that of the baseline noise (Mandriol *et al.*, 2006) and was calculated for DA.

7.2.4.6. Extraction yield, precision and accuracy of the method

Standard solutions (N=3) at three different concentrations of DA were added to 0.4mL of blank plasma, in order to obtain plasma analyte concentrations of 150000µg, 15000 µg and 0.8ng for DA; these mixtures were subjected to the SPE procedure and injected into the UPLC system.

Percentage extraction yield for the samples was calculated by comparing the peak areas of analytes obtained employing the SPE method to those obtained from standard solutions at the same theoretical concentration.

Intra-day (multiple injections of samples during a 24 hr period N=3) and inter-day (multiple injections of samples over 3 consecutive days, N=3 for each day) sampling provided the data for precision and accuracy.

7.2.4.7. CSF and blood preparation for UPLC analysis

Samples (plasma and CSF) were removed from the freezer (-70°C). Acetonitrile (0.4mL) was added to each sample and placed in the centrifuge (Optima[®] LE-80K, Beckman, USA) @15000rpm for 10min. The supernatant was removed, placed in testtubes and centrifuged @5000rpm for a further 5min. The resultant was thereafter subjected to the SPE procedure as detailed in 7.4.3. and spiked with internal standard (0.1mL). The samples were then placed in Waters certified vials (1.5mL) for analysis (Li *et al.*, 2005) and analysed on the Waters Acquity Ultra Performance LC system (Waters, Milford, MA, USA).

7.3. Results and Discussion

7.3.1. Brain damage in the rat from the surgical implantation of the NESD

The procedure (Figure 7.4) was associated with a small amount of cortical contusion. However when damage to the brain was found to be of no clinically detectable neurological deficit. It was found that a significant number of rats suffered severe and even lethal complications from the surgical procedure leading to the reevaluation and development of the implantation procedure.



Figure 7.4: Photographic representation of the surgical procedure (a) manual drill used for incision, (b) actual perforation of the skull and (c) suturing of the incision

7.3.2. Modifications to surgical implantation procedure

The rats were placed in a Kopf stereotaxic frame and a straight midline incision was made from nasion to occiput. The skin and perisoteum was reflected exposing the dorsal surface of the skull. This was done in order to facilitate identification of the cranial sutures and to ensure the skull trephination was made in the frontal bone. An electric drill was used to decrease the pressure exerted on the scalp so as to minimize any excess bleeding. The mass of rats was increased (350-400g) as it was found that smaller rats had more complications as a result of surgery.

7.3.3. Evaluation of modifications to surgical implantation technique

The employment of a stereotaxic frame allowed for the accurate implantation of the implant into the parenchyma beneath the frontal bone thereby avoiding motor and eliminating the outcome of paralysis in the rats. Furthermore, larger rats exhibited a more positive effect to the implant due to their increased brain volume. Overall, rats exposed to the modified surgical technique displayed good health (weight and grooming techniques).

7.3.4. Biocompatibility of the NESD systems employed in the study

7.3.4.1. Pathological diagnosis of rat brain specimens implanted with DA-free NESD

Histological analysis of all specimens was representative of cortical grey and white matter as well as the ventricular and cerebellum regions of the rat brain.

Day 5 and 7: There was no evidence of inflammatory cells within the brain parenchyma and Virchow's Robin spaces. No evidence of ischemia or morphological features of demyelinating disorder.

Day 14: Extremely sparse and scanty inflammatory lymphocyte were scattered in the white matter. Minute inflammation was present in the Virchow's Robin spaces. There was no indication of ischemic injury and demyelinating disorder.

Day 21: There was mild inflammation within the meningeal covering, neural parenchyma and in the periventricular area. Once again, there were no findings of inflammation in the Virchow's Robin spaces. Mature lymphocytes were found sparsely dispersed in the white and grey matter. In addition congested blood vessels were present in the meninges.

Day 30: Mild inflammation was identified in the cortical white and grey matter as well as periventricular areas. There was also mild chronic inflammation in the meninges and congested blood vessels.

7.3.4.2. Pathological diagnosis of rat brain specimens implanted with NESD

The histological findings (Figure 7.5) in the rat brain for the NESD showed the same pathological features as in 7.3.5.1.

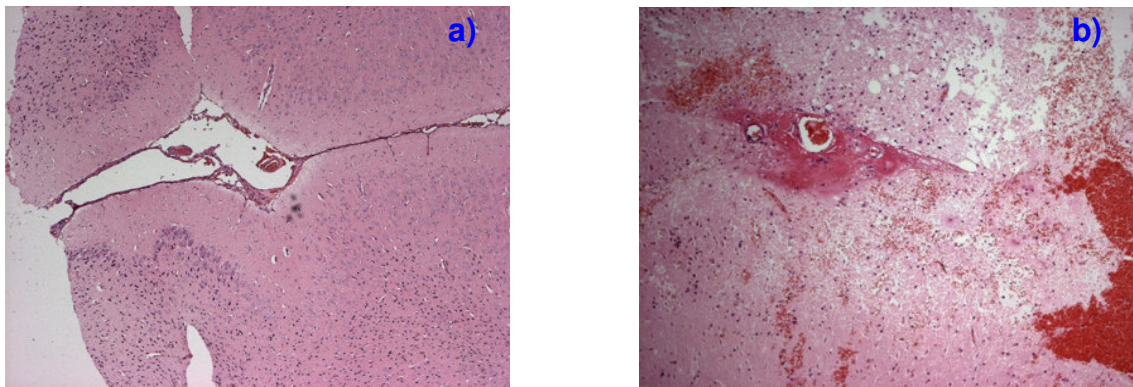


Figure 7.5: Light microscope images of histological slides of the site of implantation of the NESD into the brain, stained using H & E, in (a) control and (b) test brain tissue following 5 days of implantation of the NESD

7.3.5. Bioerosion of NESD post-implantation

Figure 7.6 represents the mass loss from the NESD over a period of 30 days post-implantation. Bioerosion was 16% at 7 days (Figure 7.7) and thereafter minimal erosion took place (26% bioerosion at 30 days). The erosion profile proved that the device should remain intact throughout the treatment period (at least 30 days) and thereby possibly contribute to controlled drug release. In addition, results confirmed that the device was in fact biodegradable and so there was no need for a second surgical to remove the device once the drug is depleted.

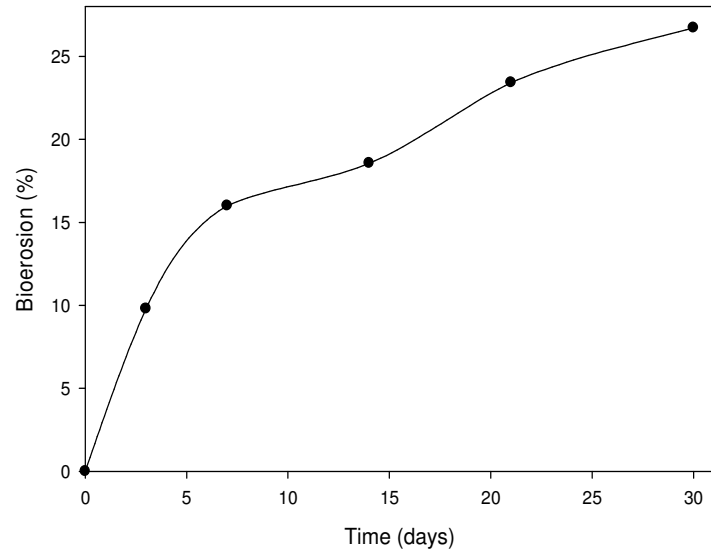


Figure 7.6: In vivo bioerosion profile for NESD over a period of 30 days ($SD \leq 0.78$)

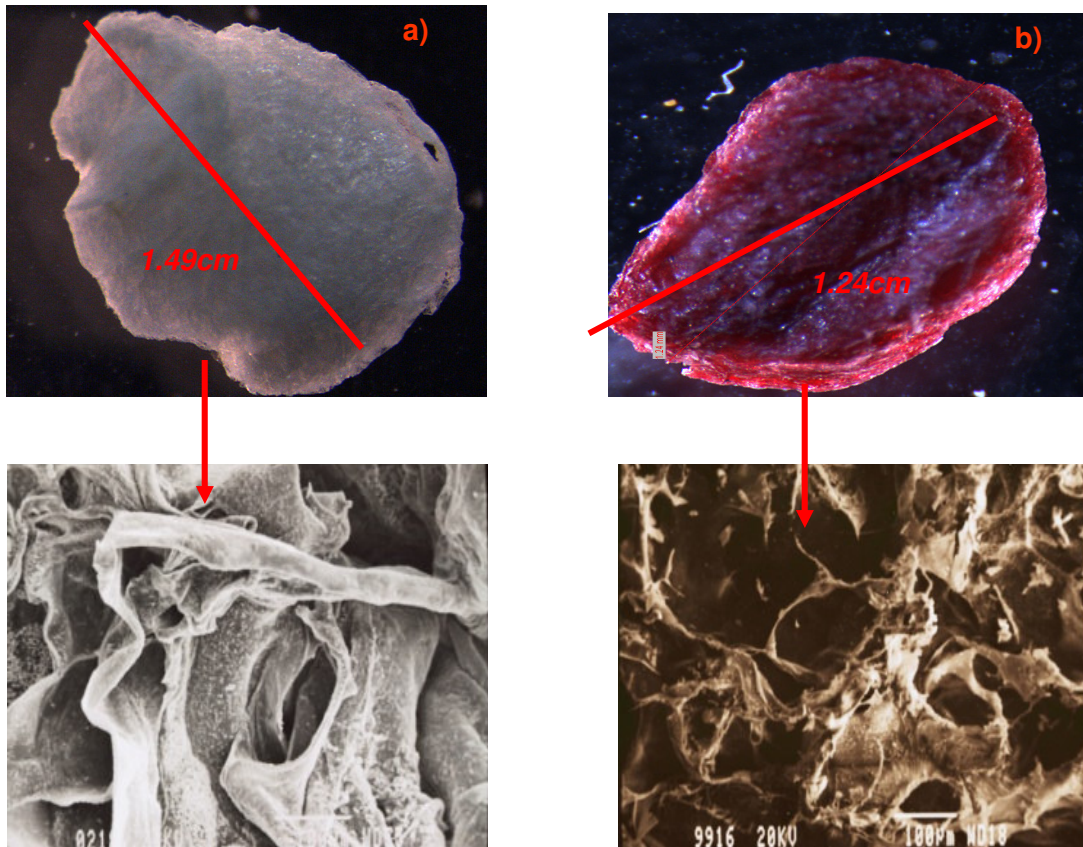


Figure 7.7: Light microscope (top) and SEM (bottom) images of NESD matrix (a) pre-implantation and (b) blood perfused post-euthanasia and removal from rat brain post-7 day implantation showing 16% bioerosion

7.3.6. SPE of DA from plasma

The optimized SPE technique was selected to remove plasma constituent interferences and isolate the drug in the CSF and blood samples. The employment of HLB cartridges for the extraction offered the advantage of retaining polar compounds, as is DA, and thereby removing impurities. Serial dilutions of methanol solutions (5-100%^{v/v}), represented in Figure 7.6, with either the addition of an acid (CH₃COOH) or a base (NaOH) was employed in the SPE technique. It was noted that during the acidic phase (CH₃COOH) higher integral UPLC peaks and extraction yields were obtained as compared to the basic phase (NaOH), in particular, at 70%^{v/v} methanol with 2%^{v/v} acetic acid. An additional wash-step of 45%^{v/v} methanol produced even larger recoveries and level chromatographic baselines.

7.3.7. Chromatograms for standards and plasma

A typical chromatogram of a standard solution of DA (Figure 7.8), theophylline (Figure 7.9) and a blood sample obtained from the cardiac vein in the rat model post-implantation of the NESD is displayed in Figure 7.8. The chromatograms proved that the method for extraction was successful in eluting dopamine and internal standard.

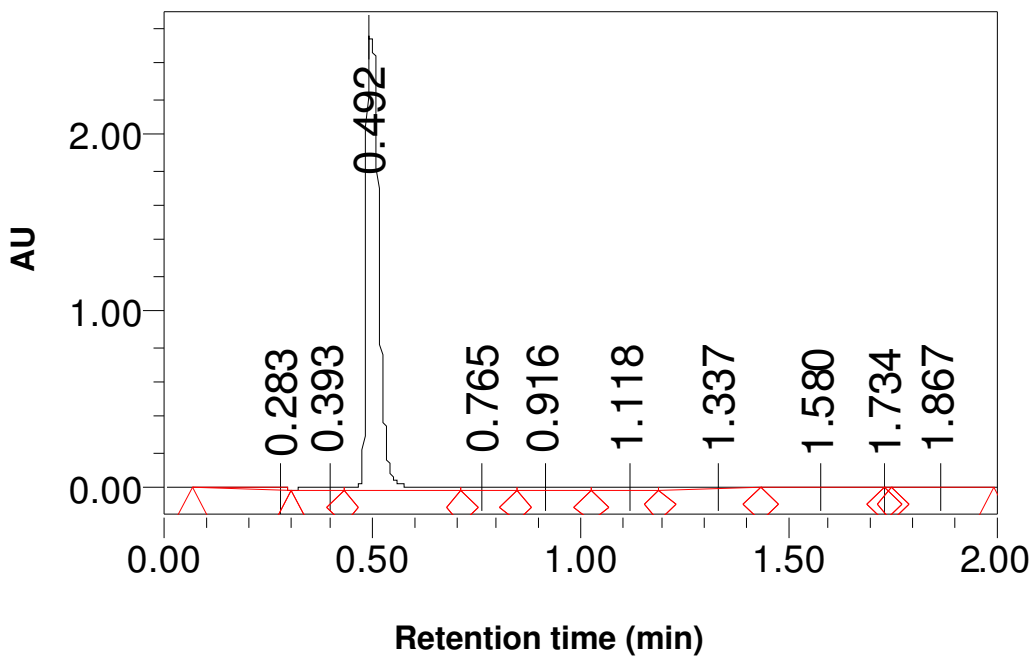


Figure 7.8: A typical chromatograph depicting the peak ($R_t = 0.4925$) for DA employing UPLC at 280nm in double deionised water

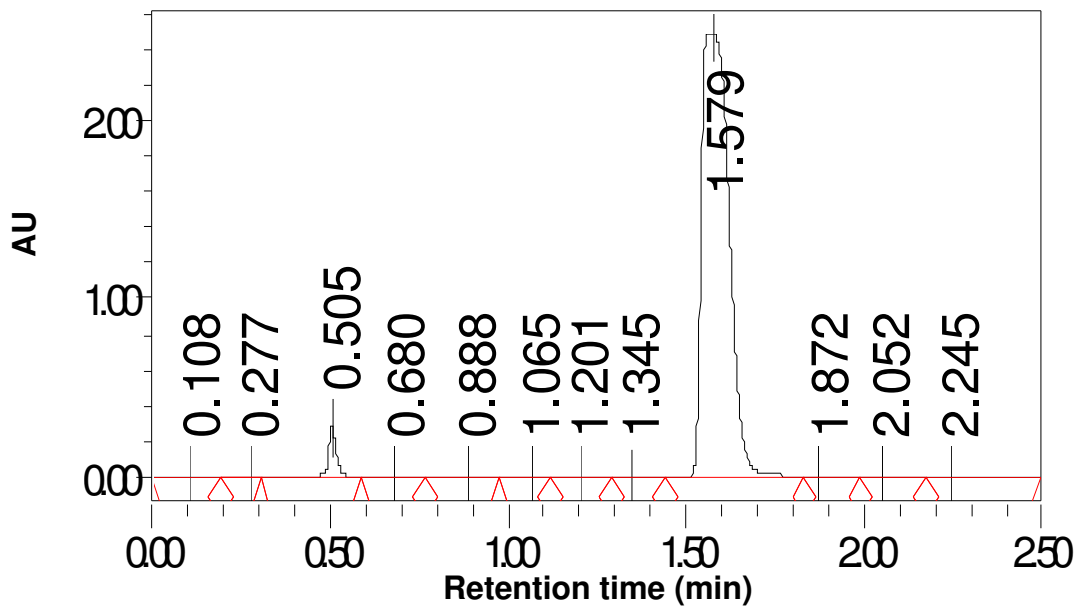


Figure 7.9: A typical chromatograph depicting the peak ($R_t = 1.579$) for theophylline (internal standard) employing UPLC at 280nm in double deionised water

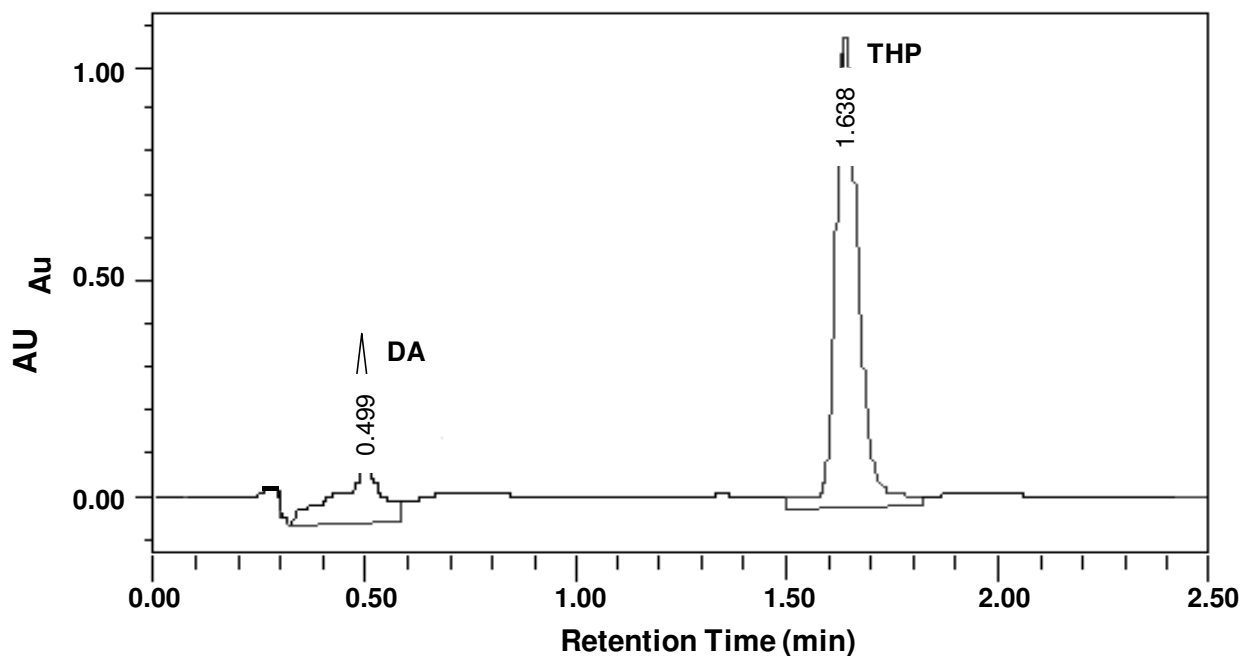


Figure 7.10: A typical UPLC chromatogram depicting the distinct separation of DA ($R_t=0.49$) and theophylline ($R_t=1.64$) at 280nm from the Sprague Dawley rat plasma samples

7.3.8. Calibration curve and lower limit of quantification of DA

Figure 7.11. displays the calibration curve for DA in plasma samples employing the UPLC (Waters, Milford, MA, USA) and PDA detector set at 280nm. Concentrations of 150000-0.8ng/mL offered good linearity ($R_2 = 0.9811$).

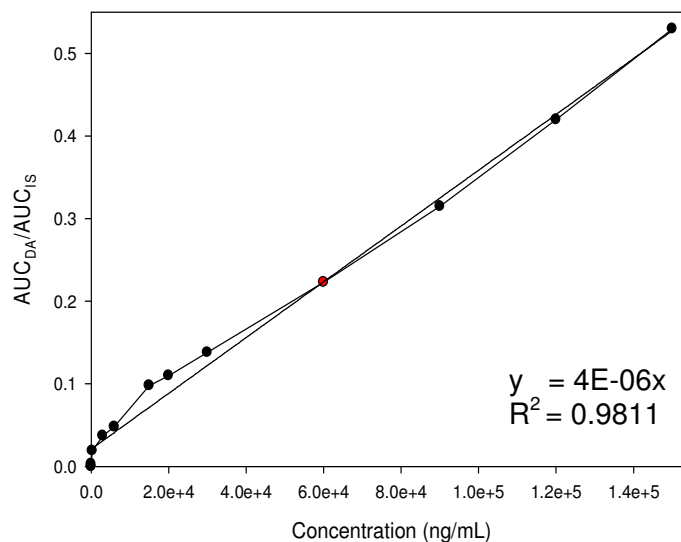


Figure 7.11: DA calibration curve at 280nm in plasma employing UPLC at 280nm in double deionised water

The lower limit of quantification for this study was noted as 0.8ng/mL.

7.3.9. Method validation for the analysis of DA in plasma employing UPLC analysis

The method validation data (extraction efficiency, intra- and inter-day variation) for the analyte are summarized in Table 7.1.

The extraction recoveries ranged from 95.89 to 101.02%, while the precision values ranged from 1.5 to 7.4% over the three concentrations (i.e., 0.8, 15000 and 150000ng/ml) evaluated over 3 consecutive days. These results indicated that the implemented solid phase extraction method has an acceptable accuracy and precision.

Table 7.1: Illustrates the data obtained to assess the validation of the method

Concentration added (ng/mL)	Extraction yield (%)	Intra-day		Inter-day	
		SD	CV	SD	CV
0.8	95.89	0.000007	0.036	0.000014	0.074
15000	98.98	0.0014	0.015	0.0021	0.022
150000	101.02	0.0021	0.041	0.0028	0.055

7.3.10. *In vivo* DA release profile for NESD

The *in vivo* drug release profiles for the control preparation (Sinemet[®]) (Figure 7.12) and the NESD (Figure 7.13) showed indirect proportionality to each. The drug release for the group receiving Sinemet[®] was carried out over a period of 10hr while the drug release study for the test group was carried over a month. The drug release from Sinemet[®] (Figure 7.12) was quite clearly substantially reduced, approximately 10-fold, in the CSF in comparison to the plasma. And while $C_{max} = 0.000053\%$ was noted at 2hr in the plasma, the peak plasma concentrations in the CSF only took place at 8hr with 0.000012% of DA being released.

The drug release for the NESD (Figure 7.13) produced a peak at 3 days for both the CFS and plasma, the CSF concentration of DA being 28% while the plasma concentration was only 1.2% of the total concentration administered. The DA release profile for plasma maintained low drug release throughout the 30 days of the study whereas the CSF concentration of DA peaked at 3 days and thereafter maintained reduced drug release for the remainder of the study.

Overall, the NESD was implanted at the site of action and therefore drastically improved the delivery of DA to the brain tissue comparatively to the Sinemet[®]. In addition, DA concentrations found in the plasma were minimalistic and therefore could result in the alleviation of the systemic side-effects from the oral administration of levodopa preparations.

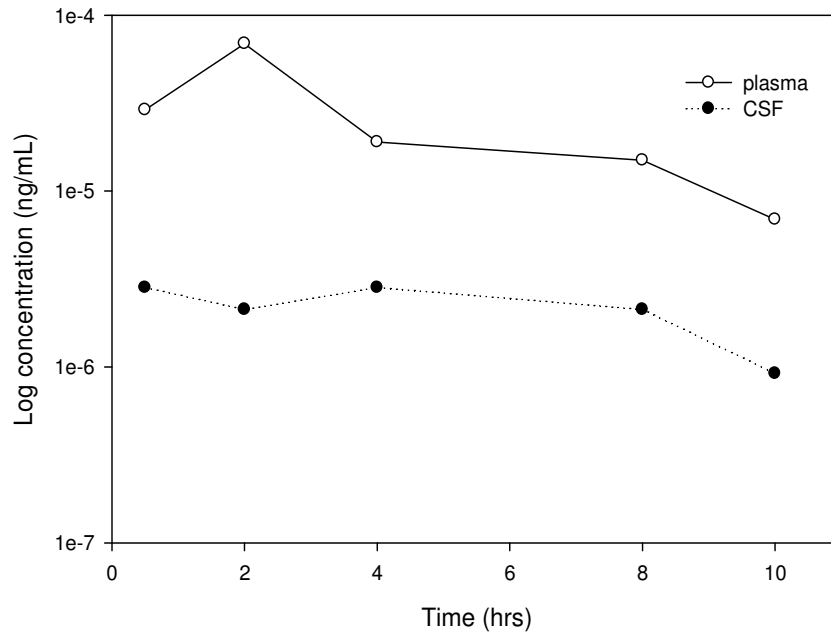


Figure 7.12: In vivo profile for DA release from Sinemet[®] ($SD \leq 0.000001$)

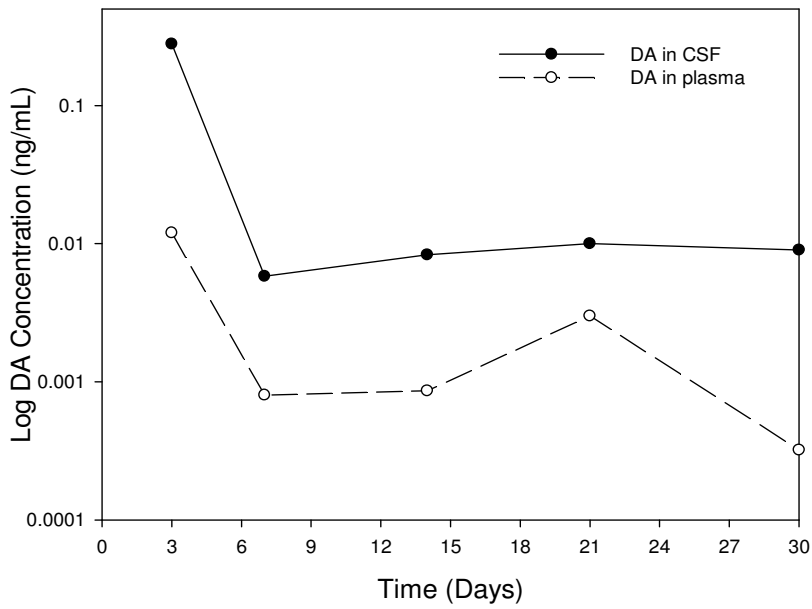


Figure 7.13: In vivo profile for DA release from the NESD ($SD \leq 0.003$)

7.4. Concluding Remarks

The *in vivo* chapter sought to address the biocompatibility and *in vivo* DA release of the NESD in the rat brain employing novel surgical approaches, SEM and UPLC techniques.

A surgical protocol for implantation of the NESD into the parenchyma of the frontal lobe of the rat brain was developed that resulted in only minor clinical implications for the rat model post-surgery.

Biocompatibility was addressed in this chapter and findings proved that the placebo as well as the NESD had no significant effects on the brain tissue with no evidence of ischemia or morphological events in the brain cells.

The bioerosion profile of the NESD mimicked that of the *in vitro* degradation studies with minimal erosion post day 7 of implantation proving the device would remain intact throughout the treatment period but also retained its biodegradation characteristics.

UPLC analysis was undertaken for the determination of DA in the plasma and CSF. Method development and validation studies were undertaken in the establishment of the technique. DA release profiles illustrated concentrations of DA in the plasma and the CSF of both the group receiving Sinemet[®] and the NESD. The NESD proved to be superior in terms of drug release to the brain tissue and also reduced systemic circulation of DA thereby possibly decreasing side-effects experienced from the drug.

Overall, results obtained in the chapter showed that the NESD was biocompatible, biodegradable and had a positive effect of the concentrations of DA in the brain.

CHAPTER 8 CONCLUSIONS AND RECOMMENDATIONS

8.1. Conclusions

In January 2008, the cause of PD still remains unknown (Richter *et al.*, 2008) and with chronic treatment being limited and ineffective, the disease holds grave consequences for its sufferers. A cure is nowhere in sight and so pharmacological and non-pharmacological agents are the sole promise of a normal life for these patients.

The R & D process is a lengthy one and with gene therapy still in the early stages of human clinical trials (Lewis and Standaert, 2008) and advancements in non-pharmacological treatment being leisurely, researchers need to look at the development of other possible agents to treat this rapidly growing disease.

Young-onset/ baby boomers PD now affects 5–10% of patients while 1% of the aging population (60 yrs and older) will suffer from PD (Samii *et al.*, 2004) and it's number of victims continue to climb. Patient's medical needs increase significantly for the years following the onset of PD (Fiandaca *et al.*, 2008) and depression is now a common symptom (Barrero *et al.*, 2005). The suffering continues to the patient's family and caregiver/s and so the disease knows no end.

This research undertook to develop a drug delivery system consisting of DA-loaded CAP nanoparticles dispersed within Ba-alginate scaffolds for implantation into the parenchyma of the frontal lobe of the brain. The concept is novel in that it incorporates two unique drug delivery systems that complement each other in the achievement of controlled release.

Extensive *in vitro* testing resulted in the establishment of the NESD. Preliminary investigations on both the Ba-alginate scaffold and DA-loaded CAP nanoparticles allowed for the selection of appropriate crosslinkers and polymers to be employed in their formulation. DA-loaded CAP nanoparticles were subjected to vigorous *in vitro* release studies to determine MDT and zetasize analysis to determine their stability and quintessentially their particle size and zeta potential. While the structural integrity and matrix erosion kinetics were imperative characteristics for Ba-alginate scaffold design.

Formulations of the Ba-alginate scaffold and DA-loaded CAP nanoparticles were both optimised employing the Box-Behnken design which saw the *in vitro* testing (Matrix Resilience and Matrix Erosion for the Ba-alginate scaffold and MDT, Particle Size and Zeta Potential for DA-loaded CAP nanoparticles) of 27 formulations each. A single candidate formulation was chosen for each system. The combinatory NESD was then subjected to simulated CSF and it's *in vitro* drug release was confirmed.

The promise of the NESD lead to it's evaluation *in vivo*. The parenchyma of the frontal lobe of the brain of rat models were implanted with the NESD followed by histological, bioerosional and *in vitro* DA analysis at predetermined time intervals.

Futhermore, preliminary *in vitro* evaluation was undertaken on other possible nanosystems that may be used to treat PD. Characterization and *in vitro* release of L-dopa-loaded PLGA and NT-loaded CAP nanoparticles as well as DA-loaded polymeric nanofibers showed that there is a possibility for these systems to be employed in the treatment of PD and that further testing should be undertaken.

While this drug delivery system has been developed with the incorporation of DA in the treatment of PD, it is not exclusive to this disease as the NESD may be applicable to numerous other chronic CNS conditions. The addition of different combinations of polymers and drug may impart a range of different properties to the device thereby allowing it to be used for the treatment of other ailments. The strategic implantation of the device into the brain will circumvent the allows for targeted drug delivery and thereby allow numerous other CNS drugs to be delivered to the brain tissue, mostly unchanged and eliminating systemic side effects.

8.2. Recommendations

Nanosystems (L-dopa-loaded PLGA and NT-loaded CAP nanoparticles and DA-loaded polymeric nanofibers) need to be more extensively researched both *in vitro* and *in vivo* so as to provide potential alternatives for the treatment of PD.

Major variations in drug-loaded polymeric nanoparticle size were noticed for all formulations, methods and mechanisms need to be investigated so as to limit and even provide uniformity to particle size.

In vitro drug release in the brain is still in its early stages and therefore lacks a standard protocol for the conditions that need to be maintained to simulate the *in vivo* environment.

Animal studies in the rat model have shown great promise and so these studies need to move to research in larger mammalian models such as apes. These results will be more significant in that they will more closely represent the human model (human clinical trials being the next stage).

Fluorescent markers should be attached to the drug-loaded polymeric nanoparticles *in vivo*, so as to determine their transportation and distribution throughout the brain and even the body. This will allow us to evaluate the exact numbers and mechanisms of nanoparticulate drug delivery.

The minute size of the NESD for *in vivo* implantation posed limitations for bioerosion studies. Future studies need to investigate the possibility of attaching a string to the device or the addition of a biocompatible colourant so as to ensure the device may be found upon termination of the study.

Futuristically, scientists are currently attempting the construction of nanorobots. The intention of the design is for them to travel throughout the human body using molecular motors and computers, store and transport molecules, perform operations and communicate with physicians (Freitas, 2001).

REFERENCES

1. A guide to freeze drying for the laboratory- An industry service publication, Labconco, 2007.
2. Abbott N.J and Romero I.A, Transporting therapeutics across the blood-brain barrier, **Molecular Medicine Today**, **2**(3), March 1996, 106-113.
3. Abidian M.R, Kim D.H, D. C. Martin D.C, Conducting-Polymer Nanotubes for Controlled Drug Release, **Advanced Materials**, **18**(4), 2006, 405 - 409.
4. Agid Y, Parkinson's disease: pathophysiology, **Lancet**, **337** (8753), 1991, 1321–1324.
5. Agnihotri S.A, Mallikarjuna N.N, Aminabhavi T.M, Recent advances on chitosan-based micro- and nanoparticles in drug delivery, **Controlled Release** , **100**(1), November 2004, 5-28.
6. Ahmad F.J. and Khan R.K., Nanotechnology: A Revolution in the Making, **The Pharma Review**, **75**(7), 2005, 801-2.
7. Alexis F, Rhee J, Richie J.P, Radovic-Moreno A.F, Langer R, Farokhzad O.C, **New frontiers in nanotechnology for cancer treatment, Urologic Oncology: Seminars and Original Investigations**, **26**(1), January-February 2008, 74-85.
8. Anderson L and Caldwell M.A, **Human neural progenitor cell transplants into the subthalamic nucleus lead to functional recovery in a rat model of Parkinson's disease, Neurobiology of Disease**, **27**(2), August 2007, 133-140.
9. Antolín I, Mayo J.C, Sainz R.M, del Brío M, Herrera F, Martín V, Rodríguez C, Protective effect of melatonin in a chronic experimental model of Parkinson's disease, **Brain Research**, **943**(2), 2002, 163-173.
10. Arica B, Kas H.S, Moghdam A, Akalan N, Hincal A.A, Carbidopa/levodopa-loaded biodegradable microspheres: in vivo evaluation on experimental Parkinsonism, **Controlled Release**, **102**(3), February 2005, 689-697.
11. Barnes C.P, Sell S.A, Boland E.D, Simpson D.G, Bowlin G.L, Nanofiber technology: Designing the next generation of tissue engineering **scaffolds, Advance Drug Delivery Reviews**, **59**(14), 2007, 1413-33.
12. Barone C, Landriscina M, Quirino M, Basso M, Pozzo C, Schinzari G, Di Leonardo G, D'Argento E, Trigila N and Cassano A, Schedule-dependent activity of 5-fluorouracil and irinotecan combination in the treatment of human colorectal cancer: in vitro evidence and a phase I dose-escalating clinical trial, **British Journal of Cancer**, **96**, December 2006, 21-28.

13. Barrero FJ, Ampuero I, Morales B, Vives F, de Dios Luna Del Castillo J, Hoenicka J, García Yébenes J, Depression in Parkinson's disease is related to a genetic polymorphism of the cannabinoid receptor gene (CNR1), **Pharmacogenomics**, **5**(2), 2005, 135-41
14. Bawa R, The future of Nanomedicine, **Patents and Nanomedicine**, **2**(3), 2007, 351-374.
15. Becker J.B, Robinson T.E, Barton P, Sintov A, Siden R and Levy R.J, Sustained Behavioral Recovery from Unilateral Nigrostriatal Damage Produced by the Controlled Release of Dopamine from Silicon Polymer Pellet Placed into the Denervated Striatum, **Brain Research**, **508**, 1990, 60-64.
16. Becker T.A, Kipke D.R, Brandon T, Calcium alginate gel: a biocompatible and mechanically stable polymer for endovascular embolization, **Biomedical Material Research**, **54**, 2001, 76–86.
17. Benbir G, Özekmekçi S, Apaydin H, Sakir Delil S, Erginöz E, A hospital-based study: Risk factors in development of motor complications in 555 Parkinson's patients on **levodopa** therapy, **Clinical Neurology and Neurosurgery**, **108**(8), December 2006, 726-732 .
18. Betarbet R, Sherer T.B, Greenamyre J.T, Animal models of Parkinson's disease, **BioEssays**, **24**(4), 2002, 308-318.
19. Bilati .U, Allémann .A, Doelker. E, Development of a nanoprecipitation method intended for the entrapment of hydrophilic drugs into nanoparticles, **European Journal of Pharmaceutics**, **24**, (1) , 2005, 67-75.
20. Bilensoy **E**, **Tumor targeted nanoparticles for cancer therapy**, **European Journal of Pharmaceutical Sciences**, **32**(1), 2007, S10.
21. Bjerkvig R, Alginate capsules for use in the treatment of brain tumor, United States Patent 6926888, 2005.
22. Bjorklund A, Dunnett S.B, Brundin P, Stoessl A.J, Freed C.R, Breeze R.E, Levivier M, Peschanski M, Studer L, Barker R, Neural transplantation for the treatment of Parkinson's disease, **Lancet Neurology**, **2**, 2003, 437–445.
23. Blum D, Torch S, Lambeng N, Nissou M, Benabid A.L, Sadoul R, Verna J.M, Molecular pathways involved in the neurotoxicity of 6-OHDA, dopamine and MPTP: contribution to the apoptotic theory in Parkinson's disease, **Progressive Neurobiology**, **65**, 2001, 135–172.
24. Borges O, Da Silva A, Romeijn S.G, Amidi M, De Sousa A, Borchard G, Junginger H.E, Uptake studies in rat Peyer's patches, cytotoxicity and release studies of alginate coated chitosan nanoparticles for mucosal vaccination, **Controlled Release**, **114**(3), 2006, 348-358.

25. Bounous DI, Campagnoli RP, Brown J, Comparison of MTT colorimetric assay and tritiated thymidine uptake for lymphocyte proliferation assays using chicken splenocytes, **Avian Diseases**, **36**(4), Oct-Dec 1992,1022-1027.
26. Bové J, Prou D, Perier C, Przedborski S, Toxin-induced models of Parkinson's Disease, **Neurotherapeutics** , **2**(3), 484–494.
27. Bower J.H, Maraganore D.M, McDonnell S.K and Rocca W.A, Incidence and distribution of parkinsonism in Olmsted County, Minnesota, 1976–1990, **Neurology**, **52** 1999, 1214–1220.
28. Boylan LS, Pullman SL, Lisanby SH, Spicknall KE, Sackeim HA, Repetitive transcranial magnetic stimulation to SMA worsens complex movements in Parkinson's disease, **Clinical Neurophysiology**, **112**(2), February 2001, 259-264.
29. Brannon-Peppas L and Blanchette J.O, Nanoparticle and targeted systems for cancer therapy, **Advanced Drug Delivery Reviews**, **56**(11), 2004, 1649-1659.
30. Brevig T, Holgersson J, Widner H, Xenotransplantation for CNS repair: immunological barriers and strategies to overcome them, **Trends in Neurosciences**, **23**(8), 1 August 2000, 337.
31. Buckley C.T and O'Kelly K.U, Chapter 5: Regular Scaffold Fabrication Techniques for Investigations in Tissue Engineering, **Topics in Bio-Mechanical Engineering**, 2004, 147-166.
32. Burkersroda V.F, Schedl L, Gopferich A, Why degraded polymers go under surface erosion or bulk erosion, **Biomaterials**, **23**, (21), 2002, 4221-4231.
33. Burn D, Parkinson's disease: an overview, **The Pharmaceutical Journal**, **264**(7085), February 26, 2000, 333-337.
34. Cabot Corporation Nanogel™, Manchester, New Hampshire, US.
35. Calcium alginate gel: A biocompatible and mechanically stable polymer for endovascular embolization, **Biomedical Materials Research**, **54**(1), October 2000, 76 – 86.
36. Calvin L.Y.L, Polymer Scaffold Structure for Tissue Engineering, In: http://staff.science.nus.edu.sg/~scilooe/srp_2003/sci_paper/chem_eng/research_paper/la_u_yao_loong_calvin.pdf, 2003.
37. Carson-De Witt, R. Parkinson's disease, 2003.
38. **Caruthers S.D**, Wickline S.A, Lanza **G.M**, **Nanotechnological applications in medicine**, **Current Opinion in Biotechnology**, **18**(1), February 2007, 26-30.
39. Chan L.W, Lee H.Y and Heng P.W.S, **Production of alginate microspheres by internal gelation using an emulsification**, **International Journal of Pharmaceutics**, **242**(1-2), August 2002, 259-262.

40. Chan V.S, Nanomedicine: An unresolved regulatory issue, **Regulatory Toxicology and Pharmacology**, **46**(3), 2006, 218-24.
41. Cheah C.M, Leong K.F, Chua C.K, Low K.H, Quek H.S, Characterization of microfeatures in selective laser sintered drug delivery devices, **Proceedings of the Institution of Mechanical Engineers, Part H: Journal of Engineering in Medicine**, **216**(6), 2002, 369–383.
42. Chen H, Zhang S.M, Hernán M.A, Schwarzschild M.A, Willett W.C, Colditz G.A, Speizer F, Ascherio A, Nonsteroidal Anti-inflammatory Drugs and the Risk of Parkinson Disease , **Archives of Neurology**, **60**, 2003, 1059-1064.
43. Chen J.J and Obering C, A review of intermittent subcutaneous apomorphine injections for the rescue management of motor fluctuations associated with advanced Parkinson's disease, **Clinical Therapeutics**, **27**(11), 2005, 1710-1724.
44. Cho S, Jarrett B.R, Louie A.Y, Kauzlarich S.M, Gold-coated iron nanoparticles: a novel magnetic resonance agent for T1 and T2 weighted imaging, **Nanotechnology**, **17**, 2006, 640-644.
45. Chua C.K, Chou S, Chou S. M, Lin S. C, Lee S. T, Saw C. A, Fabricating facial prosthesis models using rapid prototyping tools, **Integrated Manufacturing Systems - The International Journal of Manufacturing Technology Management**, **11**(1), 2000, 42–53.
46. Ciofani G, Raffa V, Pizzorusso T, Menciassi A, Dario P, **Characterization of an alginate-based drug delivery system for neurological applications**, **Medical Engineering & Physics**, **30**(7), September 2008, 848-855..
47. Clement M, Hua L, Jeyakumar R, Barry H, The cytotoxicity of dopamine may be an artefact of cell culture, **Neurochemistry**, **81**(3), May 2002, 414-421.
48. Cochrane C, Gan Q, Walker G, Allen S.J, Preparation of Composite PCL-Chitosan Porous Scaffolds by Freeze -Drying for Tissue Engineering Applications, Bioengineering In Ireland Conference, January 27-28, 2006, 91.
49. Colosimo C, Fabbrini G, Berardelli A, Drug Insight: new drugs in development for Parkinson's disease, **Nature Clinical Practice Neurology**, **2**, 2006, 600-610.
50. Comella CL, Tanner CM, Ristanovic RK. Polysomnographic sleep measures in Parkinson's disease patients with treatment-induced hallucinations, **Annals of Neurology**, **34**(5), 1993, 710-714.
51. Costa G, Abin-Carriquiry J.A, Dajas F, **Nicotine prevents striatal dopamine loss produced by 6-hydroxydopamine lesion in the substantia nigra**, **Brain Research**, **888**(2), 2001, 336-342.

52. Curodeau, A, Sachs E, Caldarise S, Design and fabrication of cast orthopedic implants with freeform surface textures from 3-D printed ceramic shell, **Biomedical Materials Research**, **53**(5), 2000, 525–535.
53. Cutson T.M , Laub K.C. Shenkman M, Pharmacological and Nonpharmacological Interventions in the Treatment of Parkinson's Disease, **Physical Neurology**, **75**(5), 1995, 363-373.
54. Czerniczyniec A, Bustamante J, Lores-Arnaiz S, Dopamine enhances mtNOS activity: Implications in mitochondrial function, **Biochimica et Biophysica Acta (BBA) Bioenergetics**, **1767**(9), September 2007, 1118-1125.
55. Dahlin M and Björk E, Nasal administration of a physostigmine analogue (NXX-066) for Alzheimer's disease to rats, **International Journal of Pharmaceutics**, **212**(2), 2001, 267-274.
56. Damgé C, Maincent P, Ubrich P, Oral **delivery of insulin associated to polymeric nanoparticles in diabetic rats**, **Controlled Release**, **117**(2), 12 February 2007, 163-170.
57. Dauer W and Przedborski S, Parkinson's Disease Mechanisms and Models, **Neuron**, **39**(6), 2003, 889-909.
58. Davidson, Gow A.J, Lee T.H, Ellinwood E.H, Methamphetamine neurotoxicity: necrotic and apoptotic mechanisms and relevance to human abuse and treatment, **Brain Research Review**, **36**, 2001, 1–22.
59. Dayal P, Pillay V, Babu RJ, Singh M, Box-Behnken Experimental Design in the Development of a Nasal Drug Delivery System of Model Drug Hydroxyurea: Characterization of Viscosity, In Vitro Drug Release, Droplet Size, and Dynamic Surface Tension, **AAPS PharmSciTech**, **6**(4), 2005, E573-E585.
60. de Rijk M.C, Launer L.J, Berger K, Breteler M.M, Dartigues J.F, Baldereschi M, Fratiglioni L, Lobo A, Martinez-Lage J, Trenkwalder C, Hofman A, Prevalence of Parkinson's disease in Europe: a collaborative study of population-based cohorts, **Neurology**, **54**(11), 2000, 21–23.
61. de Vos P, Faas M.M, Strand B, Calafiore R, **Alginate**-based microcapsules for immunoisolation of pancreatic islets, **Biomaterials**, **27**(32), November 2006, 5603-17.
62. Debeir T, Ginestet L, François C, Laurens S, Martel J, Chopin P, Marien M, Colpaert F, Raisman-Vozari R, Effect of intrastriatal 6-OHDA lesion on dopaminergic innervation of the rat cortex and globus pallidus , **Experimental Neurology**, **193**(2), June 2005, 444-454.

63. del Olmo M, Bello O, Cudeiro J, Transcranial magnetic stimulation over dorsolateral prefrontal cortex in Parkinson's disease, **Clinical Neurophysiology**, **118**(1), 131-139.
64. Denizot F and Lang R, Rapid colorimetric assay for cell growth and survival : Modifications to the tetrazolium dye procedure giving improved sensitivity and reliability, **Immunological Methods**, **89**(2), May 1986, 271-277.
65. Derjaguin B.V, *Kolloid Z.* **69**, 1934, 155.
66. Derjaguin B.V, On the repulsive forces between charged colloid particles and on the theory of slow coagulation and stability of lyophobic sols, Transactions of the Faraday Society, **36**, 1940, 203-215.
67. Dewey R.B, Management of motor complications in Parkinson's disease, **Neurology**, **62**(6), 2004, S3-S7.
68. Diamond A, Shahed J, Jankovica J, The effects of subthalamic nucleus deep brain stimulation on parkinsonian tremor, **Neurological Sciences**, **260**(1-2), September 2007, 199-203.
69. Dietz G.P.H and Böhr M, **Delivery of bioactive molecules into the cell: the Trojan horse approach**, **Molecular and Cellular Neuroscience**, **27**(2), October 2004, 85-131.
70. Dojindo labs, Rockville, Maryland, USA
71. Dongre V.G, Karmuse P.P, Rao P.P, Kumar A, Development and validation of UPLC method for determination of primaquine phosphate and its impurities, **Pharmaceutical and Biomedical Analysis**, **46**(2), January 2008, 236-242.
72. Drucker-Colin R and Verdugo-Diaz L, Cell Transplantation for Parkinson's disease: present status, Cellular and Molecular **Neurobiology**, **24**(3), 2004, 301-316.
73. du Toit L, Pillay V, Choonara Y.E, Pillay S, Harilall S, Patenting of Nanopharmaceuticals in Drug Delivery, No Small Issue, **Recents Patents on Drug Delivery and Formulation**, **1**(2), 2007, 131-134.
74. Dziubla T.D, Shuvaev V.V, Hong N.K, Hawkins B.J, Madesh M, Takano H, Simone E, Nakada M.T, Fisher A, Albelda S.M, Muzykantov V.R, Endothelial targeting of semi-permeable polymer nanocarriers for enzyme therapies, **Biomaterials**, **29**(2), January 2008, 215-227.
75. Edgar K.J, Buchanan C.M, Debenham J.S, Rundquist P.A, Seiler B.D, Shelton M.C, Tindall D, Advances in cellulose ester performance and application, **Pharmacology And Experimental Therapeutics**, **80**(3), 250-255.
76. Edlund U and Albertsson A.C. Degradable polymer microspheres for controlled drug delivery, **Advanced Polymer Science**, **157**, 2001, 67-112.

77. Efentakis M and Politis S, Comparative evaluation of various structures in polymer controlled drug delivery systems and the effect of their morphology and characteristics on drug release, **European Polymer** , **42**(5), May 2006, 1183-1195.
78. Elbaz A and Tranchant C, Epidemiologic studies of environmental exposures in Parkinson's disease, **Neurological Science**, **262**(1-2), July 2007, 37-44.
79. Elkharraz K, Faisant N, Guse C, Siepmann F, Arica-Yegin B, Oger J.M, Gust J, Goepferich A, Benoit J.P, Siepmann J, Paclitaxel-loaded microparticles and implants for the treatment of brain cancer: Preparation and physicochemical characterization, **International Journal of Pharmaceutics**, **314**(2), May 2006, 127-136.
80. Ellis-Behnke R.G, Liang Y, Tay D.K.C, Kau P.W.F, Schneider G.E , Zhang S, Wu W, Kwok-Fai So, immediate hemostasis at the nanoscale, Nano hemostat solution: immediate hemostasis at the nanoscale, **Nanomedicine: Nanotechnology, Biology and Medicine**, **2**(4), 2006, 207-215.
81. Emerich D.F and Thanos C.G, The pinpoint promise of nanoparticle-based **drug delivery** and molecular diagnosis, **Biomolecular Engineering**, **23**(4), 2006, 171-84.
82. Erhardt A, Sillaber I, Welt T, Müller M.B, Singewald N, Keck M.E, Repetitive Transcranial Magnetic Stimulation Increases the Release of Dopamine in the Nucleus Accumbens Shell of Morphine-Sensitized Rats During Abstinence, **Neuropsychopharmacology**, **29**, 2004, 2074–2080.
83. European Medicines Agency, London, England, 2006
84. Everley R and Croley R, Ultra-performance liquid chromatography/mass spectrometry of intact proteins, **Chromatography A**, **1192**(2), May 2008, 239-247.
85. Factor S.A , Molho E.S, Feustel P.J, Brown D.L, Evans S.M, Long-Term Comparative Experience with Tolcapone and Entacapone in Advanced Parkinson's Disease. **Clinical Neuropharmacology**, **24**(5), 2001, 295-299.
86. Farokhzad O.C and Langer R, Nanomedicine: Developing smarter therapeutic and diagnostic modalities, **Advanced Drug Delivery Reviews**, **58**(14), 2006, 1456-1459.
87. Feng S.S, Zhao L, Zhang Z, Bhakta G, Win K.Y, Dong Y and Shu Chien, **Chemotherapeutic engineering: Vitamin E TPGS-emulsified nanoparticles of biodegradable polymers realized sustainable paclitaxel chemotherapy for 168 h in vivo**, **Chemical Engineering Science**, **62**(23), 2007, 6641-6648.
88. Ferrero M.C, Velasco M.V, Ford J.L, Rajabi-Siahboomi A.R, Muñoz A, Jiménez-Castellanos M.R, Determination of glass transition temperatures of some new methyl methacrylate copolymers using modulated temperature differential scanning calorimetry (MTDSC), **Pharmaceutical. Research**, **16**(9)1999, 1464–1469.

89. Fessi H, Puisieux F, Devissaguet J.Ph, Ammoury N, Benita S, Nanocapsule formation by interfacial polymer deposition following solvent displacement. **International Journal of Pharmaceutics**, **55**, 1989, 1–4.
90. Fiandaca, M, Forsayeth, J, Bankiewicz, K, Current status of gene therapy trials for Parkinson's disease, **Experimental Neurology**, **209**, 2007, 51–53.
91. Fiandaca, M. S, Forsayeth, J. R, Dickinson, P. J, and Bankiewicz, K. S, Image-guided convection-enhanced delivery platform in the treatment of neurological diseases, **Neurotherapeutics**, **5**, 2008, 123-127
92. Filmore D, Breaching the Blood-brain barrier, **Modern Drug Discovery**, **5(6)**,2002, 22–24.
93. Finotelli P.C, de Aragão Sampaio D, MoralesM.A, Ca Alginate as Scaffold for Iron Oxide Nanoparticles Synthesis, 2nd Mercosur Congress on Chemical Engineering and 4th Mercosur Congress on Process Systems Engineering, 2005.
94. FMC Biopolymer, Philadelphia USA
95. Follett K.A, The Surgical Treatment of Parkinson's disease, **Annual Review of Medicine**, **51**, 2000, 135–147.
96. Fournier E, Passirani C, Montero-Menei C.N, Benoit J.P, Biocompatibility of implantable synthetic polymeric drug carriers: focus on brain biocompatibility, **Biomaterials**, **24(19)**, August 2003 , 3311-3331(21).
97. Frankish H, Coenzyme Q10 could slow functional decline in Parkinson's disease, **The Lancet**, **360(9341)**, 2002, 227-1227.
98. Freimoser F.M, Jakob C.A, Aebi M, Tuor U, The MTT [3-(4,5-Dimethylthiazol-2-yl)-2,5-Diphenyltetrazolium Bromide] Assay Is a Fast and Reliable Method for Colorimetric Determination of Fungal Cell Densities, **Applied and Environmental Microbiology**, **65(8)** August 1999, 3727-3729.
99. Freitas R, How Nanorobots Can Avoid Phagocytosis by White Cells, Part I, IMM Report Number 27: **Nanomedicine**, June 2001, In conjunction with *Foresight Update 45*.
100. Gaillard P.J and de Boer A.G, **A novel opportunity for targeted drug delivery to the brain, Controlled Release**, **116(2)**, November 2006, 60-62.
101. Galindo-Rodríguez S.A, Puel F, Briançon S, Allémann E, Doelker E, Fessi H, Comparative scale-up of three methods for producing ibuprofen-loaded nanoparticles, **European Journal of Pharmaceutical Sciences**, **25(4-5)**, July-August 2005, 357-367.

102. Gasmi M, Brandon E.P, Herzog C.D, Wilson A, Bishop K.M, Hofer E.K, Cunningham J.J, Printz M.A, Kordower J.H, Bartus R.T, AAV2-mediated delivery of human neurturin to the rat nigrostriatal system: Long-term efficacy and tolerability of CERE-120 for Parkinson's disease, **Neurobiology of disease**, **27**(1), July 2007, 67-76.
103. Gelperina S, Kisich K, Iseman M.D, Heifets L, The Potential Advantages of Nanoparticle Drug Delivery Systems in Chemotherapy of Tuberculosis, **American Journal of Respiratory and Critical Care Medicine**, **172**, 2005, 1487-1490.
104. Gerlach M and Riederer P, Animal models of Parkinson's disease: an empirical comparison with the phenomenology of the disease in man, **Neural Transmission**, **103**(8-9), 1996, 987-1041.
105. Goodman Gilman A, Hardman J.G, Limbird L.E, The pharmacological basis of therapeutics, International 10TH edition, 2001, 549–555.
106. Gulwadi A.G, Korpinen C.D, Mailman R.B, Nichols D.E, Sit S.Y, Taber M.T, Dinapsoline: Characterization of a D₁ Dopamine Receptor Agonist in a Rat Model of Parkinson's Disease, **Pharmacology and Experimental Therapeutics**, **296**(2), 2001, 338-344.
107. Guo L.J, Nanostructure Fabrication and Applications, Nanoscale Science and Engineering, One-Page Summaries of Faculty Research Projects in the College of Engineering, March 2005, 13.
108. Gutman R.L, Peacock G, D. Robert Lu, Targeted drug delivery for brain cancer treatment, **Controlled Release**, **65**(1-2), 2000, 31-41.
109. Guttman M, Kish S.J, Furukawa Y, Current concepts in the diagnosis and management of Parkinson's disease, **Canada's Leading Medical Journal**, **168** (3), 2003, 544.
110. Häfeli U.O, Magnetically modulated therapeutic systems, **International Journal of Pharmaceutics**, **277**, 2004, 19–24.
111. Haik K.L, Shear D.A, Schroeder U, Sabel B.A, Dunbar G.L, Quinolinic Acid Released from Polymeric Brain Implants Causes Behavioral and Neuroanatomical Alterations in a Rodent Model of Huntington's Disease, **Experimental Neurology**, **163**, 2000, 430–439.
112. Halbach O, Modeling Neurodegenerative Diseases in vivo, **Neurodegenerative Diseases**, **2**(6), 2005, 313-320.
113. Hall V.J, Li J, Brundin P, **Restorative cell therapy for Parkinson's disease: A quest for the perfect cell**, **Seminars in Cell & Developmental Biology**, **18**(6), December 2007, 859-869.

114. Hallett M, Litvan I. The Task Force on Surgery for Parkinson's Disease. Evaluation of surgery for Parkinson's disease: A report of the Therapeutics and Technology Assessment Subcommittee of the American Academy of Neurology, **Neurology**, **53**, 1999, 1910–1921.
115. Haque M.E, Asanuma M, Higashi Y, Miyazaki I, Tanaka K, Ogawa N, Apoptosis-inducing neurotoxicity of dopamine and its metabolites via reactive quinone generation in neuroblastoma cells, **Biochimica Et Biophysica Acta**, **1619**, 2003, 39–52.
116. Hastings T.G, Lewis D.A, Zigmond M.J, Role of oxidation in the neurotoxic effects of intrastriatal dopamine injections, Proceedings of the National Academy of Sciences in the USA, 93(5), March 1996, 1956-1961.
117. Healy K.E Whang K, Thomas C.H, Method of fabricating emulsion freeze-dried scaffold bodies and resulting products, US Patent 5723508, 1998.
118. Hely M.A, Fung V.S.C, Morris J.G.L, **Treatment of Parkinson's disease**, **Clinical Neuroscience**, **7**(6), November 2000, 484-494.
119. Hodge H.C, The chronic toxicity of cellulose acetate phthalate in rats and dogs, **Pharmacology Experimental Therapy**, **80**, 1944, 250-255.
120. Horton M.A and Khan A, Medical nanotechnology in the UK: a perspective from the London Centre for Nanotechnology, **Nanomedicine: Nanotechnology, Biology and Medicine**, **2**(1), 2006, 42-48.
121. Hu G and Li D, Multiscale phenomena in microfluidics and nanofluidics, **Chemical Engineering Science**, **62**(13), July 2007, 3443-3454.
122. Huang Z, Yin G, Liao X, Yao Y, Kang Y, Preparation and magnetic properties of Cu-ferrite nanorods and nanowires, **Colloid and Interface Science**, **317**(2), January 2008, 530-535.
123. Hughes AJ, Daniel SE, Kilford L, Lees AJ. Accuracy of clinical diagnosis of idiopathic Parkinson's disease: a clinico-pathological study of 100 cases, **Neurology and Neurosurgical Psychiatry**, **55**(3), March 1992, 181-184.
124. Hughes G.A, Nanostructure-mediated drug, **Biology and Medicine**, **1**(1), 2005, 22-30.
125. Hymann-Newman Institute for Neurology and Neurosurgery, Parkinson's disease.
126. Ishak R.A.H, Awad G.A.S, Mortada N.D, Nour S.A.K, **Preparation, in vitro and in vivo evaluation of stomach-specific metronidazole-loaded alginate beads as local anti-Helicobacter pylori therapy**, **Controlled Release**, **119**(2), June 2007, 207-214
127. Jain K.K, The role of nanobiotechnology in drug discovery, **Drug Discovery Today**, **10**(21), 2005, 1435-1442.

128. Jain R.A, The manufacturing technique of various drug loaded biodegradable poly(lactide-coglycolide)(PLGA) devices, **Biomaterials**, **21**(23), 2000, 2475-2490.
129. Jain T.K, Morales M.A, Sahoo S.K, Leslie-Pelecky D.L, Labhassetwar V, Review of Iron Oxide Nanoparticles for Sustained Delivery of Anticancer Agents, **Molecular Pharmaceutics**, **2**(3), 2005, 194-205.
130. Jaina J.P, Modia S, Dombb A.J, Kumara N, Role of polyanhydrides as localized drug carriers, **Controlled Release**, **103**(3), 2005, 541-563.
131. Jenner P and Olanow W.C, The pathogenesis of cell death in Parkinson's disease, **Neurology**, **66**, 2006, S24-S36.
132. Kabanov V and Gendelman H.E, Nanomedicine in the diagnosis and therapy of neurodegenerative disorders, **Progress in Polymer Science**, **32**(8/9), August-September 2007, 1054-1082.
133. Kadanthode R.J, An investigation into the neuroprotective effects of melatonin in a model of rotenone-induced neurodegeneration, Masters of Pharmacy, 2003.
134. Kanno M, Matsumoto M, Togashi H, Yoshioka M, Mano Y, Effects of acute repetitive transcranial magnetic stimulation on dopamine release in the rat dorsolateral striatum, **Neurology Science**, **217**, 2004, 73–81.
135. Katz J, Developments in Medical Polymers for Biomaterials Applications, Medical Device & Diagnostic Industry Magazine, 2001.
136. Katzung B.G, Basic & clinical Pharmacology, International 9TH edition, 2004, 447-459.
137. Kawasaki E.S, Player A, **Nanotechnology** nanomedicine, and the development of new, effective therapies for cancer, **Nanomedicine: Nanotechnology, Biology and Medicine**, **1**(2), 2005, 101-109.
138. Kemper E.M, Boogerd W, Thuis I, Beijnen J.H, van Tellingen O, **Modulation of the blood–brain barrier in oncology: therapeutic opportunities for the treatment of brain tumours**, **Cancer Treatment Reviews**, **30**(5), August 2004, 415-423.
139. Kenawy E.R, Abdel-Hay F.I, El-Newehy M.H, Wnek G.E, **Controlled release of ketoprofen from electrospun poly(vinyl alcohol) nanofibers**, **Materials Science and Engineering: A**, **459**(1-2), June 2007, 390-396.
140. Keyes L.D and Douglas T, Process and materials for producing soluble biological mediators from white blood cells, United States Patent 4591557, 1986.
141. Kim D, El-Shall H, Dennis D, Morey T, Interaction of PLGA nanoparticles with human blood constituents, **Colloids and Surfaces B Biointerfaces**, **40**(2), 2005,83-91.

142. Kim H and Fassihi R, Application of a binary polymer system in drug release rate modulation II influence of formulation variables and hydrodynamic conditions on release kinetics, **Pharmaceutics Science**, **86**, 1997, 323-328.
143. Kim J, Lee S, Kim K, Jeon H, Park R, Kim I , Choia Kand, Kwon I.C, Polymeric nanoparticles for protein kinase activity, **The Royal Society of Chemistry**, **13**, April 2007, 1346-1348.
144. Kingsley J.D, Dou H, Morehead J, Rabinow B, Gendelman H.E, Destache C.J, Nanotechnology: A Focus on Nanoparticles as a Drug Delivery System, **Neuroimmune Pharmacology**, **1**, 2006, 340–350.
145. Kohane S, Microparticles and Nanoparticles for Drug Delivery, **Biotechnology and Bioengineering**, **96**(2), 2006, 203-209.
146. Kolchinsky A, Neurosurgical intervention for **Parkinson's** disease: an update, **Surgical Neurology**, **56**(4), 2001, 277-281.
147. Kong L and Pan C, Preparation of dendrimer-like copolymers based on polystyrene and poly (l-lactide) and formation of hollow microspheres, **Polymer**, **49**(1), January 2008, 200-210.
148. Kou H, Emmet C, Shen P, Aswani S, Iwamoto T, Vaghefi F, Cain G, Sanders, Bioerosion and biocompatibility of poly(d,l-lactic-co-glycolic acid) implants in brain, **Controlled Release**, **43** (2-3), 123-130.
149. Kozirowski D and Friedman A, Levodopa drug holiday with amantadine infusions as a treatment of complications in Parkinson's disease, **Movement Disorders**, **22**(7), 1033-1036.
150. Kreuter J, Nanoparticulate systems for brain delivery of drugs, **Advanced Drug Delivery Reviews**, **47**(1), March 2001, 65-81.
151. Kumar A, Calne S.M, Schulzer M, Mak E, Wszolek Z, Van Netten C, Tsui J. K. C, Stoessl A.J, Calne D.B, Clustering of Parkinson Disease: Shared Cause or Coincidence, **Archives of Neurology**, **61**(7), July 2004, 1057-1060.
152. Kuo Y.C and Su **F.L**, **Transport of stavudine, delavirdine, and saquinavir across the blood–brain barrier by polybutylcyanoacrylate, methylmethacrylate-sulfopropylmethacrylate, and solid lipid Nanoparticles**, **International Journal of Pharmaceutics**, **340**(1-2), August 2007, 143-152.
153. Kurkowska-Jastrzbska I, Czonkowski A, Czonkowska A, Ibuprofen and the mouse model of Parkinson's disease, **Annals of Neurology**, **59**(6), 2006, 988-989.

154. Kusuhara H and Sugiyama Y, **Efflux transport systems for drugs at the blood–brain barrier and blood–cerebrospinal fluid barrier**, *Drug Discovery Today*, **6**(3), February 2001, 150-156.
155. Kwon N.H, Beaux M.F, Ebert C, Wang L, Nanowire-Based Delivery of Escherichia coli O157 Shiga Toxin 1 A Subunit into Human and Bovine Cells, *Nano Letters*, **7**(9), 2007, 2718-2723.
156. Lai C and Yu P.H, R(-)-Deprenyl Potentiates Dopamine-Induced Cytotoxicity toward Catecholaminergic Neuroblastoma SH-SY5Y Cells **Toxicology and Applied Pharmacology**, **142**(1), January 1997, 186-191.
157. Landa N, Feinberg M.S, Holbova R, Miller L, Smader C, Leor J, Novel injectable **alginate scaffold** attenuates progressive infarct expansion and preserves left ventricular systolic and diastolic function late after myocardial infarction, *European Heart Journal*, **27**, 2006, 149.
158. Langer R, Drug delivery and targeting, *Nature*, **392**, April 1998, 5-10.
159. Langer R, Hsieh D.S.T, Rhine W, Folkman J, Control of Release Kinetics of macromolecules from polymers, *Membrane Science*, **7**, 1980, 333–350.
160. Latimer K.S, Kircher I.M, Andreasen C.B, Separation of turkey heterophils from blood using two-step ficoll-hypaque discontinuous gradients, *Avian Diseases*, **33**, 1989, 571-573.
161. Layre A, Couvreur P, Chacun H, Richard J, Passirani C, Requier D, Benoit J.P, Gref R, Novel composite core-shell nanoparticles as busulfan carriers, *Controlled Release*, **111**(3), April 2006, 271-280.
162. Lee J, Park J, Jung Y, Kim J, Jong H, Kim T, Bang Y, Histone deacetylase inhibitor enhances 5-fluorouracil cytotoxicity by down-regulating thymidylate synthase in human cancer cells, *Molecular Cancer Therapy*, **5**, 2006, 3085-3095.
163. Leong KF, Cheah CM, Chua CK, Solid freeform fabrication of threedimensional scaffolds for engineering replacement tissues and organs, *Biomaterials*, **24**, 2003, 2363-2378.
164. Lesnik M.S, Upadhyay U, Goodwin R, Tyler B, Brem H, Local Delivery of Doxorubicin for the Treatment of Malignant Brain Tumors in Rats, *Anticancer Research* **2005**, **25**(6B), November 2006, 3825–3831.
165. Levy R.A, Chu T.M, Halloran J.W, Feinberg S.E, Hollister S, CT-generated porous hydroxyapatite orbital floor prosthesis as a prototype bioimplant, *American Journal of Neuroradiology*, **18**(8), 1997, 1522–1525.

166. Lewis T.B and Standaert D.G, **Design of clinical trials of gene therapy in Parkinson disease**, *Experimental Neurology*, **209**(1), January 2008, 41-47.
167. Li Z, Ramay H.R, Hauch K.D, Xiao D, Zhang M, Chitosan–alginate hybrid scaffolds for bone tissue engineering, *Biomaterials*, **26** (18), June 2005,3919-3928.
168. Lim E, A Walk Through the Management of Parkinson’s Disease, *Annual Academy Medicine Singapore*, **34**, 2005, 188-9.
169. Liu G, Garrett M.R, Men P, Zhu X, Perry G, Smith M.A, Nanoparticle and other metal chelation therapeutics in Alzheimer disease, *Biochimica et Biophysica Acta: Molecular Basis of Disease*, **1741**(3), September 2005, 246-252.
170. Liu H and Webster T.J, Nanomedicine for implants: A review of studies and necessary experimental tools, *Biomaterials* , **28**(2), 2007, 354-369.
171. Liu L.S, Liu S.Q, Ng S.Y, Froix M, Ohno T, Heller J, **Controlled release of interleukin-2 for tumour immunotherapy using alginate/chitosan porous microspheres**, *Controlled Release*, **43**(1), January 1997, 65-74.
172. Liu X, Fawcett J.R, Thorne R.G, DeFor T.A , Frey W.H, **Intranasal administration of insulin-like growth factor-I bypasses the blood–brain barrier and protects against focal cerebral ischemic damage**, *Neurological Sciences*, **187**(1-2), June 2001, 91-97.
173. Liu Z, Li J, Nie S, Liu H, Ding P, Pan W, Study of an alginate/HPMC-based in situ gelling ophthalmic delivery system for gatifloxacin, *International Journal of Pharmaceutics*, **315**(1-2), June 2006, 12-1.
174. Lu B, Wen R, Yang H, He Y, Sustained-release tablets of indomethacin-loaded microcapsules: Preparation, in vitro and in vivo characterization, *International Journal of Pharmaceutics*, **333**(1/2), October 2006 87-94.
175. Lu Y, Aguilar C.A, Chen S, Shaping biodegradable polymers as nanostructures: Fabrication and applications, *Drug Discovery Today: Technologies*, **2**(1), 2005, 97-102.
176. Mandrioli R, Saracino M.A, Ferrari S, Berardi D, Kenndler, Raggi M.A, HPLC analysis of the second-generation antidepressant sertraline and its main metabolite N-desmethylsertraline in human plasma, *Chromatography B*, **836**(1-2), May 2006, 116-119.
177. Marin C, Aguilar E, Mengod G, Cortes R, Rodriguez-Oroz M.C, Obeso J.A, Entacapone potentiates the long-duration response but does not normalize levodopa-induced molecular changes, *Neurobiology of Disease*, **32**(3), December 2008, 340-348.

178. Marsden C.D, Parkes J.D, Rees J.E, A year's comparison of treatment of patients with parkinson's disease with levodopa and carbidopa versus treatment with levodopa alone, **The Lancet**, **302**(7844), December 1973, 1459-1462.
179. Marsh L, Neuropsychiatric Aspects of Parkinson's Disease, **Psychosomatics**, **41**, 2000, 15-23.
180. Martinsen A, Skjak Braek G, Smidsrod O, Alginate as immobilization material: I. Correlation between chemical and physical properties of alginate beads, **Biotechnology and Bioengineering**, **33**, 1989, 79–89.
181. Matsuoka M, Wispriyono B, Igisu H, Increased cytotoxicity of cadmium in fibroblasts lacking c-fos, **Biochemical Pharmacology**, **59**(12), June 2000, 1573-6.
182. Matthews R.T, Ferrante R.J, Klivenyi P, Yang L, Klein A.M, Mueller G, Kaddurah-Daouk R, Beal M.F, Creatine and cyclocreatine attenuate MPTP neurotoxicity, **Experimental Neurology**, **157**(1), May 1999, 142-149.
183. McRae-Degueurce A, Hjorth S, Dillon D.L, Mason D.W, Thomas R, Implantable microencapsulated dopamine (DA): a new approach for slow-release DA delivery into brain tissue, **Neuroscience Letter**, **92**(3), 1988, 303-309.
184. Middleton J and Tipton A, Synthetic biodegradable polymers as medical devices, **Medical Plastics and Biomaterials Magazine**, March 1998.
185. Mikos A.G and Temenoff J.S, Formation of highly porous biodegradable scaffolds for tissue engineering, **Electronic Journal of Biotechnology**, **3**(2), 2000.
186. Mishra TS, PR Intranasal delivery: An approach to bypass the blood brain barrier, **Indian Journal of Pharmacology**, **36**(3), 2004, 140-147.
187. Misra, Shahiwala G.S.A, Shah S.P, Drug delivery to the central nervous system: a review, **Pharmacy & Pharmaceutical Sciences**, **6**(2), August 2003, 252-273.
188. Mitra S, Gaur U, Ghosh P.C, Maitra A.N, **Tumour targeted delivery of encapsulated dextran–doxorubicin conjugate using chitosan nanoparticles as carrier**, **Controlled Release**, **74**(1-3), 6 July 2001, 317-323.
189. Miyawaki E, Lyons K, Pahwa R, Motor complications of chronic levodopa therapy in Parkinson's disease, **Clinical Neuropharmacology**, **20**(6), 1997, 523–530.
190. Mladenovska K, Raicki R.S, Janevik E.I, Ristoski T, Pavlova M.J, Kavrovski Z, Dodov M.G, Goracinova K, **Colon-specific delivery of 5-aminosalicylic acid from chitosan-Ca-alginate microparticles**, **International Journal of Pharmaceutics**, **342**(1-2), September 2007, 124-136.
191. Moghimi S.M, Hunter A.C, Murray J.C, Nanomedicine: current status and future prospects, **The FASEB Journal**, **19**, 2005, 311-330.

192. Mohanraj VJ and Chen Y, Nanoparticles – A Review, **Tropical Journal of Pharmaceutical Research**, **5** (1), June 2006, 561-573.
193. Molho S.A, Feustel E.S, Brown P.J, Evans D.L, Stewart S.M, The Biochemistry and Metabolism of Levodopa: Long-Term Comparative Experience, **Clinical Neuropharmacology**, **24**(5), 2001, 295-299.
194. Moos T, Jensen P.H, Absence of prostate apoptosis response-4 protein in substantia nigra of Parkinson's disease autopsies, **Acta Neuropathologica**, **107**(1), January 2004, 23-26.
195. Moshfeghia A.A, Peymanb GA, Micro- and nanoparticulates, **Advanced Drug Delivery Reviews**, **57**(14), 2005, 2047-2052.
196. Mosley R.L, Benner E.J, Kadiu I, Thomas M, Boska M.D, Hasan K, Laurie C, Gendelman H.E, Neuroinflammation, oxidative stress, and the pathogenesis of **Parkinson's** disease, **Clinical Neuroscience Research**, **6**(5), December 2006, 261-281.
197. Mosmann T. Rapid colorimetric assay for cellular growth and survival: application to proliferation and cytotoxicity assays, **Immunological Methods**, **65**, 1983, 55–63.
198. Murbe J, Rechtenbach A, Topfer J, Synthesis and physical characterization of magnetite nanoparticles for biomedical applications, **Nanotechnology, Germany Materials Chemistry and Physics**, **110** , 2008, 426–433.
199. National Cancer Institute, Nanotechnology in Cancer.
200. National Institute of Neurological Disorders and Stroke (NINDS)
201. Nijhara R and Balakrishnan K, Bringing nanomedicines to market: regulatory challenges, opportunities, and uncertainties, **Nanomedicine: Nanotechnology, Biology and Medicine**, **2**(2), 2006, 127-136.
202. Nishiyamaa N, Kataoka K, Current state, achievements, and future prospects of polymeric micelles as nanocarriers for drug and gene delivery, **Pharmacology & Therapeutics**, **112**(3), 2006, 630-648.
203. Nyholm D, The rationale for **continuous** dopaminergic stimulation in advanced Parkinson's disease, **Parkinsonism & Related Disorders**, **13**(1), September 2007, S13-S17.
204. Oberdörster G, Oberdörster E, Oberdörster J. Nanotoxicology: an emerging discipline evolving from studies of ultrafine particles, **Environmental Health Perspective**, **113**, 2005, 823–839.
205. Okun M.S., Stover N.P, Subramanian T, Gearing M, Wainer B.H, Holder C.A, Complications of Gamma Knife Surgery for Parkinson Disease, **Archives of Neurology**, **58**, 2001, 1995-2002.

206. Olbrich C, Gessner A, Schröder W, Kayser O, Müller R.H, **Lipid–drug conjugate nanoparticles of the hydrophilic drug diminazene—cytotoxicity testing and mouse serum adsorption**, *Controlled Release*, **96**(3), May 2004, 425-435.
207. Olivi A, Ewend M.G, Utsuki T, Tyler B, Domb A.J, Brat D.J, Brem H, Interstitial delivery of carboplatin via biodegradable Polymers is effective against experimental glioma in the rat, *Cancer Chemotherapy and Pharmacology*, **39**(1-2), November 1996, 90-96.
208. Olivier A, **Drug Transport to Brain with Targeted Nanoparticles**, *Neurotherapeutics*, **2**(1), January 2005, 108-119.
209. Ono I, Tateshita T, Satou, M, Sasaki T, Matsumoto M, Kodama N, Treatment of large complex cranial bone defects by using hydroxyapatite ceramic implants, *Plastic and Reconstructive Surgery*, **104**(2), 1999, 339–349.
210. Orive G, Carcaboso A.M, Hernández R.M, Gascón A.R, Pedraz J.L, Biocompatibility Evaluation of Different Alginates and Alginate-Based Microcapsules, *Biomacromolecules*, **6**(2), 2005, 927 -931.
211. Owen A.D, Jenner P, Marsden C , Schapira H.V, Oxidative Stress and Parkinson's disease, *Annals of the New York Academy of Sciences*, **786**(1), 1996, 217–223.
212. Palfi, S., Leventhal, L., Chu, Y., Ma, S.Y., Emborg, M., Bakay, R., Deglon, N., Hantraye, P., Aebischer, P. and Kordower, J.H., Lentivirally delivered glial cell line-derived neurotrophic factor increases the number of striatal dopaminergic neurons in primate models of nigrostriatal degeneration, *Neuroscience*, **22**, 2002, 4942–4954.
213. Panikar D and Kishore A, Deep brain stimulation for Parkinson's disease, *Neurology India*, **51**(2), 2003, 167-175.
214. Papapetropoulos S and Mash DC, Psychotic symptoms in Parkinson's disease: from description to etiology, *Neurology*, **252**, 2005, 753–764.
215. Parak W.J, Geriou D, Pellegrino T, Zanchet D, Micheel C, Williams S.C, Boudreau R, Le Gros M.A, Larabell C.A, Alivisatos A.P, Biological applications of colloidal nanocrystals, *Nanotechnology*, **14**, 2003, 15–27.
216. Pardridge W, Blood-Brain Barrier Drug Targeting: The Future of Brain Drug Development, *Molecular Interventions*, **3**, 2003, 90-105.
217. **Pardridge W, Strategies for drug delivery through the blood-brain barrier**, *Neurobiology of Aging*, **10**(5), September-October 1989, 636-637.
218. Pardridge W.M **Molecular Trojan horses for blood–brain barrier drug delivery**, *Current Opinion in Pharmacology*, **6**(5), October 2006, 494-500.

219. Pardridge W.M, **Blood–brain barrier delivery of protein and non-viral gene therapeutics with molecular Trojan horses**, **Controlled Release**, **122**(3), October 2007, 345-348.
220. Pardridge W.M, **Blood–brain barrier delivery**, **Drug Discovery Today**, **12**(1-2), January 2007, 54-61.
221. Pardridge W.M, **The Blood-Brain Barrier: Bottleneck in Brain Drug Development**, **Neurotherapeutics**, **2**(1), January 2005, 3-14.
222. Parkinson J, An essay on the shaking palsy, **Neuropsychiatry Clinical Neuroscience**, **14**, May 2002, 223-236.
223. Patel R, Mechanistic Profiling of Novel Wafer Technology Developed for Rater-Modulated Oramucosal Drug Delivery, Masters in Pharmacy Dissertation, 2005.
224. Pathak P, Meziani M.J, Sun Y.P, Supercritical fluid technology for enhanced drug delivery, **Expert Opinion on Drug Delivery**, **2**(4), 2005, 747-761.
225. Pathirana W, Kariyawasam S Himani, Tibbotumunuwa Hemamali, Perera K, Brain targeted transcranial route of drug delivery of diazepam, **Indian Journal of Pharamceutics**, **68**(4), 2006, 493-496.
226. Peleg-Raibstein D and Feldon J, Effects of dorsal and ventral hippocampal NMDA stimulation on nucleus accumbens core and shell dopamine release, **Neuropharmacology**, **51**(5), 2006, 947-957.
227. Peltonen L, Aitta J, Hyvönen S, Karjalainen M, Hirvonen J, Improved Entrapment Efficiency of Hydrophilic Drug Substance During Nanoprecipitation of Poly(l)lactide Nanoparticles, **Pharmaceutical Science and Technology**, **5**(1), 2004.
228. Peng J, Xie L, Stevenson F.F, Melov S, Di Monte D.A, Andersen J.K, Nigrostriatal Dopaminergic Neurodegeneration in the Weaver Mouse Is Mediated via Neuroinflammation and Alleviated by Minocycline Administration, **Neuroscience**, **26**, 2006, 11644-11651.
229. Perry J.C, Cunha C.D, Anselmo-Franci J, Andreatini R, Miyoshi E, Tufik S, Vital M, Behavioural and neurochemical effects of phosphatidylserine in MPTP lesion of the substantia nigra of rats, **European Journal of Pharmacology**, **484**(2-3), January 2004, 225-233.
230. Peschanski M, Defer G, Nguyen JP, Ricolfi F, Monfort JC, Remy P, Geny C, Samson Y, Hantraye P, Jeny R, Gatson A, Keravel Y, Degos JD, Cesaro P. Bilateral motor improvement and alteration of L-dopa effect in two patients with parkinson's disease following intrastriatal transplantation of fetal ventral mesencephalon, **Brain**, **117**, 1994, 487-499.

231. Pfeiffer R.F, A Promising new technology for Parkinson's disease, **Neurology**, **65**, 2005, S6-S10.
232. Pfeiffer R.F, Transdermal drug delivery in Parkinson's disease, **Summary Aging Health**, **3**(4), 2007, 471-482.
233. Piñón-Segundo E, Ganem-Quintana A, Alonso-Pérez V, Quintanar-Guerrero D, Preparation and characterization of triclosan nanoparticles for periodontal treatment , **International Journal of Pharmaceutics**, **294** (1-2), April 2005, 217-232.
234. Poletto F.S, Fiel L.A, Donido B, Ré M.I, Guterres S.S, Pohlmann A.R, Controlling the size of poly(hydroxybutyrate-co-hydroxyvalerate) nanoparticles prepared by emulsification–diffusion technique using ethanol as surface agent, **Colloids and Surfaces A: Physicochemical and Engineering Aspects**, **324**(1-3), July 2008, 105-112.
235. Polikov V.S, Tresco P.A, Reichert W.A, Response of **brain** tissue to chronically implanted neural electrodes, **Neuroscience Methods**, **148**(1), October 2005, 1-18.
236. Popovic N and Brundin P, Local Controlled Drug Delivery to the Brain: Therapeutic potential of controlled drug delivery systems in neurodegenerative diseases, **International Journal of Pharmaceutics**, **314**(2), 2006,120-126.
237. Popovic N and Brundin P, Therapeutic potential of controlled drug delivery systems in neurodegenerative diseases, **International Journal of Pharmaceutics**, **314**(2), 2006, 120-6.
238. Porter N.L, Pilliar R.M, Grynepas M.D, Fabrication of porous calcium polyphosphate implants by solid freeform fabrication: A study of processing parameters and in vitro degradation characteristics, **Biomedical Materials Research**, **56**(4), 2001, 504–515.
239. Price D.A, Klenerman P, Booth B.L, Phillips R.E, Sewlall A.K, Cytotoxic T lymphocytes, chemokines and antiviral immunity, **Immunology Today**, **20**(5), May 1999, 212-216.
240. Product Information: Azilect®, rasagiline. Teva Pharmaceutical Industries Ltd., Kfar Saba, Israel (PI issued May 2006).
241. Prunier C, Bézard E, Montharu J, Mantzarides M, Besnard J, Baulieu J, Gross C, Guilloteau D, Chalon S, Presymptomatic diagnosis of experimental Parkinsonism with ¹²³I-PE2I SPECT, **NeuroImage**, **19**(3), July 2003, 810-816.
242. Rajeev A. Jain, The manufacturing techniques of various drug loaded biodegradable poly (lactide-co-glycolide) (PLGA) devices, **Biomaterials**, **21**(23), 12000, 2475-2490.
243. Rajput A.H, Environmental toxins accelerate Parkinson's disease onset, **Neurology**, **56**, 2001, 4-5.

244. Rao S.S, Hofmann L.A, Shakil A, Parkinson's Disease: Diagnosis and Treatment, **American Family Physician**, **74**(12), 2006, 2046-2054.
245. Rapoport S.I, Osmotic Opening of the Blood–Brain Barrier: Principles, Mechanism and Therapeutic Applications, **Cellular and Molecular Neurobiology**, **20**(2), April 2000, 217-230.
246. Rascol O, Transdermal delivery of dopaminergic agents, **Neurology**, **65**, 2005, S1-S2.
247. Rastogi R, Sultana Y, Aqil M, Ali A, Kumar S, Chuttani K, Mishra A.K, **Alginate microspheres of isoniazid for oral sustained drug delivery**, **International Journal of Pharmaceutics**, **334**(1-2), April 2007, 71-7.
248. Reading M, Modulated differential scanning calorimetry—a new way forward in materials characterization, **Trends Polymer. Science**, **1**, 1993, 248–253.
249. Redhead M, Davis S.S, Illum L, Drug delivery in poly(lactide-co-glycolide) nanoparticles surface modified with poloxamer 407 and poloxamine 908: in vitro characterisation and in vivo evaluation, **Controlled Release**, **70**(3), 2001, 353-363.
250. Reignier J and Huneault M.A, **Preparation of interconnected poly (ϵ -caprolactone) porous scaffolds by a combination of polymer and salt particulate leaching**, **Polymer**, **47**(13/14) June 2006, 4703-471.
251. Reneker D.H and Yarin A.L, Electrospinning jets and polymer nanofibers, **Polymer**, **49**(10), May 2008, 2387-2425.
252. Richardson-Burns S.M, Hendricks J.L, Foster B, Povlich L.K, Kim D.W, Martin D.C, Polymerization of the conducting polymer poly(3,4-ethylenedioxythiophene) (PEDOT) around living neural cells, **Biomaterials**, **28**(8), March 2007, 1539-1552.
253. **Richter F, Hamann M, Richter A, Moderate degeneration of nigral neurons after repeated but not after single intrastriatal injections of low doses of 6-hydroxydopamine in mice**, **Brain Research**, **1188**(10) January 2008, 148-156.
254. Roberts R.L, Fine R.E Sandra A, Receptor-mediated endocytosis of transferrin at the blood-brain barrier, **Cell Science**, **104**, 1993, 521-532.
255. Roos R.A.C, Tijssen M.A.J, E. A. van der Velde E. A. and D. D. Breimer D. D, The influence of a standard meal on Sinemet CR absorption in patients with Parkinson's disease, **Clinical Neurology and Neurosurgery**, **95**(3), 1993, 215-219.
256. Rotigotine. Microdex ® Healthcare Series, 131.Licensed Subscription, June 2007.
257. Rusted J.M, Newhouse P.A, Levin E.D, Nicotinic treatment for degenerative neuropsychiatric disorders such as Alzheimer's disease and Parkinson's disease, **Behavioural. Brain Research**, **113**(1–2), 2000, 121–129.

258. Sabel B.A, Freese A, Saltzman W.M, Controlled drug delivery systems for treatment of neural disorders, United States Patent 4883666, 1989.
259. Saladin M and Naschie EI, Nanotechnology for the developing world, **Chaos, Solutions & Fractals**, **30**(4), 2006, 769-773.
260. Salvagea J.P, Rosea S.F, Phillipsa G.J, Hanlona G.W, Lloyd A.W, Mab I.Y, Armesb S.P, Billinghamb N.C, Lewisc A.L, Novel biocompatible phosphorylcholine-based self-assembled nanoparticles for drug delivery, **Controlled Release**, **104**(2), 2005, 259-270.
261. **Samii A**, Nutt J.G, Ransom B.R, **Parkinson's disease**, **The Lancet**, **363**(9423), May 2004, 1783-1793.
262. Sandor M, Bailey N.A Mathiowitz E, Characterization of polyanhydride microsphere degradation by DSC, **Polymer**, **43**(2), 2002, 279–288.
263. Sarre S, Ebinger G, Michotte Y, Levodopa biotransformation in hemi-**Parkinson rats**: effect of dopamine receptor agonists and antagonists, **European Journal of Pharmacology**, **296**(3), February 1996, 247-260.
264. Sayles M, Jain M, Baker R.A, The cellular repair of the brain in Parkinson's disease- past, present and future, **Transplant Immunology**, **12**(3-4), 2001, 321-342.
265. **Schallert T**, Fleming S.M, Leasure J.L, **Tillerson J,L**, Bland S.T, CNS plasticity and assessment of forelimb sensorimotor outcome in unilateral rat models of stroke, cortical ablation, parkinsonism and spinal cord injury, **Neuropharmacology**, **39** (5), April 2000, 777-787.
266. Schneider J. S, Rothblat D. S, Differences in release and clearance of extracellular dopamine in the striatum after spontaneous or GM1-ganglioside-stimulated recovery from experimental Parkinsonism, **Restorative Neurology and Neuroscience**, **16**(2), 2000, 97-104.
267. Schroeder U, Sommerfeld P, Sabel B.A, **Efficacy of Oral Dalargin-loaded Nanoparticle Delivery across the Blood–Brain Barrier**, **Peptides**, **1**(4), April 1998, 777-780.
268. Schwarz A.J, Danckaert A, Reese T, Gozzi A, **Paxinos G**, **Watson C**, V. Merlo-Pich E.V, Bifone A, A stereotaxic MRI template set for the rat brain with tissue class distribution maps and co-registered anatomical atlas: Application to pharmacological MRI, **NeuroImage**, **32**(2), August 2006, 538-550.
269. Shetty R.C, Potential pitfalls of nanotechnology in its applications to medicine: Immune incompatibility of nanodevices, **Medical Hypotheses**, **65**(5), 2005, 998-999.
270. Shim S.S, Hammonds M.D, Ganocy S.J, Calabrese J.R, Effects of sub-chronic lithium treatment on synaptic plasticity in the dentate gyrus of rat hippocampal slices, **Progress**

- in **Neuro-Psychopharmacology and Biological Psychiatry**, **31**(2), March 2007, 343-347..
271. Shin Y, Bae I, Arey B.W, Exarhos G.J, Simple preparation and stabilization of nickel nanocrystals on cellulose nanocrystal, **Materials Letters**, **61**(4-15) June 2007, 3215-3217.
272. Shwartz Pharma Neupro ®, A New Alternative to Conventional Parkinson's Therapy, **European Neurological Disease**, 2006.
273. Sibongile Sibambo, Mechanisms for Modifying the Physicochemical and Physicomechanical Properties of Poly Lactic Co-Glycolic Acid: Impact on Controlled Drug Delivery, Masters in Pharmacy Dissertation, 2008.
274. Siepmann J and Siepmann F, Microparticle used as drug delivery systems, **Colloid and Polymer Science**, **133**, 2006, 15-21.
275. Silva G.A, Nanotechnology approaches for drug and small molecule delivery across the blood brain barrier, **Surgical Neurology**, **67**(2), 2007, 113-116.
276. Singh N, Configuration of Crosslinked Multi-Polymeric Multi-Units for Site-Specific Delivery of Nicotine, Masters in Pharmacy Dissertation, 2007.
277. Singh N, Pillay V, Choonara Y.E, Advances in the treatment of Parkinson's disease, **Progress in Neurobiology**, **81**(1) , 2007, 29-44.
278. Sokolsky-Papkov M, Agashi K, Olaye A, Shakesheft K, Domb A.J, Polymer carriers for tissue engineering, **Biomaterials**, **20**, October 2002, 4087-94.
279. Stocchi F, Rasagiline: Defining the Role of a Novel Therapy in the Treatment of Parkinson's disease, **International Journal of Clinical Practice**, **60**(2), February 2006, 215-221..
280. Stokes A.H, Hastings T.G, Vrana K.E, Cytotoxic and genotoxic potential of dopamine, **Neuroscience Research**, **55**(6), 659-665.
281. Subramanian N, Yajnik A, Murthy R.S.R , Artificial Neural Network as an Alternative to Multiple Regression Analysis in Optimizing Formulation Parameters of Cytarabine Liposomes, **AAPS Pharm. Sci. Tech**, **5**(1), 2004, 1-9.
282. Summerfield S.G, Read K, Begley D.J , Obradovic T, Hidalgo I.J, Coggon S, Lewis A.V, Porter R.A, Jeffrey P, Central Nervous System Drug Disposition: The Relationship between in Situ Brain Permeability and Brain Free Fraction, **Pharmacology And Experimental Therapeutics**, **322**, 2007, 205-213.
283. Surgical Procedures for Parkinson's disease, University of Pittsburgh Medical Centre, 2007.

284. Tang Z.G, Black R.J , Curran J.M, Hunt J.A, Rhodes N.P, Williams D.F, Surface properties and biocompatibility of solvent-cast poly[ε-caprolactone] films, **Biomaterials**, **25**(19), August 2004, 4741-4748.
285. Taylor H and Minger S.L , Regenerative medicine in **Parkinson's disease**: generation of mesencephalic dopaminergic cells from embryonic stem cells, **Current Opinion in Biotechnology**, **16**(5), 2005, 487-492 .
286. Teixeira M, Alonsoc MJ, Pintoa M.M.M, Barbosad C.M, Development and characterization of PLGA nanospheres and nanocapsules containing xanthone and 3-methoxyxanthone, **European Journal of Pharmaceutics and Biopharmaceutics**, **59**(3), 2005, 491-500.
287. The Merck Manual of Geriatrics , Chapter 46, Section 6, June 2006
288. Thomas M and Le W. D, Minocycline: Neuroprotective Mechanisms in Parkinson's disease, **Current Pharmaceutical Design**, **10**(6), February 2004, 679-686(8).
289. Thompson P.D, Deep brain stimulation is superior to ablative surgery for Parkinson's disease: the case against, **Clinical Neuroscience**, **8**(3), May 2001, 291-292.
290. Tiyaboonchai W and Limpeanchob N, **Formulation and characterization of amphotericin B–chitosan–dextran sulfate Nanoparticles**, **International Journal of Pharmaceutics**, **329**(1-2), February 2007, 142-149.
291. Toda H, Hamani C, Lozano A, Deep brain stimulation in the treatment of dyskinesia and dystonia, **Neurology Focus**, **17**(1), 2004, 9-13.
292. Tsuji A, Small Molecular Drug Transfer across the Blood-Brain Barrier via Carrier-Mediated Transport Systems, **Neurotherapeutics**, **2**(1), 2005, 54–62.
293. Tuğcu-Demiröz F, Acartürk F, Takka S, Konuş-Boyunağa O, **Evaluation of alginate based mesalazine tablets for intestinal drug delivery**, **European Journal of Pharmaceutics and Biopharmaceutics**, **67**(2), September 2007, 491-497.
294. Uitti R.J, Vingerhoets F.J.G, Hayward M, Cooper S, Snow B.J, Positron Emission Tomography (PET) Measurements of Striatal D2 Receptors in Untreated Parkinson's Disease Patients with Follow-up after 6 and 12 Months' Treatment with SINEMET@ or SINEMET@ CR, **Parkinsonism and Related Disorders**, **3**(1), 1997, 43-46.
295. University of Washington, St Louis, Schlesinger lab, Research Gallery, 2000-2008.
296. Uskoković V, **Nanotechnologies: What we do not know**, **Technology in Society**, **29**(1), January 2007, 43-6.
297. Vats A, Bielby R.C, Tolley N.S, Nerem R, Polak J.M, Stem cells, **Lancet**, **366**(9485), August 2005, 592-602.

298. Verveij E.J.W and Overbeek J.T.G., Theory of the Stability of Lyophobic Colloids, Amsterdam–New York, 1948.
299. Voges J , Lehrke R, Kim D.G, Lucas C, Schröder R, Sturm V, Stricker H, Tissue reactions after long-term intracerebral implantation of three different types of biodegradable polylactide rods in the rat, **Experimental Therapeutics and Oncology**, **2**, March/April 2002, 70.
300. von Burkersroda F, Schedlb L, Göpferich A, Why degradable polymers undergo surface erosion or bulk erosion, **Biomaterials**, **23**(21) , 2002, 4221-4231.
301. Wakabayashi K, Mori F, Takahashi H, **Progression patterns of neuronal loss and Lewy body pathology in the substantia nigra in Parkinson's disease**, **Parkinsonism & Related Disorders**, **12**(2), October 2006, S92-S98.
302. Walkinson G and Waters C.M, Induction of apoptosis in catecholaminergic PC12 cells by L-DOPA: Implications for the treatment of Parkinson's disease, **Clinical Investigation**, **95**(6), June 1995, 2458-2464.
303. Walter BL and Vitek JL. Surgical treatment for Parkinson's disease, **Lancet Neurology**, **3**, 2003, 719–28.
304. Wang X, Zhang K, Zhu M, Yu H, Zhou Z, Chen Y, Hsiao B.S, Continuous polymer nanofiber yarns prepared by self-bundling electrospinning method, **Polymer**, **49**(11), 2008, 2755-2761..
305. Wang Y , Li Y, Sun G, Zhang G, Liu H, Du J, Yang S, Bai J, Yang O, Fabrication of Au/PVP nanofiber composites by Electrospinning, **Applied Polymer Science**, **105**(6), June 2007, 3618-3622.
306. Waters Chromatography Columns and Supplies Catalog 2008-2009, Massachusetts, USA
307. Waynforth H.B, Flecknell, P.A., Cisternal puncture (and intracisternal injection): Experimental and surgical techniques in the rat, Academic Press (London), 1980, 59-61.
308. Welle A, Kroger M, Doring M, Niederer, Pindel E, Chronakis I.S, **Electrospun aliphatic polycarbonates as tailored tissue scaffold materials**, **Biomaterials**, **28**(13), May 2007, 2211-2219.
309. Whang, K, Goldstick, T.K, Healy, K.E, A Biodegradable Polymer Scaffold for Delivery of Osteotropic Factors, **Biomaterials**, **21**, 2000, 2545-2551.
310. Whitney C.M, Medications for parkinson's disease. Patient and family fact sheet, **Neurologist**, **13**(6), November 2007, 387-388.

311. Whittlesey K.J, Shea L.D, Delivery systems for small molecule drugs, proteins and DNA: the neuroscience/biomaterial interface, **Experimental Neurology**, **190**(1), 2004, 1-16.
312. Widmer H.R, Schaller B, Meyer M, Seiler R.W, Glial Cell Line-Derived Neurotrophic Factor Stimulates the Morphological Differentiation of Cultured Ventral Mesencephalic Calbindin- and Calretinin-Expressing Neurons, **Experimental Neurology**, **164**(1), July 2000, 71-81.
313. Williams D.F, The Williams Dictionary of Biomaterials, Liverpool, UK: Liverpool University Press, **40**, 1999.
314. Wilson A.P, Cytotoxicity and Viability Assays in Animal Cell Culture: A Practical Approach, **Oxford University Press**, **1**(3), 2000, 329.
315. Woolfson D.N, Ryadnov M.G, Peptide-based fibrous biomaterials: some things old, new and borrowed, **Current Opinion in Chemical Biology**, **10**(6), 2006, 559-567.
316. www.sciencelab.com
317. Xiong S, Wang Q, Xia H, Preparation of polyaniline nanotubes array based on anodic aluminum oxide template, **Materials Research Bulletin**, **39**(10), August 2004, 1569-1580.
318. Yabrov A, Okunev Y, Medicine without drugs – a new direction for application of nanotechnology, **Medical Hypotheses**, **63**(1), 2004, 149-154.
319. Yang L, Alexandridis P, Physicochemical aspects of drug delivery and release from polymer-based colloids, **Current Opinion in Colloid & interface Science**, **5**(1-2), 2000, 132-143.
320. Yedjou C.J, Moore P, Tchounwou P.B, Dose- and Time-Dependent Response of Human Leukemia (HL-60) Cells to Arsenic Trioxide Treatment, **International Journal of Environmental Research and Public Health**, **3**(2), 2006, 136-140.
321. Yeh K.C, August T.F, Bush D.F, Lasseter K.C, Musson D.G, Schwartz S, Smith M.E, Titus D.C, Pharmacokinetics and bioavailability of Sinemet CR: a summary of human studies, **Neurology**, **39**(11), 1989, 25-38.
322. Yetkin H, Senkoylu A, Cila E, Ozturk A, Simsek A, Biodegradable implants in orthopedics and traumatology, **Turkish Journal of Medical Science**, **30**, 2000, 297-301.
323. **Yulmetyev R.M**, Demin S.A, Panischev O.Y, Hänggi P, Timashev S.F and Vstovsky G.V, Regular and stochastic behavior of Parkinsonian pathological tremor signals, **Physica A: Statistical Mechanics and its Applications**, **369**(2), September 2006, 655-678.

324. Zabetian P, Samii A, Mosley A.D, Roberts J.W, Leis B.C and Yearout D., A clinic-based study of the LRRK2 gene in Parkinson disease yields new mutations, **Neurology**, **65**, 2005, 741–744.
325. Zambaux M.F, Bonneaux F, Gref R, Maincent P, Dellacherie E, Alsono M.J, Labrude P, VigNeron C, Influence of experimental parameters on the characteristics of poly(lactic acid) nanoparticles prepared by a double emulsion method, **Controlled Release**, **50**(1-3), 1998, 31-40.
326. Zaru M, Mourtas S, Klepetsanis P, Fadda A.M, Antimisiaris S.G, Liposomes for drug delivery to the lungs by nebulization, **European Journal of Pharmaceutics and Biopharmaceutics**, **67**(3), April 2007, 655-666.
327. Závířová V, Koneracká M, Štrbák O, Tomařovičová N, Kopčanský P, Timko M, Vavra I, **Encapsulation of indomethacin in magnetic biodegradable polymer Nanoparticles, Magnetism and Magnetic Materials**, **311**(1), April 2007, 379-382.
328. Zhang L, Gu F.X, Chan J.M, Wang A.Z, Langer R.S, Farokhzad O.C, Nanoparticles in Medicine: Therapeutic Applications and Developments, **Clinical Pharmacology & Therapeutic**, **83**(5), 2007.
329. Zhao Q, Han B, Wang Z, Gao C, Peng C, Shen J, **Hollow chitosan-alginate multilayer microcapsules as drug delivery vehicle: doxorubicin loading and in vitro and in vivo studies**, **Nanomedicine: Nanotechnology, Biology and Medicine**, **3**(1), March 2007, 63-74.
330. Ziv I, Melamed E, Nardi N, Luria D, Ashiron A, Offen D, Barzilai A, Dopamine induces apoptosis-like cell death in cultured chick sympathetic neurons-a possible novel pathogenic mechanism in Parkinson's disease, **Neuroscience Letters**, **170**, 1994, 136-140.
331. Zmora S, Glicklis R, Cohen S, Tailoring the pore architecture in 3-D alginate scaffolds by controlling the freezing regime during fabrication, **Biomaterials**, **23**(20), Oct 2002, 4087-94.

UNIVERSITY OF THE WITWATERSRAND, JOHANNESBURG

STRICTLY CONFIDENTIAL

ANIMAL ETHICS SCREENING COMMITTEE (AESC)

CLEARANCE CERTIFICATE NO. 2007/76/4

APPLICANT: Ms S Pillay
SCHOOL: Pharmacy and pharmacology
DEPARTMENT:
LOCATION:

PROJECT TITLE: In vivo evaluation of an implantable polymeric scaffold containing dopamine hydrochloride


Number and Species

45 Sprague dawley rats


Approval was given for to the use of animals for the project described above at an AESC meeting held on 20071127. This approval remains valid until 20091127

The use of these animals is subject to AESC guidelines for the use and care of animals, is limited to the procedures described in the application form and to the following additional conditions:

Clarify that each animal is sampled only once, must use stereotaxic equipment during surgery

Signed:  Date: 30/11/2007
(Chairperson, AESC)

I am satisfied that the persons listed in this application are competent to perform the procedures therein, in terms of Section 23 (1) (c) of the Veterinary and Para-Veterinary Professions Act (19 of 1982)

Signed:  Date: 30/11/2007
(Registered Veterinarian)

cc: Supervisor:
Director: CAS

Works 2000/lain0015/AESCCert.wps

UNIVERSITY OF THE WITWATERSRAND, JOHANNESBURG

Division of the Deputy Registrar (Research)

HUMAN RESEARCH ETHICS COMMITTEE (MEDICAL)

R14/49 Davids

CLEARANCE CERTIFICATE

PROTOCOL NUMBER M070519

PROJECT

Novel compounds in the induction of Apoptosis in various cancer cell lines

INVESTIGATORS

Dr H Davids

DEPARTMENT

Pharmacy & Pharmacology

DATE CONSIDERED

07.05.25


DECISION OF THE COMMITTEE*

APPROVED UNCONDITIONALLY

Unless otherwise specified this ethical clearance is valid for 5 years and may be renewed upon application.

DATE 07.06.14

CHAIRPERSON


(Professors PE Cleaton-Jones, A Dhai, M Vorster, C Feldman, A Woodiwiss)

*Guidelines for written 'informed consent' attached where applicable

cc: Supervisor : Dr H Davids

DECLARATION OF INVESTIGATOR(S)

To be completed in duplicate and **ONE COPY** returned to the Secretary at Room 10005, 10th Floor, Senate House, University.

I/We fully understand the conditions under which I am/we are authorized to carry out the abovementioned research and I/we guarantee to ensure compliance with these conditions. Should any departure to be contemplated from the research procedure as approved I/we undertake to resubmit the protocol to the Committee. **I agree to a completion of a yearly progress report.**

PLEASE QUOTE THE PROTOCOL NUMBER IN ALL ENQUIRIES